SUPRAMOLECULAR METAL-BASED ENTITIES FOR BIOMEDICAL AND BIOLOGICAL APPLICATIONS

EDITED BY: Angela Casini and James D. Crowley
PUBLISHED IN: Frontiers in Chemistry

frontiers Research Topics

ISSN 1664-8714
ISBN 978-2-88945-899-8
DOI 10.3389/978-2-88945-899-8

About Frontiers

Frontiers is more than just an open-access publisher of scholarly articles: it is a pioneering approach to the world of academia, radically improving the way scholarly research is managed. The grand vision of Frontiers is a world where all people have an equal opportunity to seek, share and generate knowledge. Frontiers provides immediate and permanent online open access to all its publications, but this alone is not enough to realize our grand goals.

Frontiers Journal Series

The Frontiers Journal Series is a multi-tier and interdisciplinary set of open-access, online journals, promising a paradigm shift from the current review, selection and dissemination processes in academic publishing. All Frontiers journals are driven by researchers for researchers; therefore, they constitute a service to the scholarly community. At the same time, the Frontiers Journal Series operates on a revolutionary invention, the tiered publishing system, initially addressing specific communities of scholars, and gradually climbing up to broader public understanding, thus serving the interests of the lay society, too.

Dedication to Quality

Each Frontiers article is a landmark of the highest quality, thanks to genuinely collaborative interactions between authors and review editors, who include some of the world's best academicians. Research must be certified by peers before entering a stream of knowledge that may eventually reach the public - and shape society; therefore, Frontiers only applies the most rigorous and unbiased reviews.
Frontiers revolutionizes research publishing by freely delivering the most outstanding research, evaluated with no bias from both the academic and social point of view. By applying the most advanced information technologies, Frontiers is catapulting scholarly publishing into a new generation.

What are Frontiers Research Topics?

Frontiers Research Topics are very popular trademarks of the Frontiers Journals Series: they are collections of at least ten articles, all centered on a particular subject. With their unique mix of varied contributions from Original Research to Review Articles, Frontiers Research Topics unify the most influential researchers, the latest key findings and historical advances in a hot research area! Find out more on how to host your own Frontiers Research Topic or contribute to one as an author by contacting the Frontiers Editorial Office: researchtopics@frontiersin.org

SUPRAMOLECULAR METAL-BASED ENTITIES FOR BIOMEDICAL AND BIOLOGICAL APPLICATIONS

Topic Editors:
Angela Casini, Cardiff University, United Kingdom
James D. Crowley, University of Otago, New Zealand

Research in the discovery of metal supramolecular complexes, mainly formed by the self-assembly of inorganic metal compounds with either inorganic or organic molecules via coordination (or organometallic) bonds, is a rapidly developing and newly rising highlight interdisciplinary field. This Reseach Topic is aimed at providing representative examples of supramolecular metal-based entities for different biological and biomedical applications.

Citation: Casini, A., Crowley, J. D., eds. (2019). Supramolecular Metal-Based Entities for Biomedical and Biological Applications. Lausanne: Frontiers Media.
doi: 10.3389/978-2-88945-899-8

Table of Contents

frontiers in Chemistry

EDITORIAL
published: 26 April 2019
doi: 10.3389/fchem.2019.00293

Editorial: Supramolecular Metal-Based Entities for Biomedical and Biological Applications

Angela Casini[1]* *and James D. Crowley*[2]

[1] School of Chemistry, Cardiff University, Cardiff, United Kingdom, [2] Department of Chemistry, University of Otago, Dunedin, New Zealand

Keywords: supramolecular complex, MOF (Metal-Organic-Framework), metallacages, metallacycle complexes, therapy, drug delivery systems, cancer, self-assembly

Editorial on the Research Topic

Supramolecular Metal-Based Entities for Biomedical and Biological Applications

The biomedical and biological application of supramolecular metal-based structures—including the discrete supramolecular coordination complexes (SCCs) and polymeric metal organic frameworks (MOFs)—is an emergent research area. In fact, in the last decade, a number of studies demonstrated the potential of these supramolecular compounds as novel anticancer drugs, drug delivery systems, and imaging agents, as well as for molecular recognition of relevant biomolecules.

The present article collection includes an overview of the examples of discrete 2D- and 3D-supramolecular metal-based systems, with focus on cancer therapy, in the review of Ahmedova. The review covers the specific case of 2D metalacycles, as well as 3D metallacages, helicates, capsules and barrels, and marks out some key tendencies in relation to their biological activity and potential areas of biomedical application.

Of note, the point of view of one of the pioneers in this research area, Therrien, is provided in a review focused on the role of the second coordination sphere, including H-bonding, hydrophobic, electrostatic, and van der Waals interactions, in the biological activity of arene ruthenium metalla-assemblies. These types of interactions are crucial in the design of supramolecular entities implemented for molecular recognition.

Thus, a number of original papers in this issue report on the use of selected metallacages as cytotoxic agents against human cancer cells. For example, Vasdev et al. reported on $[Pd_2L_4]^{4+}$ metallacages featuring *bis*-quinoline and bis-isoquinoline-based ligands. The *bis*-quinolone-based cage was found to be helical while the *bis*-isoquinoline-based system was lantern shaped. The binding of the anticancer drug cisplatin was also examined. It was shown that only the *bis*-isoquinoline cage interacted with the drug, suggesting that the helical twist interferes with the host-guest interaction. Both new cages were shown to be more cytotoxic against cancer cell lines than related pyridyl based systems.

Interestingly, Wang et al. provided the proof-of-concept of using nanoprecipitation to formulate hydrophobic Pt(II)-organic cages.

Along the same line, the antiproliferative effects of a self-assembled hexagonal Pd(II) macrocycle against a small panel of cancer cell lines were found comparable to cisplatin in the paper by Singh et al.

Furthermore, Sun et al. explored the potential of encapsulating Ru(II) polypyridyl complexes in macrocyclic host compounds, namely cucurbit[10]urils (Q[10]), to reduce the toxicity of Ru(II) complexes. The Q[10] encapsulation enhanced the pharmacokinetics of one of the ruthenium complexes which could potentially enable the complex to be used as a new type of antimicrobial

Edited and reviewed by:
Tony D. James,
University of Bath, United Kingdom

***Correspondence:**
Angela Casini
casinia@cardiff.ac.uk

Specialty section:
This article was submitted to Supramolecular Chemistry, a section of the journal Frontiers in Chemistry

Received: *02 April 2019*
Accepted: *10 April 2019*
Published: *26 April 2019*

Citation:
Casini A and Crowley JD (2019) Editorial: Supramolecular Metal-Based Entities for Biomedical and Biological Applications. Front. Chem. 7:293. doi: 10.3389/fchem.2019.00293

agent. The host-guest complex between twisted cucurbit[14]uril and thioflavin T was also explored for sensing of non-fluorescent triazole fungicides by Fan et al.

Peptides are highly versatile building blocks, encoding precise structural and functional information within their amino acid sequence, which can be used to design and synthesize novel supramolecular metal-based helicates structures endowed with molecular recognition properties. In the work by Gómez-González et al. the modification of the T4 Fibritin foldon with metal-chelating bipyridines allowed the obtainment of Fe helicates which display good *in vitro* DNA binding and selectivity toward three-way DNA junctions.

Among the features of supramolecular-based scaffolds, their host-guest chemistry is certainly interesting to exploit them as drug delivery systems or as biosensors. Thus, Woods et al. reported on a series of *exo*-functionalized $[Pd_2L_4]^{4+}$ metallacages featuring 2,6-bis(pyridin-3-ylethynyl)pyridine) ligands. The encapsulation of the anticancer drug cisplatin in selected cages has been studied using a combination of NMR spectroscopy methods, and the obtained results show that if the solvent is of sufficient polarity, cisplatin encapsulation can easily occur in the hydrophobic cavity of the cage despite the absence of hydrogen-bond accepting cavity-facing residues.

A novel aspect of this research field concerns the use of supramolecular organometallic complexes, whereby the (organic) linker is forming the organometallic bond to the metal node, for therapy. Thus, the antimicrobial and anticancer properties of organometallic Ag(I) and Au(I) pillarplexes were explored in different bacterial and human cancer cells, respectively (Pöthig et al.). The obtained results showed more relevant bioactivity in the case of the silver compounds.

Within this framework, Barnard et al. developed the synthesis of Au(I) and Pd(II) N-heterocyclic carbene (NHC) complexes derived from tetra-imidazolium linked macrocycles for anion sensing. Interestingly, some of the Ag(I) and the analogous Au(I) complexes adopted intriguing hexanuclear structures with the general formula $[M_6L_3]^{6+}$. It is envisaged that these novel scaffolds could allow the slow release of metal ions for the treatment of bacterial infections.

Overall, as highlighted in the contributions to this special issue, the myriad of possible metal-based supramolecular structures and their almost limitless modularity and tunability suggests that the biomedical applications of these complex chemical entities will continue to emerge.

AUTHOR CONTRIBUTIONS

All authors listed have made a substantial, direct and intellectual contribution to the work, and approved it for publication.

Conflict of Interest Statement: The authors declare that the research was conducted in the absence of any commercial or financial relationships that could be construed as a potential conflict of interest.

frontiers in Chemistry

REVIEW
published: 14 December 2018
doi: 10.3389/fchem.2018.00620

Biomedical Applications of Metallosupramolecular Assemblies—Structural Aspects of the Anticancer Activity

*Anife Ahmedova**

Laboratory of Biocoordination and Bioanalytical Chemistry, Faculty of Chemistry and Pharmacy, Sofia University, Sofia, Bulgaria

The design and development of metallosupramolecular systems has resulted in construction of a myriad of fascinating structures with highly diverse properties and potential applications. Assessment of the biomedical applications of metallosupramolecular assemblies is an emerging field of research that stems from the recently demonstrated promising results on such systems. After the pioneering works of Therrien and coworkers on organometallic Ru-cages with promising anticancer properties, this topic has evolved to the more recent studies on bioactivity of supramolecular coordination complexes built from different metal ions and various multidentate ligands. Sufficient amount of data on the anticancer activity of metallosupramolecules has already been reported and allows outlining some general tendencies in the structural aspects of the biological activity. The main structural properties of the complexes that can be readily modified to enhance their activity are the size, the shape and charge of the formed complexes. Moreover, the intrinsic properties of the building components could predetermine some of the main characteristics of the overall supramolecular complex, such as its optical properties, chemical reactivity, solubility, etc., and could, thereby, define the areas of its biomedical applications. The unique structural property of most of the metallosupramolecular assemblies, however, is the presence of a discrete cavity that renders a whole range of additional applications resulting from specific host-guest interactions. The encapsulations of small bioactive or fluorescent molecules have been employed for delivery or recognition purposes in many examples. On the other hand, metallosupramolecules have been imbedded into target-specific polymeric nanoparticles that resulted in a successful combination of their therapeutic and diagnostic properties, making them promising for theranostic application in cancer treatment. The aim of this review paper is to mark out some key tendencies in the reported metallosupramolecular structures in relation with their biological activity and potential areas of biomedical application. In this way, a useful set of guidelines can be delineated to help synthetic chemists broaden the application areas of their supramolecular systems by few structural changes.

Keywords: metallacycle, metallacage, anticancer, capsule, encapsulation

OPEN ACCESS

Edited by:
James D. Crowley,
University of Otago, New Zealand

Reviewed by:
Yaorong Zheng,
Kent State University, United States
Dong-Sheng Guo,
Nankai University, China

***Correspondence:**
Anife Ahmedova
ahmedova@chem.uni-sofia.bg

Specialty section:
This article was submitted to Supramolecular Chemistry, a section of the journal Frontiers in Chemistry

Received: *30 September 2018*
Accepted: *30 November 2018*
Published: *14 December 2018*

Citation:
Ahmedova A (2018) Biomedical Applications of Metallosupramolecular Assemblies—Structural Aspects of the Anticancer Activity. Front. Chem. 6:620. doi: 10.3389/fchem.2018.00620

INTRODUCTION

The coordination bond directed self-assembly processes have been broadly exploited in building metallosupramolecular species with diverse composition (Bilbeisi et al., 2014), discrete size and shape (Schmidt et al., 2014; Cook and Stang, 2015), and variety of useful properties. Unarguably, the aesthetics of these highly symmetric metallosupramolecules has been the initial source of inspiration for many chemists. This resulted in not only building a myriad of fascinating structures but also in establishing the main principles in the design and synthesis of metallosupramolecular complexes with predefined shapes by exploiting the bond directionality and the coordination properties of the metal ions, and intelligent design of the linking organic ligands (Datta et al., 2018). Nowadays, the main targets are the specific properties of the metallosupramolecular complexes in view of their practical applications that range from chemical catalysis to multi-purpose and stimuli-responsive advanced materials (McConnell et al., 2015). The demonstrated high potential to purposefully combine the properties of metal ions with that of organic ligands has recently attracted the attention of bioinorganic chemists which added up more facets to the range of practical use of the metallosupramolecules—their biological application for therapy and/or diagnostics (Casini et al., 2017; Leung et al., 2017).

The continuous studies related to the clinical use of Pt-complexes as anticancer drugs have evolved to establishing structure-activity relationships for this class of compounds. It is, therefore, not surprising that the first studies on the potential biological applications of metallosupramolecules had focused on anticancer activity of Pt-linked metallosupramolecular cycles (Mounir et al., 2007) and interaction of Fe- or Ru-linked metallohelicates with DNA fragments (Hotze et al., 2006; Malina et al., 2008). This had also given impetus to explore a broader range of metal complexes including the organometallic half-sandwich structures (Aird et al., 2002). Some of the initial examples for studying in details the anticancer activity profiles of coordination driven self-assemblies are the organometallic Ru(II) metallacycles and cages that have been extensively investigated (Therrien et al., 2008; Smith and Therrien, 2011; Dubey et al., 2013; Vajpayee et al., 2013). Thereby, the topic of metal-based drugs had naturally reached for the advantages that metallosupramolecular entities can provide—the major one is their encapsulation and delivery potential in addition to the intrinsic properties of their building components (Therrien et al., 2008; Schmitt et al., 2012; Therrien, 2013; Ma and Zhao, 2015).

Abbreviations: CDDP, cisplatin; SISO, cervix adenocarcinoma; A-427, lung carcinoma; LCLC-103H, large cell lung cancer; 5637, urinary bladder carcinoma; U2OS, osteosarcoma; VM-1, cisplatin resistant melanoma cell line; MCF7, breast cancer; A549, lung carcinoma; KB, oral cancer; HaCaT, skin keratinocyte; MDA-MB-231, human breast adenocarcinoma cell line; T98G, (brain tumor); SNU-80, (thyroid cancer); HEK-293, human embryonic kidney cells (non-malignant cell lines); HepG2, human hepatocellular carcinoma; DU-145, prostate cancer cells; MCF10A, immortalized non-malignant breast tissue; SKOV-3, Human ovarian cancer; HBL100 and T47D, Human breast-tumor cell lines; HT-29, colorectal adenocarcinoma cells; T-24, bladder cancer cells; SKW-3, T-cell leukemia; HL-60, acute myelocyte leukemia; HL-60/Dox and HL-60/CDDP, Doxorubicin and cisplatin-resistant counterparts of the HL-60 cells.

As a multidisciplinary field, the topic of biomedical application of metallosupramolecules requires mutual understanding between synthetic chemists and biologists with the continuing help of specialist in photochemistry, pharmacology, bioimaging, etc. With the ultimate goal to facilitate this process, we intended to describe the recent achievements in the design of metallacycles, metallacages and helicates, and metallosupramolecular capsules and barrels in view of their anticancer properties, recognition of biomolecules with therapeutic implication, as well as improved delivery of bioactive molecules for therapeutic or imaging purposes. The examples of advanced nanomaterials that are based on, or incorporate, metallosupramolecular entities have grown in number and enriched in functionality, and are, therefore, given a major importance in this review paper. While the specific areas of biological applications of the metal-based supramolecules are described, the effect of their characteristic structural features is emphasized. This includes the charge, the shape and the size of the metallosupramolecules, as well as their specific cavity, which reflect the overall stability, reactivity, encapsulation potential, etc.—all being related to the biologically relevant applications. Ultimately, the wide variety of structures with desired composition and properties that can be suitably obtained through supramolecular coordination chemistry, makes this class of compounds a generous area for exploration not only from synthetic point of view but also in view of their biological activity.

METALLACYCLES

As two-dimensional structures, the properties of metallacycles can be tuned by mere combination of the intrinsic characteristics of the metal ion and the linking organic ligands, thus forming supramolecular entities of variable size, shape, and charge. The stability issues have been overcome by employing inert metal ions as metal hinges or organometallic clips that form more robust metal-carbon bonds. Among the latter are the half-sandwich Ru(II) arene clips with bridging oxalate ligands that have been developed by Süss-Fink and coworkers and employed in the construction of the first organometallic Ru(II) metallamacrocycles (Yan et al., 1997). As the anticancer properties of ruthenium complexes came into focus after their introduction into clinical trials, and the first reports on the *in vitro* and *in vivo* cytotoxicity of a series of novel Ru(II) organometallic arene complexes (Aird et al., 2002), the topic expanded further on to the anticancer potency of metallosupramolecular assemblies with the pioneering works of Therrien and coworkers (Therrien et al., 2008; Mattsson et al., 2009). Several groups had greatly contributed in the field of biological applications of metallacycles of different shape and composition. The anticancer properties of series of tetracationic metallacycles, formed by [2+2] assembly between dipyridyl ligands and Ru(II) arene clips with oxalate or dioxydo-1,4-quinonato types of bridges of different size, have been thoroughly studied and later reviewed by Cook, Stang and coworkers (Cook et al., 2013). While this class of organometallic Ru(II)

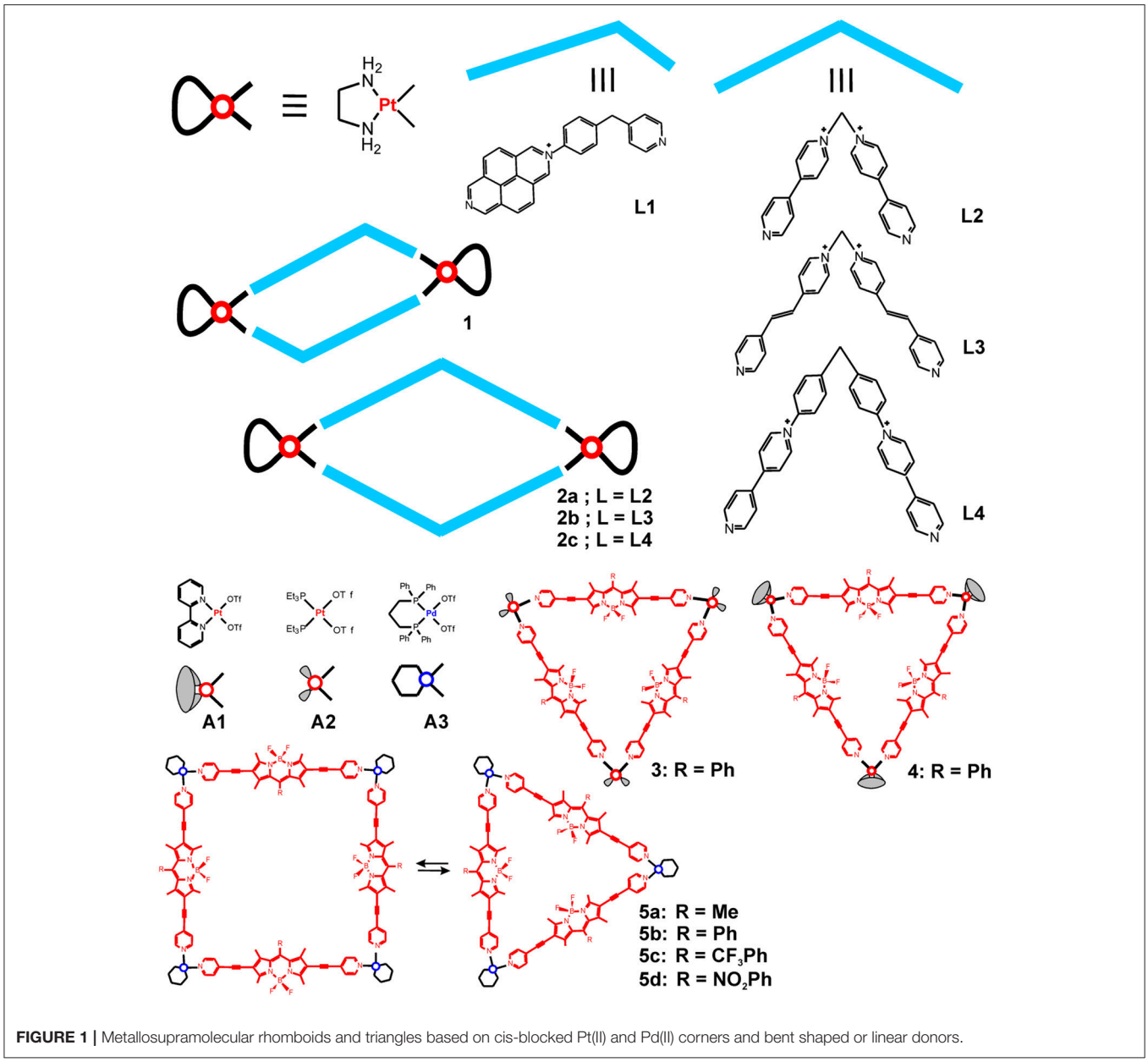

FIGURE 1 | Metallosupramolecular rhomboids and triangles based on cis-blocked Pt(II) and Pd(II) corners and bent shaped or linear donors.

metallacycles demonstrated promising cytotoxicity profiles and structure-activity relationships could be outlined, the bis-ruthenium arene clips played further role in building 3D supramolecular cages and boxes by coordinating with tripodal or tetrapodal pyridyl ligands. Thereby, additional functionality has been introduced in terms of guest-encapsulation capability that further empowered the biological potential of the organometallic arene-metallosupramolecules. This topic has been extensively reviewed (Zhang et al., 2017) and therefore shall be left outside the scope of this paper.

Pt(II) and Pd(II)-cornered square-planar complexes have long been utilized in building highly symmetric 2D and 3D structures of desired shape and size. As chemically more inert units, the ethylenediamine-Pt(II) corners have been used to form [2+2] self-assemblies with rhomboidal structures by coordinating with bent-shape bipyridyl ligands. Some recent examples utilized the cationic N-monoalkylated 4,4′-bipyridinium or 2,7-diazapyrenium based ligands (Terenzi et al., 2012; Domarco et al., 2017) depicted in **Figure 1**. Similarly to earlier reports on DNA-binding capability of tetranuclear Pt(II) squares of linear bipyridyne ligands (Mounir et al., 2007), the formed hexa- and octacationic Pt(II) rectangular metallacycles strongly bind native and G-quadruplex DNA. While the smaller size, unsymmetrical 2,7- diazapyrenium ligand is able to intercalate the DNA, the formed metallacycle (**1**) binds DNA ten times more strongly and bends its structure, thereby blocking the DNA transaction that possibly reflects on the observed anticancer activity against four types of human cancer cell lines (Terenzi et al., 2012). Similarly, the octacationic Pt(II)-cornered metallacycles **2a-c** exhibit moderate anticancer activity as compared to cisplatin

TABLE 1 | Cytotoxicity data of selected metallacycles against a panel of human cancer cells.

Compound	IC_{50} (hrs of incubation)/Type of cells (IC_{50} of ref. compound)	IC_{50} (hrs of incubation)/Type of cells (IC_{50} of ref. compound)	IC_{50} (hrs of incubation)/Type of cells (IC_{50} of ref. compound)	IC_{50} (hrs of incubation)/Type of cells (IC_{50} of ref. compound)	References
1	19.24 ± 7.13 μM (96 h)/SISO (0.24 ± 0.05/CDDP)	3.12 ± 1.22 μM (96 h)/A-427 (1.27 ± 0.25/CDDP)	9.47 ± 3.12 μM (96 h)/LCLC-103H (1.09 ± 0.40/CDDP)	7.61 ± 6.65 μM (96 h)/5637 (0.37 ± 0.08/CDDP)	Microtitre assay (Terenzi et al., 2012)
2a	37.8 ± 3.3 μM (72 h)/U2OS (3.8 ± 3.0/CDDP)	>50 μM (72 h)/VM-1 (4.43 ± 0.05/CDDP)	32.1 ± 7.4 μM (72 h)/MCF7 (6.7 ± 0.3/CDDP)		Domarco et al., 2017
2b	28.9 ± 4.1 μM (72 h)/U2OS (3.8 ± 3.0/CDDP)	31.8 ± 0.5 μM (72 h)/VM-1 (4.43 ± 0.05/CDDP)	39.4 ± 3.4 μM (72 h)/MCF7 (6.7 ± 0.3/CDDP)		Domarco et al., 2017
2c	42.3 ± 4.6 μM (72 h)/U2OS (3.8 ± 3.0/CDDP)	>50 μM (72 h)/VM-1 (4.43 ± 0.05/CDDP)	39.6 ± 4.5 μM (72 h)/MCF7 (6.7 ± 0.3/CDDP)		Domarco et al., 2017

(**Table 1**), which has also been related to their strong binding to DNA (Domarco et al., 2017). Interestingly, the size of the rectangular box determines their effect on the DNA binding and the G4 folding process—the smaller Pt-box exhibited lower binding affinity but better selectivity for a particular G4 topology. The middle-sized box **2b** showed highest anticancer activity against the tested cancer cells, including the cisplatin resistant cell line VM-1, which, however, can be associated with the detected moderate toxicity of the free ligand (**L3**) against the U2OS cells (38.2 ± 3.4 μM).

More recently, new types of cornered Pt(II) and Pd(II) square-planar complexes (**A1-A3**, **Figure 1**) have been utilized in building metallosupramolecules with potential biomedical use. Notable examples are the highly fluorescent triangles constructed from boron dipyrromethene (BODIPY) based dipodal ligands and Pt(II) or Pd(II) corners, as they combine cellular imaging and cancer treatment potency of the building components. The highly emissive BODIPY-Platinum supramolecular triangles (**3** and **4** in **Figure 1**) proved potent for intracellular visualization by confocal microscopy as well as for photodynamic therapy (PDT) and chemotherapy (Zhou et al., 2018a). Indeed, these metallacycles were used in the form of nanoparticles (NPs) that have been prepared through nanoprecipitation. More favorable cellular internalization of the NPs, formed from the cationic metallacycles **3** and **4**, has been observed in comparison with the free, pyridine functionalized BODIPY ligand. Furthermore, metallacycles **3** and **4** demonstrated strong anticancer activity against HeLa cells, which is intrinsic property of the Pt(II) corners **A1** and **A2** (**Table 2**). By light irradiation, however, the anticancer activity could be further amplified through inducing the photodynamic therapy modality, which is characteristic property of the BODIPY fluorophore, and have resulted in significant enhancement in the cytotoxicity against the cisplatin resistant cell line A2780cis. Thereby, effective theranostic agents have been obtained through combination of the chemotherapeutic potential of the platinum acceptors with the BODIPY donors as imaging probes and photosensitizers.

In another work, BODIPY derived Pd(II) metallosupramolecular triangles have been obtained by using Pd(II) hinges that are *cis*-capped with 1,3-bis-diphenylphosphino-propane, and the triangle-to-square conversion was studied (**5a-d** in **Figure 1**) (Gupta et al., 2017). The structures were fully characterized by ^{1}H, ^{31}P NMR, ESI-MS, and X-ray diffraction (of the triangle). The triangle and square topologies exist in a solvent-dependent equilibrium with the triangles being favored in higher polarity solvents. The stability of the complexes has been evaluated by UV-Vis absorption in presence of chlorides and in phosphate-buffered solution in DMSO or Dulbecco's Modified Eagle Medium, showing no change in the spectra for up to 48 h, except for the partial disruption seen upon addition of chloride ions. These BODIPY derived Pd(II) supramolecular triangles showed selective cytotoxicity against brain cancer (glioblastoma) cells U87 in comparison to that against normal brain cells WI-38. The anticancer activity of the triangles is higher or comparable to that of cisplatin, whereas the estimated selectivity is less pronounced than the selectivity of cisplatin (**Table 2**). These green fluorescent metallacycles have also been tested for fluorescence imaging of the cancer cells; the data demonstrated internalization in the cytoplasm and accumulation of aggregates in the cell membrane but not in the nucleus. Unlike the smaller precursors, the supramolecular triangles show appreciable interaction with the tested biomolecules—dsDNA, ssDNA, and BSA.

Hexagonal metallamacrocycles have been obtained by self-assembly of an organometallic platinum(II) clip **A4** with linear dipodal ligands, 4,4′-bipyridine or pyrazine, depicted in **Figure 2** (Bhowmick et al., 2018). Both macrocycles (**6a** and **7**) exhibited cytotoxicity higher than cisplatin against the human breast cancer cell line MCF7. In general, the smaller-size macrocycle **6a** showed higher anticancer activity against all cell types (**Table 3**), and induced higher cell membrane damage. The latter has been associated with eventual necrosis of the cancer cells, in addition to the apoptosis, which was related to the swollen morphology of the treated cells seen by fluorescence microscopy imaging. The difference in the observed anticancer activity of the studied macrocycles has been associated with the lower hydrophobicity and lower molecular weight of **6a**; stability in presence of biomolecules has not been tested. Similarly to the macrocycles

TABLE 2 | Cytotoxicity data of selected metallacycles against a panel of human cancer cells.

Compound	IC_{50} (hrs of incubation)/Type of cells (IC_{50} of ref. compound)	IC_{50} (hrs of incubation)/Type of cells (IC_{50} of ref. compound)	References
A1	3.60 ± 0.21 μM (24 h)/HeLa (0.81 ± 0.08/CDDP)		Zhou et al., 2018a
A2	1.76 ± 0.14 μM (24 h) HeLa (0.81 ± 0.08/CDDP)	14.2 μM (24 h)/A2780cis (12.9/CDDP)	Zhou et al., 2018a
3	2.11 ± 0.17 μM (24 h) HeLa (0.81 ± 0.08/CDDP)	18.1 μM (24 h)/A2780cis (12.9/CDDP)	Zhou et al., 2018a
4	6.41 ± 0.38 μM (24 h) HeLa (0.81 ± 0.08/CDDP)		Zhou et al., 2018a
3 + light	0.37 μM (*+24 h)/HeLa	0.76 μM (*+24 h)/A2780cis (12.9/CDDP)	Zhou et al., 2018a
4 + light	0.95 μM (*+24 h)/HeLa		Zhou et al., 2018a
BODIPY + light	4.88 μM (*+24 h)/HeLa	6.09 μM (*+24 h)/A2780cis (12.9/CDDP)	Zhou et al., 2018a
5a	4.96 ± 0.17 μM (48 h)/U87 (6.06 ± 0.12/CDDP)	16.71 ± 0.33 μM (48 h)/**WI-38** (77.25 ± 7.28/CDDP)	Gupta et al., 2017
5b	3.43 ± 0.09 μM (48 h)/U87 (6.06 ± 0.12/CDDP)	9.16 ± 0.40 μM (48 h)/**WI-38** (77.25 ± 7.28/CDDP)	Gupta et al., 2017
5c	3.73 ± 0.02 μM (48 h)/U87 (6.06 ± 0.12/CDDP)	8.01 ± 0.19 μM (48 h)/**WI-38** (77.25 ± 7.28/CDDP)	Gupta et al., 2017
5d	6.39 ± 0.28 μM (48 h)/U87 (6.06 ± 0.12/CDDP)	15.54 ± 0.22 μM (48 h)/**WI-38** (77.25 ± 7.28/CDDP)	Gupta et al., 2017

*Cell types given in bold are normal non-cancerous cells. *Irradiation by light (400–700 nm, 50 mW/cm^2) for 5 min after 12 h incubation followed by12 h incubation.*

6a and **7**, the synthesis and anticancer potency of other flexible [2 + 2] tetracationic metallamacrocycles have been estimated (Jana et al., 2018). The macrocycle **6b** exhibited moderate anticancer activity against the tested cell lines (**Table 3**) as a result of self-assembly of the non-toxic organometallic clip **A5** and the pyrazine ligand. Yet, its cytotoxicity is lower than cisplatin and no selectivity could be attained.

Recently, two supramolecular metallacycles with hexagonal and rhombic shape have been obtained by using pyrazine-based organoplatinum(II) clip **A6** and two isomeric, also pyrazine-based, ditopic pyridyl ligands (Jana et al., 2019). The *para*- isomer of the ligand **L7** is shown in **Figure 2** and leads to formation of the hexagonal metallacycle **11** upon [3+3] self-assembly with the pyrazine-based organoplatinum(II) acceptor, whereas the *meta*- isomer of **L7** forms a rhomboidal structure (not shown) upon [2+2] self-assembly with the same organoplatinum(II) acceptor. Both types of metallacycles showed slightly higher anticancer activity than the organoplatinum(II) acceptor **A6** and cisplatin (**Table 3**), which is more appreciable for the larger, hexacationic [3+3] self-assembly **11**.

The rhomboidal Pt(II)-metallacycle **9**, depicted in **Figure 2**, has been evaluated for its anticancer activity both *in vivo* and *in vitro* (Grishagin et al., 2014). The formed metallacycle shows 13 times higher emission in the visible region (400–700 nm) than the parent ligand in aqueous-DMSO solution. This property has been used to monitor the cellular uptake and the stability of the metallacycle by laser-scanning confocal microscopy in A549 and HeLa cells. The data evidenced their stability upon cellular internalization in addition to the high resistance to photobleaching under the conditions of the confocal microscopy experiment. At low concentrations (1 nM−5 μM) the rhomboidal metallacycle and the organoplatinum(II) acceptor are not toxic, as seen by MTT test after 48 h of treatment of the cancerous cells. However, in the *in vivo* experiments in immunocompromised nude mice with tumor xenografts of breast cancer MDA-MB-231, the rhomboid **9** exerted a median tumor volume reduction of 88% ($P < 0.001$) (**Figure 3**). A maximum dose of 6 mg/kg in PBS:DMSO = 1:1 (v/v) has been applied by i.p. injections of 300 μL per animal, leading to no obvious signs of toxicity in terms of weight loss and visual appearance and behavior of the treated mice. The

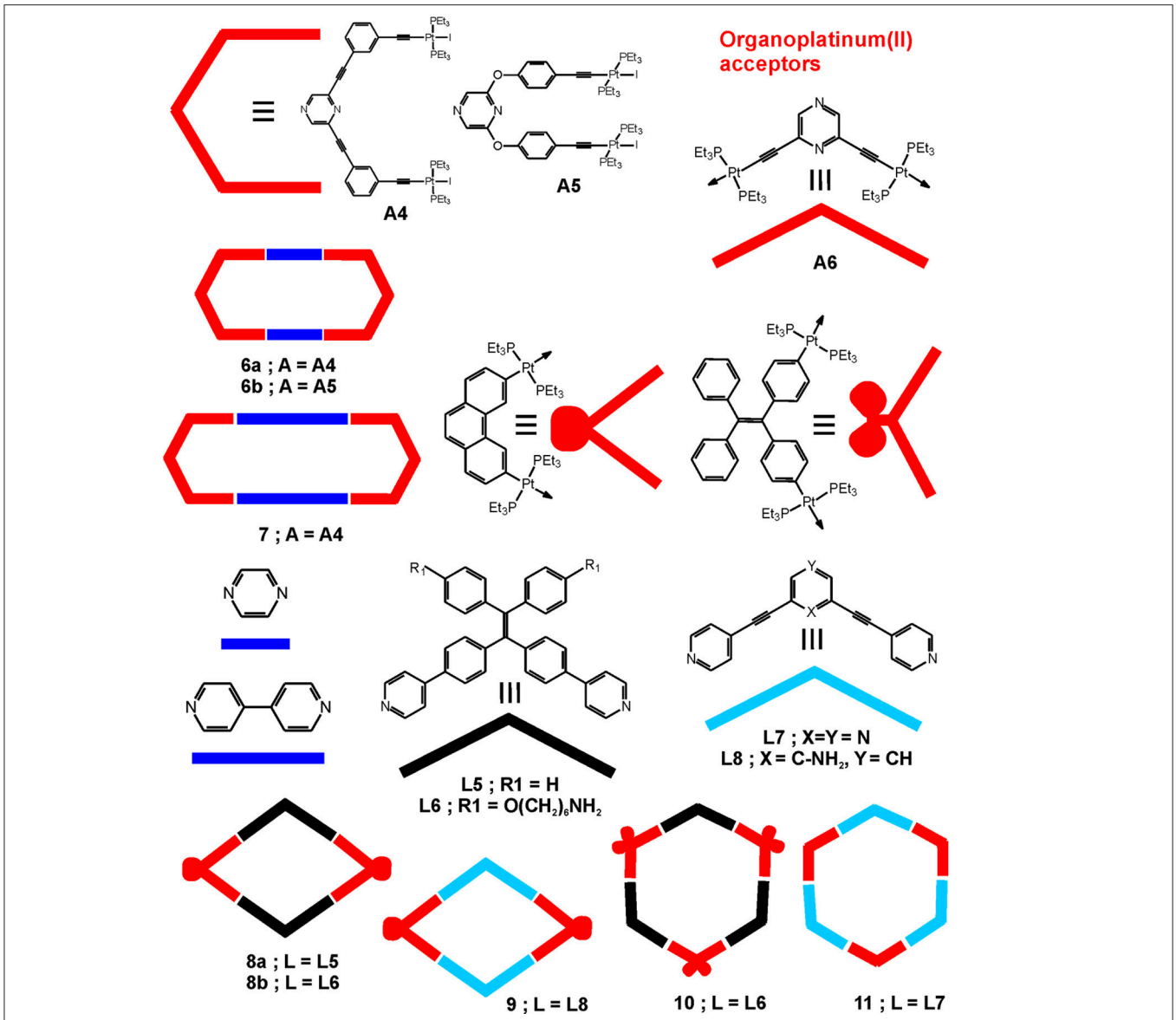

FIGURE 2 | Metallacycles built from organoplatinum(II) acceptors and bent shaped ligands.

tumor growth inhibition (T/C%) value, defined as the ratio of the median tumor volume for the treated vs. the control group at a particular day, has been estimated to 36% at the last day of the experiment of 30 days (**Figure 3** left).

Stang and coworkers prepared metallosupramolecular polymers based on an organometallic Pt-linked rhomboidal metallacycle **8b** (**Figure 2**) that was conjugated with two types of polymers via amidation reaction between alkylamine and N-hydroxysuccinimide-activated carboxylic acid (Zhang et al., 2016). These metallacycle-cored polymers P1 and P2 (**Figure 4**) have been utilized to form nanoparticles at low concentration. All synthetic modifications resulted in enhanced emission due to aggregation-induced emission properties of the tetraphenylethene-based pyridyl donor that is the main building block of the metallacycle. The fluorescence properties of these polymers were further used in cell imaging, which showed a significant enrichment in lung cells after i.v. injection into a mouse bearing an MDA-MB-231 tumor. The observed significant fluorescence of the tumor even 24 h after injection demonstrated that the studied metallosupramolecular polymer (P2) is both chemostable and photostable *in vivo*. Considering the anticancer activity of previously reported rhomboidal Pt(II) metallacycles of Grishagin et al. (2014), the authors infer that this type of fluorescent metallacycle-cored polymers can have potential applications in lung cancer theranostics.

The aggregation-induced emission could also be exploited in building metallosupramolecular species as has been described for a hexagonal [3+3] self-assembled metallacycle **10** built from

TABLE 3 | Cytotoxicity data of selected metallacycles against a panel of human cancer cells.

Com-pound	IC_{50} (hrs of incubation)/Type of cells (IC_{50} of ref. compound)	IC_{50} (hrs of incubation)/Type of cells (IC_{50} of ref. compound)	IC_{50} (hrs of incubation)/Type of cells (IC_{50} of ref. compound)	IC_{50} (hrs of incubation)/Type of cells (IC_{50} of ref. compound)	References
6a	20.0 ± 0.2 μM (48 h)/A549 (25.0 ± 0.3/CDDP)	05.0 ± 0.2 μM (48 h)/MCF7 (20.0 ± 0.3/CDDP)	16.0 ± 0.4 μM (48 h)/KB (8.0 ± 0.4/CDDP)	16.0 ± 0.5 μM (48 h)/HaCaT (12.0 ± 0.3/CDDP)	Bhowmick et al., 2018
6b	19.4 ± 0.5 μM HT-29 (1-10/CDDP)	9.1 ± 0.1 μM MCF-7 (1-10/CDDP)	9.6 ± 0.9 μM MDA-MB-231 (1-10/CDDP)	10.4 ± 0.2 μM **RC-124** (1-10/CDDP)	Jana et al., 2018
7	>30.0 μM (48 h)/A549 (25.0 ± 0.3/CDDP)	17.0 ± 0.3 μM (48 h)/MCF7 (20.0 ± 0.3/CDDP)	20.0 ± 0.1 μM (48 h)/KB (8.0 ± 0.4/CDDP)	20.0 ± 0.1 μM (48 h)/HaCaT (12.0 ± 0.3/CDDP)	Bhowmick et al., 2018
A6	21.54 ± 3.2 μM (48 h)/A549 (22.38 ± 2.9 /CDDP)	14.28 ± 1.2 μM (48 h)/HepG2 (18.89 ± 2.1 /CDDP)	19.55 ± 2.5 μM (48 h)/HeLa (10.21 ± 1.9/CDDP)		Jana et al., 2019
11	10.22 ± 1.6 μM (48 h)/A549 (22.38 ± 2.9 /CDDP)	11.02 ± 1.3 μM (48 h)/HepG2 (18.89 ± 2.1/CDDP)	8.73 ± 1.0 μM (48 h)/HeLa (10.21 ± 1.9/CDDP)		Jana et al., 2019
13	5.2 ± 2.0 μM/T98G (69.6 ± 7.9 /CDDP)	15.5 ± 2.3 μM/KB (72.6 ± 6.2 /CDDP)	18.3 ± 3.0 μM/SNU80 (49.3 ± 5.4 /CDDP)	36.2 ± 5.1 μM/**HEK293** (17.3 ± 3.6 /CDDP)	Mishra et al., 2014
14	4.5 ± 2.1 μM/T98G (69.6 ± 7.9 /CDDP)	13.0 ± 1.2 μM/KB (72.6 ± 6.2 /CDDP)	12.0 ± 2.8 μM/SNU80 (49.3 ± 5.4 /CDDP)	35.0 ± 3.8 μM/**HEK293** (17.3 ± 3.6 /CDDP)	Mishra et al., 2014

Cell types given in bold are normal non-cancerous cells.

tetraphenylethylene (TPE)-based organoplatinum(II) acceptors and the ditopic TPE-based dipyridyl ligand **L6** (**Figure 2**), as well as that of octacationic cages that were obtained from a tetrapodal tetrapyridyl ligand similar to **L6** (Yan et al., 2016). Interestingly, both types of supramolecular assemblies showed distinct photophysical properties depending on the degree of flexibility that the ligand attains after self-assembling with the TPE-based platinum(II) acceptors. The hexacationic metallacycle **10** exhibits aggregation-induced emission (AIE) by increasing the amount of hexane in the CH_2Cl_2 solutions (up to 90%) due to the formation of nanoaggregates, as seen from the scanning electron microscopy (SEM) images, whereas the cages are intrinsically highly emissive. Taking advantage of the observed aggregation-induced enhanced emission (AIEE) of these systems, the same authors applied advanced approaches to build hybrid metallosupramolecular polymeric and bio-nanoparticles. The hexacationic metallacycle **10** has been assembled with the negatively charged rod-like tobacco mosaic virus (TMV) to form three-dimensional micrometer-sized superstructures via electrostatic interactions (Tian et al., 2016). In this way the fluorescence dramatically increased and provided an easily detectable evidence for the formation of novel metallosupramolecular biohybrid materials. Interestingly, addition of tetrabutylammonium bromide disrupts the metallosupramolecular core which results in lower fluorescence. The same strategy has been used to build similar biohybrid materials with bacteriophage M13 and ferritin, although with different degree of aggregation-induced emission. The demonstrated fluorescence switching upon aggregation with negatively charged protein-based species, forming emissive bionanoparticle/metallosupramolecular hybrid complexes, and their controllable disruption, enrich significantly the possibilities for design and development of different supramolecular assemblies with dynamic optical properties and high potential to be used for both imaging and delivery of bioactive compounds.

On the other hand, aggregation-induced quenching may significantly compromise the photophysical functionality of some fluorophores such as porphyrins. In a recent paper, an alternative way to produce porphyrin functionalized hexagonal metallacycle has been reported (Chen et al., 2018). To avoid self-aggregation of the porphyrin rings, the metallacycle depicted in **Figure 5** has been produced in the confined cavity of mesoporous carbon FDU-16. Thereby, the molecules of the porphyrin-containing metallacycle have been dispersed within the mesoporous cavities, which resulted in increased stability and photocatalytic activity of the porphyrin-containing metallacycles. These properties have been demonstrated through successful use of the hybrid material in heterogeneous catalysis for photooxidation of sulfides. The six-fold faster generation of singlet ($^1O_2$), compared to that of free metallacycles in solution, is an important improvement that has been achieved. Although no biological applications have been discussed yet, the demonstrated strategy to construct well-defined porphyrin-containing metallacycles with improved stability and photoactivity may find implications in the future development of nanohybrids with improved properties for PDT.

Another strategy to build metallosupramolecules with significantly augmented photophysical properties, which allow for their use in photodynamic therapy, has recently been demonstrated for a heterometallic Ru-Pt metallacycle **12** (**Figure 6**) (Zhou et al., 2018b). The authors utilized the excellent photostability and two-photon absorption characteristics of the Ru(II) polypyridyl precursor, which after formation of the metallacycle exhibits shifted luminescence

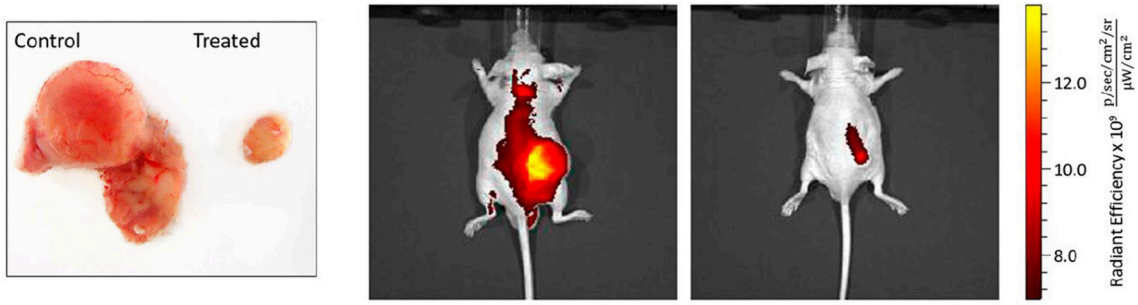

FIGURE 3 | Effect of rhomboid **9** on tumor growth rate in MDA-MB-231 xenografts. **(Left)** Representative pictures of tumors, excised from control and mice treated with rhomboid **9**. **(Right)** Localization of the near-infrared contrast agent IR-783 in the tumors of the control and treated mice. The signal was processed with Living Image software with one representative sample for each group presented above. Mice from the rhomboid **9**-treated group show lower intensity of the signal originating from the tumor-accumulated contrast agent compared with the control group. Adapted with permission from Grishagin et al. (2014).

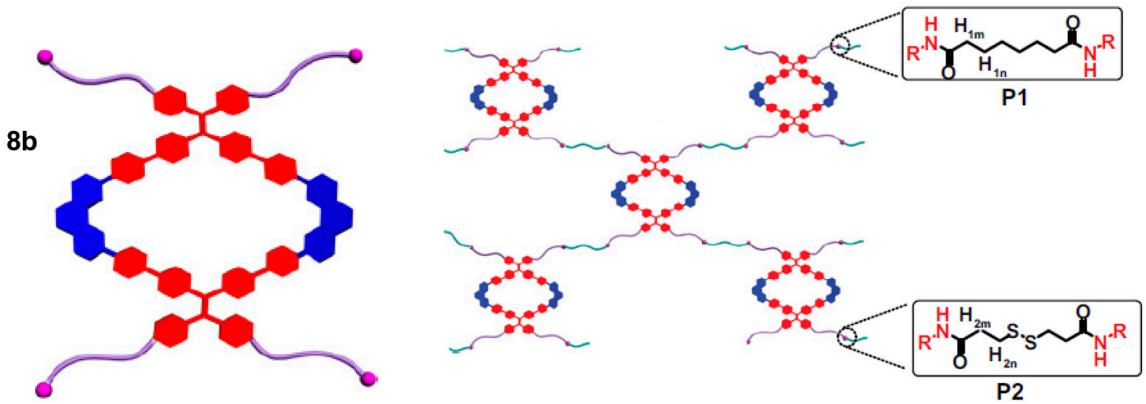

FIGURE 4 | Polymeric networks in P1 and P2 built by interconnecting metallacylces **8b**. Adapted with permission from Zhang et al. (2016).

to the near-infrared region characterized also with a larger two-photon absorption cross-section and higher singlet oxygen generation efficiency. Thereby, the formed large macrocyclic structure of **12** renders it a very potent two-photon PDT agent. It is proposed that the highly charged (decacationic) structure of **12** facilitates its internalization in cells and localization in mitochondria and nuclei as evidenced by time-dependent inductively coupled plasma MS (ICP-MS) analysis of cellular uptake and the biodistribution of **12** in A549 cells. The metallacycle exhibits very high photocytotoxicity, induced by the generation of intracellular $^1O_2$ upon irradiation and damaging the mitochondria and cellular nuclei, whereas the toxicity in the dark is very weak. These observations have also been confirmed in the *in vivo* studies which demonstrated that **12** is capable to efficiently ablate cancer tissues at low light doses with minimal system toxicity.

The tetracationic heterobimetallic cycles **13** and **14** have been obtained from an N, N′-bis(4-(pyridin-4-ylethynyl)phenyl)pyridine-2,6-dicarboxamide ligand and *cis*-blocked palladium(II) or platinum(II) 1,1′-bis(diphenylphosphino)ferrocene triflates (Mishra et al., 2014). Their structure and composition have been characterized by multinuclear NMR spectroscopy, elemental analysis, and high-resolution electrospray mass spectrometry (HR-ESMS) and further modeled by molecular mechanics calculations. The stability of the metallacycles has been tested either by monitoring the cytotoxicity effect after different periods of pre-incubation in cell culture medium (Dulbecco's modified eagle medium—DMEM) or in DMSO (for 0, 10, 25, and 50 h at 37 ^{0}C) or by fluorescence spectroscopy measurements in physiological buffer solution at pH 7.4 and in presence of redox active compounds (H_2O_2 or dithiothreitol). While both metallacycles exhibit cytotoxicity higher than cisplatin against the tested human-cancer cell lines (T98G, KB and SNU-80), they are twice less toxic to the normal human embryonic kidney cells (HEK-293) than cisplatin, which points to a much better cancer cell selectivity (**Table 3**). The stability studies indicated that under physiological conditions and even in presence of redox-active compounds the metallacycles **13** and **14** remain intact for at least 50 h, whereas in presence of DMSO a significant loss of cytotoxicity has been seen for pre-incubation periods of > 25 hours. These observations could suggest that the metallosupramolecular structure of **13** and **14** is crucial for the observed cytotoxicity profiles, since the DMSO induced disassembly is proposed as the main reason for decrease in

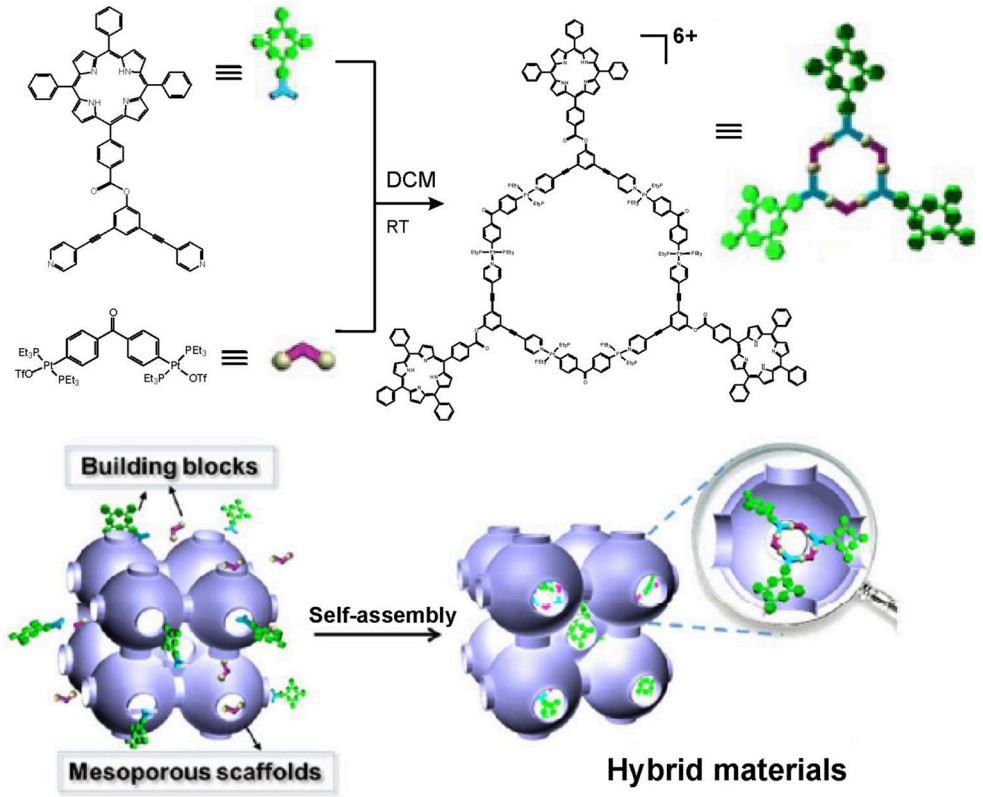

FIGURE 5 | Construction of porphyrin-containing metallacycle within the confined cavity of mesoporous carbon FDU-16. Adapted with permission from Chen et al. (2018); Copyright 2018 American Chemical Society.

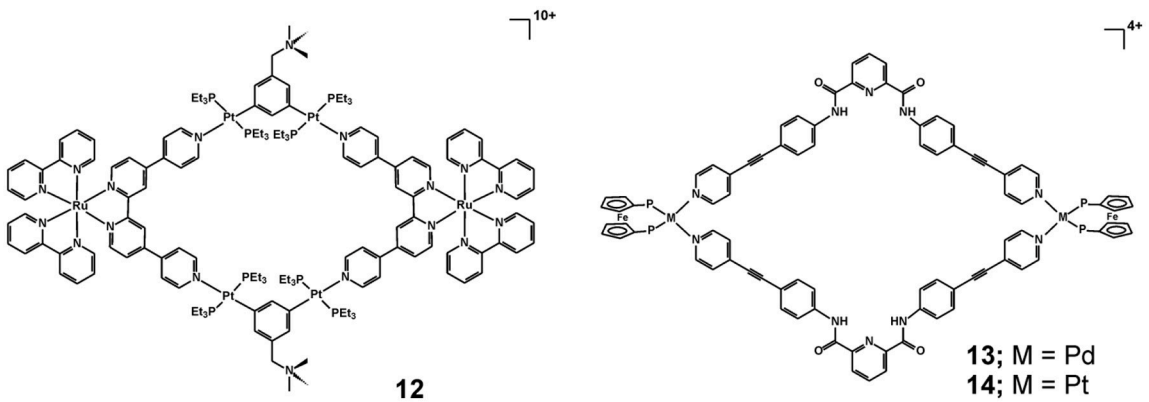

FIGURE 6 | Heterobimetallic cycles **12** – **14** with notable optical, electrochemical, and anticancer properties.

the cytotoxicity. The mode of action leading to the observed cytotoxicity has been associated with apoptosis as evidenced by the caspase-3/7 activity assays.

METALLACAGES AND HELICATES

Metallacages and helicates are 3D structures that have characteristic cavity or cylindrical shape. Thereby, except combining the properties of the building components, metallacages can be excellent hosts for a variety of guest molecules that can be encapsulated in the hollow of the cages. This particular feature of metallacages has long been utilized in the design and development of smart nanostructures for multiple applications, such as molecular flasks (Yoshizawa et al., 2009), containers (Zarra et al., 2015), for safe storage (Yamashina et al., 2014) and recognition (Rodriguez et al., 2017), etc. Metallahelicates, on the other hand, can have specific helicity that is capable of selective interactions with biomolecules with certain

conformation, such as DNA fragments. The growing interest in exploring the biomedical applications of these types of 3D metallosupramolecules has progressed to building metallacages that are either capable of encapsulating bioactive molecules or can be structurally decorated with biofunctional fragments. Thereby, the areas of potential applications of metallacages already include drug delivery and bioimaging except the initially explored biological activities that are intrinsically characteristics for their components. Similar expansion in the exploration of the properties of metallahelicates is also in progress.

Some examples of metallacages that had attracted the attention of synthetic and bioinorganic chemists are the $[Pd_2L_4]^{4+}$ cages that assemble from simple ditopic tripyridyl ligands—2,6-bis(pyridin-3-ylethynyl)pyridine or its bis(pyridin-3-ylethynyl)benzene analog (**Figure 7**). The interest has been initiated with the reported encapsulation of the anticancer drug cisplatin by the supramolecular cage **15** that can be controllably released by external stimuli (Lewis et al., 2012). The cage formation and cisplatin encapsulation proceeds virtually quantitatively and the cage **15** and its host-guest complex with encapsulated two molecules of cisplatin have been characterized by single-crystal X-ray diffraction analyses. While the cage and the host-guest complex are rather stable in organic solvents, the cage readily disassembles in presence of competing amine ligands or chlorides, and thus the encapsulated cisplatin molecules can be released. The authors studied in details the encapsulation phenomenon and highlighted the importance of the hydrogen bonding interactions between the cage and the amine ligands of the cisplatin guest. This conclusion has been suggested by the lack of encapsulation evidences when a Pd_2L_4 metallacage built from 1,3-bis(pyridin-3-ylethynyl)benzene ligand (when X=CH in **15**, **Figure 7**) has been used.

Further exploration of the observed stimuli-responsive catch and release of cisplatin by cage **15** has been focused on suitable ligand modifications to include an optically responsive fragment and/or increase the stability of the cage and the host-guest complex under biologically relevant conditions. The Cu(I)-catalyzed azide-alkyne cycloaddition "click" reaction (CuAAC) has been utilized to build a library of electrochemically or photochemically responsive cages (**16a-c**, **Figure 7**) (Lewis et al., 2013, 2014). It has been demonstrated that the formed 1,2,3-triazole units in the exo-functionalization does not affect the self-assembling process nor does it interfere with the ability of the formed cages to bind cisplatin as guest molecules. Similarly, single-crystal X-ray structure has been determined for the 1:2—host-guest complex of cage **16a** and cisplatin (Lewis et al., 2013). The cage formation does not alter the one-electron reversible oxidation characteristic for 4-ferrocenyl triazoles. The same strategy has been used to "click" photoresponsive or biological molecules, such as 4-amino-1,8-naphthalimide (in **16b**, **Figure 7**) and fac-$[Re(CO)_3]$ complex with the 4-(2-pyridyl)-1,2,3-triazolyl moiety (in **16c**, **Figure 7**) or caffeine, acetate protected-D-glucose, estradiol and dipeptide units (Lewis et al., 2014). The attachment of the organic or inorganic fluorophores (in **16b** and **16c**, respectively) transformed the virtually non-emissive cages into emissive ones, with especially efficient emission seen for cage **16b** showing quantum yield of fluorescence of 0.59.

With the ultimate goal to improve the kinetic stability of the studied Pd_2L_4 cages and evaluate their biological activity, Crowley and coworkers further modified the used tripyridyl ligands by adding NH_2-susbstituents in the terminal pyridyl rings (Preston et al., 2016). Thereby, cages **17a** and **17b** have been obtained and their kinetic and biological properties have been compared with the non-functionalized cage **18d**. The stability studies showed that 2-amino substitution on the terminal pyridine rings significantly enhances the stability of the formed cage **17a** in presence of chloride ions or histidine and cysteine—potent ligands in biological environment. Interestingly, cage **17b** has kinetic properties and cisplatin-encapsulation ability similar to that of **18d**, which points out to the importance of subtle structural modification of the self-assembling ligands on the properties of the formed metallacages. Enhanced stability of **17a** of up to several hours to almost 2 days (in presence of histidine) reflected also to the observed appreciable cytotoxicity against the cisplatin-resistant breast cancer cell line MDA-MB-231 (**Table 4**). In contrast, the **17b** and **18d** did not show appreciable cytotoxicity against the tested lung and breast cancer cell (for 24 h of incubation), which can be in favor to their stimuli-responsive cisplatin encapsulation and the suggested drug-delivery potential.

Further functionalization and cytotoxicity studies on this class of metallacages have been undertaken by Casini, Kühn and coworkers. The antiproliferative effects of Pd(II) cages of hydroxymethyl-functionalized bi- and tripyridyl ligands (**18c** and **18d** in **Figure 7**, respectively) indicated that upon 72 h of incubation the cages exert cytotoxicity against the tested cancer cells either comparable to that of cisplatin (for **18c**) or 4-times lower (for **18d**, **Table 4**) (Schmidt et al., 2016b). The other two examples of Pd(II) cages derived from differently functionalized bipyridyne ligands (**18a** and **18b** in **Figure 7**) have the same order of cytotoxicity effect as **18c**. The observed lower toxicity of **18d** and its distinctive ability to encapsulate cisplatin, as suggested earlier by Crowley and confirmed herein by X-ray data of the host-guest complex, can be regarded as favorable combination of properties for the sake of anticancer drug delivery potential (Schmidt et al., 2016b). To introduce optical functionality to the observed higher cytotoxicity of the Pd(II) cages derived from the bi-pyridyl ligands, the same authors exo-functionalized the Pd_2L_4 cages with naphthalene or anthracene fluorophores (Schmidt et al., 2016a). The formed ligands exhibit weak fluorescence and upon self-assembly and formation of the cages **19a** – **19d** (**Figure 7**) the emissive properties of the fluorophore-tagged ligands have been preserved leading to the formation of weakly or non-emissive metallacages, most probably due to the high degree of flexibility. The exo-functionalization with aromatic rings, however, reflected the cytotoxicity of the ligands and the corresponding metallacages **19a, 19b,** and **19d** that increased considerably when compared with the non-functionalized cage **19c** (**Table 4**). Interestingly, by introducing methoxy groups in the terminal pyridine rings the fluorescence of the ligands increases (Kaiser et al., 2016); upon capsule formation, however, virtually non-emissive Pd(II)- and a novel Pt(II) cage have been obtained. Interaction of the Pd(II) cages of metoxy-functionalized bi- and tri-pyridine ligands with cisplatin has been suggested by ^{1}H NMR measurements. Pd(II)

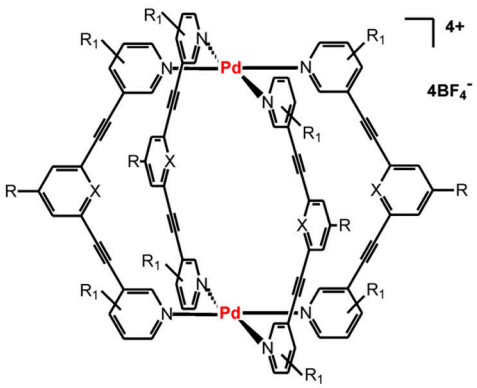

15; X = N, R = R1 = H

16a; X = N, R1 = H, R =

16b; X = N, R1 = H, R =

16c; X = N, R1 = H, R =

17a; X = N, R = CH_2OH , R_1 = *o*-NH_2

17b; X = N, R = CH_2OH , R_1 = *m*-NH_2

18a; X = CH, R_1 = H, R = NH_2

18b; X = CH, R_1 = H, R = OH

18c; X = CH, R_1 = H, R = CH_2OH

18d; X = N, R_1 = H, R = CH_2OH

20; X = N, R = H , R_1 = *m*-OCH_3

19a; X = CH, R_1 = H , R =

19b; X = CH, R_1 = H , R =

19c; X = CH, R_1 = H , R = OH

19d; X = N, R_1 = H , R =

FIGURE 7 | Metallosupramolecular cages with general formula $[Pd_2L_4](BF_4)_4$ built from a series of tri- or bi-pyridyl ditopic ligands.

cage **20** and its analog of a bi-pyridine ligand (structure not shown) have been proposed as suitable drug-delivery platforms as the estimated cytotoxicity is relatively low.

To achieve efficient targeting, functionalization of metallacages with biological fragments has been reported for the Pd_2L_4 cages of the di-pyridyl ligands depicted in **Figure 7** (Han et al., 2017). Two different approaches for exo-functionalization with a model linear peptide Ac-NLEFK-Am have been described, which are based on amide bond formation between the carboxylic (or amine) group of the exo-functionalized ligand/cage and that of the side chains of the model peptide. Better results could be obtained with the pre-conjugation approach, where the peptide is coupled to the ligand prior to the following *in situ* self-assembly and formation of the Pd_2L_4 cages. Thereby, metallacages of larger size could be obtained that can more efficiently benefit from the enhance permeability effect (EPR) for passive targeting to cancer cells and tissues. More importantly, this approach could open the prospect to bioconjugation and specific targeting of metallosupramolecules by attaching receptor-specific peptides or antibodies as an way to complement their either drug-delivery potential or intrinsic cytotoxicity (Han et al., 2017).

Metallosupramolecular systems of composition $[Pd_2L_4]^{4+}$ have been isolated by using smaller size ditopic ligands based on bis-triazoles similar to **L9** in **Figure 8** (McNeill et al., 2015). The formed complexes have the form of quadruply-stranded helicates similarly to the crystal structure of **21**, depicted in **Figure 8** and reported earlier (Crowley and Gavey, 2010). These helical structures have improved stability that is much more pronounced in the case of bis-triazole ligand with hexyl pendant arms forming the analogous complex **21-hex** (structure not shown). The increased stability in presence of chlorides, histidine and cysteine correlated with the observed higher cytotoxicity against the tested cancer cell lines in comparison of the metallacage **15** (**Table 4**). Interestingly, the complex **21-hex** attains its half-inhibitory concentration the first 2 h of treatment of the cells in contrast to the known anticancer platinum drugs. This suggested different mode of anticancer action that has been associated with loss of cellular membrane integrity as derived from fluorescence microscope imaging and enzymatic (LDH) activity assay (McNeill et al., 2015). This hypothesis also corroborated with observed lack of selectivity of the cytotoxicity of complex **21-hex**. A large library of bis(bidentate) 2-pyridyl-1,2,3-triazole ligands with various lengths have been explored for their ability to form triple helicates with Fe(II) ions with general composition $[Fe_2L_3]^{4+}$ (Vellas et al., 2013). While self-assembly and formations of cylinders have been confirmed in solution as well as in the solid state, the poor stability of these complexes hampered their potential biological activity. Molecular docking studies of these complexes suggested they could bind duplex and triplex DNA fragments.

The chiral metallohelical complexes $[Fe_2(\mathbf{L10})_3]^{4+}$ and $[Fe_2(\mathbf{L11})_3]^{4+}$, constructed by Scott, Qu and coworkers, have shown evidences to selectively target and enantioselectively inhibit amyloid-β (Aβ) aggregation (Li et al., 2014). The ability of these metal complexes to inhibit Aβ assembly suggested that they might be useful in blocking Aβ-mediated cellular

TABLE 4 | Cytotoxicity data of selected metallacages against a panel of human cancer cells (**Figure 7**).

Compound	IC_{50} (hrs of incubation)/Type of cells (IC_{50} of ref. compound)	IC_{50} (hrs of incubation)/Type of cells (IC_{50} of ref. compound)	IC_{50}(hrs of incubation)/Type of cells (IC_{50} of ref. compound)	References
15	41.4 ± 3.9 μM (24 h)/A549 (9.4 ± 0.3/CDDP)	56.7 ± 2.2 μM (24 h)/MDA-MB-231 (41.2 ± 3.9/CDDP)	70.1 ± 13.8 μM 24 h)/DU145	McNeill et al., 2015
17a	50 μM (24 h)/A549 (9.4 ± 0.3/CDDP)	36.4 ± 1.9 μM (24 h)/MDA-MB-231 (41.2 ± 3.9/CDDP)		Preston et al., 2016
18a	16.5 ± 4.3 μM (72 h)/A549 (8.9 ± 4.2/CDDP)	16.7 ± 2.0 μM (72 h)/SKOV-3 (15.4 ± 2.2/CDDP)	8.2 ± 1.6 μM (72 h)/HepG2 (6.4 ± 1.5/CDDP)	Schmidt et al., 2016b
18b	47.3 ± 1.8 μM (72 h)/A549 (8.9 ± 4.2/CDDP)	66.0 ± 10.8 μM (72 h)/SKOV-3 (15.4 ± 2.2/CDDP)		Schmidt et al., 2016b
18c	13.2 ± 2.4 μM (72 h)/A549 (8.9 ± 4.2/CDDP)	11.6 ± 1.7 μM (72 h)/SKOV-3 (15.4 ± 2.2/CDDP)	10.7 ± 0.6 μM (72 h)/HepG2 (6.4 ± 1.5/CDDP)	Schmidt et al., 2016b
18d	32.0 ± 9.7 μM (72 h)/A549 (8.9 ± 4.2/CDDP)	44.0 ± 6.2 μM (72 h)/SKOV-3 (15.4 ± 2.2/CDDP)	29.7 ± 2.6 μM (72 h)/HepG2 (6.4 ± 1.5/CDDP)	Schmidt et al., 2016b
19a	5.9 ± 1.4 μM (72 h)/A549 (8.9 ± 4.2/CDDP)	8.0 ± 1.4 μM (72 h)/SKOV-3 (15.4 ± 2.2/CDDP)		Schmidt et al., 2016a
19b	1.1 ± 0.3 μM (72 h)/A549 (8.9 ± 4.2/CDDP)	1.1 ± 0.6 μM (72 h)/SKOV-3 (15.4 ± 2.2/CDDP)		Schmidt et al., 2016a
19c	82.6 ± 15.1 μM (72 h)/A549 (8.9 ± 4.2/CDDP)	94.4 ± 7.9 μM (72 h)/SKOV-3 (15.4 ± 2.2/CDDP)		Schmidt et al., 2016a
19d	1.4 ± 0.5 μM (72 h)/A549 (8.9 ± 4.2/CDDP)	1.2 ± 0.7 μM (72 h)/SKOV-3 (15.4 ± 2.2/CDDP)		Schmidt et al., 2016a
20	71.8 ± 9.1 μM (48 h)/A549 (16.8 ± 0.7/CDDP)	44 ± 11 μM (48 h)/HepG2 (6.7 ± 0.9/CDDP)		Kaiser et al., 2016
21-hex	6.9 ± 0.9 μM (24 h)/A549 (9.4 ± 0.3/CDDP)	6.0 ± 0.6 μM (24 h)/MDA-MB-231 (41.2 ± 3.9/CDDP)	3.4 ± 0.4 μM (24 h)/DU145	McNeill et al., 2015
22	5.1 μM/HBL100 (4.9/CDDP)	6.7 μM/T47D (28.3/CDDP)		Hotze et al., 2006
23	0.16 μM/HBL100 (4.9 μM/CDDP)	0.29 μM/T47D (28.3 μM/CDDP)		Hotze et al., 2006
24	22 μM/HBL100 (4.9 μM/CDDP)	53 μM/T47D (28.3 μM/CDDP)		Pascu et al., 2007

toxicity and thereby present a therapeutic strategy for treatment of Alzheimer's disease. The selective targeting of alpha/beta-discordant stretches at the early steps of aggregation has been demonstrated by multiple biophysical and biochemical approaches. More recently, a series of analogs of $[Fe_2(\mathbf{L11})_3]^{4+}$, having linking bridges of different flexibility, have been tested for their anticancer activity and evidenced both very good water solubility and stability (Kaner et al., 2016). Interestingly, the so-called flexicates exhibit anticancer activity of sub-micromolar to nanomolar range against the tested human cancer cell lines: MDA-MB-468 (human epithelial breast adenocarcinoma), HCT116 $p53^{+/+}$ and HCT116 $p53^{-/-}$ that are genetically identical human colorectal cancer cell lines except for the presence or absence of functional p53, which is a common genetic difference associated with increased resistance to chemotherapy. In the cisplatin-sensitive cells MDA-MB-468, the glycolbridged flexicate analogous to $[Fe_2(\mathbf{L11})_3]^{4+}$ have shown a cytotoxicity ($IC_{50} = 0.2 \pm 0.1\,\mu M$) higher than cisplatin by an order of magnitude. Moreover, some of the tested flexicates were very toxic against the resistant HCT116 $p53^{-/-}$cells that lack p53 and showing cytotoxicity as low as 40 nM. Another important feature of this class of flexicates is their excellent selectivity, which is estimated to be nearly three orders of magnitude higher than that of cisplatin against healthy human retinal

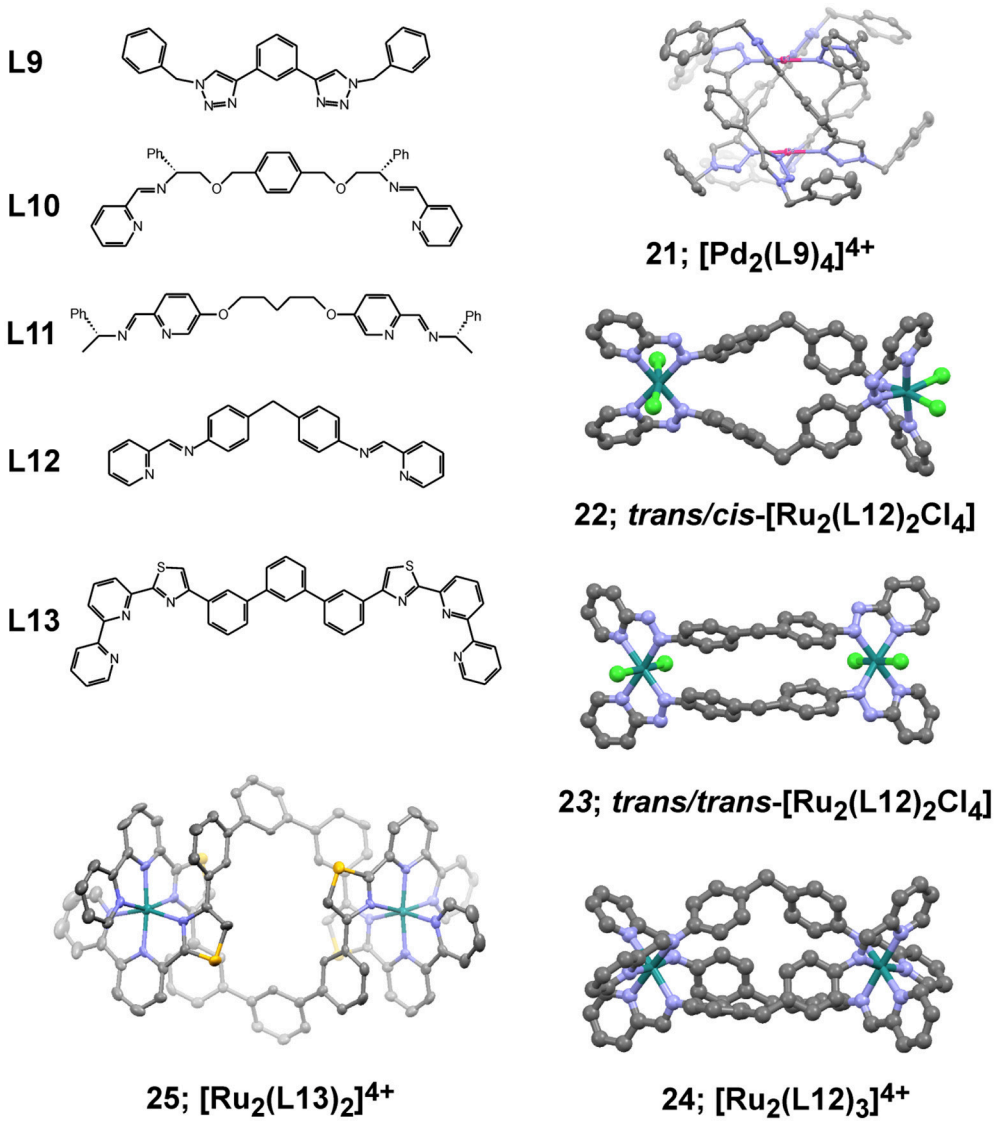

FIGURE 8 | Dipodal ligands (**L9** – **L13**) for building helical metallosupramolecules similarly to represented crystallographic views of selected examples (**21** – **25**). Views of the crystal structures are produced with Mercury3.8 software from the corresponding files: **21** – CCDC 762916; **22** – CCDC 603391; **23** – CCDC 603392; **24** – CCDC 636261; **25** – CCDC 1566897; all are freely available from www.ccdc.cam.ac.uk.

pigment epithelial (ARPE19) and lung fibroblast (WI38) cells. The helical complex $[Fe_2(\mathbf{L10})_3]^{4+}$ showed limited solubility in water and could not be fully characterized, whereas its *m*-xylenyl analog exhibited cytotoxicity as high as $0.4 \pm 0.1\,\mu M$ against the MDA-MB-468 cell lines. In some cases significant enantiomeric difference had been observed pointing to the structural and conformational importance of the helicates. Nevertheless, the investigated mode of action could not be associated with DNA interaction nor apoptosis induced cell death.

The earlier reported metallosupramolecular helicate $[Fe_2(\mathbf{L12})_3]^{4+}$ of Hannon and coworkers are capable of binding DNA Y-shaped junctions and could also unwind DNA and bind preferentially to regular alternating purine–pyrimidine sequences (Malina et al., 2008). More recent studies on the DNA interaction preferences have also revealed that this metallohelicate is capable of recognizing DNA bulges that are DNA defects consisting of one or more unpaired bases in the DNA double helical strands (Malina et al., 2014). These findings complemented the available data on the ability of the $[Fe_2(\mathbf{L12})_3]^{4+}$ helicate to recognize non-canonical structures in DNA that might have relevance with various diseases. Recent report on the ability of the $[Fe_2(\mathbf{L12})_3]^{4+}$ helicate to bind to TAR RNA, which is transactivation responsive region RNA, suggested it biological potential of inhibiting an essential step in the HIV-1 replication cycle (Malina et al., 2016). The observation

that the iron(II) supramolecular helicates binds to TAR RNA at nanomolar concentrations and inhibits the interaction between the HIV-1 transactivator protein Tat and TAR, which plays a critical role in HIV-1 transcription, broadens the scope of biological importance of metallosupramolecular helicates.

The anticancer potency of dinuclear ruthenium metallohelicates have been among the first examples of biological activity demonstrated for double-stranded (**22** and **23** in **Figure 8**) (Hotze et al., 2006) and triple-stranded (**24** in **Figure 8**) metallohelicates (Pascu et al., 2007). The two different isomers of the dinuclear $[Ru_2L_2Cl_4]$ complex exhibit slightly different cytotoxicity profiles (**Table 4**) with the symmetric **23** isomer being an order of magnitude more cytotoxic than the cis/trans isomer **22** against the tested cancer cell lines. The analogous triple-stranded helicate **24** (Pascu et al., 2007) demonstrated very high stability and capability of binding DNA. This cylinder is photoresponsive to additions of ct-DNA in terms of fluorescence enhancement from the ruthenium cylinder and a concomitant blue shift (8 nm) in the emission maximum. The observed cytotoxicity, however, is significantly lower than the double-stranded analogs and also lower than that of cisplatin (**Table 4**). More recent examples on the construction and biological activity of double-stranded Ru(II) helicates of **L13** have been reported by Rice and coworkers and suggested the formed helicate **25** as a suitable compound that can target difficult to treat tumors (Allison et al., 2018), such as the human colorectal cancer cell line HCT116. The selectivity of **25** was similar to cisplatin and oxaliplatin toward the HCT116 $p53^{+/+}$ cancer cells, but it also showed substantively higher cytotoxicity toward the $p53^{-/-}$ cells.

Advanced approaches that utilize metallosupramolecular cages as delivery system for either anticancer drugs and prodrugs or fluorescent agents have gained increasing interest as alternative ways to achieve selectivity and efficient targeting of tumor tissues for both therapeutic and imaging purposes. Among the initial examples are those that use the hexanuclear octahedral metallacage of Fujita (**Pt-cage 1** in **Figure 9**), (Ibukuro et al., 1998), which has been shown to encapsulate four molecules of adamantyl Pt(IV)-complex exhibiting prodrug properties (Zheng et al., 2015). The formed host-guest complex has a diameter of about 3 nm, as characterized by detailed NMR analyses. The cytotoxicity of the host-guest complex is much higher than these of the **Pt-cage 1** or the Pt(IV)-prodrug guest alone, and is comparable to the anticancer activity of cisplatin against a panel of human cancer cells lines. The improved anticancer activity is caused by biological reductions of the Pt(IV)-prodrug, as evidenced by adding ascorbic acid, and release of the cytotoxic cisplatin. Thereby the cisplatin resistance in the tested A280CP70 cell lines could be overcome that was explained with the high cellular uptake of the highly positive charge of the host-guest nanostructure. On the other hand, by changing the type of the Pt(II)-cornering complexes of **Pt-cage 1,** from ethilenediamine to an 1,1′-bipyridine complex, the formed octahedral cage becomes more cytotoxic than cisplatin against a panel of human cancer cells including the cisplatin-resistant celss ($IC_{50} = 3.42 \pm 0.63\,\mu M$ for A2780CP70 and $IC_{50} = 7.85 \pm 0.21\,\mu M$ for MD-MBA-231 vs. IC_{50} values for cisplatin of $6.49 \pm 1.40\,\mu M$ for A2780CP70 and $15.4 \pm 2.3\,\mu M$ for MDA-MB-231) (Zheng et al., 2016). The detailed study on the mechanism of action of this Pt_6L_4 octahedral cage showed that it interacts with DNA in a non-covalent intercalative way leading to DNA damage, and induces apoptosis through upregulation of p53 and p21 proteins.

Another strategy has been tested in building drug-loaded nanoparticles with polymeric shell of anionic block copolymer (methoxy polyethylene glycol-blockpolyglutamic acid, MPEG5k-PGA30) (Yue et al., 2018). The same octahedral metallacage (**Pt-cage 1**) has been used to encapsulate a fluorescein-linked Pt(IV) prodrug (**Figure 9B**). The Pt(IV) prodrug-loaded supramolecular nanoparticles have spherical shape, and their average size was estimated to 20 nm by cryo-TEM imaging or overall size of 80 nm including the peripheral polymers and according to the dynamic light scattering (DLS) data. The drug-release profiles speeds up dramatically under acidic conditions (pH = 5.0 in acetate buffer) and reducing environment of 1 mM ascorbic acid, that is estimated by the release half-life being 3 days in PBS and only 23 h in acidic and reducing environment. Intracellular release of the fluorescein-conjugated Pt(IV) prodrug was evidenced by fluorescence microscopy that has been enabled by the appearance of bright green fluorescence of the prodrug released from the otherwise non-fluorescent nanoparticle. Moreover, the cytotoxicity of the nanoparticles against HeLa cells is comparable to that of cisplatin ($IC_{50} = 5.02 \pm 0.67\,\mu M$ for the nanoparticles; $2.95 \pm 0.42\,\mu M$ for cisplatin, and $5.98 \pm 0.58\,\mu M$ for the Pt(IV) prodrug), whereas the metallacage (**Pt-cage 1**) is essentially non-toxic. This work demonstrates an working strategy to use anionic block copolymer, to include a cytotoxic host-guest complex into negatively charged nanoparticles of appropriate size that are able to slowly release the therapeutic content and show excellent anticancer efficacy accompanied with fluorescence imaging modality.

Alternatively, Stang and coworkers utilized a highly emissive tetraphenylethene metallacage to build supramolecular nanoparticles with 1,2-distearoyl-phosphatidylethanolamine (DSPE)/polyethylene glycol (PEG) shell (**Figure 9C**) showing excellent stability and biotin-receptor targeting ability to be used as cancer-cell selective delivery systems (Yu et al., 2016). Moreover, these supramolecular nanoparticles preserve the coordination triggered aggregation induced emission (AIE) enhancement, which renders them highly emissive in biological media and suitable for imaging purposes. The incorporated metallacage is built from Pt(II) linked triphenyl pillars, decorated with differently modified PEG-arms, and two tetraphenyl-ethene ligands each bearing four pyridines for coordination with the metal. The metal precursor is a *cis*-$Pt(Et_3P)_2(OTf)_2$ complex that exhibits high and unselective cytotoxicity. Upon formation of self-assembled polymeric aggregates with sizes of about 37 nm (as seen by TEM and DLS techniques) selective delivery to cancer cells has been achieved employing the EPR effect additionally to the biotin-mediated internalization in cancer cells. Thereby, the metallacage loaded nanoparticles combine the therapeutic with the imaging modality making them suitable for theranostic applications. Confocal laser scanning microscopy and flow cytometry confirmed the selective

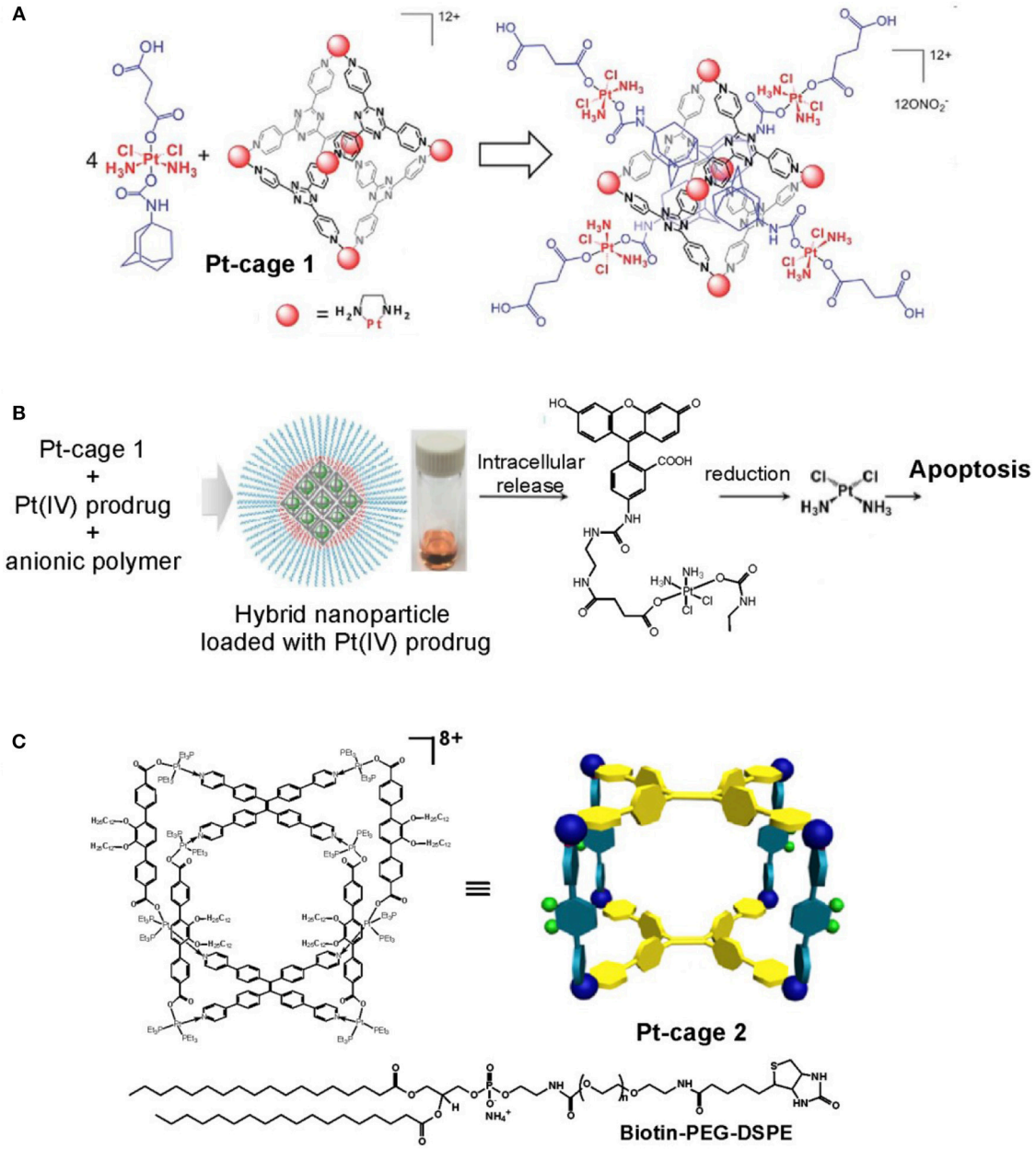

FIGURE 9 | Advanced metallo supramolecular systems constructed from platinum metallacages. **(A)** Pt(IV) adamantyl prodrug encapsulated in the rhombic **Pt-cage 1** (adapted from Zheng et al., 2015; Published by The Royal Society of Chemistry); **(B)** hybrid metallosupramolecular-polymeric nanoparticles built from host-guest complex of fluorescein-conjugated Pt(IV) prodrug and **Pt-cage 1** coated with anionic polymer shell (adapted from Yue et al., 2018; with permission from RSC); **(C)** theranostic supramolecular nanoparticles built from highly emissive metallacage, **Pt-cage 2**, and biotin-conjugated PEGylated surfactant (adapted from Yu et al., 2016).

targeting of the biotin functionalized nanoparticles to cancer cells overexpressing the corresponding receptor (HeLa and HepG2 cells) in contrast to normal cells (CHO and HEK-293), which also corroborated with their higher and selective cytotoxicity and high Pt-content in the cancer cells nuclei. The theranostic functions of the biotin-functionalized nanoparticles have been demonstrated also *in vivo* in HeLa tumor bearing female nude mice confirming their superiority than the clinical formulations of oxaliplatin, carboplatin, or cisplatin used as control. Importantly, while higher accumulation of Pt from the nanoparticles was observed in the tumor in comparison with the control Pt-drugs, administration of nanoparticles resulted in a lower Pt uptake by the liver, spleen, lung, and kidneys, which suggested that the use of PEGylated

nanoparticles also provides way to decrease the systemic toxicity of Pt-drugs.

METALLOCAPSULES AND BARRELS

The design and utilization of large aromatic panels as multidentate donor ligands enabled the construction of 3D metallosupramolecular structures with a characteristic well-confined cavity, and having capsular or barrel-like shapes. Interesting examples consist of aromatic panels with intrinsic fluorescence properties, such as anthracene and carbazole fragments in the ligands depicted in **Figure 10**. The formation of robust M_2L_4 coordination capsules have been described by Yoshizawa and coworkers (Li et al., 2012), and their fluorescence and guest-encapsulation properties have been studied in details (Kishi et al., 2011) for the sake of practical applications for safe storage of reactive compounds (Yamashina et al., 2014) or recognition purposes (Yamashina et al., 2016, 2017).

Recent results on the anticancer properties of Pd(II) and Pt(II) capsules **26** and **27** (**Figure 10**) indicated that they exhibit anticancer activity profiles much superior to cisplatin in terms of higher toxicity against two types of leukemic cells (HL-60 and SKW-3) as well as against cisplatin-resistant cells (HL-60/CDDP) (Ahmedova et al., 2016b). More importantly, the capsules showed more than 5 times better selectivity toward cancerous cells than that of cisplatin, which has been estimated by the IC_{50} of normal-to-cancer cell toxicity ratio employing human embryonic kidney cells (HEK-293) as a model for non-malignant cells. The stability tests revealed that both types of coordination capsules remain intact in presence of excess of biologically relevant molecules such as amino acids and DNA bases. However, the addition of sulfur-containing biomolecules such as cysteine, causes disassembly of the capsules that proceeds instantaneously in case of the Pd(II) capsule **26** and takes up to 3 days for the more inert Pt(II) analog **27**. Decomposition of the capsules can be easily monitored by the appearance of the characteristic strong fluorescence of the liberated bis-anthracene ligand **L16**. Further on, the effect of guest encapsulation on the stability and the cytotoxicity of the capsules have been investigated (Ahmedova et al., 2016a). A successful modulation of these properties has been achieved by encapsulation of different types of hydrophobic guest molecules (pyrene and caffeine). The stabilities of the empty hosts and the corresponding host-guest complexes have been tested in presence of glutathione – the sulfur-containing oligopeptide that has relevance to cancer evolution. The observed strong stabilization of the capsules by encapsulation of pyrene guests has resulted in virtually complete loss of cytotoxicity of the otherwise highly toxic empty hosts **26** and **27** against the tested human cancer cell lines (HT-29, T-24, HL-60 and its resistant counterparts HL-60/Dox and HL-60/CDDP). These findings have suggested that the cytotoxicity of **26** and **27** can be readily modulated by encapsulation of large aromatic guests. More interestingly, the observed cytotoxicity profiles correlated with the capsules stability in the presence of glutathione that was estimated by NMR-based kinetic experiments. The observed stability-cytotoxicity correlation allowed proposing that the glutathione-triggered decomposition of the capsules could be the reason for the observed anticancer activity of these robust capsular metallosupramolecules. This hypothesis corroborates with the reported very high selectivity of the capsules to cancerous cells as well as with their cross-resistance cytotoxicity.

Mukherjee and coworkers reported the synthesis and single-crystal X-ray structure of a Pd_8L_4 water-soluble molecular barrel **28** that self-assembled from a tetrapyridyl donor (**L17**) and a cis-blocked Pd(II) precursor [cis-(en)$Pd(NO_3)_2$] (Bhat et al., 2017). The affinity of the barrel's cavity to hydrophobic guest molecules has been employed in encapsulation of the anticancer drug curcumin, which resulted in significant stabilization of curcumin and its solubilization in water. This reflected on the increased anticancer activity of water solutions of curcumin against HeLa cancer cells demonstrating the successful utility of the metallosupramolecular barrel as a carrier and protector for photosensitive and hydrophobic drugs. Although stability and cytotoxicity of the empty barrels alone have not been investigated, this study clearly demonstrated the increased bioavailability and stability of curcumin in water solutions as seen from the fluorescence microscopy imaging of the cancer cells and the increased cytotoxicity with respect to the curcumin concentration.

A similar tetrafacial barrel with composition Pd_8L_4 (**29**, **Figure 10**) has been built from tetraimidazolyl carbazole ligand (**L18**) (Roy et al., 2015). This metallosupramolecule has a tubular morphology that was fully characterized by multinuclear 1D/2D NMR and ESI-MS as well as by single-crystal X-ray diffraction of the coronene enclosing host-guest complex. While the barrel itself is water soluble, its hydrophobic cavity renders it ideal to solubilize hydrophobic guest molecules. Moreover, the inclusion of polyaromatic hydrocarbons with strong optical absorption and emission properties is accompanied with color and/or emission change. This property has been employed in live-cell fluorescence microscopy imaging by the water soluble perylene enclosing barrel, which demonstrated enhanced cell membrane permeability of the inclusion complex. This example gives the hope for further successful utilization of water soluble metalosupramolecules as drug or probe carriers provided their biocompatibility, stability and drug release properties is proved.

The flexible tetra(pyridin-4-yl)benzene-1,4-amine (**L17**, **Figure 10**) has also been used to construct organometallic octanuclear Ru(II) cages from dinuclear p-cymene ruthenium(II) acceptors, used as bridging oxo-pillars that vary from oxalate, benzoquinones, naphthoquinones (Ajibola Adeyemo et al., 2017). The largest box was characterized by X-ray diffraction besides the NMR, ESI-MS and electronic absorption spectra that have been used for characterization of all other boxes. All Ru8 cages showed strong anticancer activity *in vitro* that is comparable with cytotoxicity of cisplatin against A549 and HeLa cells. The anticancer profiles showed increasing cytotoxicity by enlarging the aromatic unit of the oxo-bridging pillars.

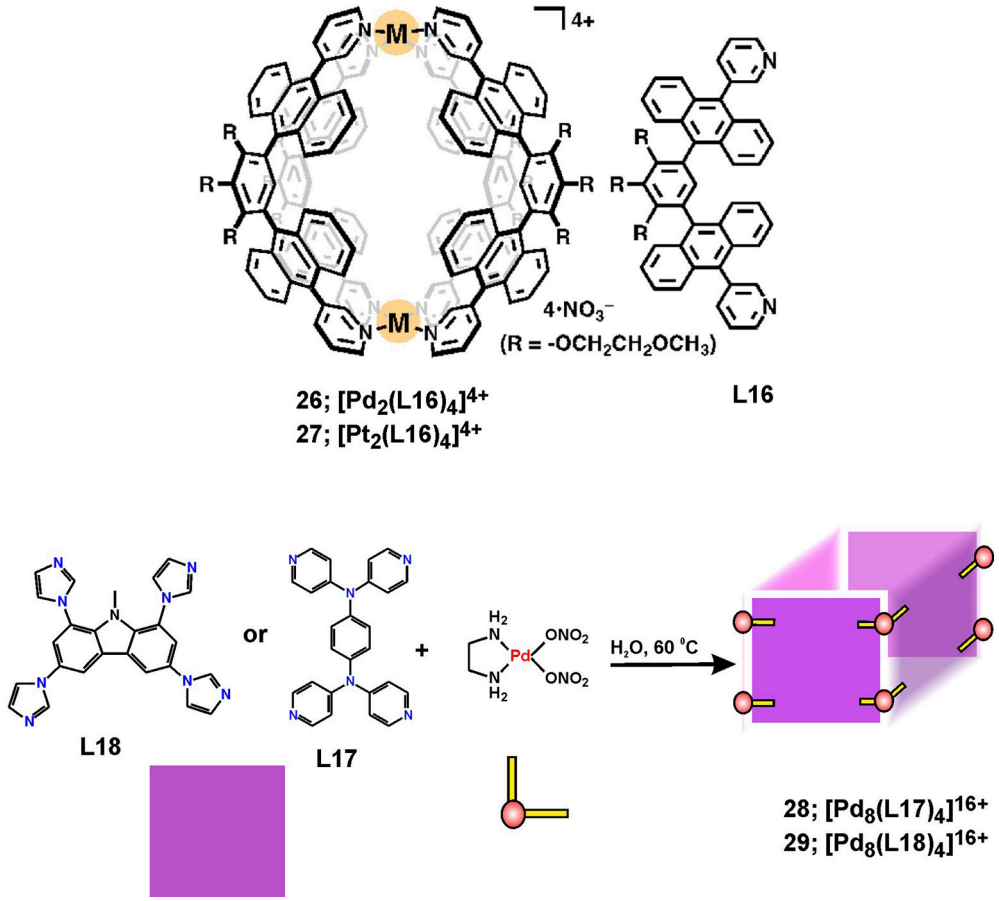

FIGURE 10 | Metallosupramolecular capsules **26** and **27** and barrels **28** and **29** with characteristic hydrophobic cavities.

CONCLUSIONS

From the presented recent examples for the fast-expanding chemotherapeutic applications of metallosupramolecular entities, it can be concluded that this class of compounds provide a rich field for exploration. The diversity in their properties stems from the fact that the metallosupramolecules can intelligently combine metal hinges of different coordination and reactivity properties as well as multidentate ligands that can be readily decorated without affecting the self-assembly processes. This has presented several working strategies to either increase the size or stability of the formed metalosupramolecular structures or to link them with receptor specific vectors. Construction of larger size composites that incorporate metallosupramolecules proved useful to target and deliver both therapeutic and imaging probes. The unique property of the 3D structures of metallacages, capsules, and barrels, is their discrete cavity which opens up further prospects for biological applications. Among the mostly explored ones are the encapsulation and delivery of bioactive molecules. Thereby, one and the same metallosupramolecular host can be used for different biological (therapeutic or diagnostic) purposes depending on the properties of the encapsulated guest molecule. The demonstrated encapsulation of Pt(IV)-prodrugs, which can be activated and subsequently released in the intracellular media by selective reduction and formation of the corresponding Pt(II)-drug, is an intriguing advancement to fully explore the potential for biomedical applications of the coordination supramolecules. Moreover, the encapsulation of a fluorescein-bearing Pt(IV)-prodrugs by the **Pt-cage 1**, shown in **Figure 9**, had actually added imaging modality to the selective anticancer treatment. The presented examples are only some of the suggestions on how to augment the cancer treatment potential of such host-guest complexes with additional imaging modality.

The showed examples can expand in the near future toward modifying or multiplying the main therapeutic action by introducing immunomodulatory, anti- or pro-oxidative molecules, or other bioactive fragments either as guest molecules or as exo-functionalization of the supramolecular hosts. The proof-of-concept for exo-functionalization of metallosupramolecules with large peptides has already been demonstrated and is expected to open additional prospect to construct hybrid systems with larger size (>30 nm) that can benefit from both the targeting properties of the attached biomolecule and the truly efficient EPR effect.

The flexibility to modulate the overall stability of the 3D metallosupramolecular structures, by simply encapsulating appropriate guest molecule is another approach to fine-tune either the delivery properties or their therapeutic potential. In the cases when the increased stability affects the biological action of the supramolecules, guest-encapsulation can be exploited to turn the toxic species into non-toxic or vice versa, and thus, transform them from toxic anticancer agents to safe drug-delivery vehicles. Exploiting also building components with interesting optical or redox properties enriches further the possibilities to adjust the structure and properties of the constructed metallosupramolecules to the desired biomedical application. Inevitably, the presented examples are an expanding source of inspiration for many synthetic and biological chemists to, hopefully, allow them fully reveal the multifaceted potential of the metallosupramolecules.

AUTHOR CONTRIBUTIONS

The author confirms being the sole contributor of this work and has approved it for publication.

ACKNOWLEDGMENTS

The National Science Fund of Bulgaria is gratefully acknowledged for the financial support (DFNI-B02/24). The support from H2020-Twinning project (Materials Networking; 692146) is gratefully acknowledged.

REFERENCES

Ahmedova, A., Mihaylova, R., Momekova, D., Shestakova, P., Stoykova, S., Zaharieva, J., et al. (2016a). M2L4 coordination capsules with tunable anticancer activity upon guest encapsulation. *Dalton Trans.* 45, 13214–13221. doi: 10.1039/C6DT01801G

Ahmedova, A., Momekova, D., Yamashina, M., Shestakova, P., Momekov, G., Akita, M., et al. (2016b). Anticancer Potencies of Pt(II) - and Pd(II)-linked M2L4 coordination capsules with improved selectivity. *Chem. Asian J.* 11, 474–477. doi: 10.1002/asia.201501238

Aird, R. E., Cummings, J., Ritchie, A. A., Muir, M., Morris, R. E., Chen, H., et al. (2002). *In vitro* and *in vivo* activity and cross resistance profiles of novel ruthenium (II) organometallic arene complexes in human ovarian cancer. *Br. J. Cancer* 86, 1652–1657. doi: 10.1038/sj.bjc.6600290

Ajibola Adeyemo, A., Shettar, A., Bhat, I. A., Kondaiah, P., and Mukherjee, P. S. (2017). Self-Assembly of discrete RuII8 molecular cages and their *in vitro* anticancer activity. *Inorg. Chem.* 56, 608–617. doi: 10.1021/acs.inorgchem.6b02488

Allison, S. J., Cooke, D., Davidson, F. S., Elliott, P. I. P., Faulkner, R. A., Griffiths, H. B. S., et al. (2018). Ruthenium-containing linear helicates and mesocates with tuneable p53-selective cytotoxicity in colorectal cancer cells. *Angew. Chem.* 130, 9947–9952. doi: 10.1002/ange.201805510

Bhat, I. A., Jain, R., Siddiqui, M. M., Saini, D. K., and Mukherjee, P. S. (2017). Water-soluble Pd8L4 self-assembled molecular barrel as an aqueous carrier for hydrophobic curcumin. *Inorg. Chem.* 56, 5352–5360. doi: 10.1021/acs.inorgchem.7b00449

Bhowmick, S., Jana, A., Singh, K., Gupta, P., Gangrade, A., Mandal, B. B., et al. (2018). Coordination-driven self-assembly of ionic irregular hexagonal metallamacrocycles via an organometallic clip and their cytotoxicity potency. *Inorg. Chem.* 57, 3615–3625. doi: 10.1021/acs.inorgchem.7b01561

Bilbeisi, R. A., Olsen, J. C., Charbonnière, L. J., and Trabolsi, A. (2014). Self-assembled discrete metal-organic complexes: Recent advances. *Inorg Chim Acta* 417, 79–108. doi: 10.1016/j.ica.2013.12.015

Casini, A., Woods, B., and Wenzel, M. (2017). The promise of self-assembled 3D supramolecular coordination complexes for biomedical applications. *Inorg. Chem.* 56, 14715–14729. doi: 10.1021/acs.inorgchem.7b02599

Chen, L. J., Chen, S., Qin, Y., Xu, L., Yin, G. Q., Zhu, J. L., et al. (2018). Construction of porphyrin-containing metallacycle with improved stability and activity within mesoporous carbon. *J. Am. Chem. Soc.* 140, 5049–5052. doi: 10.1021/jacs.8b02386

Cook, T. R., and Stang, P. J. (2015). Recent developments in the preparation and chemistry of metallacycles and metallacages via coordination. *Chem. Rev.* 115, 7001–7045. doi: 10.1021/cr5005666

Cook, T. R., Vajpayee, V., Lee, M. H., Stang, P. J., and Chi, K. W. (2013). Biomedical and biochemical applications of self-assembled metallacycles and metallacages. *Acc. Chem. Res.* 46, 2464–2474. doi: 10.1021/ar400010v

Crowley, J. D., and Gavey, E. L. (2010). Use of di-1,4-substituted-1,2,3-triazole "click" ligands to self-assemble dipalladium(ii) coordinatively saturated, quadruply stranded helicate cages. *Dalton Trans.* 39, 4035–4037. doi: 10.1039/C003683H

Datta, S., Saha, M. L., and Stang, P. J. (2018). Hierarchical assemblies of supramolecular coordination complexes. *Acc. Chem. Res.* 51, 2047–2063. doi: 10.1021/acs.accounts.8b00233

Domarco, O., Lötsch, D., Schreiber, J., Dinhof, C., Van Schoonhoven, S., García, M. D., et al. (2017). Self-assembled Pt2L2 boxes strongly bind G-quadruplex DNA and influence gene expression in cancer cells. *Dalton Trans.* 46, 329–332. doi: 10.1039/c6dt03876j

Dubey, A., Min, J. W., Koo, H. J., Kim, H., Cook, T. R., Kang, S. C., et al. (2013). Anticancer potency and multidrug-resistant studies of self-assembled arene-ruthenium metallarectangles. *Chem. Eur. J.* 19, 11622–11628. doi: 10.1002/chem.201300870

Grishagin, I. V., Pollock, J. B., Kushal, S., Cook, T. R., Stang, P. J., and Olenyuk, B. Z. (2014). *In vivo* anticancer activity of rhomboidal Pt(II) metallacycles. *Proc. Natl. Acad. Sci. U.S.A.*111, 18448–18453. doi: 10.1073/pnas.1418712111

Gupta, G., Das, A., Park, K. C., Tron, A., Kim, H., Mun, J., et al. (2017). Self-Assembled Novel BODIPY-based palladium supramolecules and their cellular localization. *Inorg. Chem.* 56, 4616–4622. doi: 10.1021/acs.inorgchem.7b00260

Han, J., Schmidt, A., Zhang, T., Permentier, H., Groothuis, G. M., Bischoff, R., et al. (2017). Bioconjugation strategies to couple supramolecular exo-functionalized palladium cages to peptides for biomedical applications. *Chem. Commun.* 53, 1405–1408. doi: 10.1039/c6cc08937b

Hotze, A. C., Kariuki, B. M., and Hannon, M. J. (2006). Dinuclear double-stranded metallosupramolecular ruthenium complexes: potential anticancer drugs. *Angew Chem.* 45, 4839–4842. doi: 10.1002/anie.200601351

Ibukuro, F., Kusukawa, T., and Fujita, M. (1998). A thermally switchable molecular lock. Guest-templated synthesis of a kinetically stable nanosized cage. *J. Am.Chem. Soc.* 120, 8561–8562. doi: 10.1021/ja980853f

Jana, A., Bhowmick, S., Kumar, S., Singh, K., Garg, P., and Das, N. (2019). Self-assembly of Pt(II) based nanoscalar ionic hexagons and their anticancer potencies. *Inorg. Chim. Acta* 484, 19–26. doi: 10.1016/j.ica.2018.09.009

Jana, A., Lippmann, P., Ott, I., and Das, N. (2018). Self-assembly of flexible [2 + 2] ionic metallamacrocycles and their cytotoxicity potency. *Inorg. Chim Acta* 471, 223–227. doi: 10.1016/j.ica.2017.11.002

Kaiser, F., Schmidt, A., Heydenreuter, W., Altmann, P. J., Casini, A., Sieber, S. A., et al. (2016). Self-assembled palladium and platinum coordination cages: photophysical studies and anticancer activity. *Eur. J. Inorg. Chem.* 2016, 5189–5196. doi: 10.1002/ejic.201600811

Kaner, R. A., Allison, S. J., Faulkner, A. D., Phillips, R. M., Roper, D. I., Shepherd, S. L., et al. (2016). Anticancer metallohelices: nanomolar potency and high selectivity. *Chem. Sci.* 7, 951–958. doi: 10.1039/c5sc03677a

Kishi, N., Li, Z., Yoza, K., Akita, M., and Yoshizawa, M. (2011). An M2L4 molecular capsule with an anthracene shell: encapsulation of large guests up to 1nm. *J. Am. Chem. Soc.* 133, 11438–11441. doi: 10.1021/ja2037029

Leung, C. H., Kang, T. S., Yang, C., Leung, K. H., and Ma, D. L. (2017). "Biological applications of supramolecular coordination complexes," in *Comprehensive Supramolecular Chemistry II*, ed J. L. Atwood (Elsevier Inc.), 3–20.

Lewis, J. E., McAdam, C. J., Gardiner, M. G., and Crowley, J. D. (2013). A facile "click" approach to functionalised metallosupramolecular architectures. *Chem. Commun.* 49, 3398–3400. doi: 10.1039/c3cc41209a

Lewis, J. E. M., Elliott, A. B. S., McAdam, C. J., Gordon, K. C., and Crowley, J. D. (2014). 'Click' to functionalise: synthesis, characterisation and enhancement of the physical properties of a series of exo- and endo-functionalised Pd2L4 nanocages. *Chem. Sci.* 5, 1833–1843. doi: 10.1039/c4sc00434e

Lewis, J. E. M., Gavey, E. L., Cameron, S. A., and Crowley, J. D. (2012). Stimuli-responsive Pd2L4metallosupramolecular cages: towards targeted cisplatin drug delivery. *Chem. Sci.* 3, 778–784. doi: 10.1039/c2sc00899h

Li, M., Howson, S. E., Dong, K., Gao, N., Ren, J., Scott, P., et al. (2014). Chiral metallohelical complexes enantioselectively target amyloid beta for treating Alzheimer's disease. *J. Am. Chem. Soc.* 136, 11655–11663. doi: 10.1021/ja502789e

Li, Z., Kishi, N., Yoza, K., Akita, M., and Yoshizawa, M. (2012). Isostructural M2L4 molecular capsules with anthracene shells: Synthesis, crystal structures, and fluorescent properties. *Chem - Eur J* 18, 8358–8365. doi: 10.1002/chem.201200155

Ma, X., and Zhao, Y. (2015). Biomedical applications of supramolecular systems based on host-guest interactions. *Chem. Rev.* 115, 7794–7839. doi: 10.1021/cr500392w

Malina, J., Hannon, M. J., and Brabec, V. (2008). DNA binding of dinuclear iron(II) metallosupramolecular cylinders. DNA unwinding and sequence preference. *Nucleic Acids Res.* 36, 3630–3638. doi: 10.1093/nar/gkn244

Malina, J., Hannon, M. J., and Brabec, V. (2014). Recognition of DNA bulges by dinuclear iron(II) metallosupramolecular helicates. *FEBS J.* 281, 987–997. doi: 10.1111/febs.12696

Malina, J., Hannon, M. J., and Brabec, V. (2016). Iron(II) supramolecular helicates interfere with the HIV-1 Tat-TAR RNA interaction critical for viral replication. *Sci. Rep.* 6: 29674. doi: 10.1038/srep29674

Mattsson, J., Govindaswamy, P., Renfrew, A. K., Dyson, P. J., Stepnicka, P., Süss-Fink, G., et al. (2009). Synthesis, molecular structure and anticancer activity of cationic arene ruthenium metallarectangles. *Organometallics* 28, 4350–4357. doi: 10.1021/om900359j

McConnell, A. J., Wood, C. S., Neelakandan, P. P., and Nitschke, J. R. (2015). Stimuli-responsive metal-ligand assemblies. *Chem. Rev.* 115, 7729–7793. doi: 10.1021/cr500632f

McNeill, S. M., Preston, D., Lewis, J. E., Robert, A., Knerr-Rupp, K., Graham, D. O., et al. (2015). Biologically active [Pd2L4](4+) quadruply-stranded helicates: stability and cytotoxicity. *Dalton Trans.* 44, 11129–11136. doi: 10.1039/c5dt01259g

Mishra, A., Lee, S. C., Kaushik, N., Cook, T. R., Choi, E. H., Kaushik, N. K., et al. (2014). Self-assembled supramolecular hetero-bimetallacycles for anticancer potency by intracellular release. *Chem. Eur. J.* 20, 14410–14420. doi: 10.1002/chem.201403372

Mounir, M., Lorenzo, J., Ferrer, M., Prieto, M. J., Rossell, O., Aviles, F. X., et al. (2007). DNA interaction and antiproliferative behavior of the water soluble platinum supramolecular squares [(en)Pt(N-N)]4(NO3)8 (en=ethylenediamine, N-N=4,4'-bipyridine or 1,4-bis(4-pyridyl)tetrafluorobenzene). *J. Inorg. Biochem.* 101, 660–666. doi: 10.1016/j.jinorgbio.2006.12.009

Pascu, G. I., Hotze, A. C., Sanchez-Cano, C., Kariuki, B. M., and Hannon, M. J. (2007). Dinuclear ruthenium(II) triple-stranded helicates: luminescent supramolecular cylinders that bind and coil DNA and exhibit activity against cancer cell lines. *Angew Chem.* 46, 4374–4378. doi: 10.1002/anie.200700656

Preston, D., McNeill, S. M., Lewis, J. E., Giles, G. I., and Crowley, J. D. (2016). Enhanced kinetic stability of [Pd2L4](4+) cages through ligand substitution. *Dalton Trans.* 45, 8050–8060. doi: 10.1039/c6dt00133e

Rodriguez, J., Mosquera, J., Couceiro, J. R., Nitschke, J. R., Vazquez, M. E., and Mascarenas, J. L. (2017). Anion recognition as a supramolecular switch of cell internalization. *J. Am. Chem. Soc.* 139, 55–58. doi: 10.1021/jacs.6b11103

Roy, B., Ghosh, A. K., Srivastava, S., D'Silva, P., and Mukherjee, P. S. (2015). A Pd8 tetrafacial molecular barrel as carrier for water insoluble fluorophore. *J. Am. Chem. Soc.* 137, 11916–11919. doi: 10.1021/jacs.5b08008

Schmidt, A., Casini, A., and Kühn, F. E. (2014). Self-assembled M2L4 coordination cages: synthesis and potential applications. *Coord. Chem. Rev.* 275 19–36. doi: 10.1016/j.ccr.2014.03.037

Schmidt, A., Hollering, M., Drees, M., Casini, A., and Kühn, F. E. (2016a). Supramolecular: Exo -functionalized palladium cages: Fluorescent properties and biological activity. *Dalton Trans.* 45, 8556–8565. doi: 10.1039/c6dt00654j

Schmidt, A., Molano, V., Hollering, M., Poethig, A., Casini, A., and Kühn, F. E. (2016b). Evaluation of new palladium cages as potential delivery systems for the anticancer drug cisplatin. *Chem. Eur. J.* 22, 2253–2256. doi: 10.1002/chem.201504930

Schmitt, F., Freudenreich, J., Barry, N. P. E., Juillerat-Jeanneret, L., Süss-Fink, G., and Therrien, B. (2012). Organometallic cages as vehicles for intracellular release of photosensitizers. *J. Am. Chem. Soc.* 134, 754–757. doi: 10.1021/ja207784t

Smith, G. S., and Therrien, B. (2011). Targeted and multifunctional arene ruthenium chemotherapeutics. *Dalton Trans.* 40, 10793–10800. doi: 10.1039/c1dt11007a

Terenzi, A., Ducani, C., Blanco, V., Zerzankova, L., Westendorf, A. F., Peinador, C., et al. (2012). DNA binding studies and cytotoxicity of a dinuclear PtII diazapyrenium-based metallo-supramolecular rectangular box. *Chem. Eur. J.* 18, 10983–10990. doi: 10.1002/chem.201201519

Therrien, B. (2013). Transporting and shielding photosensitisers by using water-soluble organometallic cages: a new strategy in drug delivery and photodynamic therapy. *Chem. Eur. J.* 19, 8378–8386. doi: 10.1002/chem.201301348

Therrien, B., Süss-Fink, G., Govindaswamy, P., Renfrew, A. K., and Dyson, P. J. (2008). The "complex-in-a-complex" cations [(acac)2M-Ru6-(p-iPrC6H4Me)6(tpt) 2(dhbq)3]6+: A trojan horse for cancer cells. *Angew. Chem. Int. Ed Engl.* 47, 3773–3776. doi: 10.1002/anie.200800186

Tian, Y., Yan, X., Saha, M. L., Niu, Z., and Stang, P. J. (2016). Hierarchical Self-Assembly of Responsive Organoplatinum(II) Metallacycle-TMV Complexes with Turn-On Fluorescence. *J. Am. Chem. Soc.* 138, 12033–12036. doi: 10.1021/jacs.6b07402

Vajpayee, V., Lee, S. M., Park, J. W., Dubey, A., Kim, H., Cook, T. R., et al. (2013). Growth inhibitory activity of a bis-benzimidazole-bridged arene ruthenium metalla-rectangle and prism. *Organometallics* 32, 1563–1566. doi: 10.1021/om301174s

Vellas, S. K., Lewis, J. E., Shankar, M., Sagatova, A., Tyndall, J. D., Monk, B. C., et al. (2013). [Fe(2)L(3)](4)(+) cylinders derived from bis(bidentate) 2-pyridyl-1,2,3-triazole "click" ligands: synthesis, structures and exploration of biological activity. *Molecules* 18, 6383–6407. doi: 10.3390/molecules18066383

Yamashina, M., Akita, M., Hasegawa, T., Hayashi, S., and Yoshizawa, M. (2017). A polyaromatic nanocapsule as a sucrose receptor in water. *Sci. Adv.* 3:e1701126. doi: 10.1126/sciadv.1701126

Yamashina, M., Matsuno, S., Sei, Y., Akita, M., and Yoshizawa, M. (2016). Recognition of multiple methyl groups on aromatic rings by a polyaromatic cavity. *Chem. Eur. J.* 22, 14147–14150. doi: 10.1002/chem.201603032

Yamashina, M., Sei, Y., Akita, M., and Yoshizawa, M. (2014). Safe storage of radical initiators within a polyaromatic nanocapsule. *Nature Commun.* 5:4662. doi: 10.1038/ncomms5662

Yan, H., Süss-Fink, G., Neels, A., and Stoeckli-Evans, H. (1997). Mono-, di- and tetra-nuclear p-cymeneruthenium complexes containing oxalato ligands. *J. Chem. Soc. Dalton Trans.* 4345–4350. doi: 10.1039/a704658h

Yan, X., Wang, M., Cook, T. R., Zhang, M., Saha, M. L., Zhou, Z., et al. (2016). Light-emitting superstructures with anion effect: coordination-driven self-assembly of pure tetraphenylethylene metallacycles and metallacages. *J. Am. Chem. Soc.* 138, 4580–4588. doi: 10.1021/jacs.6b00846

Yoshizawa, M., Klosterman, J. K., and Fujita, M. (2009). Functional molecular flasks: new properties and reactions within discrete, self-assembled hosts. *Angew. Chem. Int Ed* 48, 3418–3438. doi: 10.1002/anie.200805340

Yu, G., Cook, T. R., Li, Y., Yan, X., Wu, D., Shao, L., et al. (2016). Tetraphenylethene-based highly emissive metallacage as a component of theranostic supramolecular nanoparticles. *Proc. Natl. Acad. Sci. U.S.A.* 113, 13720–13725. doi: 10.1073/pnas.1616836113

Yue, Z., Wang, H., Bowers, D. J., Gao, M., Stilgenbauer, M., Nielsen, F., et al. (2018). Nanoparticles of metal-organic cages designed to encapsulate platinum-based anticancer agents. *Dalton Trans.* 47, 670–674. doi: 10.1039/c7dt03537c

Zarra, S., Wood, D. M., Roberts, D. A., and Nitschke, J. R. (2015). Molecular containers in complex chemical systems. *Chem. Soc. Rev.* 44, 419–432. doi: 10.1039/C4CS00165F

Zhang, M., Li, S., Yan, X., Zhou, Z., Saha, M. L., Wang, Y. C., et al. (2016). Fluorescent metallacycle-cored polymers via covalent linkage and their use as contrast agents for cell imaging. *Proc. Natl. Acad. Sci. U.S.A.* 113, 11100–11105. doi: 10.1073/pnas.1612898113

Zhang, Y.-Y., Gao, W.-X., Lin, L., and Jin, G.-X. (2017). Recent advances in the construction and applications of heterometallic macrocycles and cages. *Coord. Chem. Rev.* 344, 323–344. doi: 10.1016/j.ccr.2016.09.010

Zheng, Y. R., Suntharalingam, K., Bruno, P. M., Lin, W., Wang, W., Hemann, M. T., et al. (2016). Mechanistic Studies of the Anticancer Activity of An Octahedral Hexanuclear Pt(II) Cage. *Inorg. Chim. Acta* 452, 125–129. doi: 10.1016/j.ica.2016.03.021

Zheng, Y. R., Suntharalingam, K., Johnstone, T. C., and Lippard, S. J. (2015). Encapsulation of Pt(IV) Prodrugs within a Pt(II) cage for drug delivery. *Chem. Sci.* 6, 1189–1193. doi: 10.1039/C4SC01892C

Zhou, J., Zhang, Y., Yu, G., Crawley, M. R., Fulong, C. R. P., Friedman, A. E., et al. (2018a). Highly Emissive Self-Assembled BODIPY-Platinum Supramolecular Triangles. *J. Am. Chem. Soc.* 140, 7730–7736. doi: 10.1021/jacs.8b04929

Zhou, Z., Liu, J., Rees, T. W., Wang, H., Li, X., Chao, H., et al. (2018b). Heterometallic Ru-Pt metallacycle for two-photon photodynamic therapy. *Proc. Natl. Acad. Sci. U.S.A.* 115, 5664–5669. doi: 10.1073/pnas.1802012115

Conflict of Interest Statement: The author declares that the research was conducted in the absence of any commercial or financial relationships that could be construed as a potential conflict of interest.

frontiers in Chemistry

MINI REVIEW
published: 11 December 2018
doi: 10.3389/fchem.2018.00602

The Role of the Second Coordination Sphere in the Biological Activity of Arene Ruthenium Metalla-Assemblies

*Bruno Therrien**

Institute of Chemistry, University of Neuchatel, Neuchatel, Switzerland

For nearly 15 years, the biological and biomedical applications of arene ruthenium metalla-assemblies have flourished. Today, the synthetic strategies to generate arene ruthenium assemblies are well-established, and these compounds offer tremendous possibilities in terms of structural diversities and chemical properties. However, the second coordination sphere is often poorly considered, if not ignored, when designing such arene ruthenium metalla-assemblies. These weak interactions (hydrogen bonding, hydrophobic, ionic, electrostatic, van der Waals, π-π stacking) that take place in the solid state or in solution are generally key interactions for the foreseen applications. Therefore, in this review, we want to emphasize this important property of arene ruthenium metalla-assemblies by showing examples dealing with second coordination sphere interactions and how this can be better integrated in the design of these versatile supramolecular metal-based entities.

Keywords: arene ruthenium, metalla-assemblies, bio-inorganic, piano-stool complexes, weak interactions, second coordination sphere

OPEN ACCESS

Edited by:
Angela Casini,
Cardiff University, United Kingdom

Reviewed by:
Gilles Gasser,
Université de Sciences Lettres de Paris, France
Tatjana N. Parac-Vogt,
KU Leuven, Belgium

***Correspondence:**
Bruno Therrien
bruno.therrien@unine.ch

Specialty section:
This article was submitted to Supramolecular Chemistry, a section of the journal Frontiers in Chemistry

Received: *25 October 2018*
Accepted: *20 November 2018*
Published: *11 December 2018*

Citation:
Therrien B (2018) The Role of the Second Coordination Sphere in the Biological Activity of Arene Ruthenium Metalla-Assemblies. Front. Chem. 6:602. doi: 10.3389/fchem.2018.00602

INTRODUCTION

It is now well-known that the second coordination sphere (second shell) plays a major role in metal-based enzymatic transformations (Dudev et al., 2003). These additional interactions that take place in the proximity of the catalytic pocket can either stabilize the metal-substrate complex, stabilize the electronic state of the metal, orient the ligands to enhance the reactivity, act as proton and/or electron mediators, and so on (Ando et al., 1996; Botta, 2000; Steed, 2001; Haviv et al., 2018). More generally, these weak interactions (coordination, ionic, hydrogen bonding, hydrophobic, electrostatic, van der Waals, π-π stacking) are not only extremely important for biological processes, they are also a pillar of supramolecular chemistry. They allow the formation in the solid state of molecular networks (Hosseini, 2003), the preparation of liquid crystalline materials (Kato et al., 2018), the construction of coordination-driven assemblies (Fujita et al., 2005), as well as the generation of many other supramolecular systems (Wu et al., 2008; Zhou et al., 2017).

For many years, we have been involved in the field of coordination-driven self-assembly, using piano-stool complexes (also called half-sandwich complexes) as building blocks, and especially arene ruthenium complexes as biological agents (Therrien and Furrer, 2014; Therrien, 2015). The piano-stool unit provides three coordination sites at 90° from each other for a strategic

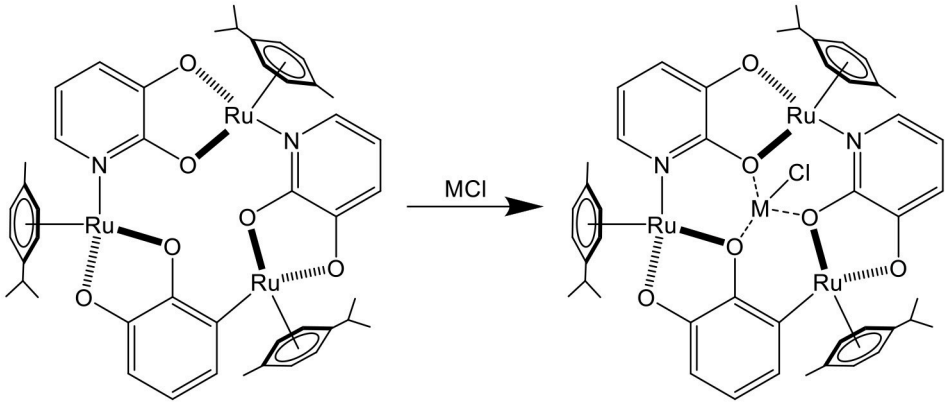

FIGURE 1 | Sensing of MCl (M = Li, Na, K) in a trinuclear arene ruthenium metalla-cycle (Piotrowski et al., 2001).

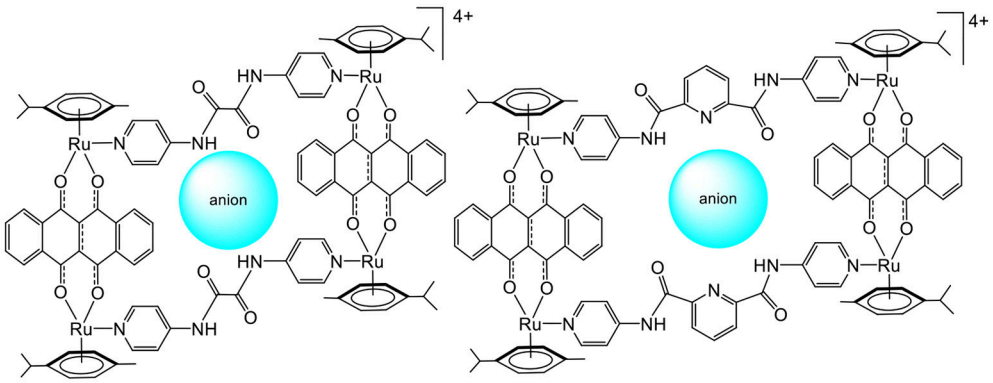

FIGURE 2 | Sensing of polyanionic species in tetranuclear arene ruthenium metalla-assemblies (Vajpayee et al., 2011; Mishra et al., 2012).

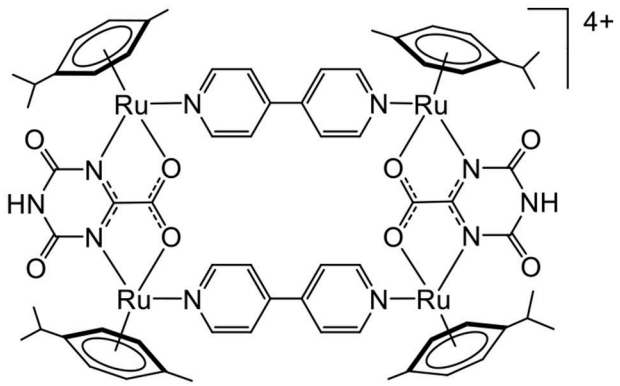

FIGURE 3 | Arene ruthenium metalla-rectangle interacting with DNA (Linares et al., 2009).

coordination of ligands on metals (Therrien, 2009), which allows the design of 2D and 3D entities (Cook et al., 2013; Singh et al., 2014; Therrien, 2018). These metalla-assemblies possess different functional groups, situated either at the periphery or at the core of the assembly. They have good stability in solution, showing no dynamic ligand exchange under ordinary conditions (Garci et al., 2014). They come in different sizes, with or without a cavity, and they can be positively charged, thus showing various properties and solubility. Among these properties, host-guest chemistry, biological activity, DNA interactions, recognition, ion binding, and others have been identified. Therefore, in this perspective review, the biological applications of arene ruthenium metalla-assemblies are discussed from the second coordination sphere point of view, to better emphasize the importance of weak interactions in diverse properties. Ultimately, it can provide to those working in the field a different angle to envision the next generation of metalla-assemblies in biomedical fields.

SENSING

The first example of arene ruthenium metalla-assemblies used for sensing was published in 2001 (Piotrowski et al., 2001). The electrochemical property of a trinuclear arene ruthenium metalla-cycle was exploited. Interestingly, upon the binding of alkali chloride salts in the triple-oxo binding site of the metalla-cycle (**Figure 1**), the oxidation potential of the trinuclear

assembly was shifted by as much as 450 mV in the presence of LiCl, thus providing a redox-responsive signal upon guest binding.

Later, the possibility of using arene ruthenium metalla-assemblies for sensing biologically relevant substrates was explored by Chi and Stang (Vajpayee et al., 2011; Mishra et al., 2012). The cavity of arene ruthenium metalla-rectangles (**Figure 2**) has shown interactions with polyanionic compounds (oxalate, citrate, tartrate). The presence of multiple amido and pyridine groups within the core of the metalla-rectangles was crucial for the recognition process to take place. Moreover, the amido groups gave some structural flexibility to the systems, thus providing binding adaptability to optimize the interactions with anions. In these systems, the size of the cavity and the capacity to form several hydrogen-bonds with anions are crucial elements for the sensing process to take place.

These are simple examples in which the nature of the functional groups incorporated in the building blocks of the arene ruthenium metalla-assemblies has provided valuable second sphere coordination interactions to develop metalla-assembled sensors.

DNA INTERACTIONS

The good water solubility and the presence of positive charges on most arene ruthenium metalla-assemblies are both advantageous properties for interactions with biomolecules. The first study dealing with arene ruthenium metalla-assemblies and DNA interactions was published in 2009 (**Figure 3**). The tetracationic bowl-shaped rectangle showed good interaction with calf-thymus DNA (Linares et al., 2009). Binding assays have suggested that the interactions take place in the major groove of the duplex DNA strand. Conformational changes in the DNA strand are probably due to electrostatic interactions between the cationic metalla-rectangle and the negatively charged surface of DNA as well as the good match

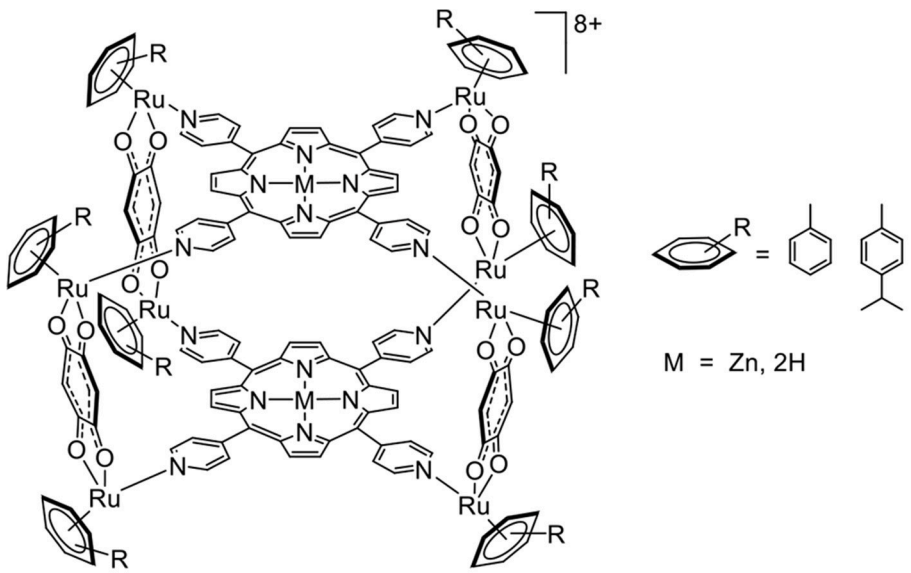

FIGURE 4 | Arene ruthenium metalla-cubes interacting with G-quadruplexes (Barry et al., 2009).

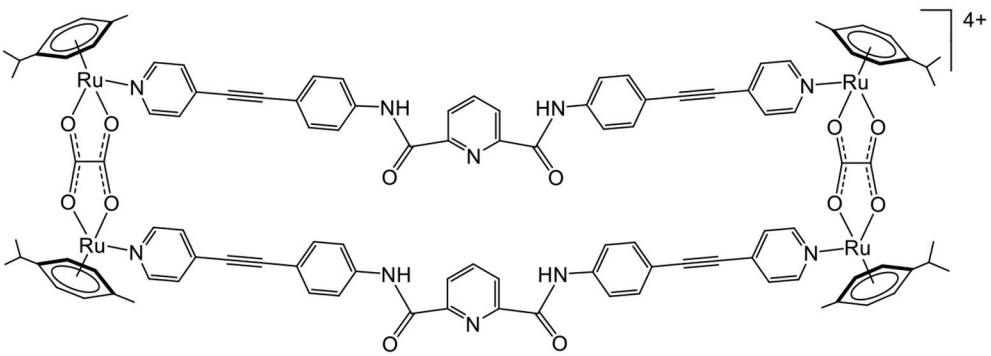

FIGURE 5 | Arene ruthenium metalla-rectangle interacting with EGF protein (Mishra et al., 2014).

between the size of the rectangle and the size of the major groove.

Following this initial study, several other arene ruthenium metalla-assemblies were tested as duplex DNA binders (Linares et al., 2010; Paul et al., 2015; Gupta et al., 2016, 2017). However, in the human genome, DNA sequences can fold into other thermodynamically stable structures such as hairpins and quadruplexes. These kinds of secondary structures are interesting targets for therapeutic applications (Zhao et al., 2010).

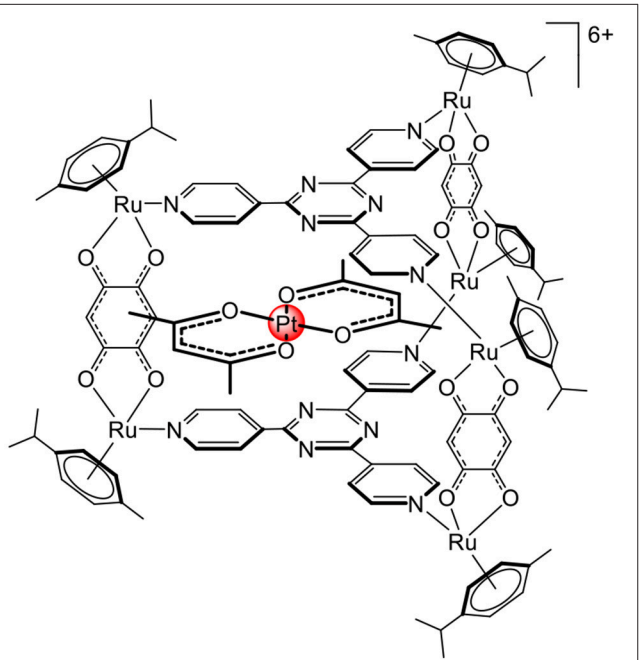

FIGURE 6 | Complex –in-a-complex arene ruthenium metalla-prism (Therrien et al., 2008).

Consequently, arene ruthenium metalla-assemblies have been used, for example, as quadruplex DNA stabilizers (Barry et al., 2009).

A G-quadruplex is composed of guanine tetrads intercalated by cations, and it possesses a planar aromatic surface (Balasubramanian and Neidle, 2009). Therefore, cationic molecules with π-stacking affinity can potentially interact with G-quadruplexes. This possibility of interaction and stabilization was confirmed from the porphyrin-based arene ruthenium metalla-cubes (**Figure 4**), which showed good stabilization of telomeric and *c-myc* DNA quadruplexes. In such systems, we can assume that a combination of electrostatic and π-stacking (hydrophobic) interactions generates second coordination sphere interactions.

PROTEIN INTERACTIONS

Like DNA, proteins can positively interact with cationic compounds, and accordingly with positively charged arene ruthenium metalla-assemblies. Different proteins interacting with such metalla-assemblies have been identified. Interestingly, these studies have shown that metalla-assemblies of different shapes, sizes, structures and numbers of charges are able to interact with proteins, confirming that interaction with biomolecules is a common feature of arene ruthenium metalla-assemblies (Dubey et al., 2015; Elumalai et al., 2016, 2017).

Indeed, an arene ruthenium metalla-rectangle with bis-amido pyridine containing linkers (**Figure 5**) shows strong interaction with enhanced green fluorescence protein (EGFP) (Mishra et al., 2014). Similarly, an arene ruthenium metalla-prism can disrupt the folded structures of albumin, transferrin, cytochrome-c, and other proteins (Paul et al., 2018), showing a great diversity of protein interactions. These examples

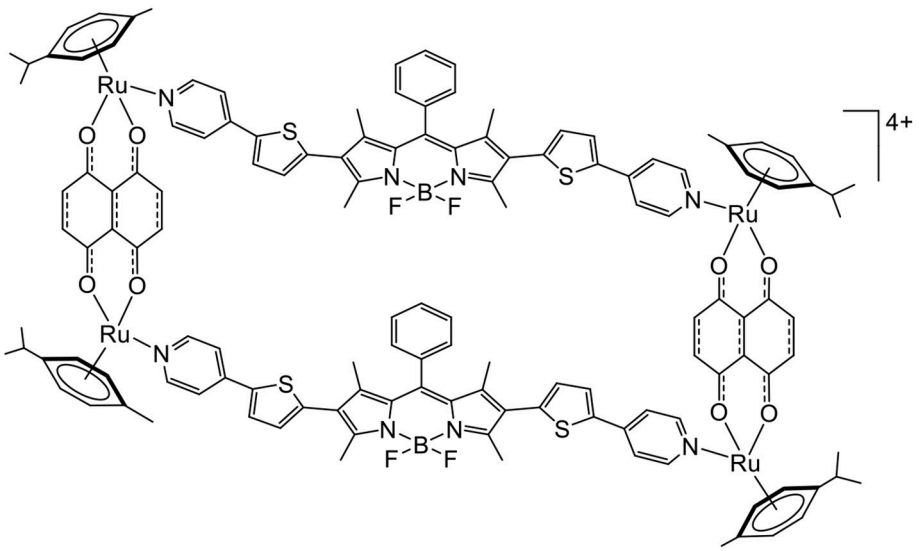

FIGURE 7 | BODIPY-based tetranuclear arene ruthenium metalla-assemblies as potential PDT agent (Gupta et al., 2017).

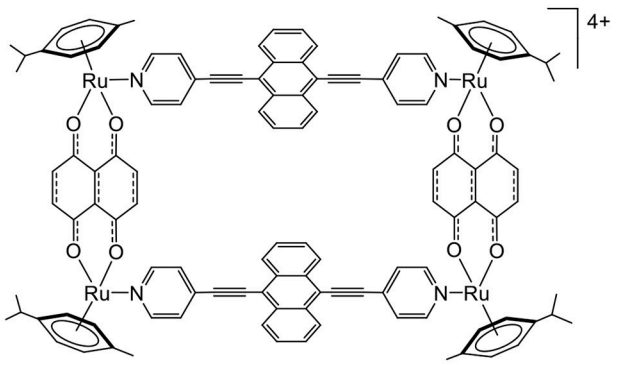

FIGURE 8 | Anthracene-based tetranuclear arene ruthenium metalla-assemblies for o_2 interactions (Gaschard et al., 2018).

suggest that the interactions between metalla-assemblies and proteins are mainly electrostatic. Therefore, to optimize the metalla-assembly protein interactions, and to gain a degree of selectivity for a specific protein, one cannot rely purely on electrostatic, hydrophobic, size-dependent or hydrogen-bond interactions. Only the multiplicity of second coordination sphere interactions can generate selective protein binders, which increases the complexity of designing arene ruthenium metalla-assemblies.

DECOMPLEXATION UPON INTERACTIONS

The first biological application of arene ruthenium metalla-assemblies was confirmed by the complex-in-a-complex system (**Figure 6**), in which a water-soluble arene ruthenium metalla-prism was used to transport the platinum acetylacetonate complex to cells (Therrien et al., 2008). Later, it was demonstrated that, after internalization, the guest complex was released, most likely upon disassembly of the cage compound (Mattsson et al., 2010). Furthermore, the metalla-prism can interact with biomolecules such as arginine, cysteine, glutathione, lysine, histidine (Paul et al., 2012a,b), and biomolecules possessing coordinating functional groups, thus being able to initiate the breakage of the cage compound. This suggests that despite being relatively robust to ligand exchange processes (Garci et al., 2014), second coordination sphere interactions can be used to disassemble arene ruthenium metalla-assemblies.

OXYGEN INTERACTIONS

In traditional photodynamic therapy (PDT), a photosensitizer interacts with oxygen to produce reactive oxygen species (ROS), and these ROS trigger cell death upon light activation (Patrice et al., 2003). Therefore, to evaluate the potential of using arene ruthenium metalla-assemblies as PDT agents, several metalla-assemblies coupled to photosensitizers were prepared and tested (Schmitt et al., 2009). The arene ruthenium units can modulate the solubility of the photosensitizers (Schmitt et al., 2008) as well as modify its photochemical behavior. Moreover, the cavity of arene ruthenium cages can transport and protect the photosensitizer (Schmitt et al., 2012).

Nevertheless, other types of molecules can interact with oxygen to generate ROS. This is the case of BODIPY, an interesting fluorescent dye with a high-quantum yield that can promote the production of ROS. Therefore, BODIPY-based linkers have been recently inserted in arene ruthenium metalla-rectangles (**Figure 7**), and the cytotoxicity of the compounds on various cancer cell lines was confirmed (Gupta et al., 2017). The fluorescence associated with the BODIPY units was exploited to localize the metalla-rectangle in the cytoplasm of cancer cells. However, the possibility of using such metalla-rectangles as PDT agents remains to be explored.

Anthracene is another molecule that can react with oxygen (Aubry et al., 2003). Anthracene forms in the presence of oxygen and light activation, an endoperoxide intermediate. The endoperoxide formation is reversible, and oxygen can be released in a different environment. Therefore, knowing that arene ruthenium metalla-assemblies can be internalized to cells and can be coupled to photosensitizers, we have recently synthesized an anthracene-based metalla-rectangle (**Figure 8**) (Gaschard et al., 2018). Despite an unsuccessful endoperoxide formation on the metalla-rectangle, the ultimate goal of this project was to transport oxygen and a photosensitizer to cells for an optimization of PDT treatments in hypoxic cancers.

CONCLUSION

As pointed out in this article, the second coordination sphere plays a major role in most biological and biomedical applications involving arene ruthenium metalla-assemblies. Therefore, the introduction of functional groups that can generate weak interactions with biomolecules on either the arene, the building blocks or the guest molecules is essential for the development of biologically active arene ruthenium metalla-assemblies. In the future, designing metalla-assemblies with second coordination sphere interactions in mind will be challenging, but it could provide the next generation of arene ruthenium derivatives for biological and biomedical applications.

AUTHOR CONTRIBUTIONS

The author confirms being the sole contributor of this work and has approved it for publication.

FUNDING

Over the years, we would like to acknowledge the financial support from the Swiss National Science Foundation, the European Union (POLYTHEA and NOAH projects) and the University of Neuchatel.

ACKNOWLEDGMENTS

The author would like to thank past and present members of his group.

REFERENCES

Ando, I., Ishimura, D., Ujimoto, K., and Kurihara, H. (1996). Effect of second-sphere coordination. 4. Factors influencing the electrochemical behavior of ruthenium-ammine complexes caused by second-sphere coordination of crown ethers. *Inorg. Chem.* 35, 3504–3508. doi: 10.1021/ic941048e

Aubry, J.-M., Pierlot, C., Rigaudy, J., and Schmidt, R. (2003). Reversible binding of oxygen to aromatic compounds. *Acc. Chem. Res.* 36, 668–675. doi: 10.1021/ar010086g

Balasubramanian, S., and Neidle, S. (2009). G-quadruplex nucleic acids as therapeutic targets. *Curr. Opin. Chem. Biol.* 13, 345–353. doi: 10.1016/j.cbpa.2009.04.637

Barry, N. P. E., Abd Karim, N. H., Vilar, R., and Therrien, B. (2009). Interactions of ruthenium coordination cubes with DNA. *Dalton Trans.* 10717–10719. doi: 10.1039/b913642h

Botta, M. (2000). Second coordination sphere water molecules and relaxivity of gadolinium(III) complexes: implications for MRI contrast agents. *Eur. J. Inorg. Chem.* 2000, 399–407. doi: 10.1002/(SICI)1099-0682(200003)2000:3<399::AID-EJIC399>3.0.CO;2-B

Cook, T. R., Vajpayee, V., Lee, M. H., Stang, P. J., and Chi, K.-W. (2013). Biomedical and biochemical applications of self-assembled metallacycles and metallacages. *Acc. Chem. Res.* 46, 2464–2474. doi: 10.1021/ar400010v

Dubey, A., Park, D. W., Kwon, J. E., Jeong, Y. J., Kim, T., Kim, I., et al. (2015). Investigation of the biological and anti-cancer properties of ellagic acid-encapsulated nano-sized metalla-cages. *Int. J. Nanomed.* 2015, 227–240. doi: 10.2147/IJN.S88289

Dudev, T., Lin, Y.-,l., Dudev, M., and Lim, C. (2003). First-second shell interactions in metal binding sites in proteins: A PDB survey and DFT/CDM calculations. *J. Am. Chem. Soc.* 125, 3168–3180. doi: 10.1021/ja0209722

Elumalai, P., Jeong, Y. J., Park, D. W., Kim, D. H., Kim, H., Kang, S. C., et al. (2016). Antitumor and biological investigation of doubly cyclometalated ruthenium(II) organometallics derived from benzimidazolyl derivatives. *Dalton Trans.* 45, 6667–6673. doi: 10.1039/C5DT04400F

Elumalai, P., Kaushik, N., Kim, D. H., Kim, H., Lee, S. J., Choi, E. H., et al. (2017). Flexible ligated ruthenium(II) self-assemblies sensitizes glioma tumor initiating cells *in vitro*. *Oncotarget* 8, 60188–60200. doi: 10.18632/oncotarget.19028

Fujita, M., Tominaga, M., Hori, A., and Therrien, B. (2005). Coordination assemblies from a Pd(II)-cornered square complex. *Acc. Chem. Res.* 38, 371–380. doi: 10.1021/ar040153h

Garci, A., Marti, S., Schürch, S., and Therrien, B. (2014). Insight into the dynamic ligand exchange process involved in bipyridyl linked arene ruthenium metalla-rectangles. *RSC Adv.* 4, 8597–8604. doi: 10.1039/c3ra46859c

Gaschard, M., Nehzat, F., Cheminel, T., and Therrien, B. (2018). Arene ruthenium metalla-assemblies with anthracene moieties for PDT applications. *Inorganics* 6, 97–113. doi: 10.3390/inorganics6030097

Gupta, G., Das, A., Panja, S., Ryu, J. Y., Lee, J., Mandal, N., et al. (2017). Self-assmbly of novel thiophene-based BODIPY Ru^{II} rectangles: potential antiproliferative agents selective against cancer cells. *Chem. Eur. J.* 23, 17199–17203. doi: 10.1002/chem.201704368

Gupta, G., Oggu, G. S., Nagesh, N., Bokara, K. K., and Therrien, B. (2016). Anticancer activity of large metalla-assemblies built from half-sandwich complexes. *CrystEngComm* 18, 4952–4957. doi: 10.1039/c6ce00139d

Haviv, E., Azaiza-Dabbah, D., Carmieli, R., Avram, L., Martin, J. M. L., and Neumann, R. (2018). A thiourea tether in the second coordination sphere as a binding site for CO_2 and a proton donor promotes the electrochemical reduction of CO_2 to CO catalyzed by a rhenium bipyridine-type complex. *J. Am. Chem. Soc.* 140, 12451–12456. doi: 10.1021/jacs.8b05658

Hosseini, M. W. (2003). Molecular tectonics: from molecular recognition of anions to molecular networks. *Coord. Chem. Rev.* 240, 157–166. doi: 10.1016/S0010-8545(03)00021-3

Kato, T., Uchida, J., Ichikawa, T., and Sakamoto, T. (2018). Functional liquid crystals towards the next generation of materials. *Angew. Chem. Int. Ed.* 57, 4355–4371. doi: 10.1002/ange.201711163

Linares, F., Galindo, M. A., Galli, S., Romero, M. A., Navarro, J. A. R., and Barea, E. (2009). Tetranuclear coordination assemblies based on half-sandwich ruthenium(II) complexes: noncovalent binding to DNA and cytotoxicity. *Inorg. Chem.* 48, 7413–7420. doi: 10.1021/ic900980y

Linares, F., Procopio, E. Q., Galindo, M. A., Romero, M. A., Navarro, J. A. R., and Barea, E. (2010). Molecular architecture of redox-active half-sandwich Ru(II) cyclic assemblies. Interactions with biomolecules and anticancer activity. *CrystEngComm* 12, 2343–2346. doi: 10.1039/C002411B

Mattsson, J., Zava, O., Renfrew, A. K., Sei, Y., Yamaguchi, K., Dyson, P. J., et al. (2010). Drug delivery of lipophilic pyrenyl derivatives by encapsulation in a water soluble metalla-cage. *Dalton Trans.* 39, 8248–8255. doi: 10.1039/c0dt00436g

Mishra, A., Ravikumar, S., Song, Y. H., Prabhu, N. S., Kim, H., Hong, S. H., et al. (2014). A new arene-Ru based supramolecular coordination complex for efficient binding and selective sensing of green fluorescent protein. *Dalton Trans.* 43, 6032–6040. doi: 10.1039/c3dt53186d

Mishra, A., Vajpayee, V., Kim, H., Lee, M. H., Jung, H., Wang, M., et al. (2012). Self-assembled metalla-bowls for selective sensing of multi-carboxylate anions. *Dalton Trans.* 41, 1195–1201. doi: 10.1039/c1dt11612f

Patrice, T., Moor, A. C. E., Ortel, B., and Hasan, T. (2003). "Mechanism of photodynamic therapy," in *Photodynamic Therapy,* ed T. Patrice (Cambridge, UK: The Royal Society of Chemistry), 19–58.

Paul, L. E. H., Therrien, B., and Furrer, J. (2012a). Investigation of the reactivity between a ruthenium hexacationic prism and biological ligands. *Inorg. Chem.* 51, 1057–1067. doi: 10.1021/ic2021935

Paul, L. E. H., Therrien, B., and Furrer, J. (2012b). Interaction of a ruthenium hexacationic prism with amino acids and biological ligands: ESI mass spectrometry and NMR characterisation of the reaction products. *J. Biol. Inorg. Chem.* 17, 1053–1062. doi: 10.1007/s00775-012-0918-8

Paul, L. E. H., Therrien, B., and Furrer, J. (2015). Reactivity of hexanuclear ruthenium metallaprisms towards nucleotides and a DNA decamer. *J. Biol. Inorg. Chem.* 20, 49–59. doi: 10.1007/s00775-014-1208-4

Paul, L. E. H., Therrien, B., and Furrer, J. (2018). The complex-in-a-complex $[Pt(acac)_2\subset(p\text{-cym})_6Ru_6(tpt)_2(dhnq)_3]^{6\pm}$: Its stability towards biological ligands. *Inorg. Chim. Acta* 469, 1–10. doi: 10.1016/j.ica.2017.08.045

Piotrowski, H., Polborn, K., Hilt, G., and Severin, K. (2001). A self-assembled metallomacrocycle ionophore with high affinity for Li^+ and Na^+. *J. Am. Chem. Soc.* 123, 2699–2700. doi: 10.1021/ja005804t

Schmitt, F., Freudenreich, J., Barry, N. P. E., Juillerat-Jeanneret, L., Süss-Fink, G., and Therrien, B. (2012). Organometallic cages as vehicles for intracellular release of photosensitizers. *J. Am. Chem. Soc.* 134, 754–757. doi: 10.1021/ja207784t

Schmitt, F., Govindaswamy, P., Süss-Fink, G., Ang, W. H., Dyson, P. J., Juillerat-Jeanneret, L., et al. (2008). Ruthenium porphyrin compounds for photodynamic therapy of cancer. *J. Med. Chem.* 51, 1811–1816. doi: 10.1021/jm701382p

Schmitt, F., Govindaswamy, P., Zava, O., Süss-Fink, G., Juillerat-Jeanneret, L., and Therrien, B. (2009). Combined arene ruthenium porphyrins as chemotherapeutics and photosensitizers for cancer therapy. *J. Biol. Inorg. Chem.* 14, 101–109. doi: 10.1007/s00775-008-0427-y

Singh, A. K., Pandey, D. S., Xu, Q., and Braunstein, P. (2014). Recent advances in supramolecular and biological aspects of arene ruthenium(II) complexes. *Coord. Chem. Rev.* 270-271, 31–56. doi: 10.1016/j.ccr.2013.09.009

Steed, J. W. (2001). First- and second-sphere coordination chemistry of alkali metal crown ether complexes. *Coord. Chem. Rev.* 215, 171–221. doi: 10.1016/S0010-8545(01)00317-4

Therrien, B. (2009). Arene ruthenium cages: Boxes full of surprises. *Eur. J. Inorg. Chem.* 2445–2453. doi: 10.1002/ejic.200900180

Therrien, B. (2015). Biologically relevant arene ruthenium metalla-assemblies. *CrystEngComm* 17, 484–491. doi: 10.1039/c4ce02146k

Therrien, B. (2018). Arene ruthenium complexes in supramolecular chemistry. *Adv. Inorg. Chem.* 71, 379–402. doi: 10.1016/bs.adioch.2017.11.008

Therrien, B., and Furrer, J. (2014). The biological side of water-soluble arene ruthenium assemblies. *Adv. Chem.* 2014:589686. doi: 10.1155/2014/589686

Therrien, B., Süss-Fink, G., Govindaswamy, P., Renfrew, A. K., and Dyson, P. J. (2008). The "complex-in-a-complex" cations $[(acac)_2M\subset Ru_6(p\text{-}i\text{Pr}C_6H_4Me)_6(tpt)_2(dhbq)_3]^{6\pm}$: A Trojan horse for cancer cells. *Angew. Chem. Int. Ed.* 47, 3773–3776. doi: 10.1002/anie.200800186

Vajpayee, V., Song, Y. H., Lee, M. H., Kim, H., Wang, M., Stang, P. J., et al. (2011). Self-assembled arene-ruthenium-based rectangles for the selective sensing of multi-carboxylate anions. *Chem. Eur. J.* 17, 7837–7844. doi: 10.1002/chem.201100242

Wu, B., Liang, J., Yang, J., Jia, C., Yang, X.-J., Zhang, H., et al. (2008). Sulfate ion encapsulation in caged supramolecular structures assembled by second-sphere coordination. *Chem. Commun*. 1762–1764. doi: 10.1039/b719019k

Zhao, J., Bacolla, A., Wang, G., and Vasquez, K. M. (2010). Non-B DNA structure-induced genetic instability and evolution. *Cell. Mol. Life Sci.* 67, 43–62. doi: 10.1007/s00018-009-0131-2

Zhou, J., Yu, G., and Huang, F. (2017). Supramolecular chemotherapy based on host-guest molecular recognition: a novel strategy in the battle against cancer with a bright future. *Chem. Soc. Rev.* 46, 7021–7053. doi: 10.1039/c6cs00898d

Conflict of Interest Statement: The author declares that the research was conducted in the absence of any commercial or financial relationships that could be construed as a potential conflict of interest.

frontiers in Chemistry

ORIGINAL RESEARCH
published: 22 November 2018
doi: 10.3389/fchem.2018.00563

Anticancer Activity and Cisplatin Binding Ability of *Bis*-Quinoline and *Bis*-Isoquinoline Derived $[Pd_2L_4]^{4+}$ Metallosupramolecular Cages

Roan A. S. Vasdev[1,2,3]*, *Lachlan F. Gaudin*[1], *Dan Preston*[1], *Jackmil P. Jogy*[3], *Gregory I. Giles*[3] *and James D. Crowley*[1,2]*

[1] Department of Chemistry, University of Otago, Dunedin, New Zealand, [2] MacDiarmid Institute for Advanced Materials and Nanotechnology, Wellington, New Zealand, [3] Department of Pharmacology and Toxicology, University of Otago, Dunedin, New Zealand

OPEN ACCESS

Edited by:
Jonathan Kitchen,
Institute of Natural and Mathematical Sciences, Massey University, New Zealand

Reviewed by:
Robert Elmes,
Maynooth University, Ireland
Nicholas White,
Australian National University, Australia

***Correspondence:**
Roan A. S. Vasdev
roan.vasdev@otago.ac.nz
James D. Crowley
jcrowley@chemistry.otago.ac.nz

Specialty section:
This article was submitted to Supramolecular Chemistry, a section of the journal Frontiers in Chemistry

Received: 29 September 2018
Accepted: 31 October 2018
Published: 22 November 2018

Citation:
Vasdev RAS, Gaudin LF, Preston D, Jogy JP, Giles GI and Crowley JD (2018) Anticancer Activity and Cisplatin Binding Ability of Bis-Quinoline and Bis-Isoquinoline Derived $[Pd_2L_4]^{4+}$ Metallosupramolecular Cages. Front. Chem. 6:563. doi: 10.3389/fchem.2018.00563

New *bis*-quinoline ($\mathbf{L_q}$) and *bis*-isoquinoline-based ($\mathbf{L_{iq}}$) ligands have been synthesized, along with their respective homoleptic $[Pd_2(\mathbf{L_q}$ or $\mathbf{L_{iq}})_4]^{4+}$ cages ($\mathbf{C_q}$ and $\mathbf{C_{iq}}$). The ligands and cages were characterized by ^{1}H, ^{13}C and diffusion ordered (DOSY) NMR spectroscopies, high resolution electrospray ionization mass spectrometry (HR-ESIMS) and in the case of the *bis*-quinoline cage, X-ray crystallography. The crystal structure of the $\mathbf{C_q}$ architecture showed that the $[Pd_2(\mathbf{L_q})_4]^{4+}$ cage formed a twisted *meso* isomer where the $[Pd(\mathbf{quinoline})_4]^{2+}$ units at either end of the cage architecture adopt the opposite twists (left and right handed). Conversely, Density Functional Theory (DFT) calculations on the $\mathbf{C_{iq}}$ cage architecture indicated that a lantern shaped conformation, similar to what has been observed before for related $[Pd_2(\mathbf{L_{tripy}})_4]^{4+}$ systems (where $\mathbf{L_{tripy}}$ = 2,6-*bis*(pyridin-3-ylethynyl)pyridine), was generated. The different cage conformations manifest different properties for the isomeric cages. The $\mathbf{C_{iq}}$ cage is able to bind, weakly in acetonitrile, the anticancer drug cisplatin whereas the $\mathbf{C_q}$ architecture shows no interaction with the guest under the same conditions. The kinetic robustness of the two cages in the presence of Cl^- nucleophiles was also different. The $\mathbf{C_{iq}}$ cage was completely decomposed into free $\mathbf{L_{iq}}$ and $[Pd(Cl)_4]^{2-}$ within 1 h. However, the $\mathbf{C_q}$ cage was more long lived and was only fully decomposed after 7 h. The new ligands ($\mathbf{L_{iq}}$ and $\mathbf{L_q}$) and the Pd(II) cage architectures ($\mathbf{C_{iq}}$ and $\mathbf{C_q}$) were assessed for their cytotoxic properties against two cancerous cell lines (A549 lung cancer and MDA-MB-231 breast cancer) and one non-cancerous cell line (HDFa skin cells). It was found that $\mathbf{L_q}$ and $\mathbf{C_q}$ were both reasonably cytotoxic ($IC_{50S} \approx 0.5\,\mu M$) against A549, while $\mathbf{C_{iq}}$ was slightly less active ($IC_{50} = 7.4\,\mu M$). $\mathbf{L_{iq}}$ was not soluble enough to allow the IC_{50} to be determined against either of the two cancerous cell lines. However, none of the molecules showed any selectivity for the cancer cells, as they were all found to have similar cytotoxicities against HDFa skin cells (IC_{50} values ranged from 2.6 to 3.0 μM).

Keywords: palladium(II), anticancer, self-assembly, metallosupramolecular, quinoline

INTRODUCTION

Metallosupramolecular architectures (MSAs) (Cook and Stang, 2015) have been attracting increasing attention over the past two decades due to their many potential applications including catalysis (Yoshizawa et al., 2009; Yoshizawa and Fujita, 2010; Martí-Centelles et al., 2018), storage (Mal et al., 2009), and sensing (Wang et al., 2011). Inspired by the success of cisplatin and other metallodrugs (Mjos and Orvig, 2014) there is emerging interest in exploiting MSAs for biomedical purposes (Cook et al., 2013; Therrien, 2015; Casini et al., 2017; Zhou et al., 2017). Several groups have examined MSAs as drug delivery vectors (Therrien et al., 2008; Schmitt et al., 2012; Yi et al., 2012; Zheng et al., 2015; Samanta et al., 2016, 2017; Bhat et al., 2017; Xu et al., 2017; Wang J.-F. et al., 2018; Yue et al., 2018). Additionally, MSAs have been shown to bind DNA (Oleksy et al., 2006; Garci et al., 2017; Zhao et al., 2017) and RNA (Phongtongpasuk et al., 2013; Malina et al., 2015), interact with proteins (Li et al., 2014; Mitchell et al., 2017) and have anticancer (Hotze et al., 2008; Faulkner et al., 2014; Grishagin et al., 2014; Dubey et al., 2015; Zheng et al., 2016; Allison et al., 2018) and antibacterial (Richards et al., 2009; Howson et al., 2012; Wang H. et al., 2018) properties.

Since the pioneering work of McMorran and Steel (McMorran and Steel, 1998) interest in $[M_2(\mathbf{L})_4]^{n+}$ cage-type structures has burgeoned (Schmidt et al., 2014). Some time ago now we reported that a $[Pd_2(\mathbf{L}_{tripy})_4]^{4+}$ cage (where $\mathbf{L}_{tripy}$ = 2,6-*bis*(pyridin-3-ylethynyl)pyridine) could host two molecules of the anticancer drug cisplatin within the cavity of the cage (Lewis et al., 2012), and thus had potential as a drug delivery vector. Disappointingly, the binding event, which was governed mainly by hydrogen bonding interactions, was weak (Preston et al., 2015). The host-guest complex formed in acetonitrile (CH_3CN) and dimethylformamide (DMF) but unfortunately, in more hydrogen bond competitive solvents such as water and dimethyl sulfoxide (DMSO) no host-guest interaction was observed. Additionally, the parent Pd(II) based cage decomposed rapidly in the presence of nucleophiles (Lewis et al., 2012; McNeill et al., 2015). Thus, in order to exploit these $[Pd_2(\mathbf{L})_4]^{4+}$ cages as cisplatin delivery vehicles these issues need to be addressed. We and others have examined a range of modifications to the parent $[Pd_2(\mathbf{L})_4]^{4+}$ cage system in order to improve the solubility (Lewis and Crowley, 2014; Preston et al., 2015; Han et al., 2017) and other properties (Lewis et al., 2013, 2014; Kaiser et al., 2016; Schmidt et al., 2016a) of the cage. Efforts have also been made to enhance the strength of the host-guest interaction (Kim et al., 2015) and the stability of the cages in the presence of biologically revelant nucleophiles (Preston et al., 2016). However, while some improvements have been made these $[Pd_2(\mathbf{L})_4]^{4+}$ cages still require further modifcations in order to be useful drug delivery vectors.

The $[Pd_2(\mathbf{L})_4]^{4+}$ cages have also been examined for their cytotoxic properties. We showed that the parent $[Pd_2(\mathbf{L}_{tripy})_4]^{4+}$ was modestly cytotoxic (IC_{50} values range from 40 to 70 μM) against a range of cancer cell lines but was less active than related bis-1,2,3-triazole $[Pd_2(\mathbf{L})_4]^{4+}$ helicates (McNeill et al., 2015). We also examined the cytotoxicity of related amino substituted $[Pd_2(\mathbf{L})_4]^{4+}$ cages against the same panel of cancer cells and found that they exhibited similar cytotoxic properties as the parent systems (Preston et al., 2016). Casini, Kühn and co-workers (Kaiser et al., 2016; Schmidt et al., 2016b) have measured the cytotoxicity of a series of related $[Pd_2(\mathbf{L})_4]^{4+}$ cages and observed similar IC_{50} values (10–70 μM). Additionally, they have measured the cytotoxicity of mixtures of the cages and cisplatin and unsurprisingly have found that those mixtures are more cytotoxic than cage alone (IC_{50} = 2–13 μM). Yoshizawa, Ahmedova and co-workers have also found that $[M_2(\mathbf{L})_4]^{4+}$ (M = Pd^{2+} or Pt^{2+}) cages with similar, but more hydrophobic, dipyridyl anthracenyl ligands ($\mathbf{L}_{anthracene}$) display high anticancer activity (IC_{50} values range from 0.9 to 37.4 μM against HL-60, HL-60/Dox, HT-29, T-24, SKW-3 cancer cell lines) (Ahmedova et al., 2016; Anife et al., 2016).

The majority of the $[Pd_2(\mathbf{L})_4]^{4+}$ cages examined to date feature pyridyl donors, as part of our efforts to improve the biological properties of these systems herein we describe the use of isoquinoline and quinoline-derived ligands for the assembly of two new $[Pd_2(\mathbf{L})_4]^{4+}$ cages. While is well-known that isoquinoline and quinoline ligands can bind with palladium(II) and platinum(II) (Bondy et al., 2004) their use as donor systems in ligands for the generation MSAs has not been extensively explored (Bloch et al., 2016, 2017). These quinoline derived systems feature different electronic and steric properties compared to the parent pyridyl systems thus we also examine the effect these changes have on the host-guest chemistry with cisplatin, the stability of the cages in the presence of nucleophiles and the antiproliferative properties of the cages.

RESULTS AND DISCUSSION

The synthesis of the new quinoline ($\mathbf{L}_q$) and isoquinoline ($\mathbf{L}_{iq}$) based ligands was facile (**Supplementary Material**). Using sequential Sonogashira carbon-carbon cross coupling reactions from commercially available building blocks the ligands were generated in good yields ($\mathbf{L}_q$ = 86% and $\mathbf{L}_{iq}$ = 78%). ^1H and ^{13}C NMR spectroscopic data were consistent with the formation of the ligands which was supported by high-resolution electrospray mass spectrometry (HR-ESIMS) (**Figure 1** and **Supplementary Material**). Peaks corresponding to protonated and sodiated ligand were observed at m/z = 382.1320 and 404.1132, respectively, for $\mathbf{L}_{iq}$ and similar peaks were observed for $\mathbf{L}_q$ (**Supplementary Material**).

With the ligands in hand, the complexation with $[Pd(CH_3CN)_4](BF_4)_2$ in acetonitrile was examined (**Figure 1**). The cage formation was monitored using ^1H NMR spectroscopy (CD_3CN, 298 K) and showed that mixing $[Pd(CH_3CN)_4](BF_4)_2$ and the $\mathbf{L}_{iq}$ ligand at room temperature (RT) in a 1:2 ratio led to the rapid (<2 min) and quantitative formation of the expected $\mathbf{C}_{iq}$ cage (**Figure 1**), similar to what was observed with the parent $\mathbf{L}_{tripy}$ system (Lewis et al., 2012). Interestingly, the behavior of $\mathbf{L}_q$with $[Pd(CH_3CN)_4](BF_4)_2$ at room temperature was very different. After 5 min at RT the reaction mixture displayed multiple proton resonances, none of which were due to free ligand, consistent with the formation of a mixture of different cage isomers. The reaction was monitored using ^1H NMR spectroscopy for 24 h at RT however little to no changes were

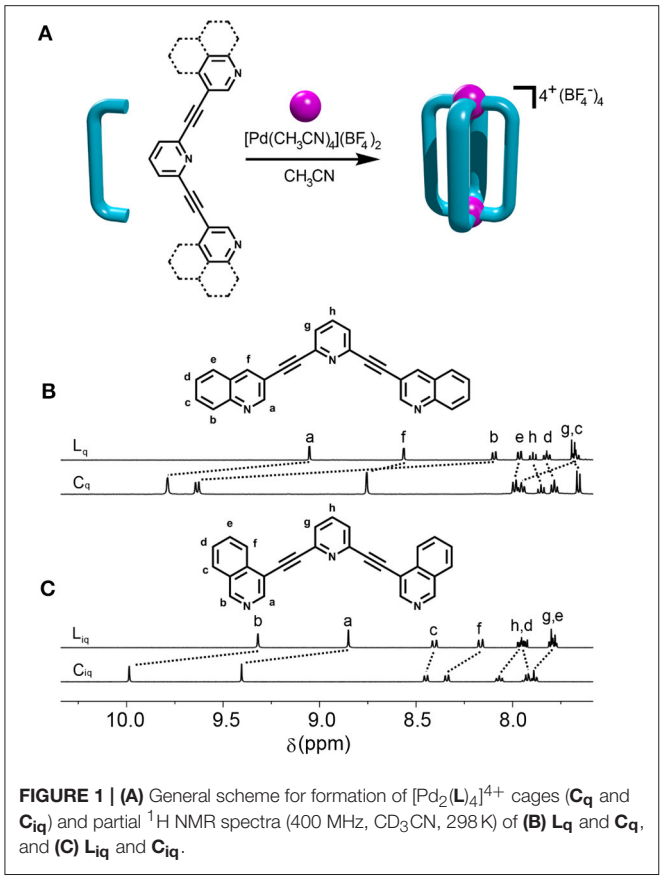

FIGURE 1 | (A) General scheme for formation of $[Pd_2(\mathbf{L})_4]^{4+}$ cages ($\mathbf{C_q}$ and $\mathbf{C_{iq}}$) and partial ^{1}H NMR spectra (400 MHz, CD_3CN, 298 K) of **(B)** $\mathbf{L_q}$ and $\mathbf{C_q}$, and **(C)** $\mathbf{L_{iq}}$ and $\mathbf{C_{iq}}$.

observed after the first hour and the spectrum still displayed multiple proton resonances. A ^{1}H DOSY experiment (CD_3CN, 298 K) on the mixture showed that all the different proton resonances had the same diffusion co-efficient consistent with the postulate that the reaction mixture contains a series of cage isomers (**Supplementary Material**).

The assembly reaction between $\mathbf{L_q}$ with $[Pd(CH_3CN)_4](BF_4)_2$ was then carried out at 65°C, in CD_3CN and again monitored using ^{1}H NMR spectroscopy (**Figure 2**). After 5 min the same complicated series of proton resonance were observed. However, with continued heating this slowly resolved into a single series of resonances (after 7 h), consistent with the formation of a single cage isomer (**Figure 2**). Pleasingly, both cages ($\mathbf{C_{iq}}$ and $\mathbf{C_q}$) could be isolated by adding diethyl ether into the acetonitrile reaction mixtures providing the cages as colorless/tan precipitates in 88% ($\mathbf{C_{iq}}$) or 92% ($\mathbf{C_q}$) yield, respectively. ^{1}H NMR spectroscopy (CD_3CN, 298 K) exhibited the expected downfield shifts of the signals pertaining to protons H_a, H_b and H_f as well as the anticipated downfield shifts of the rest of the isoquinoline and quinoline protons resonances (**Figure 1**). HR-ESIMS data also supported the formation of the cages, showing ions corresponding to the loss of 2, 3 and 4 tetrafluoroborate (BF_4^-) counterions (m/z = 956.1610 (2^+), 608.4424 (3^+), and 434.5832 (4^+), **Supplementary Material**). ^{1}H DOSY experiments (CD_3CN, 298 K) on the ligands (Diffusion coefficients (D) = 13.1 ($\mathbf{L_q}$) and 15.0 ($\mathbf{L_{iq}}$) x 10^{-10} m^2 s^{-1}) and cages (D = 4.1 ($\mathbf{C_q}$) and 4.3 ($\mathbf{C_{iq}}$) × 10^{-10} m^2 s^{-1} were also consistent with the formation of the larger $[Pd_2(\mathbf{L})_4]^{4+}$ cages (**Supplementary Material**).

Crystals of $\mathbf{C_q}$ suitable for X-ray diffraction formed during the cooling of an acetonitrile solution of the cage from 65°C to room temperature. The structure was solved in the tetragonal space group P4/*mnc* with the asymmetric unit containing one eighth of the cage and one quarter of a BF_4^- counterion (**Figure 3** and **Supplementary Material**). The other BF_4^- anions and some acetonitrile molecules could not be modeled sensibly thus the SQUEEZE routine was employed to account for the diffuse electron density (**Supplementary Material**). The data revealed the expected $[Pd_2(\mathbf{L_q})_4]^{4+}$ cage structure. The Pd-N bond lengths (Pd1-N2 2.045 Å) were similar to what have been previously observed for the related $[Pd_2(\mathbf{L_{tripy}})_4]^{4+}$ cages where the Pd-N bond lengths range from 2.016 to 2.027 Å (Lewis et al., 2012; Lewis and Crowley, 2014). The $\mathbf{L_q}$ ligands of the cage are twisted giving a V-shaped conformation where the terminal quinoline and central pyridyl heterocyclic units are not co-planar which is quite different to what was observed with the $[Pd_2(\mathbf{L_{tripy}})_4]^{4+}$ cages. In X-ray structures of the parent $[Pd_2(\mathbf{L_{tripy}})_4]^{4+}$ cages the $\mathbf{L_{tripy}}$ ligands were found in a linear conformation with the heterocyclic units coplanar. The twisting also alters the Pd1-Pd1′ distance within $\mathbf{C_q}$ related to the $[Pd_2(\mathbf{L_{tripy}})_4]^{4+}$ cages. The Pd1-Pd1′ distances for the parent $[Pd_2(\mathbf{L_{tripy}})_4]^{4+}$ cages range from 11.49 to 12.24 Å, whereas the Pd1-Pd1′ distance was found to be longer (12.506 Å) suggesting that the $\mathbf{C_q}$cage has a larger cavity despite featuring the same 2,6-diethynylpyridine linker units. The $[Pd(\mathbf{quinoline})_4]^{2+}$ units at the top and bottom of $\mathbf{C_q}$ are twisted in opposite directions, the top cationic unit has a right handed twist while the bottom cationic unit has a left handed twist giving an overall *meso* structure (**Figures 3B,C** and **Supplementary Material**). Despite extensive efforts we were unable to obtain X-ray diffraction quality single crystals of $\mathbf{C_{iq}}$. Thus, to gain further insight into the structure of $\mathbf{C_{iq}}$ we modeled the cage using Density Functional Theory (DFT) calculations (**Figures 3D,E**). Energy minimization of $\mathbf{C_{iq}}$ (DFT, BP86 def2-SVP, acetonitrile solvation, **Supplementary Material**) showed that the cage adopted a lantern shape similar to what was previously observed for $[Pd_2(\mathbf{L_{tripy}})_4]^{4+}$ cages (Lewis et al., 2012; Lewis and Crowley, 2014). The calculated Pd – N bond distances (2.049 Å) and the Pd-Pd′ distance (11.758 Å) match well with those observed crystallographically for the related $[Pd_2(\mathbf{L_{tripy}})_4]^{4+}$ cages. The $\mathbf{L_{iq}}$ ligand adopts a linear conformation with all the heterocyclic units coplanar. The DFT calculations indicated that the $\mathbf{C_{iq}}$ is structurally very similar to the parent $[Pd_2(\mathbf{L_{tripy}})_4]^{4+}$ cages whereas the $\mathbf{C_q}$ is more twisted and provided a cavity of different size and shape to the parent cages and the $\mathbf{C_{iq}}$ system.

We and others have previously shown that other similar $[Pd_2(\mathbf{L_{tripy}})_4]^{4+}$ cages can encapsulate cisplatin through hydrogen bonding interactions in CH_3CN and DMF solvents (Lewis et al., 2012, 2013, 2014; Kaiser et al., 2016; Preston et al., 2016, 2017; Schmidt et al., 2016b). Therefore, we examined the ability of $\mathbf{C_{iq}}$ and $\mathbf{C_q}$ to interact with cisplatin in CH_3CN using ^{1}H NMR spectroscopy. Addition of an excess of cisplatin to a

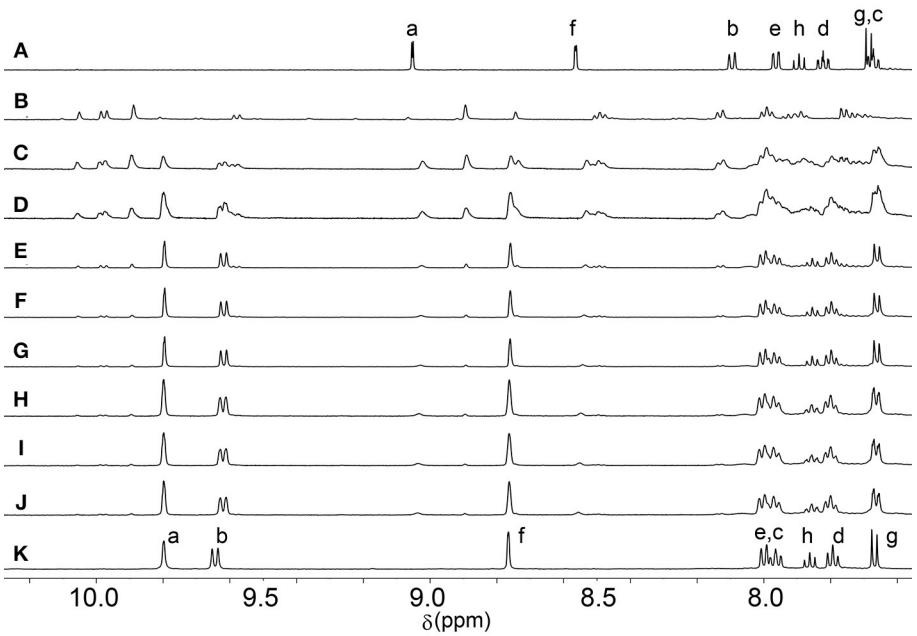

FIGURE 2 | Partial ^{1}H NMR (500 MHz, CD_3CN, 338 K) spectra showing the formation of $\mathbf{C_q}$ over time at 65°C. **(A)** $\mathbf{L_q}$, **(B)** initial complexation ($t = 0$), **(C)** $t = 30$ min, **(D)** $t = 1$ h, **(E)** $t = 2$ h, **(F)** $t = 3$ h, **(G)** $t = 4$ h, **(H)** $t = 5$ h, **(I)** $t = 6$ h, **(J)** $t = 7$ h, **(K)** isolated $\mathbf{C_q}$.

CD_3CN solution of the $\mathbf{C}_{iq}$ cage resulted in a downfield shift and broadening ($\Delta\delta = 0.03$ ppm) of the internally directed cage proton H_a (**Figures 4A,B**) indicative of cisplatin binding within the cage cavity, albeit weakly. A similar ^{1}H NMR experiment was carried out with the $\mathbf{C}_q$ cage (**Figures 4C,D**). However, with the $\mathbf{C}_q$ cage no shifts were observed for any of the cage proton resonances in the presence of an excess of cisplatin suggesting that the more twisted $\mathbf{C}_q$ cage does not interact with the anticancer agent. The behavior was similar to what has been observed with a related twisted $[Pd_2(\mathbf{L}_{2Atripy})_4]^{4+}$ cage (where $\mathbf{L}_{2Atripy}$ = 2,6-*bis*[2-(6-amino-3-pyridinyl)ethynyl]-4-pyridinemethanol) (Preston et al., 2016). The $[Pd_2(\mathbf{L}_{2Atripy})_4]^{4+}$ cage did not bind cisplatin in DMF solvent and the lack of binding was ascribed to the twisted cage cavity which was not as preorganised as those of the related lantern shaped $[Pd_2(\mathbf{L}_{tripy})_4]^{4+}$ cages. Presumably the different sized cavity and different spatial arrangement of the hydrogen bond donors and acceptors caused by the twisting observed in the crystal structure of $\mathbf{C}_q$ impedes the cisplatin-$\mathbf{C}_q$ interaction in this case.

The kinetic robustness of the related $[Pd_2(\mathbf{L}_{tripy})_4]^{4+}$ architectures in the presence of common biological nucleophiles (chloride (Cl^-), histidine and cysteine) has been determined using ^{1}H NMR competition experiments. When the parent $[Pd_2(\mathbf{L}_{tripy})_4]^{4+}$ architectures were treated with 8 equivalents of tetrabutylammonium chloride the pyridyl substituted cages were rapidly and quantitatively decomposed (in <5 min). To examine the effect of substituting the pyridyl donor units for quinoline heterocycles time-course ^{1}H NMR competition experiments were carried out in d_6-DMSO where 2 mM solutions of each cage ($\mathbf{C}_q$or $\mathbf{C}_{iq}$) were treated with 8 equivalents of tetrabutylammonium chloride at 298 K (**Figure 5** and **Supplementary Material**). Within 30 s of adding Cl^- to the $\mathbf{C}_{iq}$ cage, there were multiple species observed in the ^{1}H NMR spectrum. These were attributed to the $\mathbf{C}_{iq}$ cage, $[Cl\subset\mathbf{C}_{iq}]^{3+}$, the $[Pd_2(\mathbf{L}_{iq})_2Cl_4]$ macrocycle and free ligand based on our own previous results (Preston et al., 2015) and related literature. After 50 min, only uncoordinated ligand was visible in the ^{1}H NMR spectrum (**Supplementary Material**).

Under the same conditions, $\mathbf{C}_q$ was stable for 1 h before showing signs of decomposition (**Figure 5**). After 3 h, there was no evidence of the $\mathbf{C}_q$ cage, and the ^{1}H NMR spectrum displayed peaks corresponding to free ligand and a second metal-containing species, which based on the observed chemical shifts was most likely the neutral $[Pd_2(\mathbf{L}_q)_2Cl_4]$ macrocycle (**Figure 5H**). This degradation behavior has been seen before with the $[Pd_2(\mathbf{L}_{tripy})_4]^{4+}$ system in DMF (Preston et al., 2015). After 7 h, only free ligand could observed in the ^{1}H NMR spectrum indicating that all the ligand containing metal complexes had been completely decomposed into $[Pd(Cl)_4]^{2-}$(**Figure 5J**).

In comparison to the previously reported $[Pd_2(\mathbf{L}_{tripy})_4]^{4+}$ cage ($\tau_{1/2}$ = 2 min), the isoquinoline cage displayed an identical half-life ($\tau_{1/2}$ = 2 min), whereas the quinoline system was considerably more robust ($\tau_{1/2}$ = 2 h). Presumably the observed results reflect the different steric profiles of the two quinoline substituted cages ($\mathbf{C}_q$or $\mathbf{C}_{iq}$). The $\mathbf{C}_q$ cage has the quinoline moieties protecting the external face of the palladium, providing more impediment to nucleophilic attack from that face (**Figure 6**). The $\mathbf{C}_{iq}$ does not feature the same steric impediment as the benzene units of the isoquinoline heterocycles do not block the top face of the $\mathbf{C}_{iq}$ cage as much as they do in the quinoline $\mathbf{C}_q$(**Figure 6**).

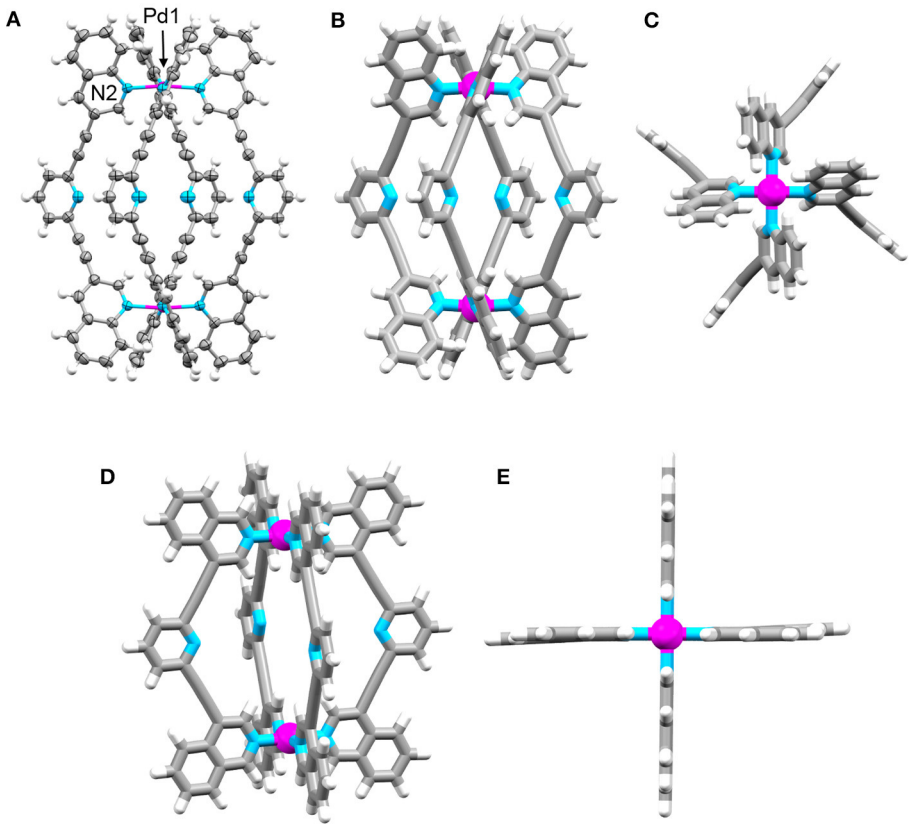

FIGURE 3 | Molecular structures of $\mathbf{C_q}$ and $\mathbf{C_{iq}}$. X-ray structure of $\mathbf{C_q}$: **(A)** ellipsoid side view, **(B)** tube side view, and **(C)** tube top view showing paddle-like array of quinoline panels over palladium(II) center. Solvent molecules and counterions have been omitted for clarity. Ellipsoids are shown at 50% probability. DFT optimized (BP86 def2-SVP) model of $\mathbf{C_{iq}}$; **(D)** side view and **(E)** top view showing lantern-shaped structure. Colors: carbon gray, nitrogen blue, palladium magenta, hydrogen white.

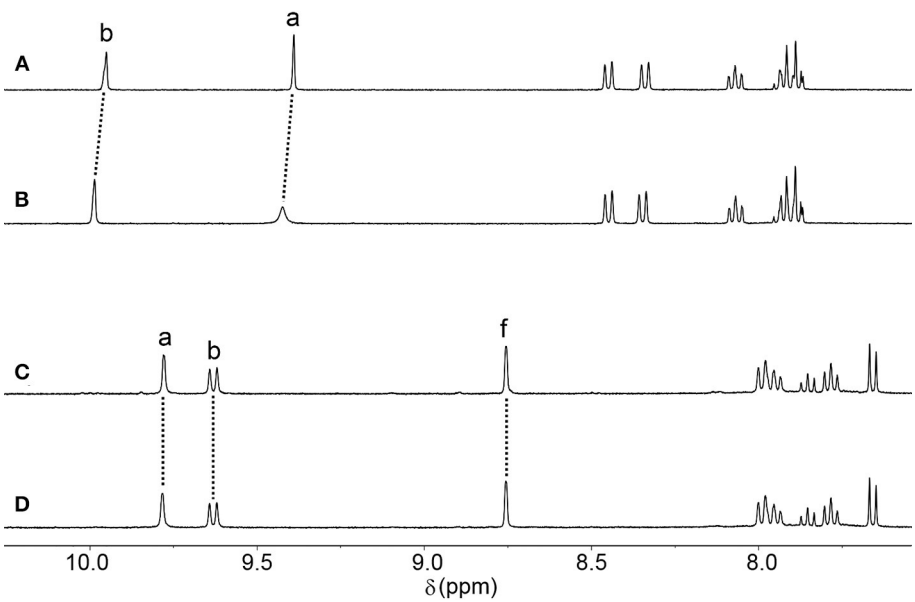

FIGURE 4 | Partial ^{1}H NMR (500 MHz, CD_3CN, 298 K) stacked plot of **(A)** $\mathbf{C_{iq}}$ **(B)** $\mathbf{C_{iq}}$ + cisplatin (10 eq.) **(C)** $\mathbf{C_q}$, and **(D)** $\mathbf{C_q}$ + cisplatin (10 eq.).

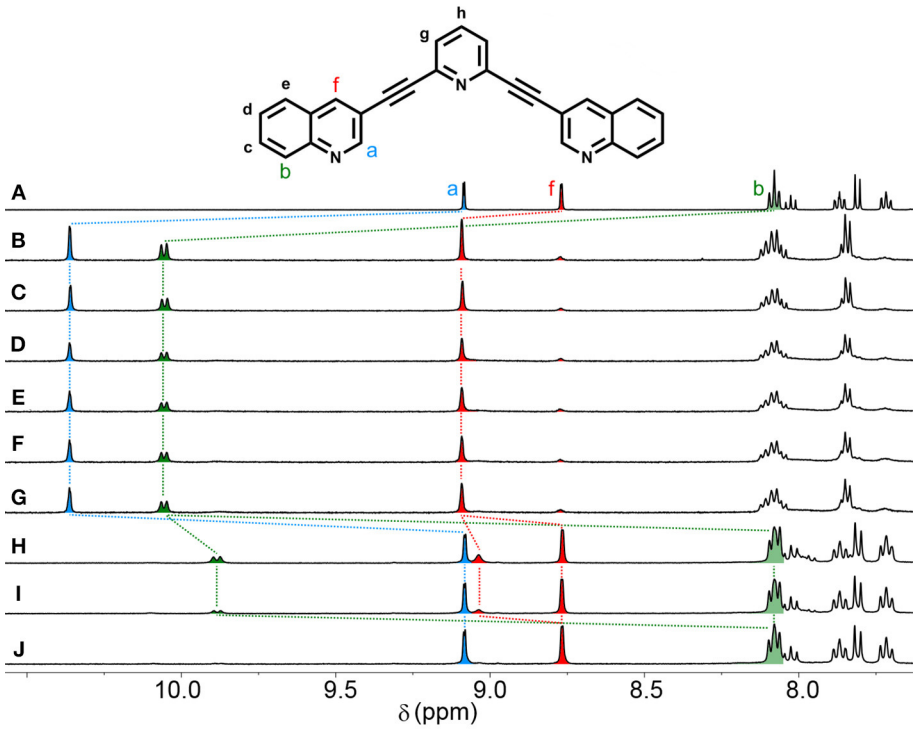

FIGURE 5 | Partial ^{1}H NMR (500 MHz, d_6-DMSO, 298 K) spectra showing the stability of $\mathbf{C_q}$ in the presence of 8 eq. Cl^- anions. **(A)** $\mathbf{L_q}$, **(B)** $\mathbf{C_q}$, **(C)** $\mathbf{C_q}$ with 8 eq. Cl^- ($t = 2$ min), **(D)** $t = 10$ min, **(E)** $t = 20$ min, **(F)** $t = 30$ min, **(G)** $t = 1$ h, **(H)** $t = 3$ h, **(I)** $t = 5$ h, **(J)** $t = 7$ h.

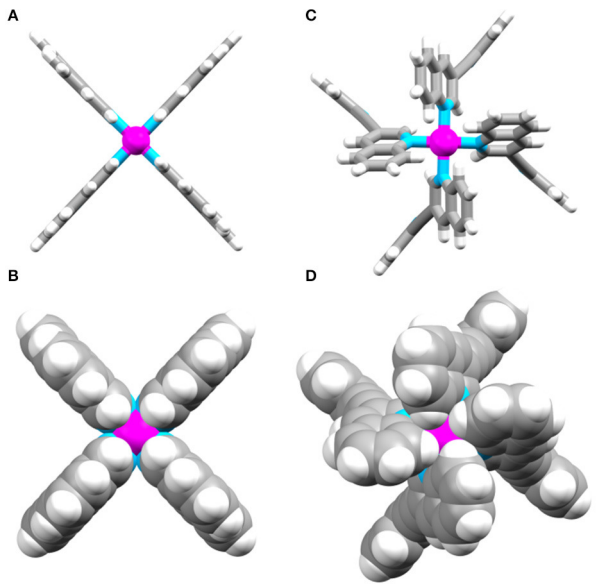

FIGURE 6 | Top down views of **(A)** and **(B)** the DFT optimized model of $\mathbf{C_{iq}}$, and **(C)** and **(D)** the X-ray structure of $\mathbf{C_q}$.

To assess biological activity, the cytotoxic effect (as half-maximal inhibitory concentrations (IC_{50})) of the ligands and cages were determined against three different cell lines: cisplatin resistant MDA-MB-231 (breast cancer) (Lehmann et al., 2011), A549 (lung cancer) and non-cancerous primary cells: adult human dermal fibroblasts (HDFa) (**Table 1** and **Supplementary Material**). The ligands $\mathbf{L_q}$ and $\mathbf{L_{iq}}$ exhibited limited solubility, and so data above the concentration of 1 μM was unattainable. Below this threshold, $\mathbf{L_{iq}}$ displayed minimal cytotoxic activity against both cell lines, while $\mathbf{L_q}$ was shown to be cytotoxic against A549 ($IC_{50} = 0.5$ μM). Both cages were observed to be cytotoxic against the malignant cell lines, with $\mathbf{C_q}$ showing the same level of toxicity as its ligand against lung cancer cells ($IC_{50} = 0.5$ μM). $\mathbf{C_q}$ was slightly less cytotoxic against MDA-MB-231 ($IC_{50} = 1.7$ μM), whereas $\mathbf{C_{iq}}$ was less cytotoxic than the quinoline analog, with the IC_{50} values ranging from 4.0 to 7.4 μM against the cancer cells. Both quinoline cages were found to be considerably more active than the related parent $[Pd_2(\mathbf{L_{tripy}})_4]^{4+}$ cage system ($IC_{50} = 41.4$ and 56.7 μM against A549 and MDA-MB-231, respectively) (McNeill et al., 2015). The quinoline cages were also more active than cisplatin against the two cancer lines examined (cisplatin IC_{50} values = 41.2 and 9.4 μM, against MDA-MB-231 and A549, respectively) (Lo et al., 2015; McNeill et al., 2015). The quinoline cages $\mathbf{C_q}$ and $\mathbf{C_{iq}}$ were more cytotoxic than all the $[Pd_2(\mathbf{L_{tripy}})_4]^{4+}$ cage systems reported in the literature (IC_{50} values for the $\mathbf{L_{tripy}}$ based systems ranged from 10 to 100 μM) (McNeill et al., 2015; Kaiser et al., 2016; Schmidt et al., 2016b). Additionally, $\mathbf{C_q}$ was also more active, albeit against different cancer cell lines (HL-60, HL-60/Dox, HT-29, T-24, SKW-3), than the hydrophobic $[Pd_2(\mathbf{L_{anthracene}})_4]^{4+}$ cages of Yoshizawa and Ahmedova (IC_{50} values ranged from 0.9 to 37.4 μM) (Ahmedova et al., 2016; Anife et al., 2016).

TABLE 1 | Half-maximal inhibitory concentrations (IC_{50}) of ligands $\mathbf{L_q}$ and $\mathbf{L_{iq}}$, and cages $\mathbf{C_q}$ and $\mathbf{C_{iq}}$ architectures at 24 h.

Compound	IC^a_{50} (μM)			
	MDA-MB-231	A549	HDFa	MCF-10A[b]
$\mathbf{L_q}$	>1[c]	0.5 ± 0.1	>1[c]	–
$\mathbf{C_q}$	1.7 ± 0.1	0.5 ± 0.1	2.6 ± 0.4	–
$\mathbf{L_{iq}}$	>1[c]	>1[c]	>1[c]	–
$\mathbf{C_{iq}}$	4.0 ± 0.3	7.4 ± 1.0	3.0 ± 0.4	–
$\mathbf{L}_{hextrz}$ *(McNeill et al., 2015)*	89.8 ± 10.7	28.5 ± 2.6	–	18.1 ± 3.1
$\mathbf{C}_{hextrz}$ *(McNeill et al., 2015)*	6.0 ± 0.6	6.9 ± 0.9	–	8.1 ± 1.2
$\mathbf{L}_{tripy}$ *(McNeill et al., 2015)*	>100	95.3 ± 9.7	–	>100
$\mathbf{C}_{tripy}$ *(McNeill et al., 2015)*	56.7 ± 2.2	41.4 ± 3.9	–	71.4 ± 3.9
cisplatin *(Lo et al., 2015; McNeill et al., 2015)*	41.2 ± 3.9	9.4 ± 0.3	–	–

$\mathbf{L}_{tripy}$, $\mathbf{C}_{tripy}$, $\mathbf{L}_{hextrz}$, $\mathbf{C}_{hextrz}$ and cisplatin (Lo et al., 2015) have been added for comparison (McNeill et al., 2015).
[a] IC_{50} values are given as mean ± SE.
[b] The $\mathbf{C}_{tripy}$ and $\mathbf{C}_{hextrz}$ cages were tested against MCF-10A as a non-cancerous control.
[c] Solubility limited the range of concentrations to below 1 μM. " – " = Not determined.

$\mathbf{C_q}$ was also more cytotoxic than a hydrophobic *bis*-hexyl-1,2,3-triazole substituted $[Pd_2(\mathbf{L}_{hextrz})_4]^{4+}$ helicate, $\mathbf{C}_{hextrz}$, we developed previously (IC_{50} values = 6.9 and 6.0 μM against A549 and MDA-MB-231, respectively) (McNeill et al., 2015). We presume that the favorable combination of high hydrophobicity and the kinetic robustness against biological nucleophiles leads to the higher observed activity of $\mathbf{C_q}$ relative to the other $[Pd_2(\mathbf{L})_4]^{4+}$ architectures. Disappointingly, neither of the cages ($\mathbf{C_q}$ and $\mathbf{C_{iq}}$) showed any selectivity for the cancer cells, they were all found to have similar cytotoxicity against HDFa skin cells (IC_{50} values ranged from 2.6 to 3.0 μM).

CONCLUSION

We have herein reported the synthesis, characterization, cisplatin binding, kinetic robustness and cytotoxicity of two new *bis*-isoquinoline and *bis*-quinoline derived $[Pd_2(\mathbf{L})_4]^{4+}$ cage complexes. The crystal structure of $\mathbf{C_q}$ architecture showed that the $[Pd_2(\mathbf{L})_4]^{4+}$ cage formed a twisted *meso* isomer where the $[Pd(\mathbf{quinoline})_4]^{2+}$ units at either end of the cage architecture adopt the opposite twists (left and right handed). Conversely, Density Functional Theory (DFT) calculations on the $\mathbf{C_{iq}}$ cage architecture indicated that a lantern shaped conformation similar to what has been observed before for related $[Pd_2(\mathbf{L}_{tripy})_4]^{4+}$ systems was generated. The different cage conformations resulted in different properties for the isomeric cages. The $\mathbf{C_{iq}}$ cage is able to bind, weakly in acetonitrile, the anticancer drug cisplatin whereas the $\mathbf{C_q}$ architecture shows no interaction with the guest under the same conditions. The kinetic robustness of the two cages in the presence of Cl^- nucleophiles was also different. The $\mathbf{C_{iq}}$ cage was completely decomposed into free $\mathbf{L_{iq}}$ and $[Pd(Cl)_4]^{2-}$ within 1 h. However, the $\mathbf{C_q}$ cage was more long lived and was only fully decomposed after 7 h. The ligands ($\mathbf{L_{iq}}$ and $\mathbf{L_q}$) and cages ($\mathbf{C_{iq}}$ and $\mathbf{C_q}$) were assessed for their cytotoxic properties against two cancerous cell lines (A549 lung cancer cells and MDA-MB-231 breast cancer cells) and one non-cancerous cell line (HDFa skin cells). It was found that $\mathbf{L_q}$ and $\mathbf{C_q}$ were both reasonably cytotoxic against A549, while $\mathbf{C_{iq}}$ was slightly less active. The higher observed cytotoxicity of $\mathbf{C_q}$ relative to the other $[Pd_2(\mathbf{L})_4]^{4+}$ architectures was presumed to be due the favorable combination of high hydrophobicity and the kinetic robustness against biological nucleophiles. However, none of the new molecules showed any selectivity for cancer cells, they were all found to have similar cytotoxicity against HDFa skin cells. A range of $[Pd_2(\mathbf{L})_4]^{4+}$ cage systems have now been shown to be cytotoxic. However, in order to advance this class of MSA as anticancer agents more in depth mode of action/mechanistic studies on the origins of the cytotoxic activity are required. Studies to this effect are now underway.

AUTHOR CONTRIBUTIONS

RV and JC conceived the idea, analyzed the data and wrote the manuscript. RV and LG conducted the synthesis. RV and DP conducted stability studies. RV, DP, and JJ conducted cytotoxicity studies. GG oversaw the cytotoxicity studies and analyzed the data. All authors provided feedback on the manuscript drafts and approved the submission.

FUNDING

JC thanks the University of Otago, Department of Chemistry and the MacDiarmid Institute for funding. RV was supported by a Claude McCarthy Fellowship. All the authors thank Charlotte Dobson, Pauline Lane and Oceanbridge for their kind donations which supported this work.

ACKNOWLEDGMENTS

RV and JJ acknowledge the University of Otago for doctoral stipends. Dr. Anna Garden and Dr. David McMorran are thanked for useful discussions. Professor Sally McCormick, Department of Biochemistry, University of Otago is thanked for kindly providing a sample of the HDFa skin cells. The authors acknowledge the contribution of the NeSI high performance computing facilities to the results of this research.

New Zealand's national facilities are provided by the New Zealand eScience Infrastructure and funded jointly by NeSI's collaborator institutions and through the Ministry of Business, Innovation and Employment's Research Infrastructure program. URL: https://www.nesi.org.

SUPPLEMENTARY MATERIAL

The Supplementary Material for this article can be found online at: https://www.frontiersin.org/articles/10.3389/fchem.2018.00563/full#supplementary-material

REFERENCES

Ahmedova, A., Mihaylova, R., Momekova, D., Shestakova, P., Stoykova, S., Zaharieva, J., et al. (2016). M2L4 coordination capsules with tunable anticancer activity upon guest encapsulation. *Dalton Trans.* 45, 13214–13221. doi: 10.1039/C6DT01801G

Allison, S. J., Cooke, D., Davidson, F. S., Elliott, P. I. P., Faulkner, R. A., Griffiths, H. B. S., et al. (2018). Ruthenium-containing linear helicates and mesocates with tuneable p53-selective cytotoxicity in colorectal cancer cells. *Angew. Chem. Int. Ed.* 57, 9799–9804. doi: 10.1002/anie.201805510

Anife, A., Denitsa, M., Masahiro, Y., Pavletta, S., Georgi, M., Munetaka, A., et al. (2016). Anticancer potencies of PtII- and PdII-linked M_2L_4 coordination capsules with improved selectivity. *Chem. Asian J.* 11, 474–477. doi: 10.1002/asia.201501238

Bhat, I. A., Jain, R., Siddiqui, M. M., Saini, D. K., and Mukherjee, P. S. (2017). Water-soluble Pd_8L_4 self-assembled molecular barrel as an aqueous carrier for Hydrophobic Curcumin. *Inorg. Chem.* 56, 5352–5360. doi: 10.1021/acs.inorgchem.7b00449

Bloch, W. M., Abe, Y., Holstein, J. J., Wandtke, C. M., Dittrich, B., and Clever, G. H. (2016). Geometric complementarity in assembly and guest recognition of a bent Heteroleptic cis-$[Pd_2LA_2LB_2]$ coordination cage. *J. Am. Chem. Soc.* 138, 13750–13755. doi: 10.1021/jacs.6b08694

Bloch, W. M., Holstein, J. J., Hiller, W., and Clever, G. H. (2017). Morphological control of Heteroleptic cis- and trans-$Pd_2L_2L'_2$ cages. *Angew. Chem. Int. Ed.* 56, 8285–8289. doi: 10.1002/anie.201702573

Bondy, C. R., Gale, P. A., and Loeb, S. J. (2004). Metal-organic anion receptors: arranging urea hydrogen-bond donors to encapsulate sulfate ions. *J. Am. Chem. Soc.* 126, 5030–5031. doi: 10.1021/ja039712q

Casini, A., Woods, B., and Wenzel, M. (2017). The Promise of Self-Assembled 3D Supramolecular coordination complexes for biomedical applications. *Inorg. Chem.* 56, 14715–14729. doi: 10.1021/acs.inorgchem.7b02599

Cook, T. R., and Stang, P. J. (2015). Recent developments in the preparation and chemistry of metallacycles and metallacages via coordination. *Chem. Rev.* 115, 7001–7045. doi: 10.1021/cr5005666

Cook, T. R., Vajpayee, V., Lee, M. H., Stang, P. J., and Chi, K.-W. (2013). Biomedical and biochemical applications of self-assembled metallacycles and metallacages. *Acc. Chem. Res.* 46, 2464–2474. doi: 10.1021/ar400010v

Dubey, A., Jeong, Y. J., Jo, J. H., Woo, S., Kim, D. H., Kim, H., et al. (2015). Anticancer activity and autophagy involvement of self-assembled arene-ruthenium metallacycles. *Organometallics* 34, 4507–4514. doi: 10.1021/acs.organomet.5b00512

Faulkner, A. D., Kaner, R. A., Abdallah, Q. M., Clarkson, G., Fox, D. J., Gurnani, P., et al. (2014). Asymmetric triplex metallohelices with high and selective activity against cancer cells. *Nat. Chem.* 6, 797–803. doi: 10.1038/nchem.2024

Garci, A., Castor, K. J., Fakhoury, J., Do, J.-L., Di Trani, J., Chidchob, P., et al. (2017). Efficient and rapid mechanochemical assembly of Platinum(II) squares for guanine quadruplex targeting. *J. Am. Chem. Soc.* 139, 16913–16922. doi: 10.1021/jacs.7b09819

Grishagin, I. V., Kushal, S., Olenyuk, B. Z., Pollock, J. B., Cook, T. R., and Stang, P. J. (2014). *In vivo* anticancer activity of rhomboidal Pt(II) metallacycles. *Proc. Natl. Acad. Sci. U.S.A.* 111, 18448–18453. doi: 10.1073/pnas.1418712111

Han, J., Schmidt, A., Zhang, T., Permentier, H., Groothuis, G. M., Bischoff, R., et al. (2017). Bioconjugation strategies to couple supramolecular exo-functionalized palladium cages to peptides for biomedical applications. *Chem. Commun.* 53, 1405–1408. doi: 10.1039/C6CC08937B

Hotze, A. C. G., Hodges, N. J., Hayden, R. E., Sanchez-Cano, C., Paines, C., Male, N., et al. (2008). Supramolecular iron cylinder with unprecedented DNA binding is a potent cytostatic and apoptotic agent without exhibiting genotoxicity. *Chem. Biol.* 15, 1258–1267. doi: 10.1016/j.chembiol.2008.10.016

Howson, S. E., Bolhuis, A., Brabec, V., Clarkson, G. J., Malina, J., Rodger, A., et al. (2012). Optically pure, water-stable metallo-helical 'flexicate' assemblies with antibiotic activity. *Nat. Chem.* 4, 31–36. doi: 10.1038/nchem.1206

Kaiser, F., Schmidt, A., Heydenreuter, W., Altmann, P. J., Casini, A., Sieber, S. A., et al. (2016). Self-assembled palladium and platinum coordination cages: photophysical studies and anticancer activity. *Eur. J. Inorg. Chem.* 2016, 5189–5196. doi: 10.1002/ejic.201600811

Kim, T. Y., Lucas, N. T., and Crowley, J. D. (2015). A diaryl-linked $[Pd_2L_4]4+$ metallosupramolecular architecture: synthesis, structures and cisplatin binding studies. *Supramol. Chem.* 27, 734–745. doi: 10.1080/10610278.2015.1063633

Lehmann, B. D., Bauer, J. A., Chen, X., Sanders, M. E., Chakravarthy, A. B., Shyr, Y., et al. (2011). Identification of human triple-negative breast cancer subtypes and preclinical models for selection of targeted therapies. *J. Clin. Invest.* 121, 2750–2767. doi: 10.1172/JCI45014

Lewis, J. E., McAdam, C. J., Gardiner, M. G., and Crowley, J. D. (2013). A facile "click" approach to functionalised metallosupramolecular architectures. *Chem. Commun.* 49, 3398–3400. doi: 10.1039/c3cc41209a

Lewis, J. E. M., and Crowley, J. D. (2014). Exo- and endo-hedral interactions of counteranions with tetracationic Pd_2L_4 metallosupramolecular architectures. *Supramol. Chem.* 26, 173–181. doi: 10.1080/10610278.2013.842644

Lewis, J. E. M., Elliott, A. B. S., McAdam, C. J., Gordon, K. C., and Crowley, J. D. (2014). 'Click' to functionalise: synthesis, characterisation and enhancement of the physical properties of a series of exo- and endo-functionalised Pd_2L_4 nanocages. *Chem. Sci.* 5, 1833–1843. doi: 10.1039/c4sc00434e

Lewis, J. E. M., Gavey, E. L., Cameron, S. A., and Crowley, J. D. (2012). Stimuli-responsive Pd_2L_4 metallosupramolecular cages: towards targeted cisplatin drug delivery. *Chem. Sci.* 3, 778–784. doi: 10.1039/c2sc00899h

Li, M., Howson, S. E., Dong, K., Gao, N., Ren, J., Scott, P., et al. (2014). Chiral metallohelical complexes enantioselectively target Amyloid β for treating Alzheimer's disease. *J. Am. Chem. Soc.* 136, 11655–11663. doi: 10.1021/ja502789e

Lo, W. K., Huff, G. S., Preston, D., McMorran, D. A., Giles, G. I., Gordon, K. C., et al. (2015). A dinuclear Platinum(II) N4Py complex: an unexpected coordination mode for N4Py. *Inorg. Chem.* 54, 6671–6673. doi: 10.1021/acs.inorgchem.5b01032

Mal, P., Breiner, B., Rissanen, K., and Nitschke, J. R. (2009). White Phosphorus is air-stable within a self-assembled tetrahedral capsule. *Science* 324, 1697–1699. doi: 10.1126/science.1175313

Malina, J., Scott, P., and Brabec, V. (2015). Recognition of DNA/RNA bulges by antimicrobial and antitumor metallohelices. *Dalton Trans.* 44, 14656–14665. doi: 10.1039/C5DT02018B

Martí-Centelles, V., Lawrence, A. L., and Lusby, P. J. (2018). High activity and efficient turnover by a simple, self-assembled "Artificial Diels-Alderase". *J. Am. Chem. Soc.* 140, 2862–2868. doi: 10.1021/jacs.7b12146

McMorran, D. A., and Steel, P. J. (1998). The first coordinatively saturated, quadruply stranded helicate and its encapsulation of a hexafluorophosphate anion. *Angew Chem. Int. Ed.* 37, 3295–3297.

McNeill, S. M., Preston, D., Lewis, J. E., Robert, A., Knerr-Rupp, K., Graham, D. O., et al. (2015). Biologically active $[Pd_2L_4]^{4+}$ quadruply-stranded helicates: stability and cytotoxicity. *Dalton Trans.* 44, 11129–11136. doi: 10.1039/C5DT01259G

Mitchell, D. E., Clarkson, G., Fox, D. J., Vipond, R. A., Scott, P., and Gibson, M. I. (2017). Antifreeze protein mimetic metallohelices with potent ice recrystallization inhibition activity. *J. Am. Chem. Soc.* 139, 9835–9838. doi: 10.1021/jacs.7b05822

Mjos, K. D., and Orvig, C. (2014). Metallodrugs in medicinal inorganic chemistry. *Chem. Rev.* 114, 4540–4563. doi: 10.1021/cr400460s

Oleksy, A., Blanco, A. G., Boer, R., Usón, I., Aymam,í, J., Rodger, A., et al. (2006). Molecular recognition of a three-way DNA junction by a Metallosupramolecular helicate. *Angew. Chem. Int. Ed.* 45, 1227–1231. doi: 10.1002/anie.200503822

Phongtongpasuk, S., Paulus, S., Schnabl, J., Sigel, R. K., Spingler, B., Hannon, M. J., et al. (2013). Binding of a designed anti-cancer drug to the central cavity of an RNA three-way junction. *Angew. Chem. Int. Ed.* 52, 11513–11516. doi: 10.1002/anie.201305079

Preston, D., Fox-Charles, A., Lo, W. K. C., and Crowley, J. D. (2015). Chloride triggered reversible switching from a metallosupramolecular $[Pd_2L_4]^{4+}$ cage to a $[Pd_2L_2Cl_4]$ metallo-macrocycle with release of endo- and exohedrally bound guests. *Chem. Commun.* 51, 9042–9045. doi: 10.1039/C5CC02226F

Preston, D., Lewis, J. E., and Crowley, J. D. (2017). Multicavity $[Pd_nL_4]^{2n+}$ cages with controlled segregated binding of different guests. *J. Am. Chem. Soc.* 139, 2379–2386. doi: 10.1021/jacs.6b11982

Preston, D., McNeill, S. M., Lewis, J. E., Giles, G. I., and Crowley, J. D. (2016). Enhanced kinetic stability of $[Pd_2L_4]^{4+}$ cages through ligand substitution. *Dalton Trans.* 45, 8050–8060. doi: 10.1039/C6DT00133E

Richards, A. D., Rodger, A., Hannon, M. J., and Bolhuis, A. (2009). Antimicrobial activity of an iron triple helicate. *Int. J. Antimicrob. Agents* 33, 469–472. doi: 10.1016/j.ijantimicag.2008.10.031

Samanta, S. K., Moncelet, D., Briken, V., and Isaacs, L. (2016). Metal-organic Polyhedron capped with Cucurbit[8]uril delivers Doxorubicin to cancer cells. *J. Am. Chem. Soc.* 138, 14488–14496. doi: 10.1021/jacs.6b09504

Samanta, S. K., Quigley, J., Vinciguerra, B., Briken, V., and Isaacs, L. (2017). Cucurbit[7]uril enables multi-stimuli-responsive release from the self-assembled Hydrophobic phase of a metal organic Polyhedron. *J. Am. Chem. Soc.* 139, 9066–9074. doi: 10.1021/jacs.7b05154

Schmidt, A., Casini, A., and Kuehn, F. E. (2014). Self-assembled M_2L_4 coordination cages: synthesis and potential applications. *Coord. Chem. Rev.* 275, 19–36. doi: 10.1016/j.ccr.2014.03.037

Schmidt, A., Hollering, M., Han, J., Casini, A., and Kühn, F. E. (2016a). Self-assembly of highly luminescent heteronuclear coordination cages. *Dalton Trans.* 45, 12297–12300. doi: 10.1039/C6DT02708C

Schmidt, A., Molano, V., Hollering, M., Pöthig, A., Casini, A., and Kühn, F. E. (2016b). Evaluation of new palladium cages as potential delivery systems for the anticancer drug Cisplatin. *Chem. Eur. J.* 22, 2253–2256. doi: 10.1002/chem.201504930

Schmitt, F., Freudenreich, J., Barry, N. P., Juillerat-Jeanneret, L., Süss-Fink, G., and Therrien, B. (2012). Organometallic cages as vehicles for intracellular release of Photosensitizers. *J. Am. Chem. Soc.* 134, 754–757. doi: 10.1021/ja207784t

Therrien, B. (2015). Biologically relevant arene ruthenium metalla-assemblies. *CrystEngComm* 17, 484–491. doi: 10.1039/C4CE02146K

Therrien, B., Suess-Fink, G., Govindaswamy, P., Renfrew, A. K., and Dyson, P. J. (2008). The "complex-in-a-complex" cations $[(acac)_2M\subset Ru_6(piPrC_6H_4Me)_6(tpt)_2(dhbq)_3]^{6+}$: a trojan horse for cancer cells. *Angew. Chem. Int. Ed.* 47, 3773–3776. doi: 10.1002/anie.200800186

Wang, H., Qian, X., Wang, K., Su, M., Haoyang, W.-W., Jiang, X., et al. (2018). Supramolecular Kandinsky circles with high antibacterial activity. *Nat. Commun.* 9:1815. doi: 10.1038/s41467-018-04247-z

Wang, J.-F., Huang, L.-Y., Bu, J.-H., Li, S.-Y., Qin, S., Xu, Y.-W., et al. (2018). A fluorescent calixarene-based dimeric capsule constructed via a M(II)-terpyridine interaction: cage structure, inclusion properties and drug release. *RSC Adv.* 8, 22530–22535. doi: 10.1039/C8RA02146E

Wang, M., Vajpayee, V., Shanmugaraju, S., Zheng, Y.-R., Zhao, Z., Kim, H., et al. (2011). Coordination-driven self-assembly of M_3L_2 trigonal cages from preorganized metalloligands incorporating octahedral metal centers and fluorescent detection of nitroaromatics. *Inorg. Chem.* 50, 1506–1512. doi: 10.1021/ic1020719

Xu, W.-Q., Fan, Y.-Z., Wang, H.-P., Teng, J., Li, Y.-H., Chen, C.-X., et al. (2017). Investigation of binding behavior between drug molecule 5-Fluoracil and M_4L_4-type Tetrahedral cages: selectivity, capture, and release. *Chem. Eur. J.* 23, 3542–3547. doi: 10.1002/chem.201606060

Yi, J. W., Barry, N. P., Furrer, M. A., Zava, O., Dyson, P. J., Therrien, B., et al. (2012). Delivery of Floxuridine derivatives to cancer cells by water-soluble organometallic cages. *Bioconjugate Chem.* 23, 461–471. doi: 10.1021/bc200472n

Yoshizawa, M., and Fujita, M. (2010). Development of unique chemical phenomena within nanometer-sized, self-assembled coordination hosts. *Bull. Chem. Soc. Jpn.* 83, 609–618. doi: 10.1246/bcsj.20100035

Yoshizawa, M., Klosterman, J. K., and Fujita, M. (2009). Functional molecular flasks: new properties and reactions within discrete, self-assembled hosts. *Angew. Chem. Int. Ed.* 48, 3418–3438. doi: 10.1002/anie.200805340

Yue, Z., Wang, H., Li, Y., Qin, Y., Xu, L., Bowers, D. J., et al. (2018). Coordination-driven self-assembly of a Pt(IV) prodrug-conjugated supramolecular hexagon. *Chem. Commun.* 54, 731–734. doi: 10.1039/C7CC07622C

Zhao, A., Howson, S. E., Zhao, C., Ren, J., Scott, P., Wang, C., et al. (2017). Chiral metallohelices enantioselectively target hybrid human telomeric G-quadruplex DNA. *Nucleic Acids Res.* 45, 5026–5035. doi: 10.1093/nar/gkx244

Zheng, Y.-R., Suntharalingam, K., Bruno, P. M., Lin, W., Wang, W., Hemann, M. T., et al. (2016). Mechanistic studies of the anticancer activity of an octahedral hexanuclear Pt(II) cage. *Inorg. Chim. Acta* 452, 125–129. doi: 10.1016/j.ica.2016.03.021

Zheng, Y.-R., Suntharalingam, K., Johnstone, T. C., and Lippard, S. J. (2015). Encapsulation of Pt(IV) prodrugs within a Pt(II) cage for drug delivery. *Chem. Sci.* 6, 1189–1193. doi: 10.1039/C4SC01892C

Zhou, J., Yu, G., and Huang, F. (2017). Supramolecular chemotherapy based on host-guest molecular recognition: a novel strategy in the battle against cancer with a bright future. *Chem. Soc. Rev.* 46, 7021–7053. doi: 10.1039/C6CS00898D

Conflict of Interest Statement: The authors declare that the research was conducted in the absence of any commercial or financial relationships that could be construed as a potential conflict of interest.

frontiers in Chemistry

ORIGINAL RESEARCH
published: 01 February 2019
doi: 10.3389/fchem.2019.00039

Nanoparticles of Metal-Organic Cages Overcoming Drug Resistance in Ovarian Cancer

Han Wang[1], *Zihan Qiu*[1], *He Liu*[2], *Amarasooriya M. D. S. Jayawardhana*[1], *Zhizhou Yue*[1], *Hala Daghlas*[1], *David J. Bowers*[1], *Bansidhar Datta*[2] *and Yao-Rong Zheng*[1]*

[1] Department of Chemistry and Biochemistry, Integrated Sciences Building, Kent State University, Kent, OH, United States, [2] Science Research Laboratory, Department of Chemistry and Biochemistry, Kent State University, Kent, OH, United States

A long-standing challenge in the treatment of ovarian cancer is drug resistance to standard platinum-based chemotherapy. Recently, increasing attention has been drawn to the use of self-assembled metal-organic complexes as novel therapeutics for cancer treatment. However, high hydrophobicity that is often associated with these structures lowers their solubility and hinders their clinical translation. In this article, we present a proof-of-concept study of using nanoprecipitation to formulate the hydrophobic metal-organic cages and facilitate their use in treating chemoresistant ovarian cancer. The Pt_6L_4 Cage **1** is an octahedral cage formed by self-assembly of six 1,10-phenanthroline-Pt(II) centers and four 2,4,6-tris(4-pyridyl)-1,3,5-triazine ligands (L). Cage **1** is able to trigger DNA damage and exhibits promising *in vitro* potency against a panel of human ovarian cancer cell lines. However, due to the large portion of aromatic components, this cage structure has very limited solubility in cell culture media (<20 μM). Notably, upon nanoformulation by using fluorescein (**2**) and a pegylated anionic polymer (**3**), the concentration of Cage **1** can reach up to 0.4 mM. Production of the nanoparticles of metal-organic cages (nMOC) is driven by the formation of the 1:1 host-guest complex of **1** and **2** in aqueous solution, which then form nanoprecipitation in presence of poly glutamic acid-*b*-poly ethylene glycol (**3**). The resulted nMOC are about 100 nm in diameter, and they serve as a delivery platform that slowly releases the therapeutic content. The use of fluorescein facilitates monitoring cell entry of nMOC and drug release using flow cytometry. Finally, comparing to cisplatin, the nMOC exhibit comparable *in vitro* efficacy against a panel of human cancer cell lines, and notably, it shows a much lower resistance factor against chemoresistant ovarian cancer cell lines.

Keywords: metal-organic cages, nanoprecipitation, DNA damage, host-guest chemistry, drug resistance

OPEN ACCESS

Edited by:
James D. Crowley,
University of Otago, New Zealand

Reviewed by:
Christian Hartinger,
The University of Auckland,
New Zealand
Ross Stewart Forgan,
University of Glasgow,
United Kingdom

***Correspondence:**
Yao-Rong Zheng
yzheng7@kent.edu

Specialty section:
This article was submitted to Supramolecular Chemistry, a section of the journal Frontiers in Chemistry

Received: *30 September 2018*
Accepted: *14 January 2019*
Published: *01 February 2019*

Citation:
Wang H, Qiu Z, Liu H, Jayawardhana AMDS, Yue Z, Daghlas H, Bowers DJ, Datta B and Zheng Y-R (2019) Nanoparticles of Metal-Organic Cages Overcoming Drug Resistance in Ovarian Cancer. Front. Chem. 7:39. doi: 10.3389/fchem.2019.00039

INTRODUCTION

Ovarian cancer is the most lethal gynecologic cancer and ranks as the fifth leading cause of death for women in the US. Each year, about 250,000 women are diagnosed with ovarian cancer in the US, and approximately half of these patients die within 5 years after their initial diagnosis (Siegel et al., 2015). The low survival rate of ovarian cancer is mainly attributed to the development

of drug resistance to the standard platinum chemotherapy (Holmes, 2015). The FDA-approved platinum drugs, cisplatin and carboplatin, are widely used as the first line treatment for ovarian cancer patients in the US and worldwide (Kelland, 2007). Initially, the patients show good responses to these compounds, but after about 12–24 months, patients commonly develop cancer relapse with drug resistance. Currently, there are very few alternative treatment options after the development of drug resistance to these platinum compounds. Thus, there is an urgent need for new, alternative therapeutics to combat chemoresistant ovarian cancer. In the past, the search of new drug candidates has largely focused on mononuclear metal complexes similar to structure of cisplatin, but there are rarely any clinically relevant breakthroughs (Wilson and Lippard, 2014; Zheng et al., 2014). Macromolecular polynuclear metal complexes emerges as a new type of therapeutic candidates to widen the spectrum of activity of current FDA-approved platinum drugs, however, studies of the therapeutic effects of such compounds are still limited (Farrell, 2015).

Metallosupramolecular coordination complexes represent a novel type of metal-organic complexes constructed by coordination-driven self-assembly (Cook and Stang, 2015). They are ordered, discrete macromolecular structures obtained by controlled aggregation of metal centers and organic ligands, and these ensembles exhibit well-defined sizes and shapes, such as metal-organic polyhedra, polygons, cages, and spheres, etc., (Harris et al., 2013; Xu et al., 2015). Due to the unique structural features, self-assembled metal-organic complexes have led to a large variety of novel research in chemistry, material science, and biology. In recent years, studies about applying such metal-organic complexes in cancer research has attracted increasing attention (Hannon, 2007; Therrien, 2012; Cook et al., 2013; Kaiser et al., 2016; Samanta et al., 2017). Stang, Chi, Therrien, Crowley, and Zheng have respectively published their works on designing new metal-organic polyhedra and cages and testing their anti-cancer efficacy (Lewis et al., 2012; Vajpayee et al., 2013; Grishagin et al., 2014; Zheng et al., 2015; Yue et al., 2018b). However, high hydrophobicity that is often associated with these structures lowers their solubility and hinders their clinical translation (Cook et al., 2013; Cook and Stang, 2015). Therefore, additional formulation of metallosupramolecular coordination complexes is critically important to resolve this issue in order to further advance the field toward clinical translation.

In this article, we present a proof-of-concept study of using nanoprecipitation to formulate the hydrophobic metal-organic cages and facilitate their use in treating chemoresistant ovarian cancer. As shown in **Scheme 1**, we can formulate Cage **1**, a cytotoxic hydrophobic metal-organic cage (**Figure 1A**) with low solubility, using fluorescein (**2**) and a pegylated anionic polymer (**3**). Driven by the host-guest interactions and electrostatic interactions, combination of the three components produces nanoparticles of metal-organic cages (nMOC) covered by PEG, therefore promoting its solubility. The resulted nMOC shows promising anticancer activities against chemoresistant ovarian cancer cells.

MATERIALS AND METHODS

General Information

All reagents were purchased from Strem, Aldrich or Alfa and used without further purification. Methoxy polyethylene glycol-*block*-polyglutamic acid ($MPEG_{5k}$-PGA_{50}) (**3**) was purchased from Polypeptide Therapeutic Solutions SL (Valencia, Spain). All reactions were carried out under normal atmospheric conditions. Deuterated solvents were purchased from Cambridge Isotope Laboratory (Andover, MA). The ^{1}H NMR spectra were recorded on a Bruker AMX 400 NMR in the Department of Chemistry and Biochemistry at Kent State University. Chemical shifts in ^{1}H NMR spectra were internally referenced to solvent signals (DMSO at $\delta = 2.50$ ppm). Elemental analysis was performed on a TruSpec Micro, CHNS analyzer from LECO Corporation. UV-Vis spectra were recorded on a VWR UV-1600PC scanning spectrophotometer. Fluorescence spectra were obtained on a Cary Eclipse fluorescence spectrophotometer. Graphite furnace atomic absorption spectroscopic (GFAAS) measurements were taken on a PerkinElmer PinAAcle 900Z spectrometer. Fluorescence images were acquired using an Olympus IX70 inverted epifluorescence microscope equipped with a digital CCD camera (QImaging). Images were processed and intensities were quantified with ImageJ software (NIH). Dynamic light scattering and zeta-potential analysis were carried out using a Horiba SZ-100 particle analyzer. 3D computational modeling was performed using Schrödinger Macromodel Suite based on MMFF force field. Flow cytometry was carried out on a BD Bioscience Accuri C6 flow cytometer. Cryo-TEM specimens were prepared using thin-film plunge freezing in a FEI Vitrobot at Liquid Crystal Institute at Kent State University. The vitrified specimens were mounted onto a Gatan 626.DH cryo-holder and transferred into a FEI Tecnai F20 TEM. Cryo-TEM observation was performed using low-dose mode. The detailed experimental setup and procedure are reported previously (Gao et al., 2014).

Synthesis of the Metal-Organic Cage (1)

Synthesis of the Pt_6L_4 cage was modified from the previous reports (Zheng et al., 2016; Yue et al., 2018a). $Pt(phen)(NO_3)_2$ (15.0 mg, 30 μmol) and 2,4,6-Tri(4-pyridyl)-1,3,5-triazine (6.0 mg, 19 μmol) were mixed in a microwave reaction vial (2–5 mL), followed by the addition of 4 mL H_2O and 4 μL of 65% HNO_3. The reaction vial was then sealed and placed in a Biotage Initiator Microwave Synthesizer. The mixture was stirred at 900 rpm and heated using a multi-step sequence (a. 90°C, 100 W for 30 min; b. 150°C, 150 W for 60 min). The mixture was centrifuged to remove possible precipitations. Then, the supernatant was collected, and the solvent was removed under reduced pressure. The resulted white solid was washed with 1 mL of water under sonication. After removing water by centrifugation, the final product was dried in vacuum. Yield: 15.7 mg, 78%. ^{1}H NMR (400 MHz, DMSO-d_6) δ 9.75 (d, J = 6.4 Hz, 24H, α-Pyridine), 9.26 (d, J = 8.0 Hz, 12H, phen), 9.16 (d, J = 6.8 Hz, 24H, β-Pyridine), 8.67 (d, J = 4.2 Hz, 12H, phen), 8.52 (d, J = 2.8 Hz, 12H, phen), 8.14 (m, 12H, phen). Anal. Calcd for $C_{144}H_{96}N_{48}O_{36}Pt_6 \cdot (H_2O)_6$: C, 39.73; H, 2.50; N, 15.44. Found: C, 39.56; H, 2.25; N, 15.09.

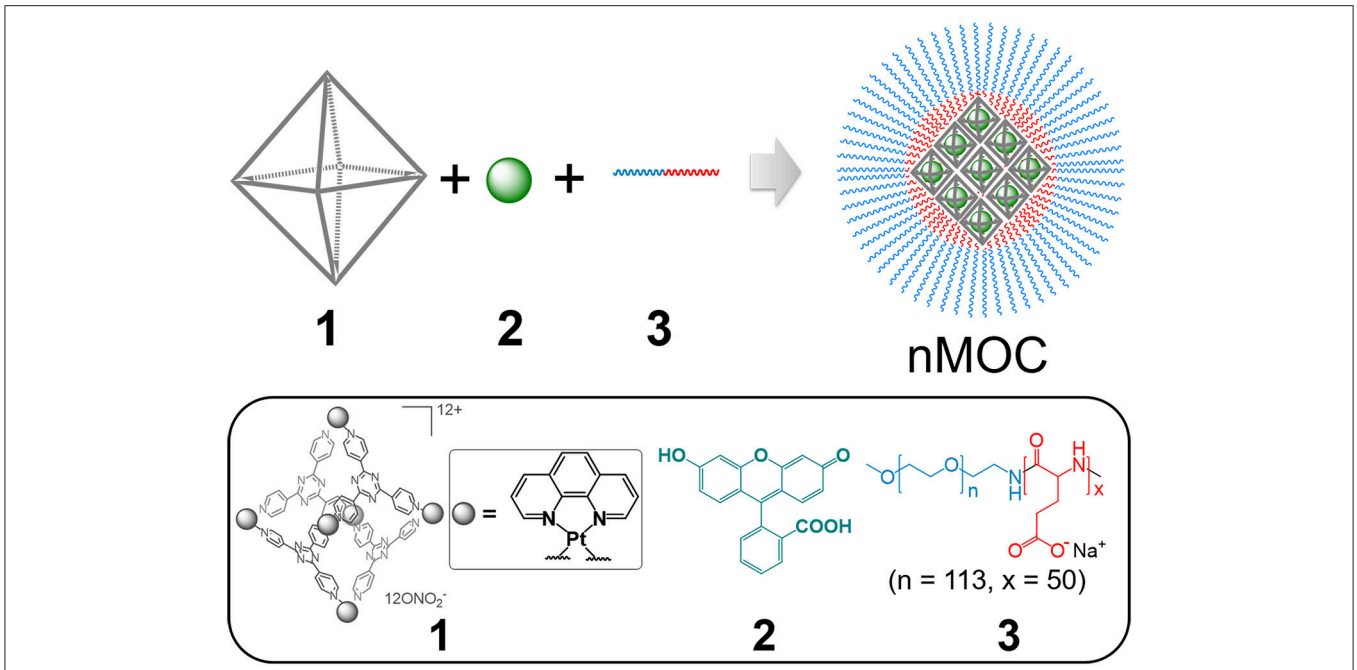

SCHEME 1 | Graphical representation of the formation of nanoparticles of metal-organic cages (nMOC): Cage 1 and fluorescein (2) form a host-guest complex in a 1:1 ratio in aqueous solution, and the use of $MPEG_{5k}$-PGA_{50} anionic block copolymer (3) enables the nanoprecipitation of this complex into nMOC, therefore promoting solubility of this cytotoxic hydrophobic cage.

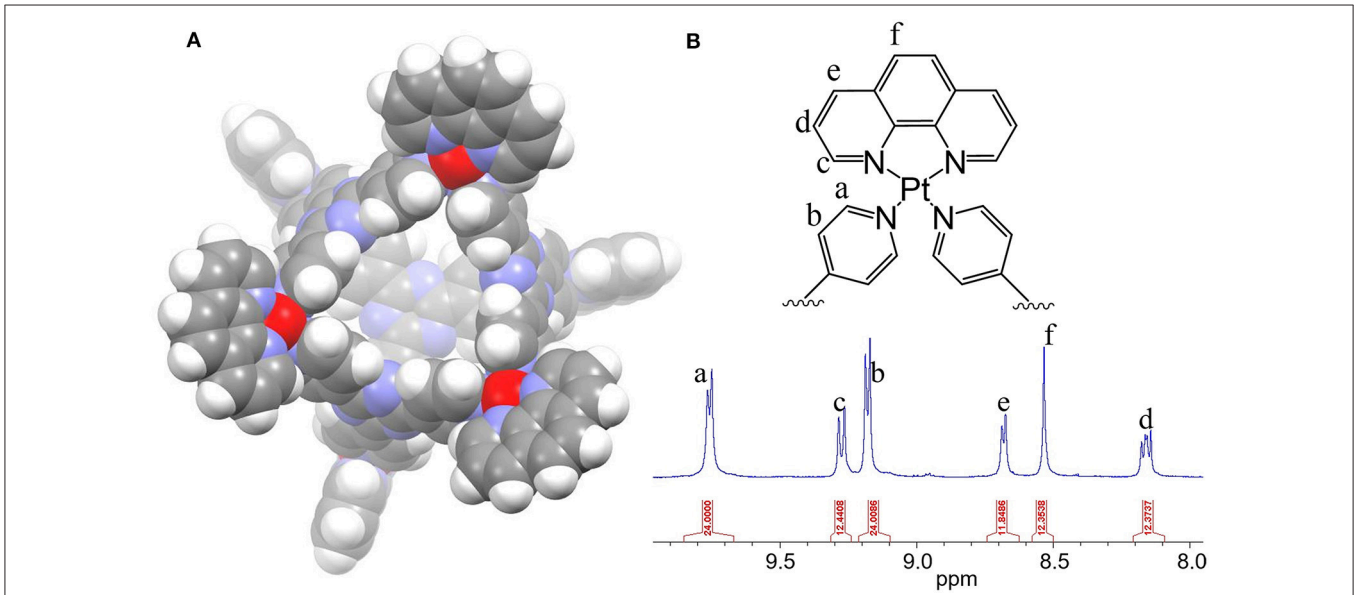

FIGURE 1 | (A) The 3D model of the Pt_6L_4 metal-organic cage (1) and **(B)** its ^{1}H NMR spectrum in DMSO-d_6.

Preparation of the Nanoparticles of Metal-Organic Cages (nMOC)

To a volume of 1 mL of PBS solution of $MPEG_{5k}$-PGA_{50} (**3**) (1.00 mg/mL) and fluorescein (**2**) (30.0 μL, 13.0 mM) was added the DMSO solution containing the metal-organic cage (**1**) (90.0 μL, 2.00 mM) under shaking at 900 rpm at room temperature (R.T.). The mixture was shaken for 10 min further at R.T. Significant color change from yellow green to red could be observed during the process, which is associated with the formation of the host-guest complex. The resulted red solution was filtered using a 0.2 μm PTFE syringe filter. The filtrate was further purified using centrifugal filtration (MWCO = 30 kDa). The solution of the

nanoparticles was concentrated to a volume of 0.8 mL. The Pt content was determined to be 768 μM using GFAAS. Each cage molecule contains six Pt centers. Therefore, the concentration of **1** in nMOC is 128 μM in PBS. Yield: 56.7%. This sample can be further concentrated up to 0.4 mM in PBS by centrifugal filtration (MWCO = 30 kDa).

Fluorescence Titration

The 2-mL PBS solution of fluorescein (**2**) (6 μM) was titrated by successive addition of Cage **1** (2.5 μL, 2.4 mM in DMSO). The total volume change during the titration is negligible. A spectra range between 500 and 650 nm was monitored during the titration.

Job Plots From UV-Vis Spectroscopy

A total of 11 samples containing Compound **1** and **2** in PBS were prepared in different molar ratio where each molar fraction varied from 0 to 1.0. The total concentration of **1** and **2** remained as constant as 10 μM. Solutions were prepared freshly and observed from 450 to 650 nm. Abs (506 nm) −ε (fluorescein) × [fluorescein] − ε (**1**) × [**1**] was plotted against the molar fraction of fluorescein, where Abs (506 nm) is the absorption of the sample at 506 nm, ε(fluorescein) is the extinction coefficient of fluorescein measured at 506 nm, ε(**1**) is the extinction coefficient of Cage **1** measured at 506 nm, and [**2**] and [**1**] are the concentration of fluorescein and Cage **1** within the sample.

Dialysis Experiments

A volume of 1 mL PBS solution (pH = 7.4) or acetate buffer (pH = 5.0) containing Cage **1** ([Pt] = 120 μM) or nMOC ([Pt] = 240 μM) were sealed in micro-dialysis bags (10 kDa MWCO) against 500 mL PBS solution or acetate buffer at R.T. A series of samples were collected within the bags for every few hours and analyzed with GFAAS. All the measurements were done in triplicate.

Cellular Uptake Evaluated by GFAAS

One million A2780cis cells were seeded on 60 × 10 mm petri dishes and incubated at 37°C overnight. These cells were treated with cisplatin ([Pt] = 25 μM), **1** ([Pt] = 25 μM), and nMOC ([Pt] = 25 μM) for 4 h at 37°C. The remaining alive cells were harvested by trypsinization and digested in 200 μL 70% HNO_3 at R.T. overnight. The platinum content in the cells were analyzed by GFAAS. All experiments were performed in triplicate.

Cellular Uptake Evaluated by Flow Cytometry

A2780cis cells were seeded on 60 × 10 mm petri dishes and incubated at 37°C overnight. These cells were treated with PBS, fluorescein ([**2**] = 3 μM), fluorescein ([**2**] = 3 μM) plus polymer, and nMOC ([**2**] = 3 μM) for 4 h at 37°C. The cells were harvested by trypsinization and with the Accuri flow cytometer and the cell populations were analyzed using the FlowJo software.

Flow Cytometric Analysis

A2780cis cells were seeded on 60 × 10 mm petri dishes and incubated at 37°C overnight. A2780cis cells were treated with the Pt compounds (nMOC [Pt] = 4 μM; cisplatin [Pt] = 10 μM) at 37°C for 72 h. The samples were analyzed with the Accuri flow cytometer and the cell populations were analyzed using the FlowJo software. Annexin V early apoptosis detection kit was used for apoptosis analysis, and the experiments were carried out by following the standard protocol supplied by the manufacturer.

Immunoblotting Analysis

A volume of 0.6 ml of RIPA buffer was added to the A2780cis cells treated with the different Pt compounds (nMOC [Pt] = 2.5, 5.0, and 7.5 μM, 48 h, and Cage **1** [Pt] = 2.5, 5.0, 7.5 μM, 48 h). The cells were gently shaken for 15 min at 4°C. Then, the cells were collected with a cell scraper, and transferred to a microcentrifuge tube. A total of 100 μg whole cell lysate with SDS loading dye was boiled for 2–3 min. A volume of 50 μl of lysate and loading dye mixture per well was loaded for gel electrophoresis (120 Volts for 90 min). Afterward, the proteins were transferred from the gel to UltraCruz® Nitrocellulose Pure Transfer Membranes, using an electroblotting apparatus according to the manufacturer's protocols. Non-specific binding was blocked using Blocker™ Blotto (30–60 min at R.T.). The blocked membrane was incubated with primary antibody with 1:1,000 dilution in Blotto for 1 h at R.T. with shaking. The membrane was washed three times for 5 min each with Tris-buffered saline, pH 7.5 with 0.5% Tween 20 (TBST). The membrane was incubated with horse-radish peroxidase (HRP) conjugated secondary antibody with dilution 1:2,000 for 1 h at R.T., with shaking. The membrane was washed three times for 5 min each with TBST. Chemiluminescence Luminol Reagent was used for detecting according to the standard protocol supplied by the manufacturer.

MTT Assays

Cells were seeded on a 96-well plate (2,000 cells per well) in 200 μL RPMI or DMEM and incubated for 24 h at 37°C. On the following day, the cells were treated with the platinum compounds of 50 μL, separately at varying concentrations for 72 h at 37°C. The cells were then treated with 30 μL fresh medium containing 3-(4,5-dimethylthiazol-2-yl)-2,5-diphenyltetrazolium bromide (MTT) (5 mg/mL) and incubated for 4 h at 37°C. The medium was removed, 200 μL of DMSO was added to the cells, and the absorbance of the purple formazan was recorded at 565 nm using a BioTek Elx800 microplate plate reader. Each experiment was performed in triplicate for each cell line. The IC_{50} values were derived from Dose Response curves to obtain the Pt concentration that could reduce cell viability to 50%. All the IC_{50} values were obtained by fitting experimental data using Origin.

LIVE/DEAD Cell Viability Assay

A2780cis cells were cultured on 35 mm sterile glass bottom culture dishes (MATTEK Corporation) for 24 h at 37°C. The cells were then treated with cisplatin ([Pt] = 10 μM), nMOC ([Pt] = 10 μM) for 48 h at 37°C. The LIVE/DEAD assay was carried out by following the standard protocol supplied by the manufacturer.

RESULTS AND DISCUSSION

Preparation of the Pt_6L_4 Metal-Organic Cage (1)

The M_6L_4 type of metal-organic cages was first developed by Fujita (Ibukuro et al., 1998). Recently, Lippard et al. reported that a Pt_6L_4 cage bearing a bpy aromatic chelator is able to trigger DNA damage and apoptosis via non-covalent binding (Zheng et al., 2016). In this report, we developed a Pt_6L_4 Cage **1** bearing a larger aromatic chelator, 1,10-phenanthroline (phen), toward generating severe DNA damage and high potency. As shown in **Figure 1A**, Cage **1** is an octahedral cage formed by self-assembly of six 1,10-phenanthroline-Pt(II) centers and four 2,4,6-tris(4-pyridyl)-1,3,5-triazine ligands (L). It is synthesized by following a reported procedure using microwave synthesis, and self-assembly was confirmed by NMR spectroscopy. The proton NMR spectrum of **1** (**Figure 1B**) matched the previous reports and the integrations confirmed a 6:4 ratio between 1,10-phenanthroline-Pt(II) centers and the pyridyl ligands (Zheng et al., 2016).

Cellular Responses of the Pt_6L_4 Metal-Organic Cage (1)

The cytotoxicity profiles of the metal-organic cage (**1**) was determined against a panel of human cancer cell lines using MTT [3-(4,5-dimethylthiazol-2-yl)-2,5-diphenyltetrazolium bromide] assays. As shown in **Figures 2A,B**, five human cancer cell lines were tested, including ovarian cancer cell line A2780, cisplatin-resistant ovarian cancer cell line A2780cis, ovarian cancer cell line SKOV-3, lung cancer cell line A549, and triple-negative breast cancer cell line MDA-MB-231. The cells were incubated with Cage **1** or cisplatin for 72 h, and the IC_{50} values (concentrations required to induce 50% viability) were derived from dose–response curves (**Figure 2A**). All of the IC_{50} values refer to platinum concentrations. As shown in **Figures 2A,B**, in A2780, A549, and MDA-MB-231, **1** exhibits IC_{50} values comparable to those of cisplatin. Notably, **1** exhibits higher cytotoxicity against A2780cis (IC_{50} = 4.50 ± 1.38 μM) than cisplatin (IC_{50} = 11.48 ± 1.09 μM). As A2780cis cells are intrinsically resistant to cisplatin, this data shows that **1** has the potential to treat chemoresistant ovarian cells. Furthermore, we used immunoblotting analysis to evaluate the DNA damage triggered by Cage **1**. As shown in **Figure 2C**, A2780cis cells incubated with **1** ([Pt] = 2.5, 5.0, and 7.5 μM) for 48 h showed a marked increase in phosphorylated H2AX (γH2AX), a classic biomarker for DNA damage. The results of MTT assays and immunoblotting analysis clearly support that Cage **1** is able to induce DNA damage and exhibit high potency against chemoresistant ovarian cancer cells. However, we found that this cage structure exhibits very limited solubility in cell culture media (<20 μM), due to the high hydrophobicity of the large aromatic components. Therefore, additional formulation is essential to promote the solubility of this hydrophobic cytotoxic cage.

Nanoformulation of the Metal-Organic Cage (1) Into nMOC

We found that combination of Cage **1** with fluorescein (**2**) and $MPEG_{5k}$-PGA_{50} (**3**) can produce nanoparticles of the metal-organic cages (nMOC) in aqueous solution. In the formulation experiment, the DMSO solution containing the metal-organic cage (**1**) (90.0 μL, 2.00 mM) was added to 1 mL PBS solution of $MPEG_{5k}$-PGA_{50} (**3**) (1.00 mg/mL) and fluorescein (**2**) (30.0 μL, 13.0 mM) with shaking at R.T. The nanoparticles were purified via centrifugal filtration, and the yield of the nanoformulation is 56.7%. As determined by GFAAS, upon nanoformulation, the concentration of **1** can reach up to 0.4 mM in aqueous solution and cell culture media. This nanoformulation is driven by the host-guest interactions and electrostatic interactions between the three components. During the formulation, significant color change from yellow green to red was observed, which is associated with the formation of the host-guest complex between Cage **1** and fluorescein (**2**). UV-vis and fluorescence spectroscopy were applied to understand such host-guest interactions. The chromatic change was characterized by UV-vis spectroscopy shown in **Figure 3A**. Increasing the molar ratio of **1** leads to red shift of the absorption spectra of **2**. Using a Job plot extracted from the UV-vis studies (the insert of **Figure 3A**), we determined the binding ratio of the cage and fluorescein to be 1:1. To further measure the dissociation constant (K_d) of the host-guest complex, we performed fluorescence titration of Cage **1** to the fluorescein (**2**) solution. As shown in **Figure 3B**, gradual addition of Cage **1** into the PBS solution of fluorescein (6 μM) resulted in the decrease in the fluorescence intensity at 525 nm. As extracted from a Scatchard plot (the insert of **Figure 3B**), the experimental K_d value was determined as 1.73 μM. These results are consistent with our previous report using a similar cage structure, and it is believed that the fluorescein molecule is encapsulated within the cavity of Cage **1** (Yue et al., 2018a). As the final product of the formulation, nMOC encapsulating fluorescein was obtained in the presence of the pegylated anionic polymer (**3**). Driven by the electrostatic interactions, the cationic host-guest complex binds to the anionic polymer, leading their aggregation in aqueous solution. By virtue of the PEG group of the polymer, such aggregations were stabilized on a nanoscale. In the cryo-EM image (**Figure 3C**), the nanoaggregation of the cages was clearly observed, and they are around 20–40 nm. These nanocores are stabilized by their peripheral PEG. As measured by DLS (**Figure 3D**), the average size of the overall nanoparticles is 98.0 ± 8.2 nm. The particle size difference between TEM and DLS is likely due to the peripheral PEG. The PEG layer of the nanoparticles cannot be detected under TEM. In addition, due to peripheral PEG, the zeta potential of the nanoparticles

A

IC_{50} (μM)	A2780 Ovarian Cancer Sensitive to cisplatin	A2780cis Ovarian Cancer Resistant to cisplatin	SKOV-3 Ovarian Cancer	A549 Lung Cancer	MDA-MB-231 Breast Cancer
Cisplatin	0.92 ± 0.22	11.48 ± 1.09	9.43±2.10	11.67 ± 3.37	27.36 ± 3.60
nMOC	3.09 ± 0.52	4.65 ± 0.73	21.64±9.70	23.29 ± 4.11	37.09 ± 10.70
1	1.63 ± 0.65	4.50 ± 1.38	36.78±13.72	15.69 ± 2.85	24.19 ± 19.64

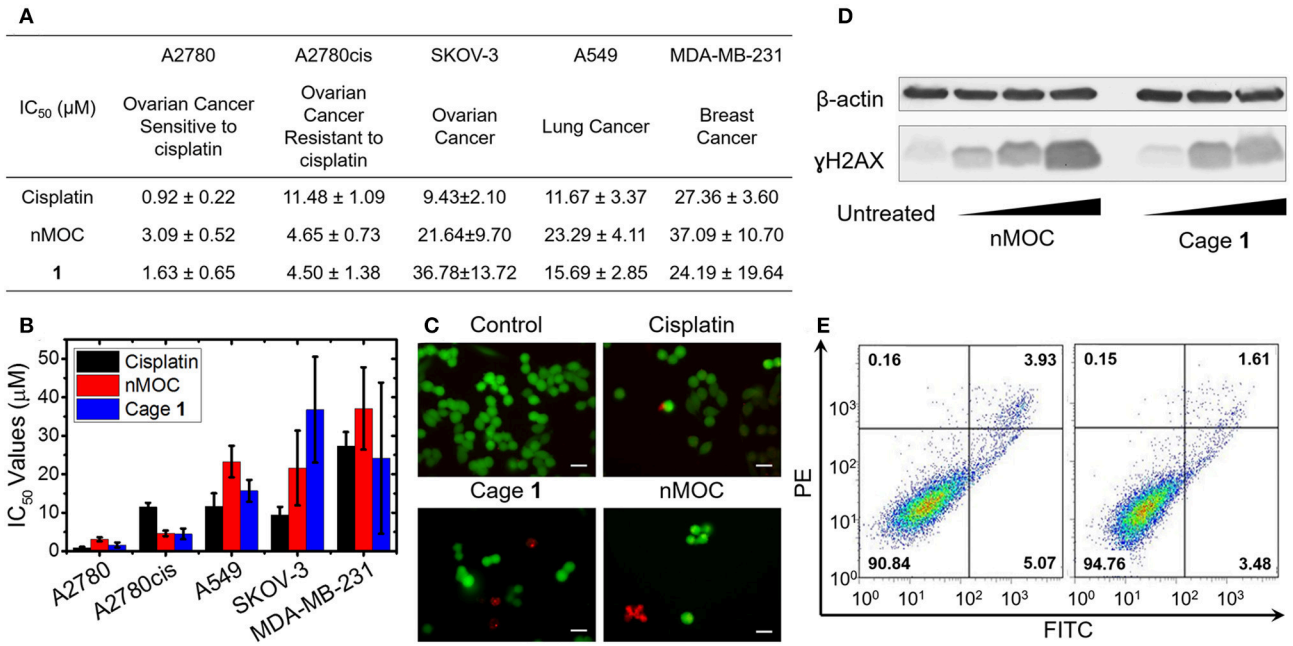

FIGURE 2 | Cellular responses of the metal-organic cage **(1)** and the nanoparticles of MOCs. **(A)** A table of the IC_{50} values of cisplatin, **1**, and nMOC determined by MTT assays; **(B)** Bar graph of IC_{50} values obtained using a panel of human cancer cell lines; **(C)** Fluorescence microscopic images obtained for the live/dead cell assay using A2780cis cells treated with cisplatin, **1**, or nMOC; **(D)** Immunoblotting analysis of γH2AX in A2780cis cell line; **(E)** Annexin V apoptosis assay using A2780cis cells treated with nMOC (left) and cisplatin (right).

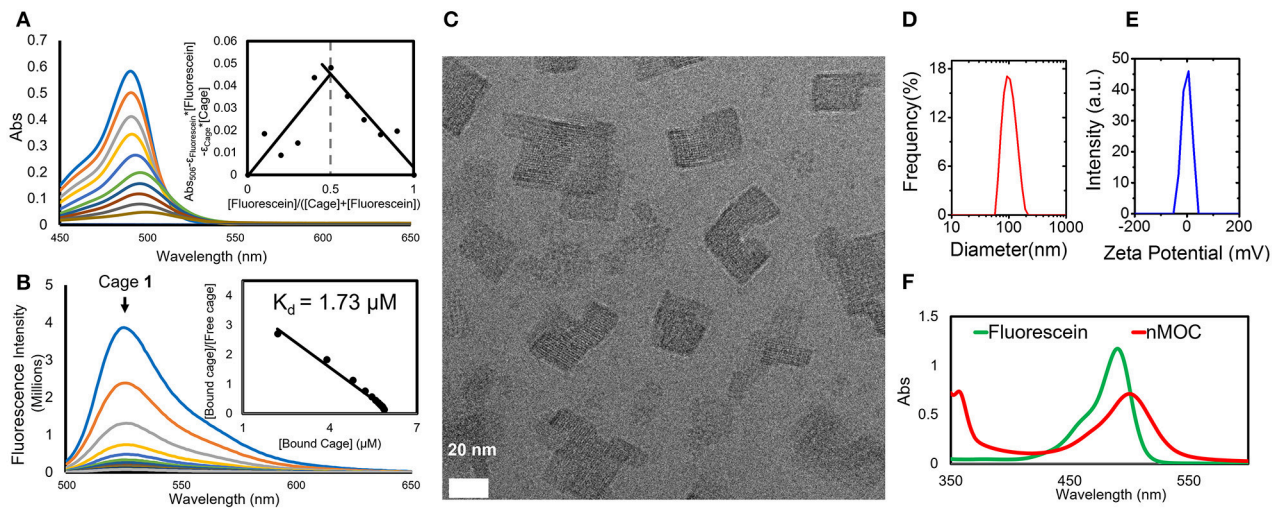

FIGURE 3 | Nanoformulation of Cage **1** using fluorescein **(2)** and $MPEG_{5k}$-PGA_{50} **(3)**. **(A)** Quenching of fluorescence emission of fluorescein by titration with **1** (6 μM) and the Scatchard plot extracted from fluorescence titration to determine K_d; **(B)** Changes of the absorption spectra of the mixture of **1** and **2** in a different molar ratio (0–1.0) and the Job plot extracted from titration to determine the binding ratio of **1** and **2**.; **(C)** A cryo-EM image (Scale bar: 20 nm) **(D)** DLS analysis of size distribution; **(E)** Zeta-potential analysis; **(F)** UV-vis spectra of fluorescein and nMOC in PBS ([**2**] = 20 μM).

is close to zero (−1.0 ± 0.4 mV) (**Figure 3E**). The integrity of the cage structure within the nanoparticles was supported by the UV-vis studies. In the UV-vis spectra (**Figure 3F**), the peak corresponding to nMOC is red-shifted compared to that of free fluorescein, and this is due to the encapsulation of fluorescein by Cage **1** within the nanoparticles. The combined evidence from spectroscopic analysis, GFAAS, TEM, and DLS clearly support that the hydrophobic cage can be readily formulated in

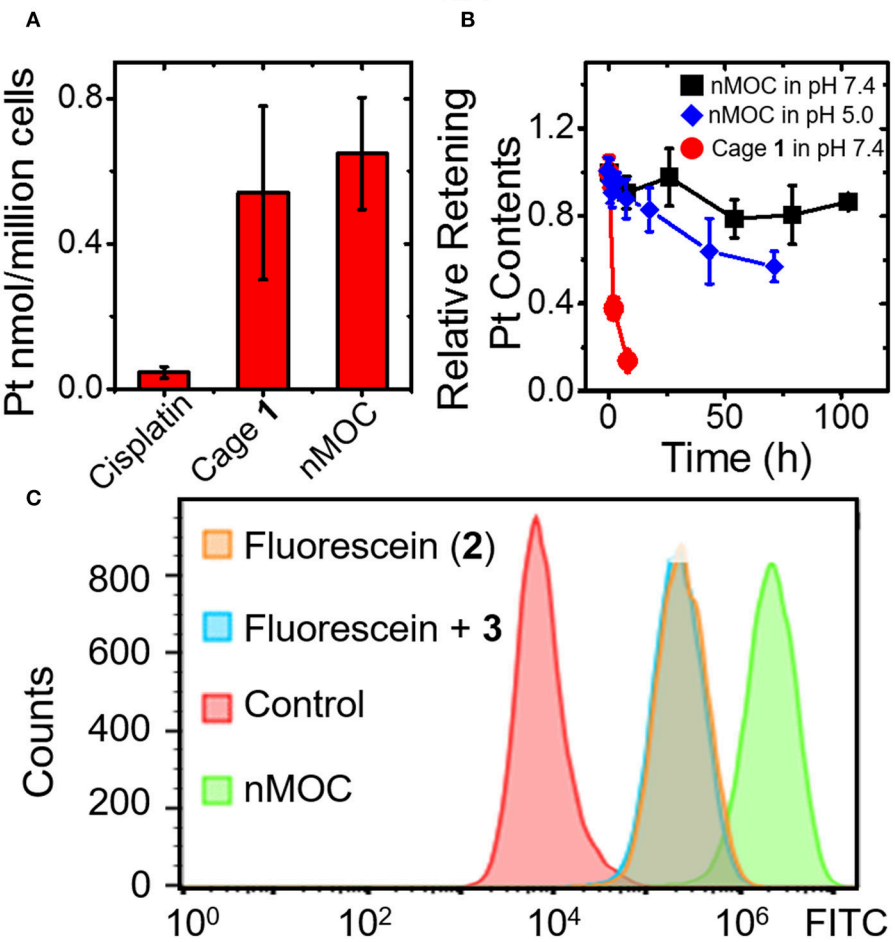

FIGURE 4 | Cellular uptake drug release profiles of the nanoparticles of MOCs. **(A)** Cellular uptake profiles of the different Pt compounds in A2780cis ovarian cancer cells analyzed by using GFAAS; **(B)** Drug release profile of nMOC and Cage **1** in PBS (pH = 7.4) or acetate buffer (pH = 5.0) at R.T.; **(C)** Cellular uptake profiles analyzed by using flow cytometry.

well-defined nanoparticles and increase its solubility in aqueous solution.

Cellular Uptake and Drug Release of nMOC

Next, we examined whether the nMOC can enter cancer cells and release Cage **1** and fluorescein (**2**). We determined the cellular uptake of the nanoparticles and compared that with cisplatin and MOCs using GFAAS. The results (**Figure 4A**) show that the cellular uptake of cisplatin was only 50 pmol/million cells in A2780cis cells, while the uptakes of MOCs and Cage **1** were 10 times higher. This results verified that the nanoparticles can readily enter cancer cells. Furthermore, the drug release profiles of these nanoparticles under different pH were analyzed using dialysis in micro-dialysis bags (10 kDa MWCO). In **Figure 4B**, the nanoparticles show a very slow release in PBS (pH = 7.4), and there's only 20% Pt contents released after 100 h. As a control, Cage **1** exhibits fast escape from the dialysis bag under the similar condition, the half-life of which is only less than 2 h. In acidic acetate buffer (pH = 5.0), the nanoparticles rapidly release the Pt contents. As shown in **Figure 4B**, almost half of the Pt contents were released within 72 h in the acetate buffer. Therefore, these nanoparticles are expected to stably hold the therapeutic contents before entering cells and then readily release the cage in the acidic environment of endosomes. Finally, we employed flow cytometry to verify the intracellular drug release. The A2780cis cells were treated with PBS, fluorescein (**2**), **2** + **3**, and nMOC. As a result shown in **Figure 4C**, the sample treated **2** exhibits a relatively low fluorescence intensity, and this is because fluorescein (**2**) itself has very poor cell penetration. As a control, addition of the anionic polymer did not increase the uptake. Notably, the cells treated with the nanoparticles showed marked increase in fluorescent intensity. Considering that the fluorescence signals of **2** is quenched by Cage **1** within the nanoparticles, the intense fluorescence observed in the flow cytometric analysis is resulted from the intracellularly released fluorescein. Therefore, we conclude that nMOC act as a promising system for delivering the hydrophobic cytotoxic metal-organic cages and the encapsulated fluorescein guest.

Cellular Responses of nMOC

Finally, the *in vitro* efficacy and cellular responses of the nanoparticles were examined. For A2780, A2780cis, A549, SKOV-3, and MDA-MB-231 cell lines in **Figures 2A,B**, the nanoparticles exhibit IC_{50} values comparable to those of Cage **1**. It is notable that nanoparticles maintain a lower IC_{50} value against A2780cis cells ($IC_{50} = 4.65 \pm 0.73\,\mu M$) compared to cisplatin ($IC_{50} = 11.48 \pm 1.09\,\mu M$). Resistance factors calculated based on IC_{50}(A2780cis)/IC_{50}(A2780) represent an important factor to evaluate how chemoresistant ovarian cancer cells response to the therapeutic candidates. As a result of the MTT assays, the nanoformulation has a much lower resistance factor compared to that of Cage **1** or cisplatin. For nMOC, the value of IC_{50}(A2780cis)/IC_{50}(A2780) is 1.50, while that of Cage **1** is 2.76 and cisplatin is 12.5. Furthermore, Live/Dead cell assay was used to confirm the anticancer activity of nMOC against A2780cis cells (**Figure 2C**). A2780cis cells treated with the nanoparticles contain a higher population of dead cells, but those treated with cisplatin remained viable. In addition, the results of the immunoblotting analysis (**Figure 2D**) show that the nanoparticles act as a DNA damaging agent like Cage **1** and induced phosphorylation of H2AX (γH2AX) in the treated A2780cis cells. Finally, annexin V flow cytometric analysis was used to further verify the apoptosis that is triggered by nanoparticles. Apoptosis represents one major cellular response to DNA damage. In healthy cells, phosphatidylserine (PS) is located on the cytoplasmic surface of the cell membrane, but in cells undergoing apoptosis, PS is translocated to the exterior of the plasma membrane, exposing PS to the external cellular environment where it can be detected by annexin V conjugates. By using annexin V and PI, both early and late stage apoptosis can be identified. As shown in **Figure 2E**, the nanoparticles induced significant populations of cells to under early- and late-stage apoptosis (5.07 and 3.93%, respectively). Variation of IC_{50} values (**Figure 2A**) of the platinum compounds across different human cell lines is attributed to different aspects of the mechanism of action. Different cell lines have different capabilities of exporting platinum compounds via efflux, different concentrations of intracellular glutathione that can deactivate platinum compounds, different nuclear DNA damaging repair capability, and different expression levels of anti-apoptotic proteins. Collectively, the cell-based studies suggest that the nanoformulation of Cage **1** maintains its mechanism of action of inducing DNA damage and apoptosis and exhibits high potency against chemoresistant ovarian cancer.

CONCLUSION

In conclusion, we have presented a novel design of formulating cytotoxic hydrophobic metal-organic cages to facilitate their use in treating chemoresistant ovarian cancer. In this work, we demonstrated that Cage **1**, a cytotoxic hydrophobic metal-organic cage with low solubility, can be formulated into pegylated nanoparticles in presence of fluorescein (**2**) and $MPEG_{5k}$-PGA_{50} (**3**). The nanoformulation is driven by the host-guest interactions between Cage **1** and Compound **2**, confirmed by using UV-vis and fluorescence spectroscopy. In presence of the anionic polymer (**3**), such cationic host-guest complexes precipitate in aqueous solution to form the nMOC covered by PEG, characterized by TEM and DLS. In the form of nMOC, the concentration of Cage **1** can reach up to 0.4 mM in aqueous solution or cell culture media. Upon entering cancer cells, the nMOC can slowly releases therapeutic content (**1**) and the fluorophore (**2**). Using MTT assays, we determined that the nMOC exhibits promising *in vitro* efficacy against a panel of human cancer cell lines, and notably, the nMOC shows a much lower resistance factor against chemoresistant ovarian cancer cell lines comparing to cisplatin. We envision that this study can deliver a threefold impact to the research field that focuses on applying metallosupramolecular coordination complexes in cancer therapy: First, this work demonstrates the feasibility of using pegylated anionic polymers to formulate hydrophobic cationic metal-organic cages toward promoting their solubility and biocompatibility, and ideally, this strategy can be applied to other metal-organic complexes. Moreover, this strategy also introduces the host-guest chemistry that can be further exploited for the delivery of different therapeutic entities, and this may further enhance the therapeutic effects of such systems. Finally, the promising therapeutic effects of the resulted nMOC make them possible therapeutic candidates for future studies toward treating chemoresistant ovarian cancer.

AUTHOR CONTRIBUTIONS

HW and ZY: synthesis and characterization of Cage **1**; HW and HD: spectroscopic studies of the host-guest complex formed by Cage **1** and fluorescein; HW and AJ: preparation and characterization of nMOC; ZQ: cell-based studies; HL and BD: analysis of phosphorylation of H2AX by western blots; Y-RZ: develop the concept and design the experiments; Y-RZ and DB: prepare the manuscript.

FUNDING

Kent State University, the Startup Fund, Farris Family Innovation Awards, LaunchPad Awards.

ACKNOWLEDGMENTS

Y-RZ thanks the financial support provided by the startup fund, Farris Family Innovation Awards, and LaunchPad Awards provided by Kent State University. The TEM data were obtained by Dr. Min Gao (or other staff member) at the (cryo) TEM facility at the Liquid Crystal Institute, Kent State University, supported by the Ohio Research Scholars Program Research Cluster on Surfaces in Advanced Materials.

REFERENCES

Cook, T., and Stang, P. (2015). Recent developments in the preparation and chemistry of metallacycles and metallacages via coordination. *Chem. Rev.* 115, 7001–7045. doi: 10.1021/cr50 05666

Cook, T. R., Vajpayee, V., Lee, M. H., Stang, P. J., and Chi, K.-W. (2013). Biomedical and biochemical applications of self-assembled metallacycles and metallacages. *Acc. Chem. Res.* 46, 2464–2474. doi: 10.1021/ar400010v

Farrell, N. P. (2015). Multi-platinum anti-cancer agents. Substitution-inert compounds for tumor selectivity and new targets. *Chem. Soc. Rev.* 44, 8773–8785. doi: 10.1039/C5CS00201J

Gao, M., Kim, Y.-K., Zhang, C., Borshch, V., Zhou, S., Park, H.-S., et al. (2014). Direct observation of liquid crystals using cryo-TEM: Specimen preparation and low-dose imaging. *Microsc. Res. Tech.* 77, 754–772. doi: 10.1002/jemt.22397

Grishagin, I., Pollock, J., Kushal, S., Cook, T., Stang, P., and Olenyuk, B. (2014). *In vivo* anticancer activity of rhomboidal Pt(II) metallacycles. *Proc. Natl. Acad. Sci. U.S.A.* 111, 18448–18453. doi: 10.1073/pnas.1418712111

Hannon, M. J. (2007). Supramolecular DNA recognition. *Chem. Soc. Rev.*36, 280–295. doi: 10.1039/B606046N

Harris, K., Fujita, D., and Fujita, M. (2013). Giant hollow MnL2n spherical complexes: structure, functionalisation and applications. *Chem. Commun.* 49, 6703–6712. doi: 10.1039/c3cc43191f

Holmes, D. (2015). Ovarian cancer: beyond resistance. *Nature* 527:S217. doi: 10.1038/527S217a

Ibukuro, F., Kusukawa, T., and Fujita, M. (1998). A thermally switchable molecular lock. Guest-templated synthesis of a kinetically stable nanosized cage. *J. Am. Chem. Soc.* 120, 8561–8562. doi: 10.1021/ja980853f

Kaiser, F., Schmidt, A., Heydenreuter, W., Altmann, P., Casini, A., Sieber, S., et al. (2016). Self-assembled palladium and platinum coordination cages: photophysical studies and anticancer activity. *Eur. J. Inorg. Chem.* 2016, 5189–5196. doi: 10.1002/ejic.201600811

Kelland, L. (2007). The resurgence of platinum-based cancer chemotherapy. *Nat. Rev. Cancer* 7, 573–584. doi: 10.1038/nrc2167

Lewis, J., Gavey, E., Cameron, S., and Crowley, J. (2012). Stimuli-responsive Pd2L4 metallosupramolecular cages: towards targeted cisplatin drug delivery. *Chem. Sci.* 3, 778–784. doi: 10.1039/C2SC00899H

Samanta, S., Quigley, J., Vinciguerra, B., Briken, V., and Isaacs, L. (2017). Cucurbit[7]uril enables multi-stimuli-responsive release from the self-assembled hydrophobic phase of a metal organic polyhedron. *J. Am. Chem. Soc.* 39, 9066–9074. doi: 10.1021/jacs.7b05154

Siegel, L. R., Miller, K. D., and Jemal, A. (2015). Cancer statistics, 2015. *CA Cancer J. Clin.* 65, 5–65. doi: 10.3322/caac.21254

Therrien, B. (2012). Drug delivery by water-soluble organometallic cages. *Top. Curr. Chem.* 319, 35–56. doi: 10.1007/128_2011_272

Vajpayee, V., Lee, S. M., Park, J. W., Dubey, A., Kim, H., Cook, T. R., et al. (2013). Growth inhibitory activity of a bis-benzimidazole-bridged arene ruthenium metalla-rectangle and prism. *Organometallics* 32, 1563–1566. doi: 10.1021/om301174s

Wilson, J. J., and Lippard, S. J. (2014). Synthetic methods for the preparation of platinum anticancer complexes. *Chem. Rev.* 114, 4470–4495. doi: 10.1021/cr4004314

Xu, L., Wang, Y., Chen, L., and Yang, H. (2015). Construction of multiferrocenyl metallacycles and metallacages via coordination-driven self-assembly: from structure to functions. *Chem. Soc. Rev.* 44, 2148–2167. doi: 10.1039/C5CS00022J

Yue, Z., Wang, H., Bowers, D. J., Gao, M., Stilgenbauer, M., Nielsen, F., et al. (2018a). Nanoparticles of metal–organic cages designed to encapsulate platinum-based anticancer agents. *Dalton Trans.* 47, 670–674. doi: 10.1039/C7DT03537C

Yue, Z., Wang, H., Li, Y., Qin, Y., Xu, L., Bowers, D. J., et al. (2018b). Coordination-driven self-assembly of a Pt(iv) prodrug-conjugated supramolecular hexagon. *Chem. Commun.* 54, 731–734. doi: 10.1039/C7CC07622C

Zheng, Y., Suntharalingam, K., Johnstone, T., and Lippard, S. (2015). Encapsulation of Pt(IV) prodrugs within a Pt(II) cage for drug delivery. *Chem. Sci.* 6, 1189–1193. doi: 10.1039/C4SC01892C

Zheng, Y.-R., Suntharalingam, K., Bruno, P. M., Lin, W., Wang, W., Hemann, M., et al. (2016). Mechanistic studies of the anticancer activity of an octahedral hexanuclear pt(ii) cage. *Inorg. Chim. Acta* 452, 125–129. doi: 10.1016/j.ica.2016.03.021

Zheng, Y.-R., Suntharalingam, K., Johnstone, T. C., Yoo, H., Lin, W., Brooks, J. G., et al. (2014). Pt(IV) prodrugs designed to bind non-covalently to human serum albumin for drug delivery. *J. Am. Chem. Soc.* 136, 8790–8798. doi: 10.1021/ja5038269

Conflict of Interest Statement: The authors declare that the research was conducted in the absence of any commercial or financial relationships that could be construed as a potential conflict of interest.

frontiers in Chemistry

ORIGINAL RESEARCH
published: 03 April 2018
doi: 10.3389/fchem.2018.00087

Self-Assembly of a [1 + 1] Ionic Hexagonal Macrocycle and Its Antiproliferative Activity

Khushwant Singh[1], *Ankit Gangrade*[2], *Sourav Bhowmick*[1], *Achintya Jana*[1], *Biman B. Mandal*[2]* *and Neeladri Das*[1]*

[1] Department of Chemistry, Indian Institute of Technology Patna, Bihta, India, [2] Department of Biosciences and Bioengineering, Indian Institute of Technology Guwahati, Guwahati, India

A unique irregular hexagon was self-assembled using an organic donor clip (bearing terminal pyridyl units) and a complementary organometallic acceptor clip. The resulting metallamacrocycle was characterized by multinuclear NMR, mass spectrometry, and elemental analyses. Molecular modeling confirmed hexagonal shaped cavity for this metallamacrocycle which is a unique example of a discrete hexagonal framework self-assembled from only two building blocks. Cytotoxicity of the Pt-based acceptor tecton and the self-assembled Pt^{II}-based macrocycle was evaluated using three cancer cell lines and results were compared with cisplatin. Results confirmed a positive effect of the metallamacrocycle formation on cell growth inhibition.

Keywords: ionic metallamacrocycle, supramolecular assemblies, cytotoxicity, cancer cell lines, heterocyclic compounds

OPEN ACCESS

Edited by:
James D. Crowley,
University of Otago, New Zealand

Reviewed by:
Sally Elisabeth Plush,
University of South Australia, Australia
Jyotirmayee Mohanty,
Bhabha Atomic Research Centre, India
Robert Elmes,
Maynooth University, Ireland

***Correspondence:**
Biman B. Mandal
biman.mandal@iitg.ernet.in;
mandal.biman@gmail.com
Neeladri Das
neeladri@iitp.ac.in;
neeladri2002@yahoo.co.in

Specialty section:
This article was submitted to Supramolecular Chemistry, a section of the journal Frontiers in Chemistry

Received: *07 February 2018*
Accepted: *12 March 2018*
Published: *03 April 2018*

Citation:
Singh K, Gangrade A, Bhowmick S, Jana A, Mandal BB and Das N (2018) Self-Assembly of a [1 + 1] Ionic Hexagonal Macrocycle and Its Antiproliferative Activity. Front. Chem. 6:87. doi: 10.3389/fchem.2018.00087

INTRODUCTION

Coordination driven self-assembly has been used conveniently in contemporary research for the construction of wide range of discrete supramolecular architectures (Chakrabarty et al., 2011; Cook et al., 2013b; Li et al., 2013; Schmidt et al., 2014; Schoedel and Zaworotko, 2014; Tanaka et al., 2014; Bhowmick et al., 2015a,b; Cook and Stang, 2015; Wang et al., 2016; Jana et al., 2017). In such complex frameworks, the building blocks (*aka* supramolecular tectons) are held together by using multiple ligand-metal coordination bonds (Lehn, 1995; Chakrabarty et al., 2011; Cook et al., 2013b; Li et al., 2013; Ward and Raithby, 2013; Han et al., 2014; Schmidt et al., 2014; Schoedel and Zaworotko, 2014; Tanaka et al., 2014; Bhowmick et al., 2015a,b; Cook and Stang, 2015; Johnson et al., 2015; Holloway et al., 2016, 2017; Wang et al., 2016; Jana et al., 2017). The dimensions of resultant abiotic supramolecules are guided by chemical information (stereo and geometric) contained in precursor moieties (Oliveri et al., 2008; Newkome and Shreiner, 2010; Inokuma et al., 2011; Cook et al., 2013b; Harris et al., 2013; Yoshizawa and Klosterman, 2014; Cook and Stang, 2015; Wang et al., 2015; Xu et al., 2016; Jana and Das, 2017). Intense research interest in understanding the complexity level of these artificial self-assembly processes is reflected in the quantum of reports published in this research domain (Barbara, 2001; Sauvage, 2001; Balzani et al., 2002; Beuerle, 2016; Fujita et al., 2016). Moreover, metal-mediated self-assembly studies are useful in understanding the fundamental principles of molecular self-organization in nature (Liu et al., 2007; Albertí et al., 2013; Chakraborty et al., 2013, 2015; Cook et al., 2013b; Galstyan et al., 2013; Saha et al., 2014; Sarkar et al., 2014; Chen et al., 2015; Cook and Stang, 2015; Li et al., 2015).

The library of discrete structures designed using the principles of coordination driven self-assembly (Pluth et al., 2009; Yoshizawa et al., 2009; Michito and Makoto, 2010; Thanasekaran et al., 2012; Cook et al., 2013b; Therrien, 2013; Young and Hay, 2013; Mishra and Gupta, 2014; Samanta and Mukherjee, 2014; Xu et al., 2014; Cook and Stang, 2015; Bhowmick et al., 2016) include two dimensional (2-D) structures such as metallamacrocycles (triangles, rectangles, pentagon, hexagon, square etc.) and three dimensional (3-D) frameworks (cages, boxes, barrels, prisms, Archimedean, and Platonic solid) (Stang and Olenyuk, 1997; Fujita et al., 2005; Takezawa and Shionoya, 2012; Cook et al., 2013b; Kishi et al., 2013; Chen et al., 2014; Liu et al., 2014; Lu et al., 2014; Cook and Stang, 2015; Manna et al., 2015; Zhang et al., 2017). Among the 2-D polygons, hexagonal frameworks are most interesting because such a shape is most abundantly observed in nature. Prominent examples of hexagonal motif observed in nature are honeycombs and graphite. Artificial self-assembly of hexagonal nanoscalar entities is challenging, as it requires convergence of several smaller components.

In recent years, an emerging application of these abiological supramolecules is to investigate their nature of interactions with biological systems (Wang and Lippard, 2005; Kelland, 2007; Wheate et al., 2010). These interactions include but are not limited to studies with cancer cells, DNA and proteins. Among purely inorganic complexes, Pt, Ru, and Au based ions are most popular (Mattsson et al., 2009; Ott, 2009; Berners-Price and Filipovska, 2011; Vajpayee et al., 2011, 2013; Lo et al., 2015; Ajibola et al., 2017). For example, Pt based cisplatin has been one of the most successful therapeutic agent in cancer treatment (Rosenberg et al., 1969; Vickers et al., 2004). However cisplatin has limitation (as a chemotherapeutic agent) such as uptake by healthy cells, resistance developed by target cancer cells, harmful side effects (such as nephrotoxicity, neurotoxicity and ototoxicity) and protein inactivation (Jung and Lippard, 2007; Yao et al., 2007; Wang and Guo, 2008; Todd and Lippard, 2009; Kaluderovic and Paschke, 2011; Barry and Sadler, 2013; Farrell, 2015). Considering these limitations of cisplatin's therapeutic use, synthetic organometallic and supramolecular entities are being explored as alternatives with potential application in treatment of cancer. These supramolecules are often constructed from organometallic precursor molecules. In this class of molecules, the metal ruthenium is clearly a leader (Yan et al., 1997; Therrien et al., 2008; Paul et al., 2012; Jo et al., 2017). Cook, Stang, and Chi have reviewed the biological interactions of metallacycles derived using coordination driven self-assembly protocol (Cook et al., 2013a). Majority of these are derived from Ru based precursors. It is obvious from this report that biochemical interactions of supramolecular frameworks bearing Pt(II) centers have not been explored, especially in the context of their potential as anticancer therapeutic agents.

This present work is in continuation of our research efforts to design unique supramolecular coordination complexes (SCCs) wherein we report synthesis of a discrete and nanoscalar hexagonal supramolecular complex using a new donor tecton. Furthermore, we have explored cytotoxicity of the new hexagonal SCC and its organometallic precursor. Additionally the results have been compared with cisplatin under similar conditions.

EXPERIMENTAL SECTION

General Details

All chemicals and anhydrous solvents used in this work were purchased from commercial sources and used without further purification. FTIR spectra were recorded in a PerkinElmer Spectrum 400 FT-IR spectrophotometer. ^{1}H and $^{31}P\{^{1}H\}$ NMR spectra were recorded on Bruker 400 MHz spectrometer. Elemental analyses were carried out using an Elementar Vario Micro Cube elemental analyzer. ESI-MS analysis was performed using a Bruker Impact ESI-Q-TOF system. Theoretical calculations of PM6 semiempirical molecular orbital method were carried out with Gaussian 09. A549 (human lung cancer cell line), KB (human oral cancer cell line) and HaCaT (human skin keratinocyte cell line) were procured from National Centre for Cell Science (NCCS), Pune. MTT [(3-(4, 5-dimethylthiazol-2-yl)-2, 5-diphenyl tetrasodium bromide] was purchased from SigmaAldrich, USA. Ethidium homodimer-1 in 2 mL pbs, propidium iodide, Ribonuclease A were also purchased from SigmaAldrich.

Synthesis of Compound 5

2,6-bis((3-iodophenyl)ethynyl)pyrazine **3** (0.050g, 0.093 mmol), 4-ethynyl-pyridine **4** (0.019 g, 0.187 mmol), CuI (0.017 g, 0.009 mmol) and bis(-triphenylphosphine)palladium(II) dichloride (6.52 mg, 0.009 mmol) were charged in a 50 ml Schlenk flask in the glove box. Subsequently, 10 ml dry THF and freshly distilled and degassed triethylamine (0.5 ml, 0.372 mmol) were added under nitrogen. The reaction mixture was stirred overnight at room temperature. After overnight stirring, the reaction mixture was filtered through a bed of celite. The filtrate obtained was evaporated to dryness on a rotary evaporator to obtain a crude product which was purified by column chromatography on neutral alumina by eluting with 35% ethyl acetate in hexane to isolate the desired product (**5**) as off white solid.

Yield: 0.037 g, 81%, mp 198–202°C; ^{1}H NMR (400 MHz, $CDCl_3$): δ 8.67 (s, 2H, Ar-H), 8.62–8.61 (dd, $J = 6$ Hz, 2H, Ar-H), 7.81–7.80 (m, 1H, Ar-H), 7.64–7.575 (m, 2H, Ar-H), 7.43–7.37 (m, 3H, Ar-H).$^{13}C\{^{1}H\}$ NMR ($CDCl_3$, 100 MHz): δ 149.8, 145.7, 139.5, 135.3, 132.9, 132.7, 130.9, 128.9, 125.5, 122.8, 121.9, 92.4, 92.3, 87.6, 86.1. IR (ATR): 3,048, 2,918, 2,849, 2,210, 1,687, 1,585, 1,503, 1,404, 1,279, 1,203, 1,154, 987, 887, 796, 671 cm^{-1}. Anal. Calcd. For $C_{34}H_{18}N_4$: C, 84.63; H, 3.76; N, 11.61. Found: C, 84.72; H, 3.84; N, 11.68.HRMS (ESI, *m/z*): Calculated for $C_{34}H_{18}N_4$ ($[M + H]^+$): 483.16; Found: 483.16.

Synthesis of Macrocycle 7

To the solution of **6** (30 mg, 0.020 mmol) in chloroform (4 mL) was added two equivalents of $AgNO_3$ (7.06 mg, 0.040 mmol) in one portion, and the reaction mixture was stirred overnight in the absence of light at room temperature. The precipitated AgI was filtered off over a bed of Celite, and the filtrate was collected as a yellow colored solution. Subsequently, a methanolic solution of the donor tecton **5** (0.02 mmol, 0.5 mL) was added drop wise to the aforementioned filtrate with continuous stirring. The reaction mixture was stirred for 15 h at room temperature. Solvents were removed by rotary evaporator and the product

obtained which was washed several times with *n*-pentane to obtain a solid that was finally dried in a vacuum. The macrocycle **7** was recrystallized as an off white microcrystalline solid by slow vapor diffusion of diethyl ether in its corresponding concentrated chloroform-methanol solution.

Macrocycle 7

Yield: 34 mg, 92%; ^{1}H NMR (400 MHz, $CDCl_3$): δ 8.89–8.87 (dd, J = 8 Hz, 4H, Ar-H), 8.68 (s, 2H, Ar-H), 8.67 (s, 2H, Ar-H), 8.00–7.99 (m, 4H, Ar-H), 7.89–7.87 (dd, J = 8 Hz, 4H, Ar-H), 7.68–7.64 (m, 4H, Ar-H), 7.47–7.45 (m, 4H, Ar-H), 7.33–7.32 (m, 4H, Ar-H), 1.86–1.83 (m, 8H, -CH_2-), 1.26–1.20 (m, 12H, -CH_3). ^{31}P NMR (162 MHz, $CDCl_3$): δ 15.70 ($^{1}J_{PPt}$ = 1,162 Hz). FTIR (ATR): 2,972, 2,922, 2,216, 2,116, 1,710, 1,602, 1,511, 1,469, 1,329, 1,145, 1,034, 888, 762, 683 cm^{-1}. Anal. Calcd. for $C_{82}H_{88}N_8O_6P_4Pt_2$: C, 54.85; H, 4.94; N, 6.24. Found: C, 54.93; H, 4.98; N, 6.28. ESI-MS *m/z* found: $[7-2NO_3]^{2+}$ = 835.76.

Preparation of Stock Solutions

Organometallic complex **6** and self-assembled macrocycle **7** were solubilized into cell culture grade dimethyl sulfoxide to make 10 mM stock solution. However, cisplatin was solubilized into saline (0.9% sodium chloride) to make 1 mM stock solution. Aliquots of the stock solutions were taken and preserved in −20°C till further use.

In Vitro Cytotoxicity

The cytotoxicity of all the compounds (**6, 7** and cisplatin) was assessed using MTT assay against A549, KB, and HaCaT cell lines. First, **6** and **7** were solubilized in DMSO to prepare stock solutions (concentration 10 mM). Subsequently, stock solutions were diluted 1,000 times in cell culture media for the treatment. The compounds were then tested at varying concentration range starts from 2.5 to 30 μM. For the assay, all the cells were trypsinized and counted using hemocytometer. Approximately 5×10^3 cells were seeded into each well of a 96 well plate and allowed to adhere for 24 h. Post adherence the cells were treated with pre-determined concentration (2.5, 5, 10, 15, 20, 25, and 30 μM) of all the compounds and incubated for 48 h. The media was then decanted, and cells were washed with phosphate buffer saline (PBS), pH 7.4. 100 μl of 10% MTT (5mg/ml stock) prepared in FBS free media was then added to each well and incubated at 37°C for 4 h. The formed formazan crystals were solubilized in DMSO and absorbance was taken at 570 nm using the Multiplate reader (Tecan Infinite Pro, Switzerland). The percentage viability was calculated by normalizing the absorbance value of test sample with anuntreated control, and the seven-point dose-dependent curve was plotted to determine the IC_{50} (IC_{50} value is the concentration of compound at which 50% of cells are viable) value of each compound.

Live/Dead Assay

The viability of cells was visualized under a fluorescence microscope using live/dead solution. The cells were seeded in a 96 well plate as mentioned earlier. Post adherence cells were treated for 48 h with **6**-**7** at 25 μM concentrations and cisplatin at 10 μM concentration. The media was decanted and after PBS (Phosphate-buffered saline) wash, cells were incubated with 100 μl working live/dead solution (1 μL of 4 mM Calcein AM and 4 μL of 2 mM ethidium homodimer-1 in 2 mL PBS) for 10 min at 37°C. The live cells fluoresce green (Excitation: 495 nm, Emission: 516 nm) due to Calcein-AM uptake however dead cells fluoresce red (Excitation: 528 nm, Emission: 617 nm) due to Ethidium homodimer-1 uptake.

RESULTS AND DISCUSSION

Synthesis and Characterization of the Organic Donor Clip (5)

Commercially available 2,6-dichloropyrazine is the synthetic precursor for both donor and acceptor tectons employed herein for the self-assembly reaction. In the first step, 2,6-diiodopyrazine (**1**) was obtained from 2,6-dichloropyrazine, which was further reacted in two steps to yield 2,6-bis((3-iodophenyl)ethynyl)pyrazine (**3**) via the formation of 2,6-diethynylpyrazine (**2**) (**Scheme 1**) (Bhowmick et al., 2017).

In the final step, **3** was further reacted with 4-ethynyl pyridine (**4**) to yield the desired organic donor clip (**5**) as depicted in **Scheme 2**. 2,6-bis((4-ethynylpyridyl)ethynyl)pyrazine) (**5**) was obtained as a white colored compound (81% isolated yield). **5** is stable in air/moisture and has high solubility in common organic solvents. **5** was fully characterized by FT-IR and NMR spectroscopy, mass spectrometry and elemental analyses.

In the ^{1}H NMR of **5** (Figure S1), signal appearing at δ = 8.62 ppm and δ = 7.64 ppm corresponds to the α and β pyridyl protons respectively. As expected, signals corresponding to these protons appear as doublets. All characteristic peaks corresponding to pyrazine, phenyl and pyridyl units of **5** were observed in ^{13}C {^{1}H} NMR spectrum (Figure S2).

Application of 5 as a Donor Tecton toward Self-Assembly of a Supramolecular Hexagon

Coordination driven self-assembly reactions have been employed for the construction of complex yet discrete metallomacrocycles. Among various shapes reported in the literature, hexagonal macrocycles are especially fascinating because of nature's preference for hexagon motif (honeycomb, graphite, snowflakes, etc.) (Pucci et al., 2000). Consequently, there is interest in mimicking nature in laboratory in the context of design and synthesis of macrocycles with hexagonal cavity. The most commonly reported methodologies involve self-organization of 12 (twelve) or 6 (six) tectons, thereby generating hexagonal assemblies that are referred to as [6 + 6] or [3 + 3] hexagonal metallacycles respectively (Cook and Stang, 2015). These syntheses are challenging as they require self-assembly of a large number of molecular components in a reaction that is entropically unfavorable. More recently, we have reported design and synthesis of hexagonal polygons requiring self-assembly of two donor and two acceptor tectons thereby yielding [2 + 2] hexagons. In this report, we have chosen donor and acceptor in such a manner that construction of a hexagonal macrocycle requires only one donor and one acceptor

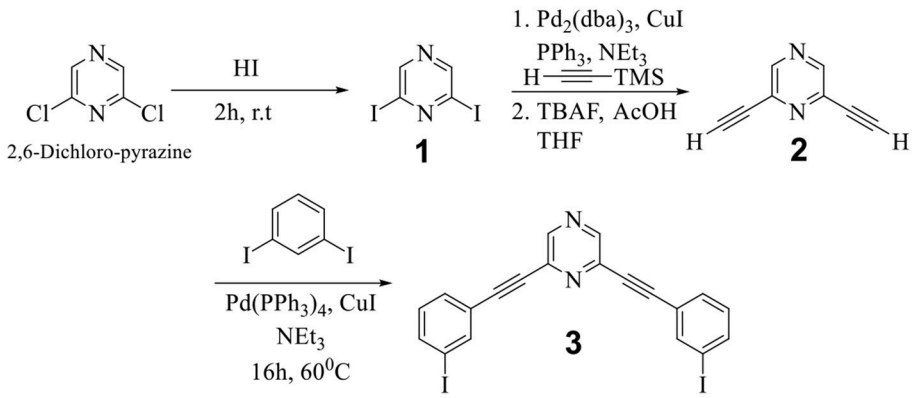

SCHEME 1 | Synthesis of 2,6-bis((3-iodophenyl)ethynyl)pyrazine (**3**).

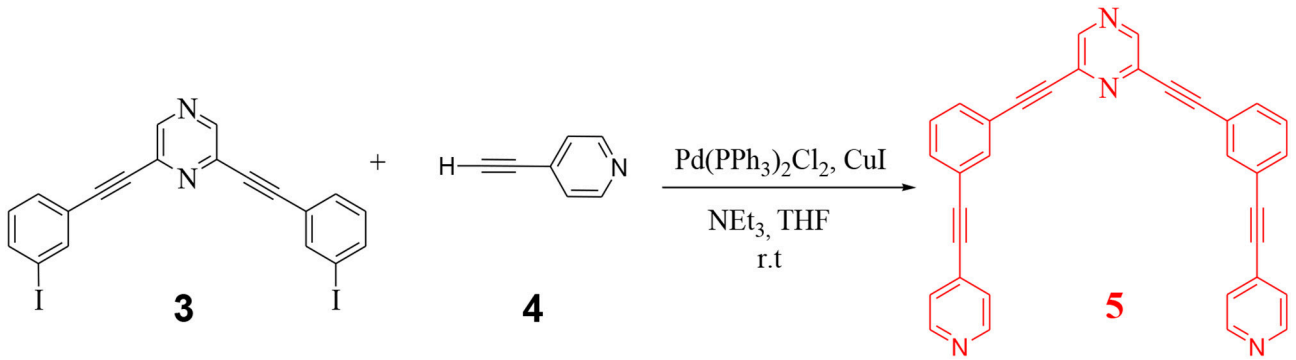

SCHEME 2 | Synthesis of organic donor clip (**5**).

tecton. Thus the anticipated framework will be a unique [1 + 1] hexagonal macrocycle requiring the least number of self-assembling molecular tectons for its construction.

In order to perform the above mentioned self-assembly reaction, first the acceptor tecton (**6**) was reacted with two equivalents of $AgNO_3$ in $CHCl_3$ to yield the corresponding dinitrate derivative which was further reacted with the donor tecton (**5**) (methanol solution) in 1:1 stiochiometric ratio at room temperature (**Scheme 3**). A solid product was obtained by evaporating the solvents. Subsequent washing (with n-pentane) and recrystallization yielded the desired product (**7**) as an off-white microcrystalline solid (yield > 90%) that was soluble in organic solvents.

The self-assembled product (**7**) was subjected to various characterization techniques to confirm its purity and composition. In $^{31}P\{^1H\}$ NMR spectrum (**Figure 1A**) a sharp singlet (δ = 15.70 ppm), accompanied with a pair of ^{195}Pt satellite peaks ($^1J_{PPt}$ = 1,162 Hz), indicated that **7** has a highly symmetrical structure, wherein all phosphorous nuclei are chemically equivalent. The ^1H NMR spectrum of **7** also suggested incorporation of both tectons (**5** and **6**) in it (**Figure 1B** and Figures S3, S4). In ^1H NMR spectrum of **7** (**Figure 1B**), two peaks appearing at 8.67 and 8.68 ppm were assigned to the protons of pyrazine moieties of donor (**5**) and acceptor clip (**6**) respectively. Four sets of signals at 8.00–7.99, 7.68–7.64, 7.49–7.45, 7.33–7.32 ppm are due to protons in phenyl ring. Two sets of signals at 8.89–8.87, 7.89–7.87 ppm are due to protons of the pyridyl ring. The ethyl protons of PEt_3 groups (attached to Pt^{II} center) are observed in the range 1.86–1.20 ppm spectrum (Figure S3).

The formation of **7** via coordination of **5** (donor tecton) with **6** (acceptor tecton) was also evident from the observed downfield shift ($\Delta\delta \sim 0.25$ ppm) of both α and β pyridyl protons present in the terminal pyridine moieties (Figure S5). This has been attributed to the decrease in electron density in pyridine rings of the donor (**5**) due to their coordination (via lone pair on nitrogen) with Pt^{II} metal centers of the acceptor tecton (**6**).

Furthermore, the purity of product **7** was confirmed by ^1H DOSY NMR spectroscopy (Figure S6), wherein a single trace spectrum indicated the formation of a single product. This result also confirms absence of other macrocyclic species or oligomers as byproduct and exclusive formation of discrete macrocyclic species. Thus NMR analyses confirm purity of the **7** and indicated formation of single, highly symmetrical species. Sharp peaks in ^1H and ^{31}P NMR are also clear indications of presence of discrete species and absence of any oligomers. Mass spectrometry was subsequently used to confirm the proposed composition of **7**. The

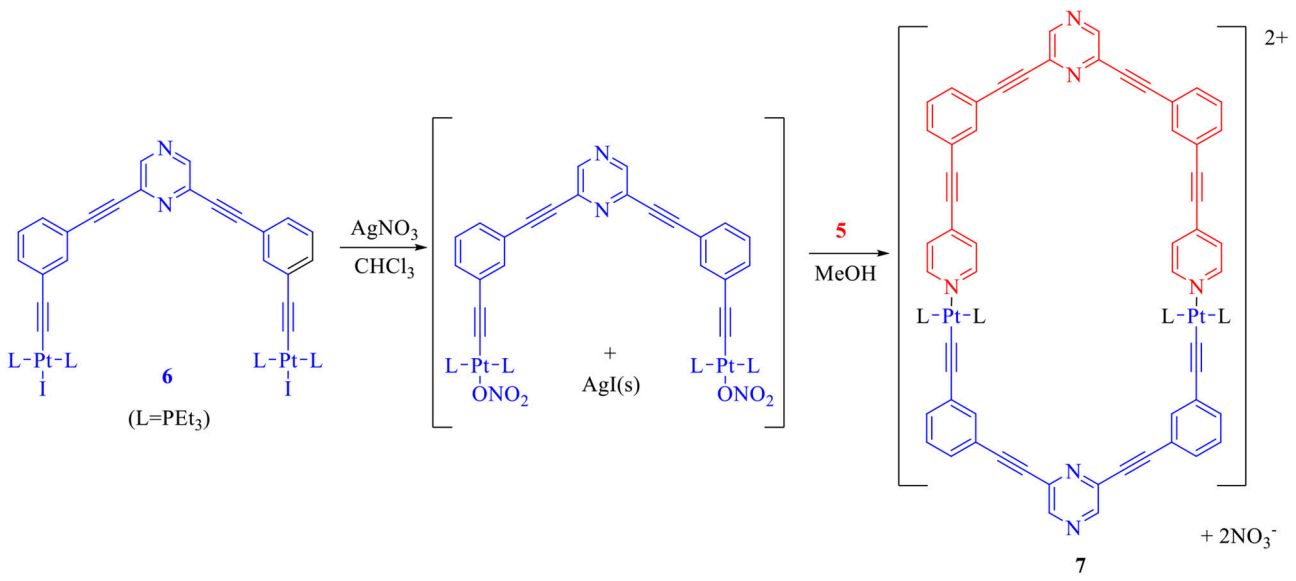

SCHEME 3 | Design and self-assembly of a hexagonal macrocycle (**7**) by employing only two molecular tectons.

ESI-TOF-MS spectrum of **7** indicated formation of desired [1 + 1] molecular ensembles (**Figure 2**). The ESI-TOF-MS spectrum of **7** showed a signal corresponding to the consecutive loss of two nitrate counter anions from the expected [1 + 1] macrocycle at m/z = 835.76 $[\mathbf{7}\text{-}2NO_3]^{2+}$. The isotopic resolution of this peak was in excellent agreement with the theoretically predicted isotopic distribution pattern of $[\mathbf{7}\text{-}2NO_3]^{2+}$ (**Figures 2A,B** and Figure S8). Thus mass spectrometric analysis of **7** confirmed the formation of a discrete [1 + 1] self-assembled macrocycle.

All attempts to grow X-ray quality single crystals of **7** were unsuccessful. In such a scenario, molecular modeling (using PM6 semiempirical MO method) (Stewart, 2007) was employed to obtain useful structural information for **7**. The energy minimized structure of **7** (**Figure 3** and Figure S7) confirms the formation of a macrocycle with hexagonal cavity. The distance between the two exocyclic nitrogen atoms of pyrazine rings was 2.53 nm. The distance between the two platinum centers was found to be 1.30 nm. The lengths of sides of hexagon were found to be 1.62 and 0.68 nm. Thus **7** may be described as an irregular hexagon since all the sides are not of equal length even though the polygonal framework is equiangular. A slight distortion from the square geometry was observed at the two Pt(II) centers.

Cytotoxicity (*in Vitro*) Assessment and Estimation of IC_{50}

Till date, platinum based molecules have been used most frequently as anticancer therapeutic agents. Cisplatin is undoubtedly the most popular anticancer drug bearing Pt(II). In the first step of its mechanism of action (as anticancer drug), the chlorides of cisplatin are substituted/exchanged by hydroxide ions or water. The resulting diaquo species subsequently bind with nucleophilic sites present in RNA or DNA. Thus cytotoxicity of cisplatin stems from the fact that Pt-Cl bonds are unstable under physiological conditions relative to the new Pt-N bonds that are formed due to adduct formation with nucleobases. Also it is known that Pt-N bonds are essentially irreversible under the same physiological conditions (Farrell, 1999). Moreover, in the context of platinum based complexes as anticancer drugs, it is well known that cisplatin is quite potent while transplatin is inactive. This is a consequence of the difference in the stereospecificity of the labile Pt-Cl bonds in these two isomers. **6** and **7** are quite different from cisplatin in this aspect as these species don't have two labile (halide/hydroxo) groups in cis orientation to facilitate adduct (bifunctional) formation with DNA (as observed with cisplatin). It was therefore our curiosity to study the cytotoxicity of Pt(II) based compounds (**6** and **7**) reported herein that don't posses two cis-oriented labile groups unlike cisplatin.

The cytotoxicity of platinum containing **6** and **7** were examined against three cell lines KB (human oral cancer), A549 (human lung cancer) and HaCaT (human skin keratinocyte) using MTT assay. Cisplatin was used as a positive control (Wang and Lippard, 2005). Toxicity of all the compounds was observed to be dose and cell dependent. The IC_{50} value is the inhibitory concentration of a compound at which 50% cells are dead. A seven-point dose-dependent plot (**Figure 4**) was recorded for each compound against each cell line for measurement of IC_{50} concentration. **7** exhibited higher toxicity (relatively lesser IC_{50} value) relative to **6** against A549 and KB cancer cells. However, for HaCaT cells, both **6** and **7** exhibited comparable IC_{50} value (**Table 1**).

From the IC_{50} values listed in **Table 1**, it is clear that compounds **6** and **7** have lesser toxicty relatively to cisplatin. This was anticipated considering the absence of two cis-oriented labile groups in **6** and **7**. In other words, the general higher activity of cisplatin over other **6** and **7** is due to the presence of cis-oriented more labile Pt-Cl bonds in cisplatin that tend to hydrolyze

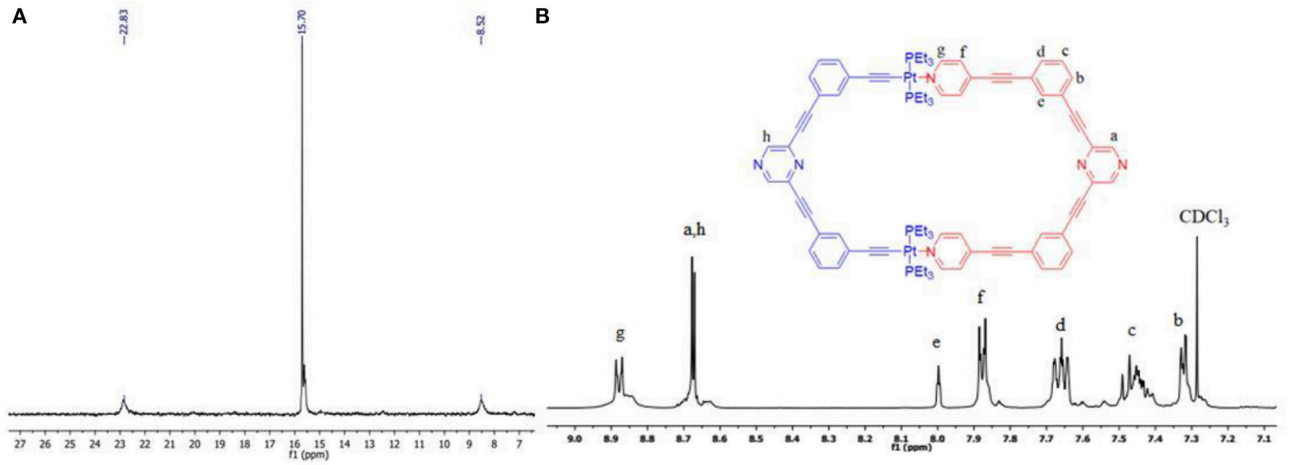

FIGURE 1 | (A) $^{31}P\{^{1}H\}$ and **(B)** ^{1}H NMR (partial) spectra of **7**. Lower case letters represent signals/peaks in proton NMR corresponding to different protons.

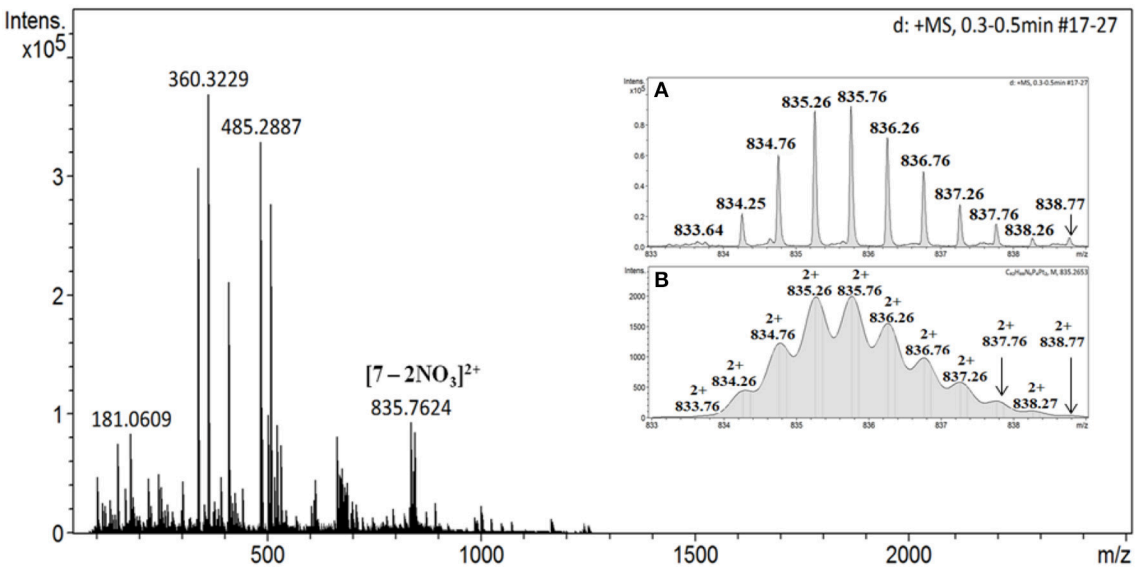

FIGURE 2 | ESI-MS data of the macrocycle **7**; inset **(A)** experimental spectrum and **(B)** theoretical isotopic distribution pattern of the fragment $[\mathbf{7}\text{-}2NO_3]^{2+}$.

easily under physiological conditions to facilitate binding with DNA/RNA. On the other hand, the Pt^{II}-based compounds in this report (**6** and **7**) have Pt-N bonds that tend to be relatively stable under such conditions.

It is however noteworthy that though **6** and **7** don't have labile groups in cis orientation to facilitate adduct (bifunctional) formation with DNA, these species show reasonable cytotoxic effect (**Table 1**). More interestingly, the macrocycle (**7**) exhibited superior cytotoxic effect when compared with cisplatin for A549 (human liver cancer) cells. Additionally, it was observed that upon self-assembly and formation of the macrocycle **7**, the resulting supramolecular framwork exhibited lower IC_{50} value relative to that observed for the acceptor tecton (**6**) in case of A549 and KB carcinoma cell. For, HaCaT cell, the IC_{50} values are comparable for both **6** and **7**. Considering the literature reported stability of Pt-N bonds under physiological conditions (Farrell, 1999), it may be assumed that macrocycle **7** remains intact under these conditions.

Subsequently, the effect of Pt-based compounds (**6** and **7**) on cell viability and attachment was studied and results compared with cisplatin. Cancer cells (KB, A549, and HaCaT) were treated with compounds (**6**, **7** and cisplatin) and these were stained with fluorescent dyes (Calcein AM and Ethidium homodimer-1). In these fluorescent imaging studies, cancer cells were treated with 25 μM **6**-**7** and 10 μM cisplatin for 48 h. Post-treatment, cells were stained with a live/dead stainsolution. Fluorescent images are shown in **Figure 5**, wherein live cells (green color) were firmly attached to tissue culture plate (TCP) surface relative to dead cells

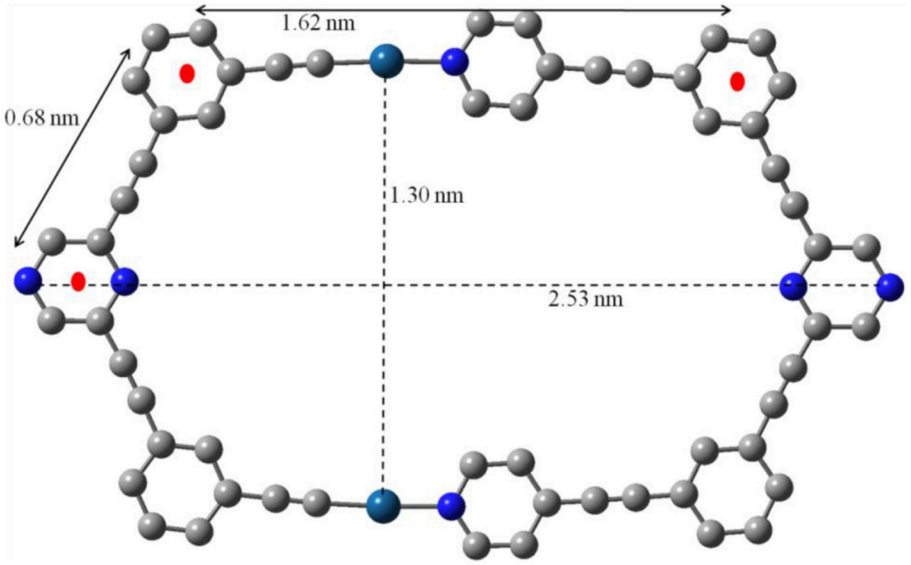

FIGURE 3 | Simulated ball and stick molecular model optimized by PM6 semiempirical molecular orbital methods of macrocycle **7** (Color code: light gray, C; dark cyan, Pt; blue, N. PEt_3 and Hare omitted for clarity).

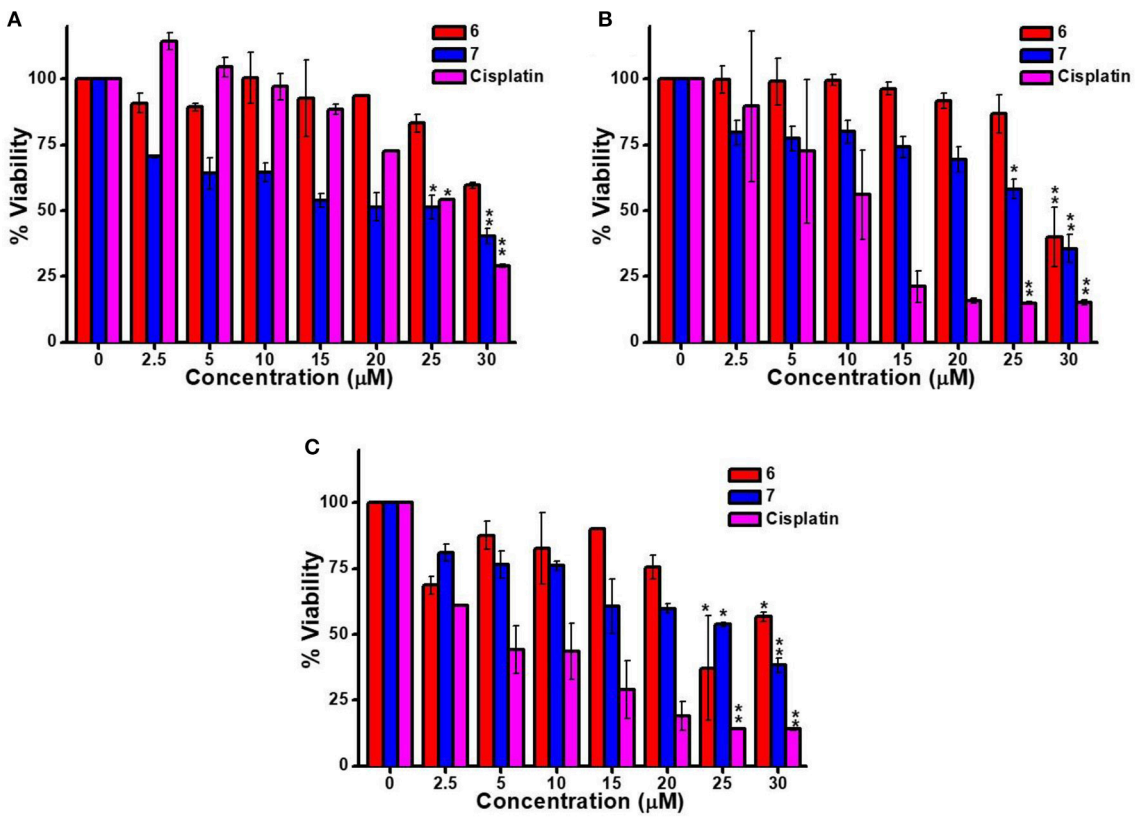

FIGURE 4 | *In vitro* cytotoxicity of **6**, **7** and cisplatin with predetermined dose range against **(A)** A549 **(B)** KB, and **(C)** HaCaT cell lines for 48 h using MTT assay. Data points represent mean ± SD for three independent experiments. $^{*}p < 0.05$ and $^{**}p < 0.01$ represent a significant decrease in the viability of cells at 25 μM compounds treated group compared to the untreated group.

(red color). Variable dead cell population was observed in each case due to either their loose attachment to TCP or difference in their respective IC_{50}. These results suggest that **6** and **7** indeed demonstrate cancer cell growth inhibition to an extent that is comparable cisplatin (a widely used Pt-drug for treatment on various forms of cancer).

CONCLUSION

In conclusion, we have reported a new donor tecton (**5**) with two pendant pyridine rings that is derived from commercially available 2,6-dichloropyrazine. **5** is a new ditopic donor tecton with 0° angular orientation of the two pyridine rings. Self-assembly reaction of **5** with a complementary ditopic acceptor tecton (**6**) resulted in the formation of a single product (**7**). NMR and elemental analyses confirmed its purity while mass spectrometry (ESI-MS) data supported the formation of a [1 + 1] supramolecular species. PM6 molecular modeling suggested formation of a macrocycle with hexagonal cavity. The product (**7**) is a unique example in literature wherein a nanoscalar, discrete and cationic hexagonal framework has been synthesized using only two tectons—one unit of donor and one unit of acceptor. Previous report of all Pt(II)-based hexagonal macrocycles utilized four, six or twelve tectons resulting in highly charged species. Furthermore the Pt^{II}-based species (**6** and **7**) were subjected to cytotoxicity studies using three different cancer cell lines, and the results were compared with cisplatin. Although **6** and **7** are less potent than cisplatin, it was observed that formation of the metallamacrocycle (**7**) improved cytotoxicity in case of treatment with A549 and KB cancer cells. This is in spite of the fact that acceptor tecton (**6**) contains labile Pt-I bonds while macrocycle **7** contains platinum bonds to nitrogen that are essentially irreversible under physiological conditions (Farrell, 1999). Interestingly, the supramolecular ensemble (**7**) showed better A549 cell growth inhibitory effect than cisplatin. The cytotoxic behavior of **6** and **7** may be attributed to their non-covalent interaction with DNA. These results will form the basis of further research on the mechanism of cell-killing action of these Pt-based species which are stereo-chemically quite different from cisplatin. Nevertheless this report is a unique example, wherein a supramolecular hexagonal framework with only two Pt(II) centers has been self-assembled and it potential application in anticancer therapy has studied. Development of similar Pt(II)-based self-assembled structures as therapeutic agents for malignant cells is currently being explored in our laboratory.

TABLE 1 | IC_{50} concentration (μM) after 48 h treatment against different cell lines.

	IC_{50}/μM		
	A549 cells	**KB cells**	**HaCaT cells**
Cisplatin	25.0 ± 2.0	11.0 ± 0.3	6.0 ± 3.0
6	>30.0	>30.0	23.0 ± 4.0
7	20.0 ± 0.4	26.0 ± 0.4	26.0 ± 0.2

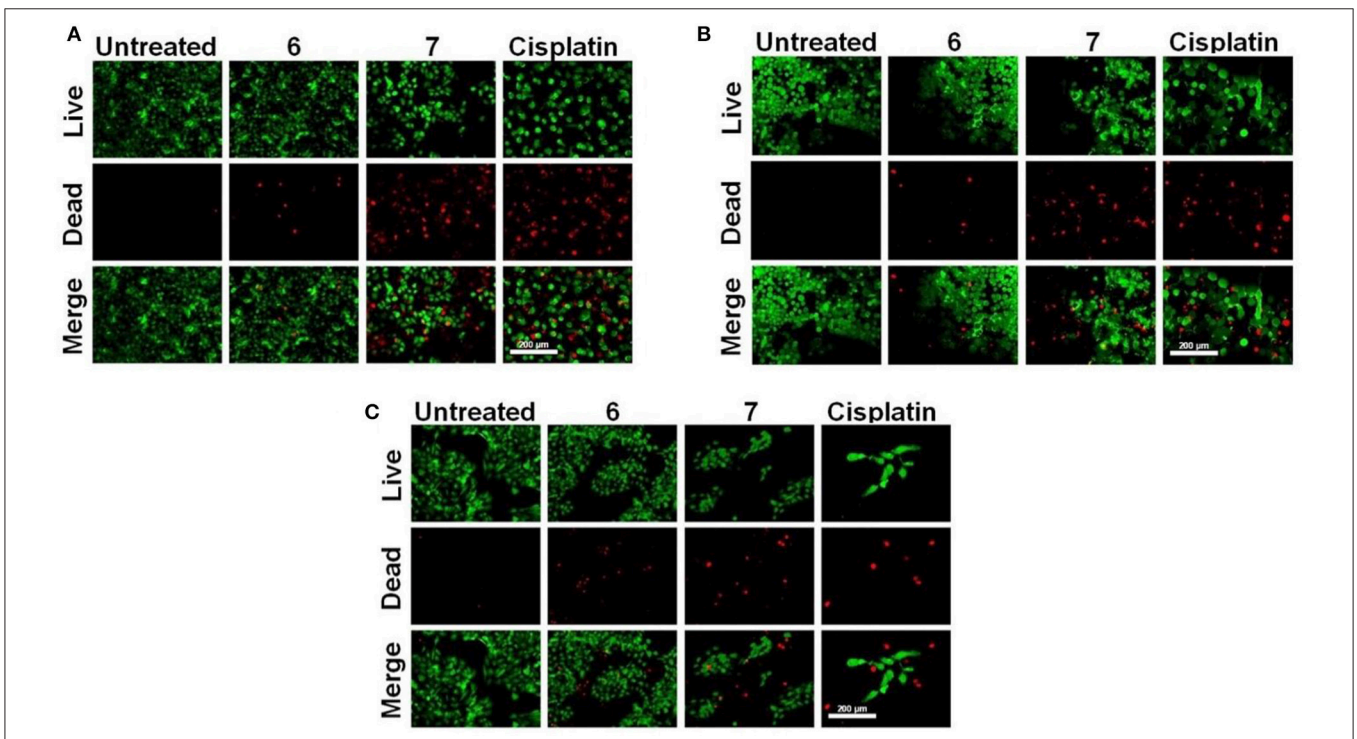

FIGURE 5 | Live/dead cell staining. **(A)** A549, **(B)** KB, and **(C)** HaCaT cells were treated with 25 μM **6**, **7** and 10 μM cisplatin for 48 h. Post-treatment cells were stained with alive/dead stain solution, and the images were captured with a fluorescence microscope (scale bar – 200 μm).

AUTHOR CONTRIBUTIONS

ND conceived the research and supervised the experimental work related to synthesis and characterization of organic/organometallic molecules reported herein. KS synthesized all new compounds reported in this manuscript. AJ optimized the energy-minimized geometry of the metallacycles **7**. SB assisted in the synthesis of some of the literature reported pyrazine precursors. AG carried out the experiments related to evaluation of biological activity of **6, 7** and cisplatin reported herein and these biological studies were supervised by BM. All authors have contributed to interpretation of results, compiled the manuscript and have approved the final manuscript.

ACKNOWLEDGMENTS

ND thanks the Indian Institute of Technology (IIT) Patna for financial support. KS and AJ thank UGC, New Delhi, India, for a Research Fellowship. SB thanks IIT Patna for an Institute Research Fellowship. The authors also acknowledge SAIF-Panjab University and SAIF-IIT Patna for analytical facilities. BM gratefully acknowledges funding support through the Department of Biotechnology and Department of Science and Technology, Government of India.

SUPPLEMENTARY MATERIAL

The Supplementary Material for this article can be found online at: https://www.frontiersin.org/articles/10.3389/fchem.2018.00087/full#supplementary-material

^{1}H and $^{13}C\{^{1}H\}$ NMR spectra of **5**, ^{1}H, $^{31}P\{^{1}H\}$ and ^{1}H DOSY NMR spectra of the metallamacrocycle (**7**), comparison ^{1}H NMR spectra of donor ligand **5** and macrocycle **7** and **s**pace-filled model of macrocycle **7** optimized by PM6 semiempirical molecular orbital method.

REFERENCES

Ajibola, A., Shettar, A., Bhat, I. A., Kondaiah, P., and Mukherjee, P. S. (2017). Self-assembly of discrete RuII8 molecular cages and their *in vitro* anticancer activity. *Inorg. Chem.* 56, 608–617. doi: 10.1021/acs.inorgchem.6b02488

Albertí, F. M., Zielinski, W., Morell Cerdà, M., Sanz Miguel, P. J., Troeppner, O., Ivanović-Burmazović, I., et al. (2013). Stepwise coordination of PtII-180° and PdII-90° metal fragments to the purine nucleobase 9-Methylhypoxanthine affords a closed octadecanuclear Pt6Pd12 cluster. *Chemistry* 19, 9800–9806. doi: 10.1002/chem.201300446

Balzani, V., Credi, A., and Venturi, M. (2002). Controlled disassembling of self-assembling systems: toward artificial molecular-level devices and machines. *Proc. Natl. Acad. Sci. U.S.A.* 99, 4814–4817. doi: 10.1073/pnas.022631599

Barbara, P. F. (2001). Molecular machines special issue. *Acc. Chem. Res.* 34:409. doi: 10.1021/ar0100881

Barry, N. P. E., and Sadler, P. J. (2013). Exploration of the medical periodic table: towards new targets. *Chem. Commun.* 49, 5106–5131. doi: 10.1039/c3cc41143e

Berners-Price, S. J., and Filipovska, A. (2011). Gold compounds as therapeutic agents for human diseases. *Metallomics* 3, 863–873. doi: 10.1039/c1mt00062d

Beuerle, F. (2016). Supramolecular chemistry: unexplored territory for self-assembly. *Nature* 540, 529–531. doi: 10.1038/540529a

Bhowmick, S., Chakraborty, S., Das, A., Nallapeta, S., and Das, N. (2015a). Pyrazine motif containing hexagonal macrocycles: synthesis, characterization, and host–guest chemistry with nitro aromatics. *Inorg. Chem.* 54, 8994–9001. doi: 10.1021/acs.inorgchem.5b01156

Bhowmick, S., Chakraborty, S., Das, A., Rajamohanan, P. R., and Das, N. (2015b). Pyrazine-based organometallic complex: synthesis, characterization, and supramolecular chemistry. *Inorg. Chem.* 54, 2543–2550. doi: 10.1021/ic502581x

Bhowmick, S., Chakraborty, S., Marri, S. R., Behera, J. N., and Das, N. (2016). Pyrazine-based donor tectons: synthesis, self-assembly and characterization. *RSC Adv.* 6, 8992–9001. doi: 10.1039/C5RA21484J

Bhowmick, S., Jana, A., Singh, K., Gupta, P., Gangrade, A., Mandal, B. B., et al. (2017). Coordination-driven self-assembly of ionic irregular hexagonal metallamacrocycles via an organometallic clip and their cytotoxicity potency. *Inorg. Chem.* doi: 10.1021/acs.inorgchem.7b01561. [Epub ahead of print].

Chakrabarty, R., Mukherjee, P. S., and Stang, P. J. (2011). Supramolecular coordination: self-assembly of finite two- and three-dimensional ensembles. *Chem. Rev.* 111, 6810–6918. doi: 10.1021/cr200077m

Chakraborty, S., Bhowmick, S., Ma, J., Tan, H., and Das, N. (2015). Size dependent effect of new organometallic triptycene tectons on the dimensions of self-assembled macrocycles. *Inorg. Chem. Front.* 2, 290–297. doi: 10.1039/C4QI00211C

Chakraborty, S., Mondal, S., Li, Q., and Das, N. (2013). Synthesis and characterization of triptycene based tripods and design of a metallasupramolecular cage. *Tetrahedron Lett.* 54, 1681–1685. doi: 10.1016/j.tetlet.2013.01.065

Chen, L., Chen, Q., Wu, M., Jiang, F., and Hong, M. (2015). Controllable coordination-driven self-assembly: from discrete metallocages to infinite cage-based frameworks. *Acc. Chem. Res.* 48, 201–210. doi: 10.1021/ar5003076

Chen, L.-J., Zhao, G.-Z., Jiang, B., Sun, B., Wang, M., Xu, L., et al. (2014). Smart stimuli-responsive spherical nanostructures constructed from supramolecular metallodendrimers via hierarchical self-assembly. *J. Am. Chem. Soc.* 136, 5993–6001. doi: 10.1021/ja500152a

Cook, T. R., and Stang, P. J. (2015). Recent developments in the preparation and chemistry of metallacycles and metallacages via coordination. *Chem. Rev.* 115, 7001–7045. doi: 10.1021/cr5005666

Cook, T. R., Vajpayee, V., Lee, M. H., Stang, P. J., and Chi, K.-W. (2013a). Biomedical and biochemical applications of self-assembled metallacycles and metallacages. *Acc. Chem. Res.* 46, 2464–2474. doi: 10.1021/ar400010v

Cook, T. R., Zheng, Y. R., and Stang, P. J. (2013b). Metal–Organic frameworks and self-assembled supramolecular coordination complexes: comparing and contrasting the design, synthesis, and functionality of metal–organic materials. *Chem. Rev.* 113, 734–777. doi: 10.1021/cr3002824

Farrell, N. P. (1999). *Uses of Inorganic Chemistry in Medicine*. Cambridge, UK: The Royal Society of Chemistry.

Farrell, N. P. (2015). Multi-platinum anti-cancer agents. Substitution-inert compounds for tumor selectivity and new targets. *Chem. Soc. Rev.* 44, 8773–8785. doi: 10.1039/C5CS00201J

Fujita, D., Ueda, Y., Sato, S., Mizuno, N., Kumasaka, T., and Fujita, M. (2016). Self-assembly of tetravalent goldberg polyhedra from 144 small components. *Nature* 540, 563–566. doi: 10.1038/nature20771

Fujita, M., Tominaga, M., Hori, A., and Therrien, B. (2005). Coordination assemblies from a Pd(II)-Cornered square complex. *Acc. Chem. Res.* 38, 369–378. doi: 10.1021/ar040153h

Galstyan, A., Sanz Miguel, P. J., Weise, K., and Lippert, B. (2013). Discrete and polymeric heteronuclear constructs derived from triangular 2,2'-bipyrazine complexes of cis-a2PtII (with a = NH3 or a2 = en). *Dalton Trans.* 42, 16151–16161. doi: 10.1039/c3dt51589c

Han, M., Engelhard, D. M., and Clever, G. H. (2014). Self-assembled coordination cages based on banana-shaped ligands. *Chem. Soc. Rev.* 43, 1848–1860. doi: 10.1039/C3CS60473J

Harris, K., Fujita, D., and Fujita, M. (2013). Giant hollow MnL2n spherical complexes: structure, functionalisation and applications. *Chem. Commun.* 49, 6703–6712. doi: 10.1039/c3cc43191f

Holloway, L. R., Bogie, P. M., Lyon, Y., Julian, R. R., and Hooley, R. J. (2017). Stereoselective postassembly ch oxidation of self-assembled metal–ligand cage complexes. *Inorg. Chem.* 56, 11435–11442. doi: 10.1021/acs.inorgchem.7b01958

Holloway, L. R., McGarraugh, H. H., Young, M. C., Sontising, W., Beran, G. J. O., and Hooley, R. J. (2016). Structural switching in self-assembled metal-ligand helicate complexes via ligand-centered reactions. *Chem. Sci.* 7, 4423–4427. doi: 10.1039/C6SC01038E

Inokuma, Y., Kawano, M., and Fujita, M. (2011). Crystalline molecular flasks. *Nat. Chem.* 3, 349–358. doi: 10.1038/nchem.1031

Jana, A., Bhowmick, S., Kaur, S., Kashyap, H. K., and Das, N. (2017). Design of a flexible organometallic tecton: host-guest chemistry with picric acid and self-assembly of platinum macrocycles. *Dalton Trans.* 46, 1986–1995. doi: 10.1039/C6DT03498E

Jana, A., and Das, N. (2017). Self-Assembly of [2+2] Platina macrocycles using a flexible organometallic clip. *Chem. Select.* 2, 4099–4105. doi: 10.1002/slct.201700479

Jo, J.-H., Singh, N., Kim, D., Cho, S. M., Mishra, A., Kim, H., et al. (2017). Coordination-Driven self-assembly using ditopic pyridyl–pyrazolyl donor and p-cymene ru(ii) acceptors: [2]catenane synthesis and anticancer activities. *Inorg. Chem.* 56, 8430–8438. doi: 10.1021/acs.inorgchem.7b01101

Johnson, A. M., Wiley, C. A., Young, M. C., Zhang, X., Lyon, Y., Julian, R. R., et al. (2015). Narcissistic self-sorting in self-assembled cages of rare earth metals and rigid ligands. *Angew. Chem. Int. Ed.* 54, 5641–5645. doi: 10.1002/anie.201500400

Jung, Y., and Lippard, S. J. (2007). Direct cellular responses to Platinum-Induced DNA damage. *Chem. Rev.* 107, 1387–1407. doi: 10.1021/cr068207j

Kaluderovic, G. N., and Paschke, R. (2011). Anticancer metallotherapeutics in preclinical development. *Curr. Med. Chem.* 18, 4738–4752. doi: 10.2174/092986711797535308

Kelland, L. (2007). The resurgence of platinum-based cancer chemotherapy. *Nat. Rev. Cancer* 7, 573–584. doi: 10.1038/nrc2167

Kishi, N., Akita, M., Kamiya, M., Hayashi, S., Hsu, H. F., and Yoshizawa, M. (2013). Facile catch and release of fullerenes using a photoresponsive molecular tube. *J. Am. Chem. Soc.* 135, 12976–12979. doi: 10.1021/ja406893y

Lehn, J. M. (1995). *Supramolecular Chemistry: Concepts and Perspectives*. Weinheim: Wiley-VCH.

Li, S., Huang, J., Cook, T. R., Pollock, J. B., Kim, H., Chi, K.-W., et al. (2013). Formation of [3]catenanes from 10 precursors via multicomponent coordination-driven self-assembly of metallarectangles. *J. Am. Chem. Soc.* 135, 2084–2087. doi: 10.1021/ja3118812

Li, Y., Jiang, Z., Yuan, J., Liu, D., Wu, T., Moorefield, C. N., et al. (2015). Facile thermodynamic conversion of a linear metallopolymer into a self-assembled hexameric metallomacrocycle. *Chem. Commun.* 51, 5766–5769. doi: 10.1039/C4CC10361K

Liu, D., Lu, K., Poon, C., and Lin, W. (2014). Metal–Organic frameworks as sensory materials and imaging agents. *Inorg. Chem.* 53, 1916–1924. doi: 10.1021/ic402194c

Liu, S., Han, Y. F., and Jin, G. X. (2007). Formation of direct metal-metal bonds from 16-electron "pseudo-aromatic" half-sandwich complexes Cp[double prime]M[E2C2(B10H10)]. *Chem. Soc. Rev.* 36, 1543–1560. doi: 10.1039/b701869j

Lo, W. K. C., Huff, G. S., Preston, D., McMorran, D. A., Giles, G. I., Gordon, K. C., et al. (2015). A dinuclear platinum(II) N4Py complex: an unexpected coordination mode for N4Py. *Inorg. Chem.* 54, 6671–6673. doi: 10.1021/acs.inorgchem.5b01032

Lu, K., He, C., and Lin, W. (2014). Nanoscale metal–organic framework for highly effective photodynamic therapy of resistant head and neck cancer. *J. Am. Chem. Soc.* 136, 16712–16715. doi: 10.1021/ja508679h

Manna, K., Zhang, T., Greene, F. X., and Lin, W. (2015). Bipyridine- and phenanthroline-based metal–organic frameworks for highly efficient and tandem catalytic organic transformations via directed C–H activation. *J. Am. Chem. Soc.* 137, 2665–2673. doi: 10.1021/ja512478y

Mattsson, J., Govindaswamy, P., Renfrew, A. K., Dyson, P. J., Štěpnička, P., Süss-Fink, G., and Therrien, B. (2009). Synthesis, molecular structure, and anticancer activity of cationic arene ruthenium metallarectangles. *Organometallics* 28, 4350–4357. doi: 10.1021/om900359j

Michito, Y., and Makoto, F. (2010). Development of unique chemical phenomena within nanometer-sized, self-assembled coordination hosts. *Bull. Chem. Soc. Jpn.* 83, 609–618. doi: 10.1246/bcsj.20100035

Mishra, A., and Gupta, R. (2014). Supramolecular architectures with pyridine-amide based ligands: discrete molecular assemblies and their applications. *Dalton Trans.* 43, 7668–7682. doi: 10.1039/C4DT00277F

Newkome, G. R., and Shreiner, C. (2010). Dendrimers derived from 1 → 3 branching motifs. *Chem. Rev.* 110, 6338–6442. doi: 10.1021/cr900341m

Oliveri, C. G., Ulmann, P. A., Wiester, M. J., and Mirkin, C. A. (2008). Heteroligated supramolecular coordination complexes formed via the halide-induced ligand rearrangement reaction. *Acc. Chem. Res.* 41, 1618–1629. doi: 10.1021/ar800025w

Ott, I. (2009). On the medicinal chemistry of gold complexes as anticancer drugs. *Coord. Chem. Rev.* 253, 1670–1681. doi: 10.1016/j.ccr.2009.02.019

Paul, L. E. H., Therrien, B., and Furrer, J. (2012). Investigation of the reactivity between a ruthenium hexacationic prism and biological ligands. *Inorg. Chem.* 51, 1057–1067. doi: 10.1021/ic2021935

Pluth, M. D., Bergman, R. G., and Raymond, K. N. (2009). Proton-mediated chemistry and catalysis in a self-assembled supramolecular host. *Acc. Chem. Res.* 42, 1650–1659. doi: 10.1021/ar900118t

Pucci, B., Kasten, M., and Giordano, A. (2000). Cell Cycle and Apoptosis. *Neoplasia* 2, 291–299. doi: 10.1038/sj.neo.7900101

Rosenberg, B., Vancamp, L., Trosko, J. E., and Mansour, V. H. (1969). Platinum compounds: a new class of potent antitumour agents. *Nature* 222, 385–386. doi: 10.1038/222385a0

Saha, M. L., Neogi, S., and Schmittel, M. (2014). Dynamic heteroleptic metal-phenanthroline complexes: from structure to function. *Dalton Trans.* 43, 3815–3834. doi: 10.1039/C3DT53570C

Samanta., D., and Mukherjee, P. S. (2014). Self-assembled multicomponent Pd6 aggregates showing low-humidity proton conduction. *Chem. Commun.* 50, 1595–1598. doi: 10.1039/c3cc47965j

Sarkar, R., Guo, K., Moorefield, C. N., Saunders, M. J., Wesdemiotis, C., and Newkome, G. R. (2014). One-step multicomponent self-assembly of a first-generation sierpinski triangle: from fractal design to chemical reality. *Angew. Chem. Int. Ed.* 53, 12182–12185. doi: 10.1002/anie.201407285

Sauvage, J. P. (2001). *Molecular Machines and Motors. Structure and Bonding*. Heidelberg: Springer-Verlag.

Schmidt, A., Casini, A., and Kühn, F. E. (2014). Self-assembled M_2L_4 coordination cages: synthesis and potential applications. *Coord. Chem. Rev.* 275, 19–36. doi: 10.1016/j.ccr.2014.03.037

Schoedel, A., and Zaworotko, M. J. (2014). [M3([small mu]3-O)(O2CR)6] and related trigonal prisms: versatile molecular building blocks for crystal engineering of metal-organic material platforms. *Chem. Sci.* 5, 1269–1282. doi: 10.1039/C4SC00171K

Stang, P. J., and Olenyuk, B. (1997). Self-Assembly, symmetry, and molecular architecture: coordination as the motif in the rational design of supramolecular metallacyclic polygons and polyhedra. *Acc. Chem. Res.* 30, 502–518. doi: 10.1021/ar9602011

Stewart, J. J. P. (2007). Optimization of parameters for semiempirical methods V: modification of NDDO approximations and application to 70 elements. *Mol. Model.* 13, 1173–1213. doi: 10.1007/s00894-007-0233-4

Takezawa, Y., and Shionoya, M. (2012). Metal-Mediated DNA base pairing: alternatives to hydrogen-bonded watson–crick base pairs. *Acc. Chem. Res.* 45, 2066–2076. doi: 10.1021/ar200313h

Tanaka, S., Tsurugi, H., and Mashima, K. (2014). Supramolecular assemblies of multi-nuclear transition metal complexes: synthesis and redox properties. *Coord. Chem. Rev.* 265, 38–51. doi: 10.1016/j.ccr.2014.01.012

Thanasekaran, P., Lee, C. C., and Lu, K. L. (2012). One-Step orthogonal-bonding approach to the self-assembly of neutral rhenium-based metallacycles: synthesis, structures, photophysics, and sensing applications. *Acc. Chem. Res.* 45, 1403–1418. doi: 10.1021/ar200243w

Therrien, B. (2013). Transporting and shielding photosensitisers by using water-soluble organometallic cages: a new strategy in drug delivery and photodynamic therapy. *Chem. Eur. J.* 19, 8378–8386. doi: 10.1002/chem.201301348

Therrien, B., Süss-Fink, G., Govindaswamy, P., Renfrew, A. K., and Dyson, P. J. (2008). The "Complex-in-a-Complex" Cations $[(acac)_2M\subset Ru_6(p\text{-}iPrC_6H_4Me)_6(tpt)_2(dhbq)_3]^{6+}$: A trojan horse for cancer cells. *Angew. Chem. Int. Ed. Engl.* 47, 3773–3776. doi: 10.1002/anie.200800186

Todd, R. C., and Lippard, S. J. (2009). Inhibition of transcription by platinum antitumor compounds. *Metallomics* 1, 280–291. doi: 10.1039/b907567d

Vajpayee, V., Lee, S., Kim, S. H., Kang, S. C., Cook, T. R., Kim, H., et al. (2013). Self-assembled metalla-rectangles bearing azodipyridyl ligands: synthesis, characterization and antitumor activity. *Dalton Trans.* 42, 466–475. doi: 10.1039/C2DT31014G

Vajpayee, V., Yang, Y. J., Kang, S. C., Kim, H., Kim, I. S., Wang, M., et al. (2011). Hexanuclear self-assembled arene-ruthenium nano-prismatic cages: potential anticancer agents. *Chem. Commun.* 47, 5184–5186. doi: 10.1039/c1cc10167f

Vickers, A. E. M., Rose, K., Fisher, R., Saulnier, M., Sahota, P., and Bentley, P. (2004). Kidney slices of human and rat to characterize cisplatin-induced injury on cellular pathways and morphology. *Toxicol. Pathol.* 32, 577–590. doi: 10.1080/01926230490508821

Wang, D., and Lippard, S. J. (2005). Cellular processing of platinum anticancer drugs. *Nat. Rev. Drug Discov.* 4, 307–320. doi: 10.1038/nrd1691

Wang, W., Sun, B., Wang, X. Q., Ren, Y. Y., Chen, L. J., Ma, J., et al. (2015). Discrete stimuli-responsive multirotaxanes with supramolecular cores constructed through a modular approach. *Chem. Eur. J.* 21, 6286–6294. doi: 10.1002/chem.201500286

Wang, W., Wang, Y. X., and Yang, H. B. (2016). Supramolecular transformations within discrete coordination-driven supramolecular architectures. *Chem. Soc. Rev.* 45, 2656–2693. doi: 10.1039/C5CS00301F

Wang, X., and Guo, Z. (2008). Towards the rational design of platinum (II) and gold (III) complexes as antitumour agents. *Dalton Trans.* 1521–1532. doi: 10.1039/B715903J

Ward, M. D., and Raithby, P. R. (2013). Functional behaviour from controlled self-assembly: challenges and prospects. *Chem. Soc. Rev.* 42, 1619–1636. doi: 10.1039/C2CS35123D

Wheate, N. J., Walker, S., Craig, G. E., and Oun, R. (2010). The status of platinum anticancer drugs in the clinic and in clinical trials. *Dalton Trans.* 39, 8113–8127. doi: 10.1039/c0dt00292e

Xu, L., Chen, L. J., and Yang, H. B. (2014). Recent progress in the construction of cavity-cored supramolecular metallodendrimers via coordination-driven self-assembly. *Chem. Commun.* 50, 5156–5170. doi: 10.1039/C3CC47484D

Xu, X. D., Yao, C. J., Chen, L. J., Yin, G. Q., Zhong, Y. W., and Yang, H. B. (2016). Facile construction of structurally defined porous membranes from supramolecular hexakistriphenylamine metallacycles through electropolymerization. *Chem. Eur. J.* 22, 5211–5218. doi: 10.1002/chem.201504480

Yan, H., Suss-Fink, G., Neels, A., and Stoeckli-Evans, H. (1997). Mono-, di- and tetra-nuclear p-cymeneruthenium complexes containing oxalato ligands. *Dalton Trans.* 4345–4350. doi: 10.1039/a704658h

Yao, X., Panichpisal, K., Kurtzman, N., and Nugent, K. (2007). Cisplatin nephrotoxicity: a review. *Am. J. Med. Sci.* 334, 115–124. doi: 10.1097/MAJ.0b013e31812dfe1e

Yoshizawa, M., Klosterman, J. K., and Fujita, M. (2009). Functional molecular flasks: new properties and reactions within discrete, self-assembled hosts. *Angew. Chem. Int. Ed. Engl.* 48, 3418–3438. doi: 10.1002/anie.200805340

Yoshizawa, M., and Klosterman, J. K. (2014). Molecular architectures of multi-anthracene assemblies. *Chem. Soc. Rev.* 43, 1885–1898. doi: 10.1039/C3CS60315F

Young, N. J., and Hay, B. P. (2013). Structural design principles for self-assembled coordination polygons and polyhedra. *Chem. Commun.* 49, 1354–1379. doi: 10.1039/C2CC37776D

Zhang, M., Saha, M. L., Wang, M., Zhou, Z., Song, B., Lu, C., et al. (2017). Multicomponent Platinum(II) cages with tunable emission and amino acid sensing. *J. Am. Chem. Soc.* 139, 5067–5074. doi: 10.1021/jacs.6b12536

Conflict of Interest Statement: The authors declare that the research was conducted in the absence of any commercial or financial relationships that could be construed as a potential conflict of interest.

frontiers in Chemistry

ORIGINAL RESEARCH
published: 30 November 2018
doi: 10.3389/fchem.2018.00595

Eukaryotic Cell Toxicity and HSA Binding of $[Ru(Me_4phen)(bb_7)]^{2+}$ and the Effect of Encapsulation in Cucurbit[10]uril

Biyun Sun[1], Ian F. Musgrave[2], Anthony I. Day[1], Kirsten Heimann[3,4], F. Richard Keene[5,6] and J. Grant Collins[1]**

[1] School of Physical, Environmental and Mathematical Sciences, University of New South Wales, Australian Defence Force Academy, Canberra, ACT, Australia, [2] Discipline of Pharmacology, Adelaide Medical School, University of Adelaide, Adelaide, SA, Australia, [3] College of Medicine and Public Health, Flinders University, Adelaide, SA, Australia, [4] College of Science and Engineering, James Cook University, Townsville, QLD, Australia, [5] Department of Chemistry, School of Physical Sciences, University of Adelaide, Adelaide, SA, Australia, [6] Australian Institute of Tropical Health and Medicine/Centre for Molecular Therapeutics, James Cook University, Townsville, QLD, Australia

OPEN ACCESS

Edited by:
James D. Crowley,
University of Otago, New Zealand

Reviewed by:
Julia Lorenzo,
Autonomous University of Barcelona, Spain
Amanda Eckermann,
Hope College, United States

***Correspondence:**
F. Richard Keene
richard.keene@adelaide.edu.au
J. Grant Collins
g.collins@adfa.edu.au

Specialty section:
This article was submitted to Supramolecular Chemistry, a section of the journal Frontiers in Chemistry

Received: 07 September 2018
Accepted: 14 November 2018
Published: 30 November 2018

Citation:
Sun B, Musgrave IF, Day AI, Heimann K, Keene FR and Collins JG (2018) Eukaryotic Cell Toxicity and HSA Binding of $[Ru(Me_4phen)(bb_7)]^{2+}$ and the Effect of Encapsulation in Cucurbit[10]uril. Front. Chem. 6:595. doi: 10.3389/fchem.2018.00595

The toxicity (IC_{50}) of a series of mononuclear ruthenium complexes containing bis[4(4′-methyl-2,2′-bipyridyl)]-1,*n*-alkane (bb_n) as a tetradentate ligand against three eukaryotic cell lines—BHK (baby hamster kidney), Caco-2 (heterogeneous human epithelial colorectal adenocarcinoma) and Hep-G2 (liver carcinoma)—have been determined. The results demonstrate that *cis*-α-$[Ru(Me_4phen)(bb_7)]^{2+}$ (designated as α-Me_4phen-bb_7, where Me_4phen = 3,4,7,8-tetramethyl-1,10-phenanthroline) showed little toxicity toward the three cell lines, and was considerably less toxic than *cis*-α-$[Ru(phen)(bb_{12})]^{2+}$ (α-phen-bb_{12}) and the dinuclear complex $[\{Ru(phen)_2\}_2\{\mu\text{-}bb_{12}\}]^{4+}$. Fluorescence spectroscopy was used to study the binding of the ruthenium complexes with human serum albumin (HSA). The binding of α-Me_4phen-bb_7 to the macrocyclic host molecule cucurbit[10]uril (Q[10]) was examined by NMR spectroscopy. Large upfield ^{1}H NMR chemical shift changes observed for the methylene protons in the bb_7 ligand upon addition of Q[10], coupled with the observation of several intermolecular ROEs in ROESY spectra, indicated that α-Me_4phen-bb_7 bound Q[10] with the bb_7 methylene carbons within the cavity and the metal center positioned outside one of the portals. Simple molecular modeling confirmed the feasibility of the binding model. An α-Me_4phen-bb_7-Q[10] binding constant of $9.9 \pm 0.2 \times 10^6$ M^{-1} was determined by luminescence spectroscopy. Q[10]-encapsulation decreased the toxicity of α-Me_4phen-bb_7 against the three eukaryotic cell lines and increased the binding affinity of the ruthenium complex for HSA. Confocal microscopy experiments indicated that the level of accumulation of α-Me_4phen-7 in BHK cells is not significantly affected by Q[10]-encapsulation. Taken together, the combined results suggest that α-Me_4phen-7 could be a good candidate as a new antimicrobial agent, and Q[10]-encapsulation could be a method to improve the pharmacokinetics of the ruthenium complex.

Keywords: ruthenium complexes, cytotoxicity, HSA binding, cucurbit[10]uril, supramolecular chemistry

INTRODUCTION

Due to the increasing resistance of bacteria, particularly Gram-negative species, to the range of drugs currently in clinical use there is significant interest in developing new antimicrobial agents (Boucher et al., 2009). While there is an on-going effort to produce new antimicrobial drugs based upon analogs of known scaffolds, e.g., β-lactam antibiotics (Boucher et al., 2009), there is an increasing focus on the use of metal-based compounds (Richards et al., 2009; Neelakantan et al., 2010; Ng et al., 2013; Pandrala et al., 2013). In particular, and reflecting a greater recognition of their therapeutic potential (Bergamo and Sava, 2007; Moucheron, 2009; Süss-Fink, 2010; Gill and Thomas, 2012; Li et al., 2018), has been the growing development of ruthenium complexes as potential antimicrobial agents (Li et al., 2015a; Southam et al., 2017; Mital and Ziora, 2018). Dwyer and co-workers demonstrated more than 60 years ago the activity of mononuclear polypyridylruthenium(II) complexes against both Gram-positive and Gram-negative bacteria (Dwyer et al., 1952, 1969). However, it has only been over the last 10 years that there has been renewed and widespread interest in examining the antimicrobial properties of a broad range of ruthenium complexes (Kumar et al., 2009, 2016; Bolhuis et al., 2011; Li et al., 2011, 2013a, 2014; Shobha Devi et al., 2013; Gorle et al., 2016).

Previous studies from our group have examined the antimicrobial properties of di-, tri- and tetra-nuclear polypyridylruthenium(II) complexes in which the metal centers are linked by the bis[4(4′-methyl-2,2′-bipyridyl)]-1,*n*-alkane ligand ("bb_n"; see **Figure 1**) (Li et al., 2011, 2016; Gorle et al., 2014). These oligonuclear ruthenium complexes showed excellent activity against Gram-positive bacteria, and maintained the activity against current drug-resistant strains such as methicillin-resistant *Staphylococcus aureus* (MRSA) and vancomycin-resistant *enterococci* (VRE) (Gorle et al., 2016). However, the oligonuclear complexes showed variable activity to Gram-negative strains, with a number of species being essentially resistant to the ruthenium complexes (Gorle et al., 2016).

As the toxicity to both bacterial and eukaryotic cells increased with the number of ruthenium centers in the oligonuclear complex (Li et al., 2012, 2015b), we sought to examine mononuclear complexes that contained the bb_n moiety as a tetradentate ligand—$[Ru(phen')(bb_n)]^{2+}$ complexes (where phen′ = 1,10-phenanthroline and a variety of its derivatives, see **Figure 2**) (Gorle et al., 2015; Sun et al., 2018). Although some of these mononuclear complexes—particularly *cis*-α-$[Ru(Me_4phen)(bb_7)]^{2+}$ (Me_4phen = 3,4,7,8-tetramethyl-1,10-phenanthroline), designated as α-Me_4phen-7; and *cis*-α-$[Ru(phen)(bb_{12})]^{2+}$, designated as α-phen-12—showed good and uniform activity against both Gram-positive and Gram-negative species, they were slightly less active than the oligonuclear complexes to most bacteria (Sun et al., 2018). However, while the toxicity toward eukaryotic cells has been established for the oligonuclear complexes (Li et al., 2015b), the corresponding data for the mononuclear complexes have yet to be reported.

Another important factor governing the clinical potential of a new compound is its ability to bind serum proteins (Kratochwil et al., 2002; Bohnert and Gan, 2013; Liu et al., 2014). Blood serum protein binding can affect the distribution and clearance of a drug in several ways: only the free (non-protein bound) drug can act as an antimicrobial agent; alternatively, non-protein bound small drugs are cleared more rapidly from the bloodstream. Again, while the binding of the oligonuclear complexes to human serum albumin (HSA)–the most abundant serum protein (0.6 mM in healthy humans)–has been determined for the oligonuclear complexes (Li et al., 2013b), it is yet to be reported for the mononuclear complexes.

In the present study, we have determined the toxicity of the mononuclear $[Ru(phen')(bb_n)]^{2+}$ complexes toward a panel of eukaryotic cells and examined their HSA binding ability. Furthermore, as encapsulation in cucurbit[*n*]urils {macrocyclic host compounds composed of *n* glycoluril monomeric units, Q[*n*]–see **Figure 3** (Lagona et al., 2005; Kim et al., 2007; Isaacs, 2009)} can potentially decrease the toxicity of a drug and modulate the drugs' ability to bind serum proteins, (Wheate et al., 2004; Jeon et al., 2005; Li et al., 2013b) we have also examined the ability of α-Me_4phen-7 to form an inclusion complex with Q[10] and determined the subsequent effect on the toxicity of the ruthenium complex toward eukaryotic cells and its ability to bind HSA.

EXPERIMENTAL

Materials

The ruthenium complexes used in this study {*cis*-α-$[Ru(phen)(bb_7)]^{2+}$ (designated as α-phen-bb_7), *cis*-α-$[Ru(Me_2phen)(bb_7)]^{2+}$ (α-Me_2phen-bb_7), *cis*-α-$[Ru(Me_4phen)(bb_7)]^{2+}$ (α-Me_4phen-bb_7), *cis*-α-$[Ru(NO_2phen)(bb_7)]^{2+}$ (α-NO_2phen-bb_7), *cis*-α-$[Ru(phen)(bb_{12})]^{2+}$ (α-phen-bb_{12}), $[Ru(Me_4phen)_3]^{2+}$ and $Rubb_{12}$} and Q[10] were synthesized as previously described (Liu et al., 2005; Pisani et al., 2010; Gorle et al., 2015; Sun et al., 2018).

Toxicity

The toxicities of the ruthenium complexes were assayed against three eukaryotic cell lines: BHK (baby hamster kidney); Caco-2 (heterogeneous human epithelial colorectal adenocarcinoma); and Hep-G2 (liver carcinoma). All cell lines were cultured in 75 mL culture flasks in DMEM culture media (Dulbecco's Modified Eagle's Medium, Gibco, Thermo Fisher, UK) supplemented with 10% fetal bovine serum (Gibco, Thermo Fisher, UK), 1% MEM Non-Essential Amino Acid (Sigma, UK) and 1% penicillin-streptomycin (Sigma) at 37°C in an atmosphere of 5% humidified CO_2. Cells used in the study were in the logarithmic growth phase, and unless stated were grown to 70% confluence, and then trypsinized with 0.5% trypsin-EDTA (Gibco, Canada) for detachment and use in the assays.

Half-maximal inhibitory concentrations (IC_{50}) of the ruthenium complexes against BHK, Caco-2 and HepG2 cell lines were performed using the mitochondrial-dependent reduction of 3-(3,4-dimethylthiazol-2-yl)-5-diphenyl tetrazolium bromide (MTT) to formazan as previously described (Sundaraneedi et al., 2017). The cells were cultured in 96-well microtiter plates containing the respective media to a cell density of 3,000 per well at 37°C in an atmosphere of air containing 5% CO_2. Cell viability was assessed after continuous exposure to various concentrations

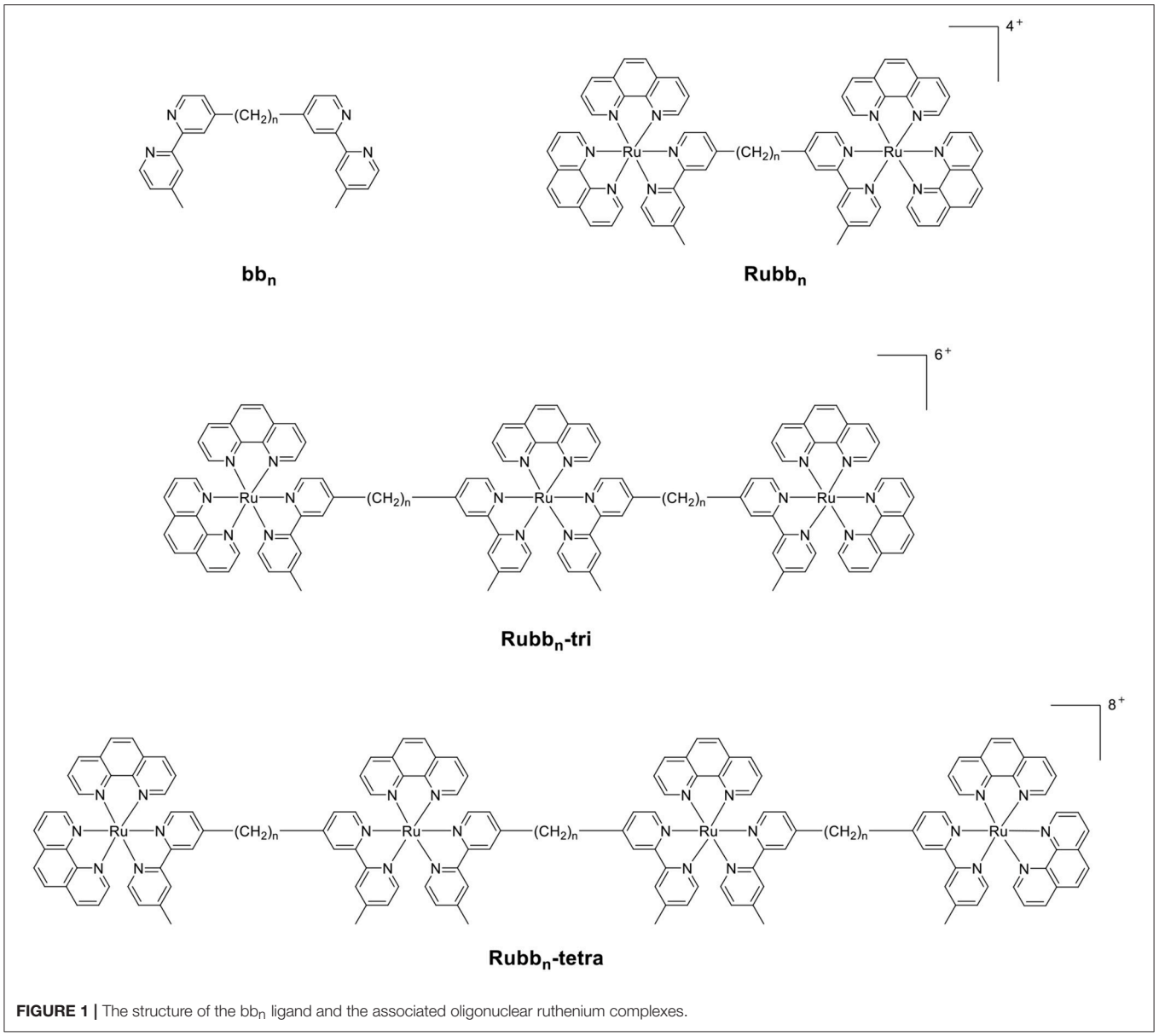

FIGURE 1 | The structure of the bb_n ligand and the associated oligonuclear ruthenium complexes.

of drugs (ranging from 0.5 to 400 μM) for 24 and 48 h. Cisplatin served as a treatment evaluation standard. Ruthenium complex stocks were made to the required concentration in sterile Milli-Q water, and cisplatin solutions were made to the required concentration in culture medium before the treatment. The amount of MTT reduced to formazan within the cells was quantified by measuring the absorbance at $\lambda = 570$ nm using a Fluostar Galaxy Microplate Reader. The average values presented are based on at least three independent experiments. The IC_{50} values were determined using GraphPad Prism 7.0 (GraphPad Software, San Diego, USA).

HSA Binding

All solutions used in the protein binding studies were dissolved in a 0.1 M sodium phosphate buffer (pH = 7.4). Protein solutions (5 μM) were titrated with the ruthenium complexes from 2 mM stock solutions, from a metal complex/protein ratio of 0.0 to 8.0. The maximum fluorescence for HSA (Sigma-Aldrich) was observed at $\lambda = 345$ nm after excitation at $\lambda = 280$ nm. All experiments were carried out in triplicate, with results presented as mean and standard deviation.

Encapsulation by Q[10]

NMR

^{1}H NMR titrations were carried out by the addition of solid Q[10] (0.4 mg) into a solution of α-Me_4phen-bb_7 (2 mM, 600 μL) to a 1:1 Q[10]:α-Me_4phen-bb_7 ratio. ROESY NMR experiments for the free and Q[10]-encapsulated α-Me_4phen-bb_7 were conducted with 2048 data points in t2 for 256 t1 values, with a pulse repetition delay set to 1.7 s and mixing times of 350 ms.

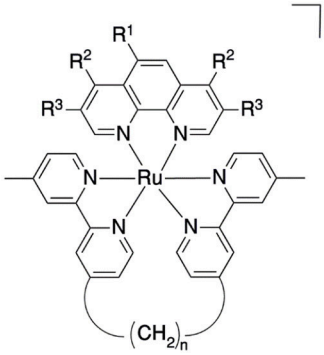

	R^1	R^2	R^3	n	Abbreviation
1	H	H	H	7	α-phen-7
2	H	Me	H	7	α-Me_2phen-7
3	H	Me	Me	7	α-Me_4phen-7
4	NO_2	H	H	7	α-NO_2phen-7
5	H	H	H	12	α-phen-12

FIGURE 2 | Structure and abbreviations for the *cis*-α-[Ru(phen′)(bb_n)]$^{2+}$ complexes {$n = 7$; phen′ = 1,10-phenanthroline (phen); 4,7-dimethyl-1,10-phenanthroline (Me_2phen); 3,4,7,8-tetramethyl-1,10-phenanthroline (Me_4phen); and 5-nitro-1,10-phenanthroline (NO_2phen), $n = 12$; phen′ = 1,10-phenanthroline}.

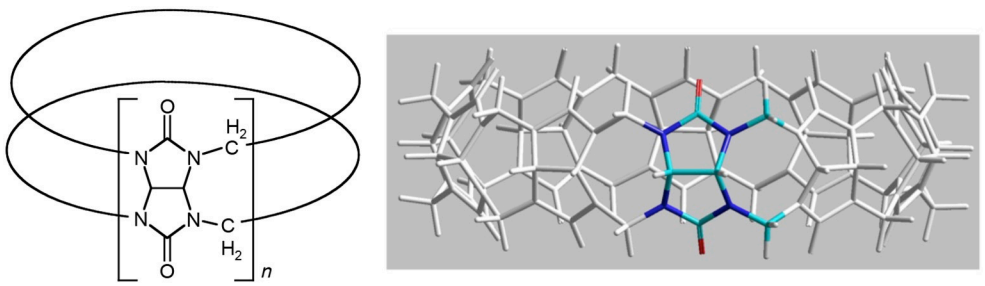

FIGURE 3 | Two representations of the structure of cucurbit[*n*]uril.

Molecular Modeling

The encapsulation of α-Me_4phen-7 in the Q[10] cavity was examined by molecular modeling using the *HyperChem* (version 8, HyperCube, Inc.) program. The bb_7 alkyl chain was positioned deep within the Q[10] cavity and the ruthenium metal center positioned at one of the portals in a manner consistent with the NMR results. The Q[10]-encapsulated α-Me_4phen-7 was then optimized using the Amber99 molecular mechanics forcefield without explicitly treating water molecules (i.e., "*in vacuo*"). Successive geometry optimizations using slightly different starting conformations and different minimization algorithms produced similar results.

Luminescence Titration

Spectra were recorded on a Horiba Scientific FluoroMax-4 fluorescence spectrophotometer at room temperature in a 1 cm quartz cuvette. Samples were excited at $\lambda = 435$ nm and emissions were recorded in the $\lambda =$ 510–800 nm range with slit widths of 5 nm in increments of 1 nm. All luminescence spectroscopy samples were prepared in Milli-Q water. Luminescence titrations were carried out by titration of 20 μL aliquots of Q[10] (12.5 μM) stock solution into a α-Me_4phen-7 (0.675 μM; 2,950 μL) solution to a 1.5:1 ratio. The sample was then sparged with argon to remove any oxygen present and allowed to equilibrate for 3 min before measurements were taken.

The binding constant (K_b) for α-Me_4phen-7 binding to Q[10] was calculated using Equation 1 (Pisani et al., 2010):

$$K_b = \frac{[MC]_b}{[MC]_f \times [Q10]_f} \quad (1)$$

where $[MC]_f$ and $[Q10]_f$ are the concentrations of free α-Me_4phen-7 and Q[10], respectively, at each titration point. $[MC]_b$ was determined using Equation 2:

$$[MC]_b = \frac{[MC]_t}{1 - \left(\frac{\delta_{obs} - \delta_b}{\delta_f(x) + \delta_b(x)}\right)} \quad (2)$$

where $[MC]_t$ is the concentration of metal complex in the sample, δ_{obs} is the luminescence intensity maxima observed at each titration point, δ_b is the luminescence intensity maximum of the bound metal complex, δ_f is the luminescence intensity maximum of the free metal complex and x is the ratio of bound/free metal complex at each titration point. The binding constant at each point was calculated and averaged to give an approximate binding constant.

Confocal Microscopy

The trypsinized BHK cells were seeded on sterile, poly L-lysine coated, coverslips in a 24-well plate. The ruthenium complex was applied to the cells in growth media to make the desired concentration (25 μM) and incubated at 37°C with 5% CO_2

for 1 h. Following the incubation, 100 nM Mitotracker® Green FM (Invitrogen) was added for mitochondrial staining. Staining was carried out in DMEM medium under standard cultivation conditions as per the manufacturer's instructions. Following staining, the coverslips were gently rinsed with phosphate buffer solution (PBS, pH = 7.1) prior to confocal laser scanning microscopy.

The cellular accumulation of the ruthenium complex was determined using a laser scanning confocal microscope (FV3000, Olympus). Samples were viewed under 60× silicone immersion using the following excitation (λ_{ex}) and emission (λ_{em}) wavelengths. Ruthenium complex (λ_{ex} = 450 nm, λ_{em} = 630 nm) and Mitotracker Green FM (λ_{ex} = 490 nm, λ_{em} = 516 nm) were excited using a blue argon laser (λ_{ex} = 488 nm), and emissions were collected at λ = 600–650 nm for the ruthenium complex and λ = 500–550 nm for Mitotracker Green. Image data acquisition and processing was performed using Olympus FV31S-SW software. The luminescence intensity of *cis*-α-$[Ru(Me_4phen)(bb_7)]^{2+}$ inside the BHK cells was quantified using the surface rendering function of Imaris 9.2.1 software, and the data analyzed for statistical difference using the Wilcoxon-test and *t*-test methods.

RESULTS

Toxicity Against Eukaryotic Cells

The toxicities of the $[Ru(phen')(bb_n)]^{2+}$ complexes against three eukaryotic cell lines {baby hamster kidney (BHK), human epithelial colorectal adenocarcinoma (Caco-2) and human hepatocellular carcinoma (Hep-G2)} were determined and compared to the values obtained for the dinuclear complex $Rubb_{12}$, $[Ru(Me_4phen)_3]^{2+}$ {designated $(Me_4phen)_3$, the most active of the mononuclear complexes originally identified by Dwyer and co-workers} and the control anticancer agent cisplatin. The BHK and Hep-G2 cell lines were chosen so that the IC_{50} results could be compared to those from our previous studies with multinuclear ruthenium complexes (Li et al., 2015b). It was also of interest to examine the toxicity of the ruthenium complexes against a third eukaryotic cell line that was distinct from kidney or liver cells—consequently, the Caco-2 cell line was also used in this study. The results are summarized in **Table 1**. The IC_{50} values determined for $Rubb_{12}$ against the BHK and Hep-G2 cell lines in this study were similar to those obtained in an earlier study (Li et al., 2015b). Of note, α-Me_4phen-7 showed no toxicity (>400 μM) against BHK and Caco-2 cells, and very low activity (≈ 150 μM) against Hep-G2 cells for a 24-h incubation and very low (BHK and Hep-G2) or no toxicity (Caco-2) for a 48-h incubation. By contrast, α-phen-12 was (2–5)-fold more toxic than α-Me_4phen-7, while $Rubb_{12}$ was generally much more toxic to the eukaryotic cells than either of the mononuclear complexes.

TABLE 1 | IC_{50} values (μM) of the ruthenium complexes against the BHK, Hep-G2 and Caco-2 cell lines for 24- and 48-h incubations.

Complexes	BHK		Hep-G2		Caco-2	
	24 h	48 h	24 h	48 h	24 h	48 h
α-phen-7	>400	250 ± 42	319 ± 26	312 ± 15	>400	219 ± 43
α-Me_2phen-7	>400	250 ± 46	358 ± 18	151 ± 30	>400	>400
α-Me_4phen-7	>400	168 ± 5	162 ±14	142 ± 8	>400	>400
α-NO_2phen-7	>400	>400	141 ± 29	99 ± 29	121 ± 18	126 ± 6
α-phen-12	92 ± 26	85 ± 16	94 ± 13	19 ± 3	227 ± 22	177 ± 17
$(Me_4phen)_3$	157 ± 25	111 ± 23	253 ± 60	72 ± 31	220 ± 43	265 ± 13
$Rubb_{12}$	44 ± 9	41 ± 7	55 ± 12	15 ± 5	10 ± 1	8 ± 3
Cisplatin	>400	146 ± 8	314 ± 8	12 ± 3	376 ± 41	25 ± 6
Q[10]-α-Me_4phen-7	>400	>400	>400	>400	>400	>400

HSA Binding

The binding of the $[Ru(phen')(bb_n)]^{2+}$ complexes to human serum albumin (HSA) was examined by fluorescence spectroscopy. HSA has one fluorescent tryptophan residue that can be used as a fluorophore in drug-binding experiments. The relative changes in HSA fluorescence upon binding of selected ruthenium complexes are shown in **Figure 4**.

All ruthenium complexes showed significant binding affinity with HSA. Consistent with a previous HSA binding study of the $Rubb_n$ complexes (Li et al., 2013b), the decrease in the tryptophan fluorescence was found to be due to static quenching, a positional change of the tryptophan residue induced by the binding of the ruthenium complex to the protein.

The static quenching via binding of the ruthenium complexes to HSA can be represented as:

$$nRu + HSA \rightarrow nRu\cdots HSA$$

where nRu...HSA denotes the quenched ruthenium complex/HSA species. A double-logarithm equation of $\log_{10}[(F_0\text{-}F)/F]$ vs. $\log_{10}[Ru]$ can then be used to express the equilibrium between the free and bound ruthenium(II) complex to determine the apparent binding constant (K_{app}) and the binding number (n) (Krause-Heuer et al., 2012).

$$\log\left[\frac{F_0 - F}{F}\right] = \log_{10} K_{app} + n \log_{10}[Ru]$$

It was not possible to determine a single apparent HSA binding constant, as a linear relationship was not observed over the entire concentration range of added ruthenium complex in the plot of $\log_{10}[(F_0 - F)/F]$ vs. $\log_{10}[Ru]$. However, two distinct linear sections could be found in the analysis of the double logarithm, corresponding to ruthenium complex to HSA ratios of (a) 0 to 2.4 and (b) 2.4 to 8. As previously observed (Li et al., 2013b), the two binding ratio regions represent an initial 1:1 binding at low ruthenium complex concentration (ratios 0–2.4), and then upon addition of further ruthenium complex, a region (2.4–8) where multiple ruthenium complexes (≥ 2:1) are bound to HSA. The higher affinity 1:1 HSA binding constant K_{app} and the binding numbers n for the ruthenium complexes determined at low ratios of added ruthenium complex are summarized in **Table 2**.

For the $[Ru(phen')(bb_7)]^{2+}$ complexes, the HSA binding affinity increased with the number of methyl substituents on

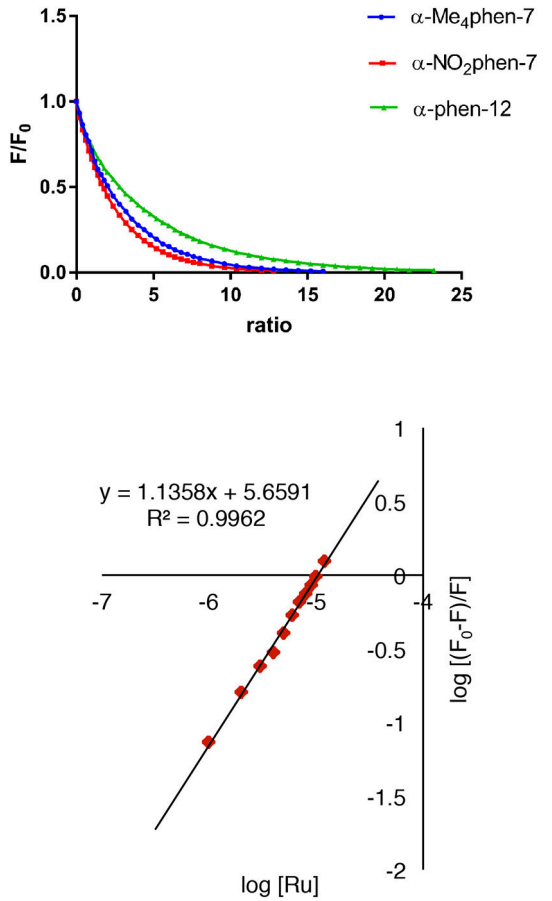

FIGURE 4 | Top: relative change in the HSA fluorescence upon binding α-Me_4phen-7, α-NO_2phen-7 and α-phen-12; bottom: the log plot of *cis*-α-[Ru(Me_4phen)(bb_7)]$^{2+}$ binding with HSA at low α-Me_4phen-7 to HSA ratios.

TABLE 2 | The n and K_{app} values for the HSA binding of the ruthenium complexes at a [Ru complex]/[HSA] ratio from 0 to 2.4.

Complex	*n*	K_{app} × 10^5 $(M)^{-1}$	R^2
$(Me_4phen)_3$	0.81	0.12 ± 0.03	0.98
α-Me_4phen-7	1.14	4.6 ± 0.90	0.996
α-Me_2phen-7	0.91	0.29 ± 0.13	0.984
α-phen-7	0.80	0.10 ± 0.00	0.991
α-NO_2phen-7	1.27	23.5 ± 4.9	0.998
α-phen-12	0.95	0.43 ± 0.17	0.993

the 1,10-phenanthroline ligand; however, the α-NO_2phen-bb_7 complex showed the highest binding affinity. Interestingly, the α-Me_4phen-7 complex bound HSA with significantly higher affinity than the [Ru(Me_4phen)$_3$]$^{2+}$ and α-phen-bb_{12} complexes, and with approximately the same affinity as previously determined for $Rubb_{12}$ ($K_{app} = 4.7 \times 10^5$ M^{-1}) (Li et al., 2013b).

Q[10] Encapsulation of α-Me_4phen-7

NMR Studies

As α-Me_4phen-7 exhibited the best differential (≈ 20-fold) between high antimicrobial activity (previously demonstrated in Sun et al., 2018) and low toxicity, it was selected for the Q[10] binding studies. **Figure 5** shows the ^{1}H NMR spectrum of α-Me_4phen-7 and the spectra of the metal complex with added Q[10] at various Q[10] to α-Me_4phen-7 ratios (R). The ^{1}H NMR resonances of α-Me_4phen-7 and the Q[10]-bound ruthenium complex were assigned from a combination of DQFCOSY and ROESY experiments. In particular, the resonances from the bb_7 ligand were assigned through the observation of an ROE from the spin-coupled bpy H5 and H5' protons (coupled to the H6 and H6' protons) to the substituted-bpy ligand methyl (Me) and chain methylene protons respectively. The bpy H3 and H3' were similarly assigned from the observed ROEs to the bpy Me and α-CH_2 protons, respectively. The phenanthroline H2/9 resonances were assigned through the observation of an ROE to the bb_7 H6 protons.

One set of exchange-broadened resonances was observed for the protons from both α-Me_4phen-7 and Q[10], indicating intermediate-exchange kinetics on the NMR timescale at 25°C for $R < 1$. Of note, the resonances from the CH_2 groups in the alkyl chain of the bb_7 ligand shifted significantly upfield (0.3–0.5 ppm). This indicates the alkyl chain is positioned deep within the Q[10] cavity, as many previous studies have established that resonances from guest protons located inside a Q[*n*] cavity shift significantly upfield, with protons positioned toward the middle of the Q[*n*] cavity exhibiting the largest (up to 1 ppm) upfield shifts (Mock and Shih, 1986; Jeon et al., 1996). This suggests that α-Me_4phen-7 binds Q[10] with the bb_7 ligand deep within the cavity and the Me_4phen ligand projecting out of the portal. Consistent with this proposal are the significant upfield shifts (≈ 0.5 ppm) for the bb_7 protons on the pyridyl ring containing the alkyl chain (H3', H5' and H6') coupled with the observed downfield shifts of the Me_4phen H2/9 and H5/6 resonances.

Interestingly, at a Q[10] to α-Me_4phen-7 ratio of 1 (as determined from the integration of the respective resonances), two sets of resonances for the bb_7 aromatic protons and the Q[10] CH_2 resonances were observed (see **Figures 5**, **6**), indicating slow-exchange binding kinetics. The inequivalence of the Q[10] methylene resonances that project toward the portals (5.83 and 5.64 ppm) and toward the cavity center (4.23 and 4.14 ppm) is due to the non-symmetric encapsulation of α-Me_4phen-7 in Q[10]. As intermediate-exchange kinetics were observed at $R < 1$ but slow-exchange at $R = 1$, it is concluded that for all values of $R < 1$ there must be some 1:2 (Q[10] to α-Me_4phen-7) binding with the rate of exchange between the 1:1 and 1:2 binding modes being in the fast-exchange regime. In the $R = 1$ spectrum, the resonances from the bpy CH_3 groups were also inequivalent, with one peak shifted downfield and the other upfield compared to equivalent bpy CH_3 resonances in the free ruthenium complex. This suggests that one bpy CH_3 is positioned inside the Q[10] cavity with the second bpy CH_3 located outside of the portal. Possibly due to the broadness of the resonances from α-Me_4phen-7, very few intermolecular ROEs were observed in ROESY spectra of the Q[10]-encapsulated ruthenium complex.

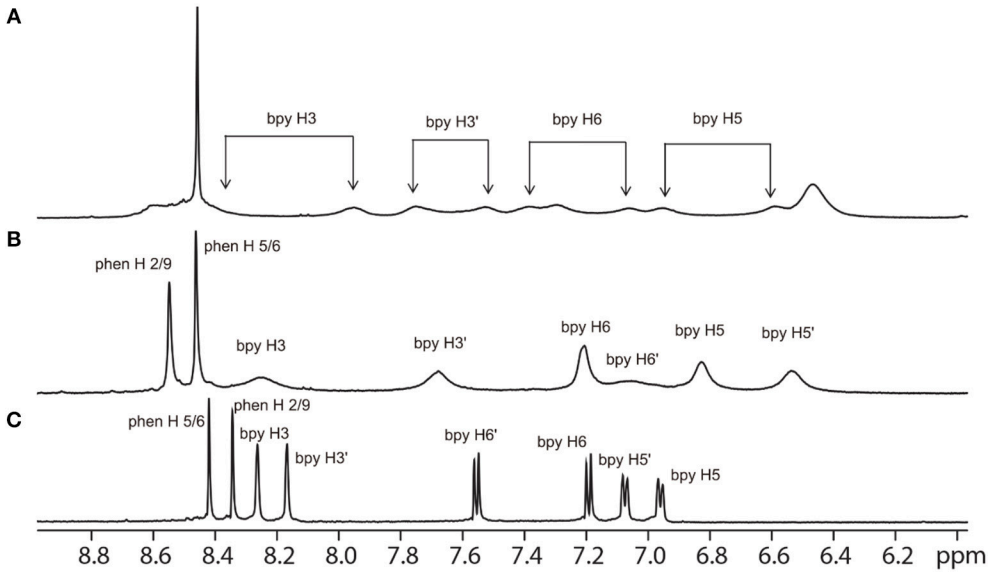

FIGURE 5 | ^{1}H NMR spectrum of the aromatic region of the free α-Me_4phen-7 **(C)** and with added Q[10], at Q[10] to α-Me_4phen-7 ratios of 0.75 **(B)** and 1.0 **(A)**.

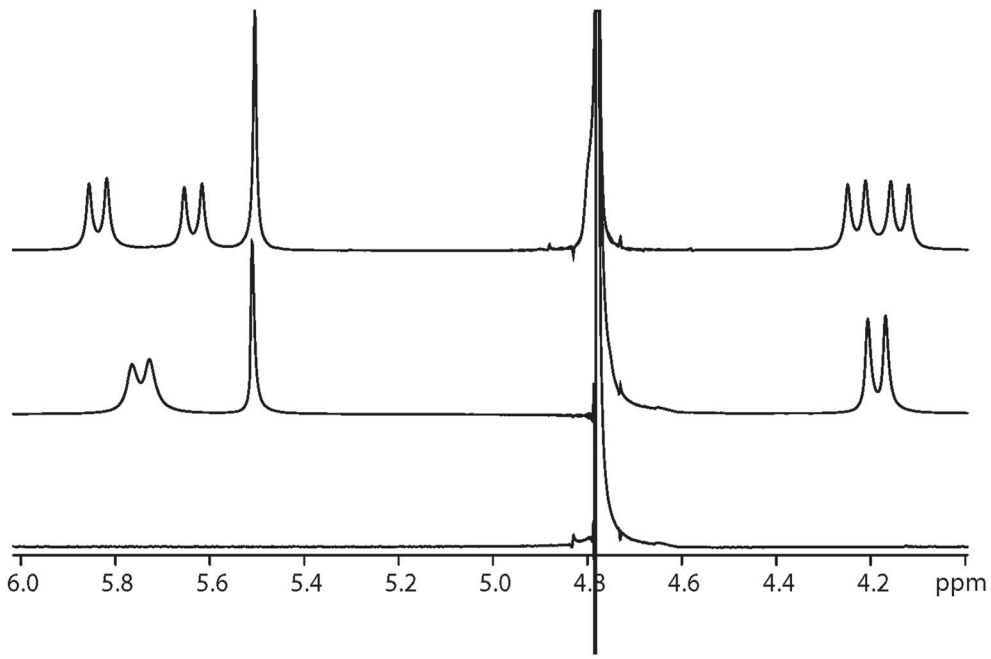

FIGURE 6 | ^{1}H NMR spectrum of the protons from Q[10], at Q[10] to α-Me_4phen-7 ratios of 0 (bottom spectrum), 0.75 (middle) and 1.0 (top).

However, ROEs was observed from the Me_4phen H2/9 and 3/8 methyl resonances to the Q[10] methylene protons that project toward the portal.

Molecular Modeling

In order to confirm the feasibility of the mode of binding suggested by the NMR data, the encapsulation of α-Me_4phen-7 within the Q[10] cavity was examined by molecular simulations using the *HyperChem* modeling software. The methylene chain of α-Me_4phen-7 was folded within the Q[10] cavity and the ruthenium metal center positioned at the portal in a manner consistent with the observed intermolecular ROEs observed in ROESY spectra. The system was then successively optimized using the Amber99 molecular mechanics forcefield. As shown in **Figure 7**, stable low energy conformations could be obtained with the methylene chain folded in the cavity and the ruthenium metal

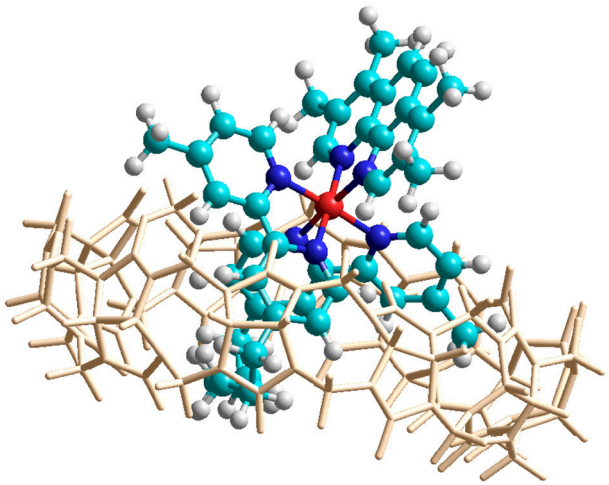

FIGURE 7 | Molecular modeling of the encapsulation of α-Me_4phen-7 with Q[10] using *HyperChem* software. The color of the atoms of α-Me_4phen-7 are: H, white; C, cyan; N, blue; and Ru, red.

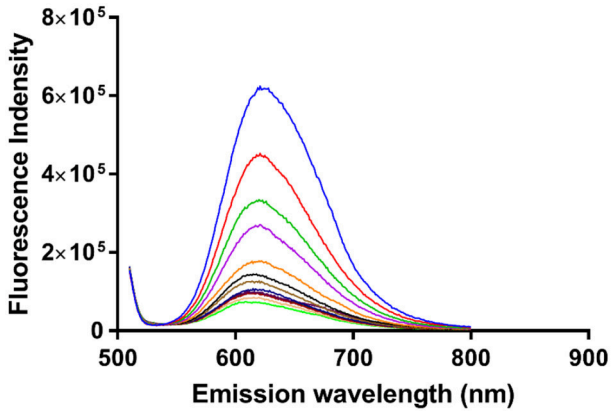

FIGURE 8 | The luminescence decrease of α-Me_4phen-bb_7 upon the addition of Q[10] to a Q[10] to α-Me_4phen-7 ratio of 1.5.

center positioned outside the portal consistent with the NMR data.

Luminescence Spectroscopy

In order to obtain an equilibrium binding constant, the association of α-Me_4phen-7 with Q[10] was studied by luminescence spectroscopy. The luminescence intensity of α-Me_4phen-7 decreased upon the addition of each aliquot of Q[10] up to $R = 1.5$ (see **Figure 8**). Binding curves were generated by plotting luminescence intensity (counts per second) against the molar ratio of added Q[10], from which a 1:1 binding constant of $9.9 \pm 0.2 \times 10^6$ M^{-1} was determined.

Biological Properties of α-Me_4phen-7 Encapsulated in Q[10]

Upon encapsulation in Q[10], α-Me_4phen-7 exhibited no toxicity to any of the cell lines for both 24- or 48-h incubations (see

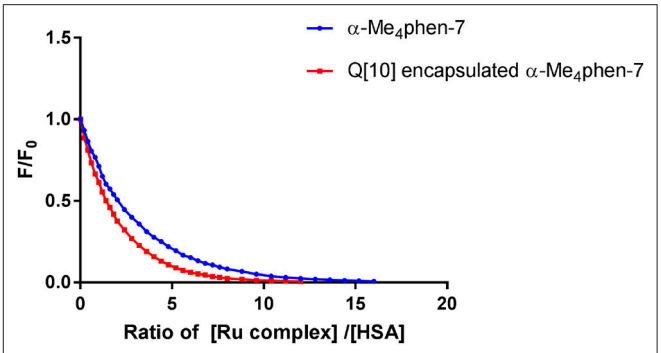

FIGURE 9 | Relative change in the HSA fluorescence upon binding α-Me_4phen-7 and α-Me_4phen-7 encapsulated in Q[10].

Table 1). Based upon the 48-h incubation toxicity to BHK and Hep-G2 cells, it can be concluded that Q[10]-encapsulation decreases the toxicity of α-Me_4phen-7 by at least (2–3)-fold. Of note, and contrary to what was observed for $Rubb_{12}$, Q[10]-encapsulation increases the affinity of α-Me_4phen-7 for HSA (see **Figure 9**). A K_{app} of $2 \pm 0.2 \times 10^6$ M^{-1} was determined for the Q[10]-encapsulated ruthenium complex.

Reducing the cellular accumulation of α-Me_4phen-7 is the simplest mechanism by which Q[10]-encapsulation could reduce toxicity. Consequently, confocal microscopy was used to obtain both a qualitative and quantitative measure of the effect of Q[10]-encapsulation on the cellular accumulation of α-Me_4phen-7 in BHK cells after a short incubation time. **Figure 10** shows confocal microscopy images of BHK cells after a 1 h incubation with free or Q[10]-encapsulated α-Me_4phen-7. Mitotracker Green (which selectively localizes in the mitochondria) was used to visualize the cells, with the nucleus of the cell being the dark circular region outlined by the green luminescence. As it appeared that the cellular accumulation was not significantly different between the free or Q[10]-encapsulated α-Me_4phen-7 samples, the luminescence intensity from α-Me_4phen-7 per cell was quantified over all the images taken. The results are shown in **Figure 11**. As seen in the "box and whiskers" diagram, and confirmed by statistical analysis (Wilcoxon-test and a *t*-test; $p = 0.13$ and 0.11, respectively), there was no difference in the level of the cellular accumulation of α-Me_4phen-7 between the experiments where the ruthenium complex was added to the BHK cells in either the free or Q[10]-encapsulated forms.

DISCUSSION

We have previously shown that some mononuclear ruthenium(II) complexes containing bb_n as a tetradentate ligand (particularly α-phen-12 and α-Me_4phen-7) exhibit good antimicrobial activity (MICs = 1–10 μM) against both Gram-positive and Gram-negative bacteria (Gorle et al., 2015; Sun et al., 2018). In this study we have examined their associated toxicity to eukaryotic cells. Importantly, although α-Me_4phen-7 was as active against Gram-negative bacteria as α-phen-12 (Sun et al., 2018), the results from the present study showed that

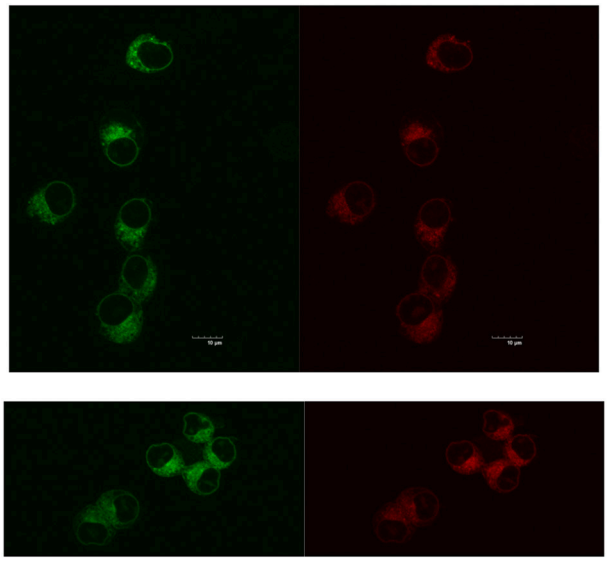

FIGURE 10 | Top, left to right: α-Me_4phen-7 accumulation in BHK cells at 25 μM after a 1-h incubation, stained by Mitotracker Green and α-Me_4phen-7 (red). Bottom, left to right: Q[10]-encapsulated α-Me_4phen-7 accumulation in BHK cells at 25 μM after a 1-h incubation, stained by Mitotracker Green and α-Me_4phen-7 (red). Scale bar = 10 μm.

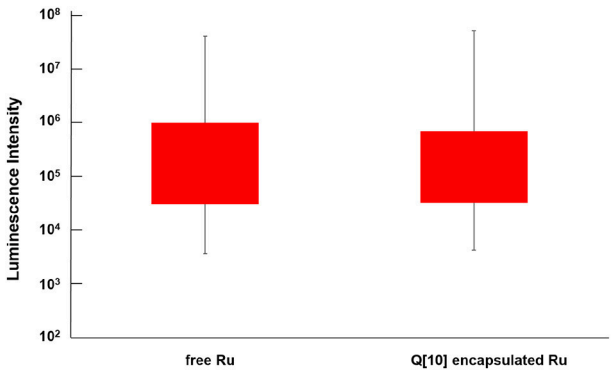

FIGURE 11 | "Box and whisker" plot of the luminescence from α-Me_4phen-7 accumulation in BHK cells at 25 μM after a 1-h incubation for both free and Q[10]-encapsulated α-Me_4phen-7. The red box region shows the 25–75% quartiles for the luminescence intensity per cell, while the whiskers show the maximum and minimum intensities per cell.

α-Me_4phen-7 was (2–5)-fold less toxic to eukaryotic cells than α-phen-12. It was also previously shown that α-phen-12 (log $P = -0.9$) accumulated in bacterial cells more rapidly and to a greater degree than did α-Me_4phen-7 (log $P = -1.33$), consistent with their respective lipophilicities (Sun et al., 2018). Consequently, α-Me_4phen-7 appears to be more toxic to Gram-negative bacteria than α-phen-12 on a molar basis. This could be due to the greater DNA binding ability of α-Me_4phen-7, compared to α-phen-12 (Sun et al., 2018). Of relevance in the present study, the preliminary confocal microscopy experiments indicated that α-Me_4phen-7 did not localize in the nucleus of BHK cells. As a consequence, α-Me_4phen-7 might not be inherently more toxic to eukaryotic cells than α-phen-12. Hence, based upon lipophilicity, it would be expected that α-phen-12 would also accumulate to greater degree in eukaryotic cells than α-Me_4phen-7, and thereby be more toxic. It was also noted that α-Me_4phen-7 was significantly less toxic than the lead oligonuclear complex, $Rubb_{12}$. In absolute terms, α-Me_4phen-7 showed very little toxicity to the eukaryotic cells and was found to be at least 20-fold more active against Gram-negative bacteria (Sun et al., 2018) than eukaryotic cells over a 24 h time period.

In terms of HSA binding, α-Me_4phen-7 bound the serum protein approximately 10-fold more tightly than α-phen-12 and α-Me_2phen-7, and with similar affinity as $Rubb_{12}$. Previous studies have demonstrated that there are a number of factors governing the binding affinity of drugs with HSA (Kratochwil et al., 2002; Bohnert and Gan, 2013; Liu et al., 2014). Lipophilicity is generally considered to be important, particularly within a series of structurally-related compounds. In this study it was found the degree of methylation of the phenanthroline ligand, and hence lipophilicity, did correlate with stronger binding. However, the α-NO_2phen-7 complex (log $P = -1.58$) bound HSA with higher affinity than α-Me_4phen-7 (log $P = -1.33$). This observation suggests that the dispersion of the 2+ charge of the ruthenium complex is also important, which is consistent with the approximate charge of HSA at physiological pH being −17 (Fogh-Andersen et al., 1993).

It is often assumed that low serum protein binding is a "good" drug property, as it increases the concentration of the free drug; however, in a recent survey of newly approved drugs, Liu and co-workers (Liu et al., 2014) found that 45 and 24% of the drugs exhibited high (>95% bound) or very high (>99%) serum protein binding, respectively. Consequently, Liu et al and others proposed that serum protein binding is neither an intrinsically "good" or "bad" property. However, a recent pharmacokinetic study of $Rubb_{12}$ in mice demonstrated that the amount of the ruthenium complex in the serum decreased very rapidly after administration by intravenous injection (Li et al., 2017). This result suggests that potential new ruthenium complexes would need to bind serum proteins at least as strongly, if not with greater affinity, than $Rubb_{12}$. Based upon this criterion, it is noted that α-Me_4phen-7 binds HSA with at least similar affinity to $Rubb_{12}$.

Given the antimicrobial potential of α-Me_4phen-7, it was of interest to examine the ability of the ruthenium complex to bind Q[10], and determine its subsequent effect on cytotoxicity and HSA binding. The results of this study showed that α-Me_4phen-7 does form a high-affinity water-soluble association complex with Q[10], with the bb_7 alkyl chain positioned deep within the cavity and the ruthenium metal center positioned at one of the portals. This binding mode, with the non-polar segment of a metal complex in the hydrophobic cavity and the cationic metal center positioned at the carbonyl-rimmed hydrophilic portals, is consistent with previous studies (Pisani et al., 2010; Alrawashdeh et al., 2016). The magnitude of the α-Me_4phen-7-Q[10] binding constant ($\approx 10^7$ M^{-1}) indicates that a large proportion of the ruthenium complex would be Q[10]-bound at the micro-molar concentrations that would be found in the blood after administration.

The effect of Q[*n*] encapsulation on the cytotoxicity of a variety of compounds toward eukaryotic cell lines has been previously examined. For example, Kim et al. reported a (5–10)-fold decrease in activity for oxaliplatin in Q[7] (Jeon et al., 2005), while Wheate et al showed that a dinuclear platinum complex maintained its activity toward L1210 cells, but was 2-fold less active against the cisplatin resistant cell line L1210/DDP (Wheate et al., 2004). Furthermore, there have been several recent reports where encapsulation in Q[*n*] was proposed to have increased the uptake of a cytotoxic agent (Konda et al., 2017; Shinde et al., 2018). In the present study, Q[10]-encapsulation decreased the toxicity of α-Me_4phen-7 toward BHK and Hep-G2 cells, while no conclusions could be drawn for the Caco-2 cells, given the lack of activity of the free ruthenium complex for both 24- and 48-h incubations. The most obvious explanation for the decreased toxicity of α-Me_4phen-7 encapsulated in Q[10] is that the concentration of the free, unbound, ruthenium complex is significantly lower in the assay medium and the Q[10]-bound ruthenium complex can not cross the cell membrane. This would consequently result in a slower and lower accumulation of the ruthenium complex inside the cells. However, the results from the confocal microscopy experiments indicated that the level of accumulation of α-Me_4phen-7 inside the cells is not significantly affected by encapsulation over a 1-h incubation.

In terms of HSA binding, Q[10]-encapsulation increased the affinity of α-Me_4phen-7 for the serum protein. Interestingly, in an earlier study it was determined that Q[10]-binding of $Rubb_{12}$ decreased the affinity of the ruthenium complex for HSA binding (Li et al., 2013b). As noted above, given the short residence time found for $Rubb_{12}$ after intravenous injection in mice, the (3–4)-fold higher HSA binding affinity is likely to be beneficial.

CONCLUSIONS

In conclusion, the results of this study have demonstrated that the most active antimicrobial mononuclear ruthenium complex against Gram-negative bacteria, α-Me_4phen-7, is also the least toxic to eukaryotic cells. Furthermore, although it exhibits slightly lower (≈ 2-fold) antimicrobial activities to Gram-negative bacteria than the lead oligonuclear complex $Rubb_{12}$ (Sun et al., 2018), α-Me_4phen-7 is also significantly less toxic to eukaryotic cells compared to the dinuclear complex. Fluorescence assays demonstrated that α-Me_4phen-7 bound HSA with similar affinity to that previously reported for $Rubb_{12}$. Taken together, the results of this study suggest α-Me_4phen-7 is a suitable candidate for further studies of its antimicrobial properties. In addition, it has been shown that α-Me_4phen-7 can form a high-affinity, water-soluble, inclusion complex with Q[10]. Q[10]-encapsulation decreases the toxicity of α-Me_4phen-7 toward eukaryotic cells and increases its HSA binding affinity. As a consequence, administration of α-Me_4phen-7 encapsulated in Q[10] may increase the potential of the ruthenium complex as an antimicrobial agent. However, the effect of Q[10]-encapsulation on the antimicrobial properties of α-Me_4phen-7 needs to be examined.

AUTHOR CONTRIBUTIONS

BS synthesized the ruthenium complexes and carried out the experiments. AD provided the Q[10], while IM, KH, FK, and JC were involved in planning the research, analysing the data, and writing the paper.

FUNDING

On invitation to contribute, it was indicated there would be no charges for this paper in the Research Topic Supramolecular Metal-Based Entities for Biomedical and Biological Applications, in the Frontiers in Chemistry—Supramolecular Chemistry Section (hosted by Angela Casini and James D. Crowley). This is submitted on the basis that there will be NO CHARGE.

ACKNOWLEDGMENTS

BS thanks UNSW Canberra for a Ph.D. scholarship and a Travel Grant to undertake the biology experiments at the University of Adelaide. The authors thank Prof H.H. Harris (University of Adelaide) for the gift of some cisplatin, and Jane Sibbons (University of Adelaide) for help in quantifying the confocal microscope images.

REFERENCES

Alrawashdeh, L. R., Cronin, M. P., Woodward, C. E., Day, A. I., and Wallace,. L. (2016). Iridium cyclometalated complexes in host-guest chemistry: a strategy for maximizing quantum yield in aqueous media. *Inorg. Chem.* 55, 6759–6769. doi: 10.1021/acs.inorgchem.6b01037

Bergamo, A., and Sava, G. (2007). Ruthenium complexes can target determinants of tumour malignancy. *Dalton Trans*. 1267–1272. doi: 10.1039/b617769g

Bohnert, T., and Gan, L.-S. (2013). Plasma protein binding: from discovery to development. *J. Pharm. Sci.* 102, 2953–2994. doi: 10.1002/jps.23614

Bolhuis, A., Hand, L., Marshall, J. E., Richards, A. D., Rodger, A., and Aldrich-Wright, J. (2011). Antimicrobial activity of ruthenium-based intercalators. *Eur. J. Pharm. Sci.* 42, 313–317. doi: 10.1016/j.ejps.2010.12.004

Boucher, H. W., Talbot, G. H., Bradley, J. S., Edwards, J. E., Gilbert, D., Rice, L. B., et al. (2009). Bad bugs, no drugs: no ESKAPE! An update from the infectious diseases society of America. *Clin. Infect. Dis.* 48, 1–12. doi: 10.1086/595011

Dwyer, F. P., Gyarfas, E. C., Rogers, W. P., and Koch, J. H. (1952). Biological activity of complex ions. *Nature* 170, 190–191. doi: 10.1038/170190a0

Dwyer, F. P., Reid, I. K., Shulman, A., Laycock, G. M., and Dixson, S. (1969). The biological actions of 1,10-phenanthroline and 2,2-bipyridine hydrochlorides, quaternary salts and metal chelates and related compounds. 1. Bacteriostatic action on selected gram-positive gram-negative and acid-fast bacteria. *Aust. J. Exp. Biol. Med.* 47, 203–218. doi: 10.1038/icb.1969.21

Fogh-Andersen, N., Bjerrum, P. J., and Siggaard-Andersen, O. (1993). Ionic binding, net charge and Donnan effect of human serum albumin as a function of pH. *Clin. Chem.* 39, 48–52.

Gill, M. R., and Thomas, J. A. (2012). Ruthenium(II) polypyridyl complexes and DNA: from structural probes to cellular imaging and therapeutics. *Chem. Soc. Rev.* 41, 3179–3192. doi: 10.1039/c2cs15299a

Gorle, A. K., Feterl, M., Warner, J. M., Primrose, S., Constantinoiu, C. C., Keene, F. R., et al. (2015). Mononuclear polypyridylruthenium(II) complexes with high

membrane permeability in gram-negative bacteria–in particular *Pseudomonas aeruginosa*. *Chem. Eur. J.* 21, 10472–10481. doi: 10.1002/chem.201500385

Gorle, A. K., Feterl, M., Warner, J. M. L., Wallace, L., Keene, F. R., and Collins, J. G. (2014). Tri- and tetra-nuclear polypyridyl ruthenium(II) complexes as antimicrobial agents. *Dalton Trans.* 43, 16713–16725. doi: 10.1039/c4dt02139h

Gorle, A. K., Li, X., Primrose, S., Li, F., Feterl, M., Kinobe, R. T., et al. (2016). Oligonuclear polypyridylruthenium(II) complexes: selectivity between bacteria and eukaryotic cells. *J. Antimicrob. Chemother.* 71, 1547–1555. doi: 10.1093/jac/dkw026

Isaacs, L. (2009). Cucurbit[n]urils: from mechanisms to structure and function. *Chem. Commun.* 619–629. doi: 10.1039/B814897J

Jeon, Y.-M., Kim, J., Wang, D., and Kim, K. (1996). Molecular container assembly capable of controlling binding and release of its guest molecules: reversible encapsulation of organic molecules in sodium ion complexed cucurbituril. *J. Am. Chem. Soc.* 118, 9790–9791. doi: 10.1021/ja962071x

Jeon, Y. J., Kim, S.-Y., Ko, Y. H., Sakamoto, S., Yamaguchi, K., and Kim, K. (2005). Novel molecular drug carrier: encapsulation of oxaliplatin in cucurbit[7]uril and its effects on stability and reactivity of the drug. *Org. Biomol. Chem.* 3, 2122–2125. doi: 10.1039/B504487A

Kim, K., Selvapalam, N., Ko, Y. H., Park, K. M., Kim, D., and Kim, J. (2007). Functionalized cucurbiturils and their applications. *Chem. Soc. Rev.* 36, 267–279. doi: 10.1039/B603088M

Konda, S. K., Malikib, R., McGrath, S., Parker, B. S., Robinson, T., Spurling, A., et al. (2017). Encapsulation of mitoxantrone within cucurbit[8]uril decreases toxicity and enhances survival in a mouse model of metastatic breast cancer. *ACS Med. Chem. Lett.* 8, 538–542. doi: 10.1021/acsmedchemlett.7b00090

Kratochwil, N. A., Huber, W., Müller, F., Kansy, M., and Gerber, P. R. (2002). Predicting plasma protein binding of drugs: a new approach. *Biochem. Pharmacol.* 64, 1355–1374. doi: 10.1016/S0006-2952(02)01074-2

Krause-Heuer, A. M., Price, W. S., and Aldrich-Wright, J. R. (2012). Spectroscopic investigations on the interactions of potent platinum(II) anticancer agents with bovine serum albumin. *J. Chem. Biol.* 5, 105–113. doi: 10.1007/s12154-012-0074-1

Kumar, K. A., Reddy, K. L., Vidhisha, S., and Satyanarayana, S. (2009). Synthesis, charcaterisation and DNA binding and photocleavage studies of $[Ru(bpy)_2BDPPZ]^{2+}$ and $[Ru(phen)_2BDPPZ]^{2+}$ complexes and their antimicrobial activity. *Appl. Organometal. Chem.* 23, 409–420. doi: 10.1002/aoc.1534

Kumar, S. V., Scottwell, S. Ø., Waugh, E., McAdam, C. J., Hanton, L. R., Brooks, H. J. L., et al. (2016). Antimicrobial properties of tris(homoleptic) ruthenium(II) 2-pyridyl-1,2,3-triazole "click" complexes against pathogenic bacteria including methicillin-resistant *staphylococcus aureus* (MRSA). *Inorg. Chem.* 55, 9767–9777. doi: 10.1021/acs.inorgchem.6b01574

Lagona, J., Mukhopadhyay, P., Chakrabarti, S., and Isaacs, L. (2005). The cucurbit[n]uril family. *Angew. Chem. Int. Edit.* 44, 4844–4870. doi: 10.1002/anie.200460675

Li, F., Collins, J. G., and Keene, F. R. (2015a). Ruthenium complexes as antimicrobial agents. *Chem. Soc. Rev.* 44, 2529–2542. doi: 10.1039/c4cs00343h

Li, F., Feterl, M., Mulyana, Y., Warner, J. M., Collins, J. G., and Keene, F. R. (2012). *In vitro* susceptibility and cellular uptake for a new class of antimicrobial agents: dinuclear ruthenium(II) complexes. *J. Antimicrob. Chemother.* 67, 2686–2695. doi: 10.1093/jac/dks291

Li, F., Feterl, M., Warner, J. M., Day, A. I., Keene, F. R., and Collins, J. G. (2013b). Protein binding by dinuclear polypyridyl ruthenium(II) complexes and the effect of cucurbit[10]uril binding. *Dalton Trans.* 42, 8868–8877. doi: 10.1039/c3dt50551k

Li, F., Feterl, M., Warner, J. M., Keene, F. R., and Collins, J. G. (2013a). Dinuclear polypyridylruthenium(II) complexes: flow cytometry studies of their accumulation in bacteria and the effect on the bacterial membrane. *J. Antimicrob. Chemother.* 68, 2825–2833. doi: 10.1093/jac/dkt279

Li, F., Gorle, A. K., Ranson, M., Vine, K., Kinobe, R. T., Feterl, M., et al. (2017). Probing the pharmacokinetics of cucurbit[7, 8 and 10]uril: and a dinuclear ruthenium antimicrobial complex encapsulated in cucurbit[10]uril. *Org. Biomol. Chem.* 15, 4172–4179. doi: 10.1039/C7OB00724H

Li, F., Harry, E. J., Bottomley, A. L., Edstein, M. D., Birrell, G. W., Woodward, C. E., et al. (2014). Dinuclear ruthenium(II) antimicrobial agents that selectively target polysomes *in vivo*. *Chem. Sci.* 5, 685–693. doi: 10.1039/C3SC52166D

Li, F., Mulyana, Y., Feterl, M., Warner, J. M., Collins, J. G., and Keene, F. R. (2011). The atimicrobial activity of inert oligonuclear polypyridylruthenium(II) complexes against pathogenic bacteria, including MRSA. *Dalton Trans.* 40, 5032–5038. doi: 10.1039/c1dt10250h

Li, X., Gorle, A. K., Ainsworth, T. D., Heimann, K., Woodward, C. E., Collins, J. G., et al. (2015b). RNA and DNA binding of inert oligonuclear ruthenium(II) complexes in live eukaryotic cells. *Dalton Trans.* 44, 3594–3603. doi: 10.1039/c4dt02575j

Li, X., Gorle, A. K., Sundaraneedi, M. K., Keene, F. R., and Collins, J. G. (2018). Kinetically-inert polypyridylruthenium(II) complexes as therapeutic agents. *Coord. Chem. Rev.* 375, 134–147. doi: 10.1016/j.ccr.2017.11.011

Li, X., Heimann, K., Li, F.,Warner, J. M., Keene, F. R., and Collins, J. G. (2016). Dinuclear ruthenium(II) complexes containing one inert metal centre and one coordinatively-labile metal centre: syntheses and biological activities. *Dalton Trans.* 45, 4017–4029. doi: 10.1039/C5DT04885K

Liu, S., Zavalij, P. Y., and Isaacs, L. (2005). Cucurbit[10]uril. *J. Am. Chem. Soc.* 127, 16798–16799. doi: 10.1021/ja056287n

Liu, X., Wright, M., and Hop, C. E. C. A. (2014). Rational use of plasma protein and tissue binding data in drug design. *J. Med. Chem.* 57, 8238–8248. doi: 10.1021/jm5007935

Mital, M., and Ziora, Z. (2018). Biological applications of Ru(II) polypyridyl complexes. *Coord. Chem. Rev.* 375, 434–458. doi: 10.1016/j.ccr.2018.02.013

Mock, W. L., and Shih, N.-Y. (1986). Structure and selectivity in host-guest complexes of cucurbituril. *J. Org. Chem.* 51, 4440–4446. doi: 10.1021/jo00373a018

Moucheron, C. (2009). From cisplatin to photoreactive Ru complexes: targeting DNA for biomedical applications. *New J. Chem.* 33, 235–245. doi: 10.1039/b817016a

Neelakantan, M. A., Esakkiammal, M., Mariappan, S. S., Dharmaraja, J., and Jeyakumar, T. (2010). Synthesis, characterization and biocidal activities of some schiff base metal complexes. *Indian J. Pharm. Sci.* 72, 216–222. doi: 10.4103/0250-474X.65015

Ng, N. S., Leverett, P., Hibbs, D. E., Yang, Q., Bulanadi, J. C., Wu, M. J., et al. (2013). The antimicrobial properties of some copper(II) and platinum(II) 1,10-phenanthroline complexes. *Dalton Trans.* 42, 3196–3209. doi: 10.1039/c2dt32392c

Pandrala, M., Li, F., Feterl, M., Mulyana, Y., Warner, J. M., Wallace, L., et al. (2013). Chlorido-containing ruthenium(II) and iridium(III) complexes as antimicrobial agents. *Dalton Trans.* 42, 4686–4694. doi: 10.1039/c3dt32775b

Pisani, M. J., Zhao, Y., Wallace, L., Woodward, C. E., Keene, F. R., Day, A. I., et al. (2010). Cucurbit[10]uril binding of dinuclear platinum(II) and ruthenium(II) complexes: association/dissociation rates from seconds to hours. *Dalton Trans.* 39, 2078–2086. doi: 10.1039/b921172a

Richards, A. D., Rodger, A., Hannon, M. J., and Bolhuis, A. (2009). Antimicrobial activity of an iron triple helicate. *Int. J. Antimicrob. Agents* 33, 469–472. doi: 10.1016/j.ijantimicag.2008.10.031

Shinde, M. N., Rao, S. S., Gejji, S. P., and Kumbhar, A. A. (2018). Distinct photophysical behavior and transport of cell-impermeable $[Ru(bpy)_2dppz]^{2+}$ in live cells. *Dalton Trans.* 48, 3857–3863. doi: 10.1039/C7DT04230B

Shobha Devi, C., Kumar, D. A., Singh, S. S., Gabra, N., Deepika, N., Kumar, Y. P., et al. (2013). Synthesis, interaction with DNA, cytotoxicity, cell cycle arrest and apoptotic inducing properties of ruthenium(II) molecular "light switch" complexes. *Eur. J. Med. Chem.* 64, 410–421. doi: 10.1016/j.ejmech.2013.04.006

Southam, H. M., Butler, J. A., Chapman, J. A., and Poole, R. K. (2017). The microbiology of ruthenium complexes. *Adv. Microb. Physiol.* 71, 1–96. doi: 10.1016/bs.ampbs.2017.03.001

Sun, B., Southam, H. M., Butler, J. A., Poole, R. K., Burgun, A., Tarzia, A., et al. (2018). Synthesis, isomerisation and biological properties of mononuclear ruthenium complexes containing the bis[4(4'-methyl-2,2'-bipyridyl)]-1,7-heptane ligand. *Dalton Trans.* 47, 2422–2434. doi: 10.1039/C7DT04595F

Sundaraneedi, M. K., Tedla, B. A., Eichenberger, R. M., Becker, L., Pickering, D., Smout, M. J., et al. (2017). Polypyridylruthenium(II) complexes exert anti-schistosome activity and inhibit parasite acetylcholinesterases. *PLoS Negl.Trop. Dis.* 11:e0006134. doi: 10.1371/journal.pntd.0006134

Süss-Fink, G. (2010). Arene ruthenium complexes as anticancer agents. *Dalton Trans.* 39, 1673–1688. doi: 10.1039/b916860p

Wheate, N. J., Day, A. I., Blanch, R. J., Arnold, A. P., Cullinane, C., and Collins, J. G. (2004). Multi-nuclear platinum complexes encapsulated in cucurbit[n]uril as an approach to reduce toxicity in cancer treatment. *Chem. Commun.* 1424–1425. doi: 10.1039/b404358h

Conflict of Interest Statement: The authors declare that the research was conducted in the absence of any commercial or financial relationships that could be construed as a potential conflict of interest.

frontiers in Chemistry

ORIGINAL RESEARCH
published: 21 March 2019
doi: 10.3389/fchem.2019.00154

Supramolecular Fluorescence Probe Based on Twisted Cucurbit[14]uril for Sensing Fungicide Flusilazole

Ying Fan[1,2], *Rui-Han Gao*[2], *Ying Huang*[2], *Bing Bian*[3], *Zhu Tao*[2]* and *Xin Xiao*[2]*

[1] State Key Laboratory Breeding Base of Green Pesticide and Agricultural Bioengineering, Key Laboratory of Green Pesticide and Agricultural Bioengineering, Ministry of Education, Guizhou University, Guiyang, China, [2] Key Laboratory of Macrocyclic and Supramolecular Chemistry of Guizhou Province, Guizhou University, Guiyang, China, [3] College of Chemical and Environmental Engineering, Shandong University of Science and Technology, Qingdao, China

The host-guest complex of the common dye, thioflavin T (ThT), and twisted cucurbit[14]uril (*t*Q[14]) was selected as a fluorescent probe to determine non-fluorescent triazole fungicides, including flusilazole, azaconazole, triadimefon, tebuconazole, tricyclazole, flutriafol, penconazole, and triadimenol isomer A, in an aqueous solution. The experimental results reveal that the ThT@*t*Q[14] probe selectively responded to flusilazole with significant fluorescence quenching and a detection limit of 1.27×10^{-8} mol/L. In addition, the response mechanism involves not only a cooperation interaction—ThT occupies a side-cavity of the *t*Q[14] host and the triazole fungicide occupies another side-cavity of the *t*Q[14] host—but also a competition interaction in which both ThT and the triazole fungicide occupy the side-cavities of the *t*Q[14] host.

Keywords: twisted cucurbit[14]uril, thioflavin T, fluorescent probe, triazole fungicides, flusilazole

OPEN ACCESS

Edited by:
Angela Casini,
Cardiff University, United Kingdom

Reviewed by:
Dong-Sheng Guo,
Nankai University, China
Simin Liu,
Wuhan University of Science and Technology, China

***Correspondence:**
Zhu Tao
gzutao@263.net
Xin Xiao
gyhxxiaoxin@163.com

Specialty section:
This article was submitted to Supramolecular Chemistry, a section of the journal Frontiers in Chemistry

Received: *30 August 2018*
Accepted: *01 March 2019*
Published: *21 March 2019*

Citation:
Fan Y, Gao R-H, Huang Y, Bian B, Tao Z and Xiao X (2019) Supramolecular Fluorescence Probe Based on Twisted Cucurbit[14]uril for Sensing Fungicide Flusilazole. Front. Chem. 7:154. doi: 10.3389/fchem.2019.00154

INTRODUCTION

Triazole systemic fungicides, particularly flusilazole (1-{[*bis*(4-fluorophenyl) (methyl)silyl] methyl}-1*H*-1,2,4-triazole), are widely used in fruit, vegetable, and grain crops during cultivation and storage with high efficiency and good sterilization ability (**Figure 1**) (Zhang Y. H. et al., 2016). However, they still have somewhat toxic or other undesirable side effects on non-target organisms. Extensive or inappropriate use can cause soil and water pollution, and thus threaten human health (Ma et al., 2016). Therefore, it is necessary to develop sensitive and selective methods for the analysis of triazole fungicides, which are usually present in trace amounts.

The most common analytical method used for the trace determination of triazoles, particularly flusilazole residues in water, is chromatography e.g., liquid chromatography-tandem mass spectrometry (LC-MS/MS) (García-Valcárcel and Tadeo, 2011; Fu et al., 2017), high-performance liquid chromatography (HPLC) with ultraviolet light, diode-array detection (DAD), photodiode-array (PDA) detection (Bordagaray et al., 2013, 2014; Qi et al., 2014; Ma et al., 2016; Zhang Y. H. et al., 2016), gas chromatography (GC) with nitrogen-phosphorous detection (NPD) or electron capture detection (ECD) (Lozowicka et al., 2015; Im et al., 2016), and GC-mass spectrometry (GC-MS) (Tseng et al., 2014; Chu et al., 2015), and with tandem MS (GC-MS/MS) (Xu et al., 2013). Nevertheless, these chromatographic techniques necessitate experienced workers, costly devices, and lengthy specimen preparation. In comparison with the above-mentioned methods, spectrofluorimetry is the most favorable analytical strategy employed to analyze different biological specimens due to its innate simplicity, high sensitivity, and accessibility in the majority of quality-control and clinical laboratories (Yao et al., 2013). However, determination

of the existence of many common triazoles cannot be performed directly using typical fluorimetric techniques since the aqueous solutions with triazoles do not have native fluorescence.

It is noteworthy that the complexation of a fluorescent dye with a macrocycle host can induce significant change in its fluorescence (Zhou et al., 2008; Zhang et al., 2012; Kogawa et al., 2014). Such assays depend on an indicator-displacement technique in which the analyte competitively supplants a fluorescent guest that results in an alteration in its fluorescence intensity (You et al., 2015; Sayed and Pal, 2016). Various macrocyclic compounds, including cyclodextrins, calix[*n*]arenes, and pillar[*n*]arenas, have long been employed as the hosts in several macrocyclic-dye supramolecular systems (Choudhury et al., 2010; Lau and Heyne, 2010; Liu et al., 2015b; Sun et al., 2015). In particular, cucurbit[*n*]urils (Q[*n*]s) are made up of n glycoluril units connected via 2n methylene bridges (Day et al., 2000; Kim et al., 2000; Cong et al., 2016). These hosts have highly polar carbonyl-fringed portals with hydrophobic cavities that can create remarkably stable complexes with different guest molecules (Kim, 2002; Dsouza et al., 2011; Gao et al., 2017; Liu J. et al., 2017; Murray et al., 2017; Yang et al., 2018). The origination of inclusion complexes frequently improves or interrupts the photo-physical and photo-chemical characteristics of the guest molecules. For example, using different Q[*n*]s to encapsulate some dyes can change the fluorescent characteristics of the guest molecules (Praetorius et al., 2008; Baumes et al., 2009, 2011; Choudhury et al., 2009). The dye@Q[*n*] complexes can be composed of supramolecular fluorescent probes with high sensitivity and selectivity to recognize and detect analytes, such as metal ions, amines, pesticides, drugs, and DNA (Wheate, 2008; Mohanty et al., 2009; Nau et al., 2009; Zhou et al., 2009; Day and Collins, 2012; Xing et al., 2013; Elbashir and Aboul-Enein, 2015; Liu W. Q. et al., 2017; Xi et al., 2017; Tang et al., 2018; Wang et al., 2018).

Thioflavin T, 3,6-dimethyl-2-(4-dimethylaminophenyl) benzthiazolium cation (ThT) is a benzthiazolium dye (**Figure 1**). An aqueous solution of ThT reveals a weak native fluorescence. Nevertheless, as revealed by previous evaluations, the fluorescence of ThT in an aqueous solution can be vastly improved in the presence of Q[7], Q[8], and twisted cucurbit[14]uril (*t*Q[14]). It was found that ThT can form ThT@Q[*n*] inclusion complexes with different stoichiometric ratios, which can be applied to identify both alkali-metal and alkaline-earth-metal ions (Choudhury et al., 2009, 2010; Mohanty et al., 2009; Wang et al., 2018). In the present study, a procedure was proposed to determine the residues of triazole fungicides, such as azaconazole, triadimefon, tebuconazole, tricyclazole, flutriafol, penconazole, and triadimenol isomer A in aqueous solution (**Figure 1**).

RESULTS AND DISCUSSION

Fluorescence Quenching of ThT@*t*Q[14] With Flusilazole

Previous studies have proven that the fluorescence of ThT in an aqueous solution over a wide range of interaction ratios can be enhanced by its interaction with *t*Q[14] via different interaction models due to the multiple cavity features of the *t*Q[14] molecule and two active moieties (the benzothiazole and dimethylaminobenzene moieties) in ThT (Wang et al., 2018). In the current work, we focused on the inclusion complexes of ThT@*t*Q[14] with 1:1 and 1:5 interaction ratios in the presence of the eight selected triazoles, the corresponding fluorescence spectra of which can be seen in **Figure 2** and **Figures S1–S3**. A significant fluorescence quenching of the ThT@*t*Q[14] inclusion complex probe (1:1) was only observed upon increasing the amount of flusilazole; ∼60% of the fluorescence intensity was lost when $C_{flusilazole}/C_{ThT@tQ[14]}$ was ∼4 (**Figure 2A**). **Figure 2B** shows the plot of the fluorescence intensity at $\lambda_{em} = 488$ nm upon increasing the flusilazole concentration; $K_{observed}$ was calculated by the nonlinear-least-squares method to be $(8.2 \pm 0.4) \times 10^5$ L/mol obtained (**Figure S4**), which is likely due to the influence of the interaction of *t*Q[14] with flusilazole on the interaction of *t*Q[14] with ThT. Moreover, the ThT@*t*Q[14] fluorescent probe presented high selectivity for flusilazole because the probe showed little or almost no response to the other seven triazole fungicides studied (**Figure 3** and **Figure S1**). The ThT@*t*Q[14] inclusion complex probe at a molar ratio of 1:5 was also selected to investigate its response to triazole pesticides with the addition of flusilazole also leading to a fluorescence quenching of the ThT@*t*Q[14] inclusion complex probe; only ∼22% of the fluorescence intensity was lost when $C_{flusilazole}/C_{ThT@tQ[14]}$ was ∼4 (**Figure S2**). However, the ThT@*t*Q[14] fluorescent probe also showed little or almost no response to the other triazole fungicides studied (**Figure S3**).

Analytical Characteristics of ThT@*t*Q[14] Probe

The standard calibration curve (**Figure S5**) of the complexes of flusilazole with ThT@*t*Q[14] (1:1) was obtained using the plot of fluorescence intensity *F* compared to flusilazole concentration. The linear range was (0.0–1.0) $\times 10^{-6}$ mol/L for flusilazole with a correlation coefficient of 0.9888. For flusilazole, the limit of detection (LOD) was 1.27×10^{-8} mol/L and the linear regression equation $F = -216.24C + 576.26$. Although the ThT@*t*Q[14] (1:5) inclusion complex was less sensitive to flusilazole, it still exhibited a very low LOD (2.80×10^{-8} mol/L) and the linear regression equation was $F = -98.25C + 863.26$ (**Figure S6**).

Effects of Interfering Substances

In the present work, the impacts of different common interfering substances on the determination of flusilazole using the ThT@*t*Q[14] probe were also investigated. The tolerance limit was established as the concentration of an added interfering substance that causes a relative error of $< \pm 5\%$ in the flusilazole determination. The samples consisted of a fixed amount of flusilazole (1.0 μM) and ThT@*t*Q[14] (1.0 μM) with an increasing amount of different interfering substances; the corresponding results are shown in **Table 1** and **Figure S7**. It is clear that the determination was free from interference in the presence of the common metal ions and anions in aqueous solutions, except Ca^{2+}. Structural analysis revealed that *t*Q[14] had a similar portal size to those of Q[6] and

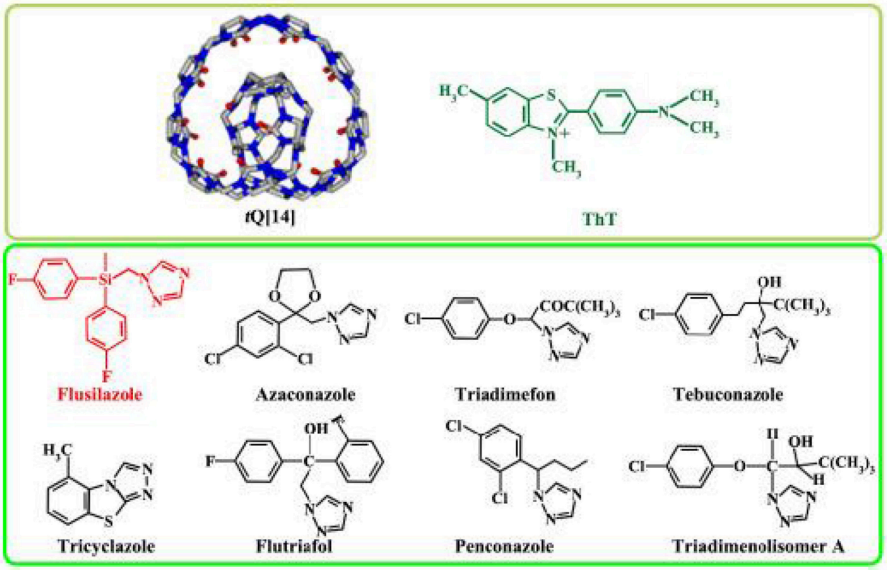

FIGURE 1 | Structures of *t*Q[14], ThT, and eight fungicide triazoles, namely flusilazole, azaconazole, triadimefon, tebuconazole, tricyclazole, flutriafol, penconazole, and triadimenol isomer A.

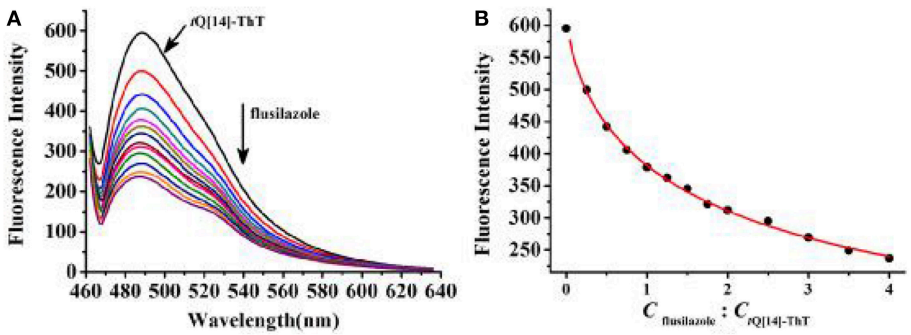

FIGURE 2 | (A) Fluorescence titration spectra (λ_{ex} = 448 nm) for ThT@*t*Q[14] (1:1, 1 μM) in the presence of flusilazole of the following different stoichiometries in μM: 0, 0.25, 0.5, 0.75, 1.0, 1.25, 1.5, 1.75, 2.0, 2.5, 3.0, 3.5, and 4.0; **(B)** Plot obtained for fluorescence intensity of ThT@*t*Q[14] vs. $C_{flusilazole}/C_{ThT@tQ[14]}$.

Q[7] (Cheng et al., 2013; Liu et al., 2015a; Li et al., 2016; Zhang J. et al., 2016; Zhang et al., 2017), and a higher portal carbonyl intensity (Cheng et al., 2013; Liu et al., 2015a; Zhang J. et al., 2016; Zhang et al., 2017), which could exhibit a higher affinity for metal cations, particularly the Ca^{2+} cation (Cheng et al., 2013; Qiu et al., 2017; Wang et al., 2018). The titration fluorescence spectra recorded for the *t*Q[14]-ThT-flusilazole (1:1:1) system upon increasing the amount of Ca^{2+} showed that the fluorescence of the ternary interaction system could be further decreased due to the influence of the Ca^{2+} cation (**Figure S8**). The titration ^{1}H nuclear magnetic resonance (NMR) spectra for the *t*Q[14]-ThT-flusilazole (1:1:1) system in the presence of Ca^{2+} also showed that the guest molecules, ThT and flusilazole, were gradually pushed out from the cavity area upon increasing the amount of Ca^{2+} (**Figure S9**).

Preliminary Exploration of the Response Mechanism of ThT@*t*Q[14] Fluorescent Probe Toward Flusilazole

Titration ^{1}H NMR Spectra

We have found that the ThT@*t*Q[14] fluorescent probe was selectively sensitive toward flusilazole and could be used to detect flusilazole via a significant fluorescence quenching process. Why is the ThT@*t*Q[14] fluorescent probe selectively sensitive to flusilazole? How does the flusilazole molecule influence the interaction between the ThT molecule with the *t*Q[14] host molecule? What could the interaction mode be? To understand the selectivity and response mechanism of the ThT@*t*Q[14] fluorescent probe toward flusilazole, titration ^{1}H NMR spectra were recorded upon the gradual addition of one of the selected triazole fungicides into the solution of the ThT@*t*Q[14] (1:1) fluorescent probe. The detailed interaction of ThT and *t*Q[14]

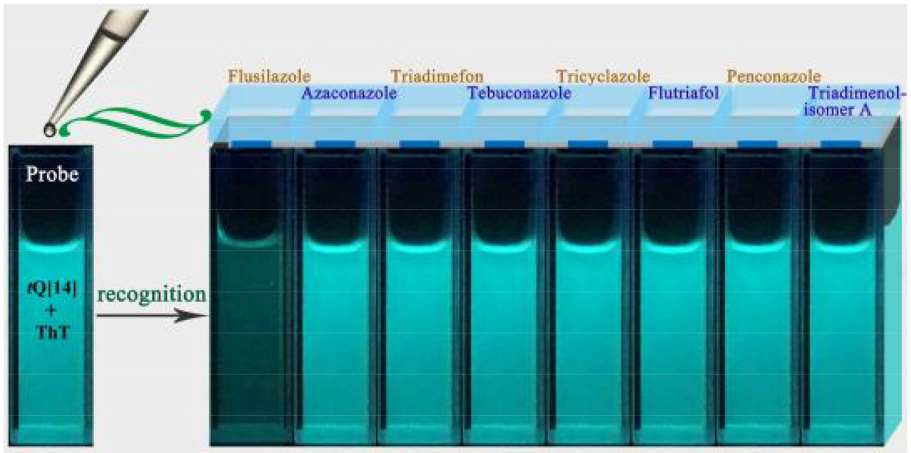

FIGURE 3 | Fluorescence images of ThT@*t*Q[14] (50 μM) upon addition of eight triazole pesticides (50 μM) under UV-lamp irradiation (365 nm).

TABLE 1 | Impact of interfering substances (tolerance error ± 5%).

Interfering	Tolerance (mol/L)	Relative error (%)
Na^+	6.0×10^{-5}	−3.38
K^+	5.0×10^{-5}	−1.94
Zn^{2+}	1.0×10^{-3}	−2.65
Mg^{2+}	1.0×10^{-3}	−2.45
Cu^{2+}	5.0×10^{-5}	−4.67
Cl^-	4.0×10^{-5}	−3.97
Br^-	5.0×10^{-5}	−1.38
NO_3^-	6.0×10^{-5}	−4.63
HSO_4^-	5.0×10^{-5}	−1.38
$H_2PO_4^-$	4.0×10^{-5}	−2.77

has been discussed in a previous work (**Figures 4A,B**) (Wang et al., 2018). **Figure 4F** shows the ^{1}H NMR spectrum for the flusilazole in the presence of *t*Q[14]. When compared with the ^{1}H NMR spectrum for the unbound flusilazole molecule (**Figure 4G**), the proton resonances corresponding to H5 and H6 on the triazole moiety of the bound flusilazole molecule underwent slightly down-field shifts (0.01 and 0.01 ppm, respectively), whereas the other proton resonances experienced slightly up-field shifts, suggesting that a weak interaction existed between *t*Q[14] and the flusilazole guest molecule or π · ·· π stacking of the aryl groups of the flusilazole guest molecules. **Figures 4C–E** show the titration ^{1}H NMR spectra for the *t*Q[14]-ThT complex upon increasing the amount of flusilazole. The addition of flusilazole appeared to pull the bound ThT out of the interaction area of the *t*Q[14] host because the proton resonances were closer to those of the unbound ThT molecule. However, the proton resonances of flusilazole, in particular, the H5 and H6 experienced down-field shift, suggesting that ThT was still interacting with the host and flusilazole was located in the de-shielding region of *t*Q[14] (probably at portal area). Similar phenomena could be observed for the other *t*Q[14]-ThT-triazole fungicide systems, in which the addition of the triazole fungicide could lead to a change in the interaction between *t*Q[14] and ThT. Moreover, both ThT and the triazole fungicide exhibited an interaction with the *t*Q[14] host (**Figures S10–S16**). At first, it seemed that it was difficult to obtain the required information using the titration ^{1}H NMR method. A closer inspection revealed that the addition of different triazole fungicides could lead to different chemical shifts for the proton resonances corresponding to the ThT molecule, and the effects of the different triazole fungicides on the bound ThT were compared with the chemical shift corresponding to proton Hg. The data in **Table 2** reveal that flusilazole resulted in the larger change in the chemical-shift values ($\Delta\delta = 0.05$) when the *t*Q[14]-ThT-triazole fungicide ratio was 1:1:2.

2D diffusion-ordered NMR spectroscopy (DOSY) experiments were performed to afford further evidence for the formation of the *t*Q[14]-ThT-flusilazole (1:1:1) ternary interaction species. **Figure S17** depicts the DOSY spectra of *t*Q[14], ThT, flusilazole, and *t*Q[14]-ThT-flusilazole (1:1:1) ternary interaction species in D_2O at 298 K and the corresponding diffusion coefficients (D) are 3.49×10^{-10}, 5.46×10^{-10}, 3.88×10^{-10}, and 2.92×10^{-10}, respectively. According to the values of four species, the *t*Q[14]-ThT-flusilazole (1:1:1) ternary interaction species is the smallest, suggesting that the ternary species could be the largest species, moreover, all the proton signals of the host and the guest display the same diffusion coefficient ($D = 2.92 \times 10^{-10} \cdot m^2 \cdot s^{-1}$), indicating that they are part of the same species.

Isothermal Titration Calorimetry

Isothermal titration calorimetry (ITC) experiments were conducted to determine the association constants and thermodynamic parameters of the host-guest interaction between *t*Q[14] and ThT with the triazole fungicides in an aqueous solution to further explore the fluorescence-quenching mechanism of ThT@*t*Q[14] with flusilazole (**Figures S18–S26**). From the data acquired (**Table 3**), all the association constants obtained for the triazole fungicides@*t*Q[14] complexes

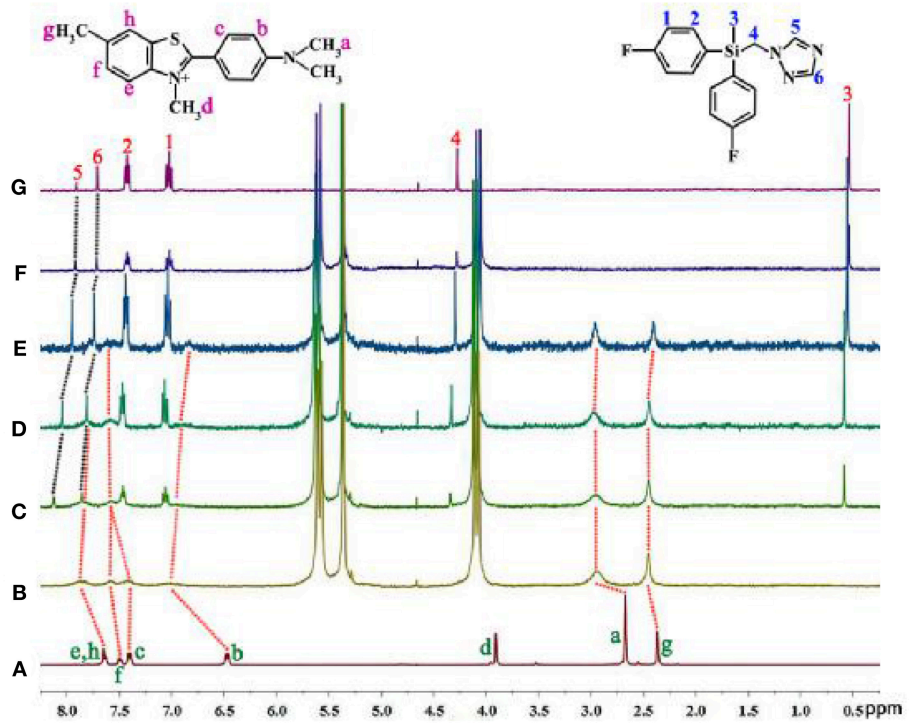

FIGURE 4 | ^{1}H NMR spectra (400 MHz, D_2O) for **(A)** ThT, **(B)** *t*Q[14]-ThT (1:1), **(C)** *t*Q[14]-ThT-flusilazole (1:1:0.5), **(D)** *t*Q[14]-ThT-flusilazole (1:1:1), **(E)** *t*Q[14]-ThT-flusilazole (1:1:2), **(F)** *t*Q[14]-flusilazole, and **(G)** flusilazole.

TABLE 2 | Chemical shifts corresponding to proton Hg of ThT.

Guest	δ [Q14-ThT (1:1)]	δ [Q14-ThT-G (1:1:2)]	Δδ
Flusilazole	2.469	2.419	0.050
Azaconazole	2.453	2.439	0.014
Triadimefon	2.458	2.429	0.029
Tebuconazole	2.449	2.422	0.027
Tricyclazole	2.450	2.432	0.018
Flutriafol	2.453	2.429	0.024
Penconazole	2.451	2.430	0.021
Triadimenol isomer A	2.457	2.437	0.020

TABLE 3 | Thermodynamic parameters of *t*Q[14] and ThT with eight triazole pesticides in aqueous solution at 298.15 K.

Complex	*Ka* (m $^{-1}$)	Δ*H*(kJ/mol)	*T*Δ*S*(kJ/mol)
*t*Q[14]-ThT	$(1.28 \pm 0.03) \times 10^5$	−48.4	−19.2
*t*Q[14]-flusilazole	$(8.39 \pm 0.05) \times 10^5$	−38.4	−4.6
*t*Q[14]-azaconazole	$(5.45 \pm 0.08) \times 10^5$	−36.8	−4.0
*t*Q[14]-triadimefon	$(1.46 \pm 0.04) \times 10^5$	−64.3	−34.9
*t*Q[14]-tebuconazole	$(3.00 \pm 0.09) \times 10^5$	−42.7	−11.4
*t*Q[14]-tricyclazole	$(5.01 \pm 0.12) \times 10^5$	−36.8	−4.2
*t*Q[14]-flutriafol	$(1.97 \pm 0.05) \times 10^5$	−64.6	−34.3
*t*Q[14]-penconazole	$(5.23 \pm 0.08) \times 10^5$	−38.8	−6.2
*t*Q[14]-triadimenol isomer A	$(4.31 \pm 0.10) \times 10^5$	−39.0	−6.9

[(1.46–8.39) × 10^5 L/mol] were slight larger than that of the ThT@*t*Q[14] complex (1.28 × 10^5 L/mol), but there are no significant differences. The titration ^{1}H NMR study has proved that these pesticides could not replace ThT to form pesticide@*t*Q[14] inclusion complexes.

The fluorescence enhancement mechanism of ThT could be due to the restriction of the freely rotating dimethylamine group on the benzene moiety, making the lone pair electrons on nitrogen atoms conjugate to the ThT aromatic system. The shell-like cavity structure of *t*Q[14] can provide such controlled environment, the inclusion of dimethylamino phenyl moiety of ThT inhibited dimethylamino free rotation, moreover, the shell-like cavity structure of *t*Q[14] could prevent ThT from threading through the side cavity of *t*Q[14] (Liu et al., 2015a; Li et al., 2016). Therefore, we can observe ThT fluorescence enhancement. Unlike HMeQ[6] and Q[7] which have similar portal sizes to that of the side portals of *t*Q[14], ThT could thread through their cavities, and show a weak fluorescence emission (referring the fluorescence spectra as shown in **Figure S27**). On the other hand, the fluorescence emission of ThT is also affected by its electron-pushing group (dimethylamine group) and electron-withdrawing group (quaternary ammonium moiety). The titration ^{1}H NMR spectra could provide the interaction images of this ternary system: the flusilazole was located in the de-shielding region of *t*Q[14] (probably at portal area), which caused the chemical shift change of ThT proton resonance to move

toward the free ThT, in particular, the interaction of the azole moiety and quaternary ammonium moiety could weaken the electron-withdrawing capacity of quaternary ammonium moiety, resulting in partial quenching of the fluorescence of the *t*Q[14]-ThT-flusilazole interaction system (**Figure 5**). According to the suggested interaction mode, whether the fluorescence quenching of ThT@*t*Q[14] is caused mainly depends on the interaction of the azole moiety of pesticides and quaternary ammonium moiety of ThT and the ability of pesticides to pull ThT out of the side cavity of *t*Q[14]. While the NMR and ITC measurement results showed that the flusilazole has the biggest impact, although the differences from other triazole fungicides are subtle.

CONCLUSIONS

In order to further expand the application of Q[*n*]-based host-guest chemistry, especially the host-guest complexes with fluorescent properties, in detection and recognition, a known host-guest complex of ThT@*t*Q[14] (1:1) was used as a fluorescent probe to determine non-fluorescence triazole fungicides, including flusilazole, azaconazole, triadimefon, tebuconazole, tricyclazole, flutriafol, penconazole, and triadimenol isomer A. This new and simple fluorometry method proved to be highly selective and sensitive to one of triazole fungicides—flusilazole, and the determination was free from interference by the common metal ions and anions in aqueous solutions, except Ca^{2+}. The investigation of the response mechanism revealed that a side-cavity of the *t*Q[14] host includes the dimethylamino phenyl moiety of ThT, resulting in the ThT fluorescence enhancement; the addition of flusilazole results in the interaction of the azole moiety of flusilazole and quaternary ammonium moiety of ThT, which could weaken the electron-withdrawing capacity of quaternary ammonium moiety, resulting in partial quenching of the fluorescence of the *t*Q[14]-ThT-flusilazole interaction system. This unusual phenomenon results from the novel structural feature of *t*Q[14], namely that *t*Q[14] possesses a central-cavity and two of the same side-cavities.

EXPERIMENT

Materials

*t*Q[14] was set up and purified in our laboratory according to a procedure detailed in the literature (Cheng et al., 2013). Analytical grade flusilazole (99.5%), azaconazole (99.5%), triadimefon (99.0%), tebuconazole (99.0%), tricyclazole (99.0%), flutriafol (98.6%), penconazole (99.5%), and triadimenol isomer A (95.4%) were purchased from Dr. Ehrenstorfer GmbH (Augsburg, Germany) and used as-received without any further purification. Double-distilled water was used for each of the experiments.

^{1}H NMR

Each of the ^{1}H NMR spectra, including those for titration experiments, were documented at 25°C on a JEOL JNM-ECZ400s spectrometer using $SiMe_4$ as an internal reference. D_2O was utilized as a field-frequency lock and the chemical shifts documented in parts per million (ppm).

ITC

Microcalorimetric experiments were conducted with a Nano ITC (TA, USA) isothermal titration calorimeter. Then, 25 consecutive 10-μL aliquots of a 1 mM *t*Q[14] solution were introduced into the microcalorimetric reaction cell, which contained 1.3 mL of a 0.1-mM guest molecule solution at 25°C. The heat of reaction was

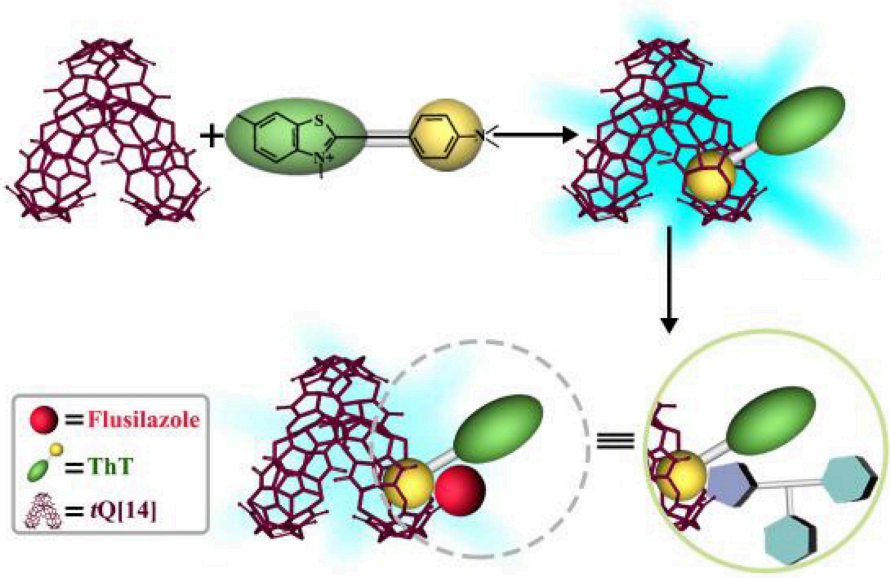

FIGURE 5 | Possible response mechanism for fluorescent probe ThT@*t*Q[14] with flusilazole.

corrected for the heat of dilution of the guest molecule solution, which was determined in a separate experiment. Each of the solutions were de-gassed before the titration via ultrasonication. Computer simulations (curve fitting) were conducted with Nano ITC analysis software.

Fluorescence Titration

The fluorescence spectra of the host-guest complexes were documented at 25°C using a Varian Cary Eclipse spectrofluorometer (Varian, Inc., Palo Alto, CA, USA). Stock solutions of *t*Q[14] (1×10^{-3} mol L^{-1}), ThT (1×10^{-3} mol L^{-1}), and flusilazole (1×10^{-4} mol L^{-1}) were set up in water. Working solutions were set up by diluting the stock solutions to the necessary concentrations.

A *t*Q[14]-ThT (1:1) complex solution was set up at a fixed concentration of 1×10^{-6} mol·L^{-1} in H_2O, which was subsequently combined with flusilazole at guest/host ratios of 0, 0.25:1, 0.5:1, 0.75:1, 1:1, …, and 4:1. Fluorescence spectrophotometric titrations were established as detailed prior ($\lambda_{ex} = 448$ nm and $\lambda_{em} = 488$ nm). For each experiment, three replicate measurements were recorded.

LOD Measurement

The calculation technique used for the LOD was based on the standard derivation of 10 measurements without the guest molecule (σ) and the slope of the linear calibration curve (K) based on the formula $LOD = 3\sigma/K$.

The standard deviation of 10 measurements without the guest molecule could be determined based on the following relationship: $\sigma = \sqrt{\frac{1}{n-1}\sum_{i=1}^{n}(x_i - \bar{x})^2}$,where n is the number of measurements ($n = 11$).

AUTHOR CONTRIBUTIONS

YF, R-HG, YH, and BB undertook the acquisition and analysis of data for the work. ZT and XX drafted the work and revised it critically for important intellectual content.

ACKNOWLEDGMENTS

We acknowledge the support of the National Natural Science Foundation of China (Grant No. 21562015), the Creative Research Groups of Guizhou Provincial Education Department (2017-028), and the Innovation Program for High-level Talents of Guizhou Province (No. 2016-5657).

SUPPLEMENTARY MATERIAL

The Supplementary Material for this article can be found online at: https://www.frontiersin.org/articles/10.3389/fchem.2019.00154/full#supplementary-material

REFERENCES

Baumes, L. A., Buaki, M., Jolly, J., Corma, A., and Garcia, H. (2011). Fluorimetric detection and discrimination of a-amino acids based on tricyclic basic dyes and cucurbiturils supramolecular assembly. *Tetrahedron Lett.* 52, 1418–1421. doi: 10.1016/j.tetlet.2011.01.071

Baumes, L. A., Sogo, M. B., Montes-Navajas, P., Corma, A., and Garcia, H. (2009). First colorimetric sensor array for the identification of quaternary ammonium salts. *Tetrahedron Lett.* 50, 7001–7004. doi: 10.1016/j.tetlet.2009.09.165

Bordagaray, A., García-Arrona, R., and Millán, E. (2013). Development and application of a screening method for triazole fungicide determination in liquid and fruit samples using solid-phase microextraction and HPLC-DAD. *Anal. Methods* 5, 2565–2571. doi: 10.1039/c3ay26433e

Bordagaray, A., García-Arrona, R., and Millán, E. (2014). Determination of triazole fungicides in liquid samples using ultrasound-assisted emulsification microextraction with solidification of floating organic droplet followed by high-performance liquid chromatography. *Food Anal. Methods* 7, 1195–1203. doi: 10.1007/s12161-013-9733-2

Cheng, X. J., Liang, L. L., Chen, K., Ji, N. N., Xiao, X., Zhang, J. X., et al. (2013). Twisted cucurbit[14]uril. *Angew. Chem. Int. Ed.* 52, 7252–7255. doi: 10.1002/anie.201210267

Choudhury, S. D., Mohanty, J., Pal, H., and Bhasikuttan, A. C. (2010). Cooperative metal ion binding to a cucurbit[7]uril-thioflavin T complex: demonstration of a stimulus-responsive fluorescent supramolecular capsule. *J. Am. Chem. Soc.* 132, 1395–1401. doi: 10.1021/ja908795y

Choudhury, S. D., Mohanty, J., Upadhyaya, H. P., Bhasikuttan, A. C., and Pal, H. (2009). Photophysical studies on the noncovalent interaction of thioflavin T with cucurbit[*n*]uril macrocycles. *J. Phys. Chem. B* 113, 1891–1898. doi: 10.1021/jp8103062

Chu, S. P., Tseng, W. C., Kong, P. H., Huang, C. K., Chen, J. H., Chen, P. S., et al. (2015). Up-and-down-shaker-assisted dispersive liquid–liquid microextraction coupled with gas chromatography–mass spectrometry for the determination of fungicides in wine. *Food Chem.* 185, 377–382. doi: 10.1016/j.foodchem.2015.04.015

Cong, H., Ni, X. L., Xiao, X., Huang, Y., Zhu, Q. J., Xue, S. F., et al. (2016). Synthesis and separation of cucurbit[n]urils and their derivatives[J]. *Org. Biomol. Chem.* 14, 4335–4364. doi: 10.1039/C6OB00268D

Day, A. I., Arnold, A. P., and Blanch, R. J. (2000). Method for synthesis of cucurbiturils. *PCT Int. Appl.* 112.

Day, A. I., and Collins, J. G. (2012). Cucurbituril receptors and drug delivery. *Supramol. Chem.* 3, 983–1000. doi.org/10.1002/9780470661345.smc056

Dsouza, R. N., Pischel, U., and Nau, W. M. (2011). Fluorescent dyes and their supramolecular host/guest complexes with macrocycles in aqueous solution. *Chem. Rev.* 111, 7941–7980. doi: 10.1021/cr200213s

Elbashir, A., and Aboul-Enein, H. Y. (2015). Supramolecular analytical application of cucurbit[n]urils using fluorescence spectroscopy. *Crit. Rev. Anal. Chem.* 45, 52–61. doi: 10.1080/10408347.2013.876354

Fu, Y., Yang, T., Zhao, J., Zhang, L., Chen, R. X., and Wu, Y. L. (2017). Determination of eight pesticides in Lycium barbarum by LC-MS/MS and dietary risk assessment. *Food Chem.* 218, 192–198. doi: 10.1016/j.foodchem.2016.09.014

Gao, R. H., Chen, L. X., Chen, K., Tao, Z., and Xiao, X. (2017). Development of hydroxylated cucurbit[n]urils, their derivatives and potential applications. *Coordinat. Chem. Rev.* 348, 1–24. doi: 10.1016/j.ccr.2017.07.017

García-Valcárcel, A. I., and Tadeo, J. L. (2011). Determination of azoles in sewage sludge from Spanish wastewater treatment plants by liquid chromatography-tandem mass spectrometry. *J. Sep. Sci.* 34, 1228–1235. doi: 10.1002/jssc.201000814

Im, S. J., Rahman, M. M., El-Aty, A. M. A., Kim, S. W., Kabir, H., Farha, W., et al. (2016). Simultaneous detection of fluquinconazole and flusilazole in lettuce using gas chromatography with a nitrogen phosphorus detector: decline patterns at two different locations. *Biomed. Chromatogr.* 30, 946–952. doi: 10.1002/bmc.3634

Kim, J., Jung, I. S., Kim, S. Y., Lee, E., Kang, J. K., Sakamoto, S., et al. (2000). New cucurbituril homologues: syntheses, isolation, characterization, and X-ray

crystal structures of cucurbit[n]uril (n = 5, 7, and 8). *J. Am. Chem. Soc.* 122, 540–541. doi: 10.1021/ja993376p

Kim, K. (2002). Mechanically interlocked molecules incorporating cucurbituril and their supramolecular assemblies. *Chem. Soc. Rev.* 31, 96–107. doi: 10.1039/a900939f

Kogawa, C., Zoppi, A., Quevedo, M. A., Salgado, H. R. N., and Longhi, M. R. (2014). Increasing doxycycline hyclate photostability by complexation with beta-cyclodextrin. *AAPS PharmSciTech*. 15, 1209–1217. doi: 10.1208/s12249-014-0150-7

Lau, V., and Heyne, B. (2010). Calix[4]arene sulfonate as a template for forming fluorescent thiazole orange H-aggregates. *Chem. Commun.* 46, 3595–3597. doi: 10.1039/c002128h

Li, Q., Qiu, S. C., Chen, K., Zhang, Y., Wang, R. B., Huang, Y., et al. (2016). Encapsulation of alkyldiammonium ions within two different cavities of twisted cucurbit[14]uril. *Chem. Commun*. 52, 2589–2592. doi: 10.1039/C5CC08642F

Liu, J., Lan, Y., Yu, Z. Y., Tan, C. S. Y., Parker, R. M., Abell, C., et al. (2017). Cucurbit[n]uril-based microcapsules self-assembled within microfluidic droplets: a versatile approach for supramolecular architectures and materials. *Acc. Chem. Res*. 50, 208–217. doi: 10.1021/acs.accounts.6b00429

Liu, Q., Li, Q., Cheng, X. J., Xi, Y. Y., Xiao, B., Xiao, X., et al. (2015a). A novel shell-like supramolecular assembly of 4,4-bipyridyl derivatives and a twisted cucurbit[14]uril molecule. *Chem. Commun*. 51, 9999–10001. doi: 10.1039/C5CC02653A

Liu, Q., Yang, Y., Li, H., Zhu, R., Shao, Q., Yang, S., et al. (2015b). NiO nanoparticles modified with 5,10,15,20-tetrakis(4-carboxyl pheyl)-porphyrin: promising peroxidase mimetics for H_2O_2 and glucose detection. *Biosens Bioelectron.* 64, 147–153. doi: 10.1016/j.bios.2014.08.062

Liu, W. Q., Samanta, S. K., Smith, B. D., and Isaacs, L. (2017). Synthetic mimics of biotin/(strept)avidin. *Chem. Soc. Rev*. 46, 2391–2403. doi: 10.1039/C7CS00011A

Lozowicka, B., Abzeitova, E., Sagitov, A., Kaczynski, P., Toleubayev, K., and Li, A. (2015). Studies of pesticide residues in tomatoes and cucumbers from Kazakhstan and the associated health risks. *Environ. Monit. Assess.* 187:609. doi: 10.1007/s10661-015-4818-6

Ma, J. P., Yao, Z. D., Hou, L. W., Lu, W. H., Yang, Q. P., Li, J. H., et al. (2016). Metal organic frameworks (MOFs) for magnetic solid-phase extraction of pyrazole/pyrrole pesticides in environmental water samples followed by HPLC-DAD determination. *Talanta* 161, 686–692. doi: 10.1016/j.talanta.2016.09.035

Mohanty, J., Choudhury, S. D., Upadhyaya, H. P., Bhasikuttan, A. C., and Pal, H. (2009). Control of the supramolecular excimer formation of thioflavin T within acucurbit[8]uril host: a fluorescence on/off mechanism. *Chem. Eur. J.* 15, 5215–5219. doi: 10.1002/chem.200802686

Murray, J., Kim, K., Ogoshi, T., Yao, W., and Gibb, B. C. (2017). The aqueous supramolecular chemistry of cucurbit[n]urils, pillar[n]arenes and deep-cavity cavitands. *Chem. Soc. Rev*. 46, 2479–2496. doi: 10.1039/C7CS00095B

Nau, W. M., Ghale, G., Hennig, A., Bakirci, H., and Bailey, D. M. (2009). Substrate-selective supramolecular tandem assays: monitoring enzyme inhibition of arginase and diamine oxidase by fluorescent dye displacement from calixarene and cucurbituril macrocycles. *J. Am. Chem. Soc.* 131, 11558–11570. doi: 10.1021/ja904165c

Praetorius, A., Bailey, D. M., Schwarzlose, T., and Nau, W. M. (2008). Design of a fluorescent dye for indicator displacement from cucurbiturils: a macrocycle-responsive fluorescent switch operating through a pK_a shift. *Org. Lett*. 10, 4089–4092. doi: 10.1021/ol8016275

Qi, R. F., Jiang, H. C., Liu, S. X., and Jia, Q. (2014). Preconcentration and determination of pesticides with graphene-modified polymer monolith combined with high performance liquid chromatography. *Anal. Methods* 6, 1427–1434. doi: 10.1039/c3ay41688g

Qiu, S. C., Chen, K., Wang, Y., Hua, Z. Y., Li, F., Huang, Y., et al. (2017). Crystal structure analysis of twisted cucurbit [14]uril conformations. *Inorg. Chem. Commun*. 86, 49–53. doi: 10.1016/j.inoche.2017.09.024

Sayed, M., and Pal, H. (2016). Supramolecularly assisted modulations in chromophoric properties and their possible applications: an overview. *J. Mater. Chem. C* 4, 2685–2706. doi: 10.1039/C5TC03321G

Sun, N. N., Xiao, X., Li, W., and Jiang, J. Z. (2015). Multi-stimuli sensitive behavior of novel bodipy-involved pillar[5]arene-based fluorescent [2]rotaxane and its supramolecular gel. *Adv. Sci.* 2, 1500082–1500090. doi: 10.1002/advs.201500082

Tang, Q., Zhang, J., Sun, T., Wang, C. H., Huang, Y., Zhou, Q. D., et al. (2018). A turn-on supramolecular fluorescent probe for sensing benzimidazole fungicides and its application in living cell imaging. *Spectrochim. Acta Part A Mol. Biomol. Spectrosc.* 191, 372–376. doi: 10.1016/j.saa.2017.10.042

Tseng, W. C., Chu, S. P., Kong, P. H., Huang, C. K., Chen, J. H., Chen, P. S., et al. (2014). Water with low concentration of surfactant in dispersed solvent-assisted emulsion dispersive liquid–liquid microextraction for the determination of fungicides in wine. *J. Agric. Food Chem*. 62, 9059–9065. doi: 10.1021/jf5036096

Wang, H., Tang, Q., Zhang, J., Yao, Y. Q., Xiao, X., Huang, Y., et al. (2018). Alkaline earth cation-mediated photoluminescent complexes of thioflavin T with twisted cucurbit[14]uril. *N. J. Chem*. 42, 9244–9251. doi: 10.1039/C7NJ04115B

Wheate, N. J. (2008). Improving platinum(II)-based anticancer drug delivery using cucurbit[n]urils. *J. Inorgan. Biochem.* 102, 2060–2066. doi: 10.1016/j.jinorgbio.2008.06.005

Xi, Y. Y., Tang, Q., Huang, Y., Tao, Z., Xue, S. F., Zhou, Q. D., et al. (2017). A novel fluorescent indicator displacement assay for sensing the anticancer drug gefitinib. *Supramol. Chem*. 29, 229–235. doi: 10.1080/10610278.2016.1202413

Xing, X. Q., Zhou, Y. Y., Sun, J. Y., Tang, D. B., Li, T., and Wu, K. (2013). Determination of paraquat by cucurbit[7]uril sensitized fluorescence quenching method. *Anal. Lett.* 46, 694–705. doi: 10.1080/00032719.2012.729240

Xu, M., Lu, S. Y., Chen, D. J., Lan, J. C., G., Zhang, Z., et al. (2013). Determination of ten pesticides of pyrazoles and pyrroles in tea by accelerated solvent extraction coupled with gas chromatography-tandem mass spectrometry. *Chinese J. Chromatogr.*. 31, 218–222. doi: 10.3724/SP.J.1123.2012.10003

Yang, L. G., Kan, J. L., Wang, X., Zhang, Y. H., Tao, Z., Liu, Q. Y., et al. (2018). Study on the binding interaction of the α,α′,δ,δ′-tetramethylcucurbit[6]uril with biogenic amines in solution and the solid state. *Front. Chem.* 6:289. doi: 10.3389/fchem.2018.00289

Yao, F. H., Liu, H. L., Wang, G. Q., Du, L. M., Yin, X. F., and Fu, Y. L. (2013). Determination of paraquat in water samples using a sensitive fluorescent probe titration method. *J. Environ. Sci*. 25, 1245–1251. doi: 10.1016/S1001-0742(12)60124-7

You, L., Zha, D. J., and Anslyn, E. V. (2015). Recent advances in supramolecular analytical chemistry using optical sensing. *Chem. Rev*. 115, 7840–7892. doi: 10.1021/cr5005524

Zhang, H. Y., Liu, L. L., Gao, C., Sun, R. Y., and Wang, Q. C. (2012). Enhancing photostability of cyanine dye by cucurbituril encapsulation. *Dyes Pigm*. 94, 266–270. doi: 10.1016/j.dyepig.2012.01.022

Zhang, J., Tang, Q., Gao, Z. Z., Huang, Y., Xiao, X., and Tao, Z. (2017). Stimuli-responsive supramolecular assemblies between twisted cucurbit[14]uril and hemicyanine dyes and their analysis application. *J. Phys. Chem. B* 121, 11119–11123. doi: 10.1021/acs.jpcb.7b10285

Zhang, J., Xi, Y. Y., Li, Q., Tang, Q., Wang, R. B., Huang, Y., et al. (2016). Supramolecular recognition of amino acids by twisted cucurbit[14]uril. *Chem. Asian J*. 11, 2250–2254. doi: 10.1002/asia.201600803

Zhang, Y. H., Zhang, Y., Zhao, Q. Y., Chen, W. J., and Jiao, B. N. (2016). Vortex-assisted ionic liquid dispersive liquid-liquid microextraction coupled with high-performance liquid chromatography for the determination of triazole fungicides in fruit juices. *Food Anal. Methods* 9, 596–604. doi: 10.1007/s12161-015-0223-6

Zhou, Y. Y., P., Yu, H., Zhang, L., Xu, H. W., Wu, L., et al. (2009). A new spectrofluorometric method for the determination of nicotine base on the inclusion interaction of methylene blue and cucurbit[7]uril. *Microchim. Acta* 64, 63–68. doi: 10.1007/s00604-008-0032-3

Zhou, Y. Y., Yu, H. P., Zhang, L., Sun, J. Y., Wu, L., Lu, Q., et al. (2008). Host properties of cucurbit[7]uril: florescence enhancement of acridine orange. *J. Inclusion Phenom. Macrocyc. Chem*. 61, 259–264. doi: 10.1007/s10847-008-9414-8

Conflict of Interest Statement: The authors declare that the research was conducted in the absence of any commercial or financial relationships that could be construed as a potential conflict of interest.

frontiers in Chemistry

ORIGINAL RESEARCH
published: 30 October 2018
doi: 10.3389/fchem.2018.00520

Directed Self-Assembly of Trimeric DNA-Bindingchiral Miniprotein Helicates

Jacobo Gómez-González[1], Diego G. Peña[2], Ghofrane Barka[1], Giuseppe Sciortino[3,4], Jean-Didier Maréchal[3], Miguel Vázquez López[1]* and M. Eugenio Vázquez[2]**

[1] Centro Singular de Investigación en Química Biolóxica e Materiais Moleculares (CiQUS), Departamento de Química Inorgánica, Universidade de Santiago de Compostela, Santiago de Compostela, Spain, [2] Centro Singular de Investigación en Química Biolóxica e Materiais Moleculares (CiQUS), Departamento de Química Orgánica, Universidade de Santiago de Compostela, Santiago de Compostela, Spain, [3] Departament de Química, Universitat Autònoma de Barcelona, Cerdanyola, Spain, [4] Dipartimento di Chimica e Farmacia, Università di Sassari, Sassari, Italy

We propose that peptides are highly versatile platforms for the precise design of supramolecular metal architectures, and particularly, for the controlled assembly of helicates. In this context, we show that the bacteriophage T4 Fibritin foldon (T4Ff) can been engineered on its N-terminus with metal-chelating 2,2′-bipyridine units that stereoselectively assemble in the presence of Fe(II) into parallel, three-stranded peptide helicates with preferred helical orientation. Modeling studies support the proposed self-assembly and the stability of the final helicate. Furthermore, we show that these designed mini-metalloproteins selectively recognize three-way DNA junctions over double-stranded DNA.

Keywords: metallopeptide, self-assembly water, DNA recognition, enantioselectivity, peptide motifs, coordination chemistry

OPEN ACCESS

Edited by:
Angela Casini,
Cardiff University, United Kingdom

Reviewed by:
Olga Iranzo,
Center National de la Recherche Scientifique Marseille, France
Guzman Gil-Ramirez,
University of Lincoln, United Kingdom

***Correspondence:**
Jean-Didier Maréchal
jeandidier.marechal@uab.cat
Miguel Vázquez López
miguel.vazquez.lopez@usc.es
M. Eugenio Vázquez
eugenio.vazquez@usc.es

Specialty section:
This article was submitted to Supramolecular Chemistry, a section of the journal Frontiers in Chemistry

Received: *20 August 2018*
Accepted: *09 October 2018*
Published: *30 October 2018*

Citation:
Gómez-González J, Peña DG, Barka G, Sciortino G, Maréchal J-D, Vázquez López M and Vázquez ME (2018) Directed Self-Assembly of Trimeric DNA-Bindingchiral Miniprotein Helicates. Front. Chem. 6:520. doi: 10.3389/fchem.2018.00520

INTRODUCTION

Peptides are excellent supramolecular building blocks that encode precise structural and functional information within their amino acid sequence. Accordingly, researchers have explored diverse peptide motifs, such as coiled-coils, β-hairpins, or peptide amphiphiles, as the basis of biofunctional devices and materials (Matsuura et al., 2005, 2010; Gazit, 2007; Ulijn and Smith, 2008; Apostolovic et al., 2010; Robson Marsden and Kros, 2010; Boyle and Woolfson, 2011; Lai et al., 2012; Pazos et al., 2016). Curiously, despite the enormous potential for controlling stereochemistry, nuclearity and stoichiometry, the controlled supramolecular assembly of inorganic complexes with peptide motifs has been somewhat overlooked, and only a handful of systems based on modified coiled-coil motifs have been reported (Lieberman and Sasaki, 1991; Ghadiri et al., 1992; Li et al., 2000; Peacock et al., 2012; Ball, 2013; Berwick et al., 2014; Luo et al., 2016). On the other hand, helicates are discrete metal complexes in which one or more organic ligands are coiled around—and coordinating—two or more metal ions (Piguet et al., 1997; Albrecht, 2001, 2005) as a result of ligand coiling, helicates are inherently chiral species that can appear as two enantiomers according to the orientation in which the ligands twist around the helical axis defined by the metal centers. Besides their intrinsic interest in basic supramolecular chemistry, helicates have shown promising DNA-binding properties that have been associated with antimicrobial and antitumoral effects (Howson et al., 2012; Kaner et al., 2015). However, more than 20 years after the pioneering studies by Prof. Jean-Marie Lehn (Lehn et al., 1987; Ulijn and Smith, 2008), helicates are still not viable alternatives to traditional

DNA-binding agents. The slow development in the applied chemistry of metal helicates ultimately derives from the shortcomings associated with the classic synthetic approaches with organic ligands that complicate the structural control of the final helicates (i.e., oligomerization state, relative orientation of asymmetric ligands, supramolecular helicity) and hampers their efficient structural and functional optimization. Indeed, despite some noteworthy examples (Haino et al., 2009; Cardo et al., 2011; Howson et al., 2012; Chen et al., 2017; Mitchell et al., 2017; Guan et al., 2018), no general approach for the efficient and versatile stereoselective synthesis of helicates is yet available, making of these systems a challenging test case to demonstrate the potential of peptides for the controlled assembly of metallostructures.

Our strategy relied in the selection of a synthetically-accessible and structurally well-defined trimeric peptide domain as scaffold for the programmed assembly of the helicate. As an alternative (and orthogonal) platform to the ubiquitous leucine zippers, we focused our attention on the C-terminal domain of the bacteriophage T4 Fibritin foldon (T4Ff), a trimeric β-propeller-like structure formed by the self-assembly of a short 27-amino acid peptide (Tao et al., 1997; Papanikolopoulou et al., 2004; Habazettl et al., 2009). The intrinsic stability and structural resilience of the T4Ff scaffold has been exploited for the stabilization of trimeric structures of a number of peptides and engineered proteins (Stetefeld et al., 2003; Du et al., 2011; Berthelmann et al., 2014; Kobayashi et al., 2015), and given those precedents we envisioned that the T4Ff could also be used as a robust platform for the programmed assembly of chiral dinuclear helicates, thus offering an alternative for the integration of coordination and peptide chemistry beyond other widely explored peptide scaffolds.

MATERIALS AND METHODS

General

All reagents were acquired from the regular chemical suppliers. All solvents were dry and synthesis grade, unless specifically noted $(NH_4)Fe_2(SO_4)_2 \bullet 6\ H_2O$ salt from *Sigma-Aldrich* was used as Fe(II) ion source. Reactions were followed by analytical UHPLC-MS with an *Agilent 1200* series LC/MS using a *SB C18* (1.8 μm, 2.1 × 50 mm) analytical column from *Phenomenex*. Standard conditions for analytical UHPLC consisted on a linear gradient from 5 to 95% of solvent B for 12 min at a flow rate of 0.35 mL/min (A: water with 0.1% TFA, B: acetonitrile with 0.1% TFA). Compounds were detected by UV absorption at 222, 270, and 330 nm. Electrospray Ionization Mass Spectrometry (ESI/MS) was performed with an *Agilent 6120 Quadrupole* LC/MS model in positive scan mode using direct injection of the purified peptide solution into the MS detector.

Computational Methods

The model for the ΛΛ-[$(\boldsymbol{\beta}$**AlaBpy**$)_2$-**T4Ff**$]_3Fe_2^{+4}$ helicate was built with UCSF chimera1.12 (Pettersen et al., 2004), starting from the NMR resolved structure of the trimeric Foldon of the T4 phagehead fibritin (PDB code: 1RFO) mutating the carboxyl C-Termini to amide groups (see *Results and Discussion* section). Based on previous work, the model of ΛΛ-[$(\boldsymbol{\beta}$**AlaBpy**$)_2$-**T4Ff**$]_3Fe_2^{+4}$ helicate were built connecting the N-termini of the T4Ff peptides. Molecular Dynamics (MD) simulations were set up with the *xleap*, solvating the model with a box of pre-equilibrated TIP3P water molecules and the total charge was balanced with Cl^- ions (*ions94.lib* library). The AMBER14SB force field was used for standard residues (Hornak, Abel, Okur, Strockbine, Roitberg and Simmerling., 2006), while the GAFF force field was adopted for the remaining atoms. Fe-bonding force constants and equilibrium parameters were obtained through the Seminario method, using Gaussian09 to compute the geometry and harmonic frequencies at DFT level (Frisch et al., 2010), with the B3LYP functional (Yanai et al., 2004), combined with scalar-relativistic Stuttgart–Dresden SDD pseudopotential and its associated double-ζ basis plus a set of *f* polarization functions for the metal ion (Ehlers et al., 1993). The 6-31G(d,p) basis set was used for H, C, O, and N. Point charges were derived using the RESP (Restrained ElectroStatic Potential) model (Bayly et al., 1993). The force field building operations were carried out using the MCPB.py (Li and Merz, 2016). The solvent and the whole system were sequentially submitted to 3,000 energy minimization steps to relax possible steric clashes. Then, thermalization of water molecules and side chains was achieved by increasing the temperature from 100 K up to 300 K. MD simulations under periodic boundary conditions were carried out during 100 ns with OpenMM engine through OMMProtocol (Eastman et al., 2017; Pedregal et al., 2018). Analysis of the trajectories was carried out by means of *cpptraj* implemented in ambertools16 (Case et al., 2016).

Solid-Phase Peptide Synthesis (SPPS)

All peptide synthesis reagents, as well as the Fmoc amino acid derivatives were purchased from *GL Biochem* (Shanghai) Ltd., Fmoc-β-Ala-OH was from *Sigma Aldrich*. C-terminal amide natural T4Ff peptides were synthesized following standard Fmoc-peptide synthesis protocols on a 0.1 mmol scale using a 0.5 mmol/g loading *H-Rink amide ChemMatrix* resin (35–100 mesh) from *Sigma Aldrich* with a *Liberty Lite* automatic microwave assisted peptide synthesizer from *CEM Corporation*. The amino acids were coupled in 5-fold excess using oxyme as an activating agent. Couplings were conducted for 4 min at 90°C. Deprotection of the temporal Fmoc protecting group was performed by treating the resin with 20% piperidine in DMF for 1 min at 75°C. Once the synthesis is finished, the peptide was acetylated with a solution of 0.8 ml AcOH, 2 ml of DIEA/DMF (0.2 M) and 3.2 ml of DMF. The last non-natural Fmoc-β-Ala-Bpy-OH residues were coupled by hand in 4-fold excess using HATU as activating agent. Each amino acid was activated for 1 min in DIEA/DMF 0.2 M before being added onto the resin. These manual couplings were conducted for 60 min. Deprotection of the temporal Fmoc protecting group was performed by treating the resin with 20% piperidine in DMF for 20 min. Cleavage and deprotection of the peptide were simultaneously performed using standard conditions by incubating the resin for 2.5 h with an acidic mixture containing 50 μL CH_2Cl_2, 25 μL of H_2O, 25 μL of TIS (triisopropylsilane), and 900 TFA μL. The resin was filtered, and the TFA filtrate was concentrated under a nitrogen stream to an approximate volume of 1 mL, and then added onto

ice-cold diethyl ether (20 mL). After 10–30 min, the precipitate was centrifuged and washed again with 5 mL of ice-cold ether. The solid residue was dried under argon and redissolved in acetonitrile/water 1:1 (2–5 mL) and purified by semi-preparative RP-HPLC.

Peptides were purified by preparative RP-HPLC with an *Waters 1500* series Liquid Chromatograph using a *Sunfire Prep C18 OBD* (5 μm, 19 × 150 mm) reverse-phase column from *Waters*. Standard conditions for analytical and preparative RP- HPLC consisted on an isocratic regime during the first 2 min, followed by a linear gradient from 15 to 75% of solvent B for 30 min (A: water 0.1% TFA, B: acetonitrile 0.1% TFA). Compounds were detected by UV absorption (222 nm) and by ESI/MS. The fractions containing the products were freeze-dried and their identity was confirmed by ESI/MS and MALDI-TOF. Matrix-assisted laser desorption/ionization mass spectrometry (MALDI/MS) was performed with a Bruker *Autoflex MALDI/TOF* model in positive scan mode by direct irradiation of the matrix-absorbed peptide.

Spectroscopic Measurements

UV measurements were made in a *Jasco V-630* spectrophotometer coupled to a *Jasco ETC-717* temperature controller, using a standard *Hellma* semi-micro cuvette (108.002-QS) with a light path of 10 mm. Measurements were made at 20°C. Luminescence experiments were made with a *Varian Cary Eclipse* Fluorescence Spectophotometer coupled to a *Cary Single Cell peltier accessory (Agilent Technologies)* temperature controller. All measurements were made with a *Hellma* semi-micro cuvette (108F-QS) at 20°C. Circular dichroism measurements were made with a *Jasco J-715* coupled to a *Neslab RTE-111* termostated water bath, using a *Hellma* 100-QS cuvette (2 mm light pass).

Electrophoretic Mobility Shift Assays

EMSA were performed with a *BioRad Mini Protean* gel system, powered by an electrophoresis power supplies *PowerPac* Basic model, maximum power 150 V, frequency 50–60 Hz at 140 V (constant V). Binding reactions were performed over 30 min in 1.8 mM Tris-HCl (pH 7.5), 90 mM KCl, 1.8 mM $MgCl_2$, 0.2 mM TCEP, 9% glycerol, 0.11 mg/mL BSA, and 2.2% NP-40. For the experiments we used 200 nM of the DNAs (twDNA and dsDNA), and a total incubation volume of 20 μL. After incubation for 30 min at room temperature, products were resolved by PAGE using a 10% non-denaturing polyacrylamide gel and 1 × TBE buffer (0.445 M Tris, 0.445 M Boric acid) for 35 min at 25°C, and analyzed by staining with SyBrGold (Molecular Probes: 5 μL in 50 mL of 0.5 × TBE) for 10 min and visualized by fluorescence (*BioRad GelDoc XR+* molecular imager).

RESULTS AND DISCUSSION

As metal-chelating unit we chose 2,2′-bipyridine, a ligand that has been extensively used in coordination chemistry and yields stable complexes with a variety of metal ions (Kaes et al., 2000). Furthermore, we have previously described an Fmoc-protected 2,2′-bipyridine dipeptide derivative that can be readily implemented into standard Fmoc solid-phase peptide synthesis (SPPS) protocols, and have showed that the structure of this chelating unit, in which the 2,2′-bipyridine ligand is integrated in the peptide backbone, effectively couples the conformational preferences of the peptide chain with the geometry of the resulting metal complexes (Rama et al., 2012; Gamba et al., 2013, 2014, 2016; Salvadó et al., 2016).

The chelating 2,2′-bipyridine residue was obtained following an optimized synthetic route (Rama et al., 2012), based on the work carried out by the Newkome and Imperiali groups (Newkome et al., 1997; Torrado et al., 1998). The key step in the synthesis being the desymmetrization of a diethyl [1,1′-biphenyl]-4,4′-dicarboxylate intermediate with hydrazine monohydrate under conditions that allow the selective precipitation of the monocarbohydrazide, which is oxidized into the corresponding azyl azide, and then transformed into a carbamate through a Curtius rearrangement (Rama et al., 2012). Simultaneous hydrolysis of the carbamate and the ester group gives the desired bipyridine amino acid, which is derivatized in the form of a dipeptide to obtain the Fmoc-βAlaBpy-OH building block for increased solubility, stability, and solubility that allow its use following standard solid-phase peptide synthesis protocols (Ishida et al., 2006).

Inspection of the structure of T4Ff (PDB IDs 4NCU or 1RFO; Güthe et al., 2004; Berthelmann et al., 2014) showed that the N-terminal Gly residues are relatively close to each other and could accommodate the chelating 2,2′-bipyridine units without noticeable distortion of the T4Ff scaffold upon metal coordination. Moreover, we envisioned that the natural twist of the N-terminal polyproline helices in the folded T4Ff trimer should induce a ΛΛ-configuration (*M* helicity) on its derived helicate (Tao et al., 1997), which would be the preferred chirality for the efficient recognition of three-way DNA junctions (Oleksy et al., 2006; Gamba et al., 2016). Therefore, we synthesized the desired **(βAlaBpy)$_2$-T4Ff** helicate precursor ligand following standard Fmoc SPPS methods as outlined in **Figure 1** (Coin et al., 2007). The final peptide ligand was purified by HPLC and its identity confirmed by ESI-MS.

Having at hand the desired peptides we proceeded with the study of their metal binding properties. Surprisingly, while 2,2′-bipyridine is weakly emissive, and is even considered non-fluorescent (Dhanya and Bhattacharyya, 1992; Yagi et al., 1994), we found that the asymmetric 5′-amido-[2,2′-bipyridine]-5-carboxamide unit within the βAlaBpy residue was highly emissive, displaying intense band at c.a. 420 nm with a quantum yield of 0.37 (Dong et al., 2017). Additionally, the emission was quenched by coordination to Fe(II) ions, which could be exploited to monitor the formation of the β-annulus helicate. Thus, we recorded the emission spectra of a 3 μM solution (9 μM monomer) of [**(βAlaBpy)$_2$-T4Ff**]$_3$ in phosphate buffer (1 mM, pH 6.5) in the presence of increasing concentrations of $(NH_4)_2Fe(SO_4)_2 \bullet 6\ H_2O$ (Mohr salt) as source of Fe(II) ions ($\lambda exc = 305$ nm), and observed a concentration-dependent quenching of the emission intensity of the bipyridine ligands. The emission intensity profile of the titration nm could be fitted to a 1:2 binding mode with dissociation constants for the first, and second iron coordination of $K_{D1} = 5.5 \pm 3.3$ μM and a

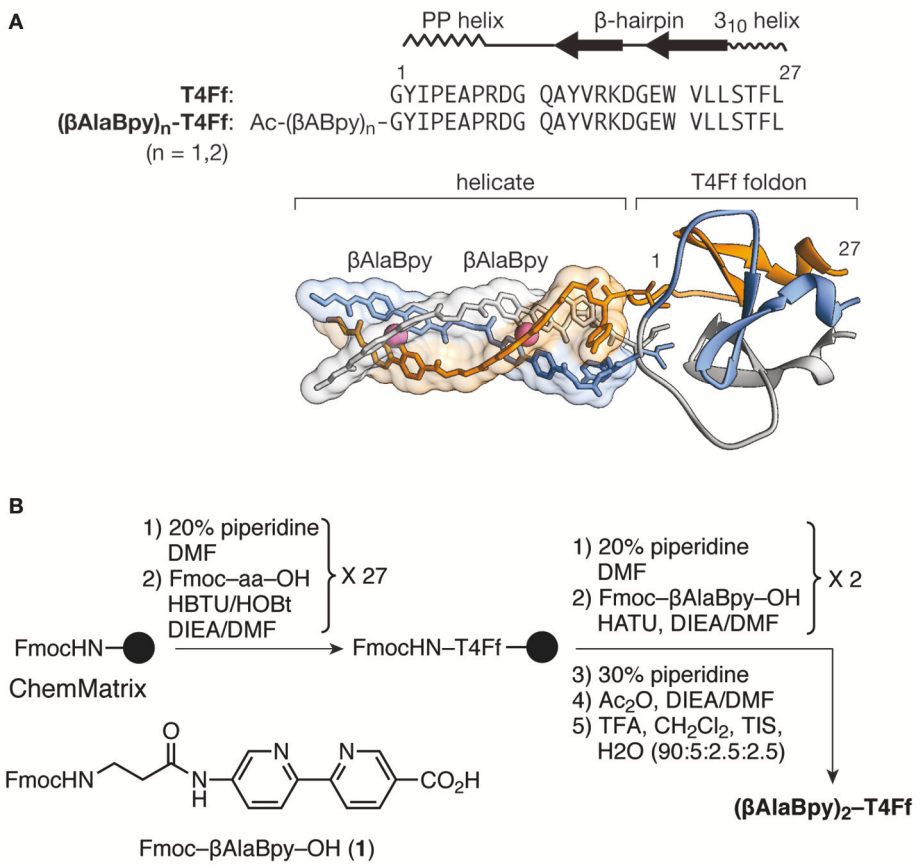

FIGURE 1 | (A) Structural elements and sequence of the natural T4Ff, and proposed structure of the **(βAlaBpy)$_2$-T4Ff** helicate at the N-terminus of the T4Ff scaffold. The three chains of the T4Ff are shown with different colors (orange, blue, light gray) for clarity. The ΛΛ- chirality is induced by the natural twisting of the T4Ff N-terminal polyproline helices. **(B)** Synthetic procedure for obtaining the T4Ff helicates, and structure of the chelating Fmoc-βAlaBpy-OH amino acid.

$K_{D2} = 6.6 \pm 0.7\,\mu M$, respectively (**Figure 2**, left; Kuzmic, 1996, 2009). UV/Vis titrations were also qualitatively consistent with the fluorescence data, showing a weak MLCT at about 535 nm in the presence of Fe(II) ions (See **Supplementary Material**). The formation of the expected $[[(\mathbf{\beta AlaBpy)_2\text{-}T4Ff}]_3Fe_2]^{4+}$ complex was also confirmed by mass spectrometry of the final solution of the titrations, which showed a peak at the expected mass of the molecular ion ($m/z = 11084.6$).

In order to study the chirality induction around the metal centers we measured the circular dichroism spectra of the trimeric $[(\mathbf{\beta AlaBpy)_2\text{-}T4Ff}]_3$ ligand, and its Fe(II) complex $[(\mathbf{\beta AlaBpy)_2\text{-}T4Ff}]_3Fe_2^{+4}$. As expected from the original structural analysis, the observed positive Cotton effect at c.a. 330 nm is consistent with the formation of a ΛΛ-helicate. Furthermore, the small change in the CD spectra upon addition of Fe(II) also suggests that the bipyridine ligands are strongly preorganized, even in absence of the metal, and that only a small rearrangement of the chromophores takes place upon coordination (**Figure 2**, right). This is consistent with earlier computational studies with related bis-bipyridyl peptide ligands, which showed that the bipyridine residues have a large tendency to stack on top of each other (Rama et al., 2012). This stacking interaction will presumably rigidify the bis-bipyridyl trimer and facilitate the helical induction by the foldon domain.

In order to gain some insight into the structure and stability of the peptide helicate we performed Molecular Dynamics (MD) simulations in explicit solvent and periodic boundary conditions (see Methods section for details). The structure of the ΛΛ-$[(\mathbf{\beta AlaBpy)_2\text{-}T4Ff}]_3Fe_2^{+4}$ unit appears highly stable along all the MD trajectory retaining its helicity conformation and the Fe(II) octahedral coordination geometry. Moreover, the T4Ff scaffold appears stable during the simulation showing no appreciable deformations as a result of the introduction of the artifical $(\beta AlaBpy)_2$ unit. The root-mean square deviation (RMSD) of the whole system was computed along the MD using the minimized initial structures as a reference, the trajectories attain relative stable RMSD after the first ∼20 ns, that reach up to 1.99 ± 0.62 Å in average (See **Supplementary Material**). A cluster analysis was performed on the full length MD experiments showing a predominant conformations occupying about ∼40% of the total conformation repartition. Overall, the results highlight that the computed model is very stable along the 100 *ns* of the MD and results consistent with the experimental data. Interestingly, the

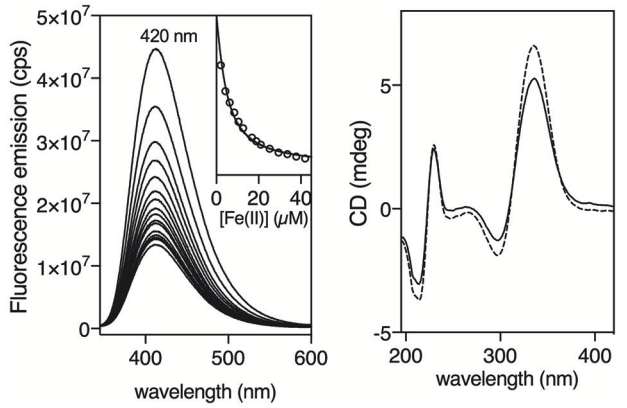

FIGURE 2 | Fluorescence titration of a 3 μM (9 μM monomer) solution of **[(βAlaBpy)$_2$-T4Ff]**$_3$ with increasing concentrations of Fe(II). Inset shows emission at 420 nm upon excitation at 305 nm with increasing concentrations of Fe(II), and the best fit to a 1:2 binding mode (Hellman and Fried, 2007; Peberdy et al., 2007). Experiments were made in triplicate. Right. Circular Dichroism of a 6 μM solution (18 μM monomer) of **[(βAlaBpy)$_2$-T4Ff]**$_3$ (dashed line) and in the presence of 90 μM Fe(II) (solid line). All experiments were made in 1 mM phosphate buffer, pH 6.5, 10 mM NaCl at 20°C.

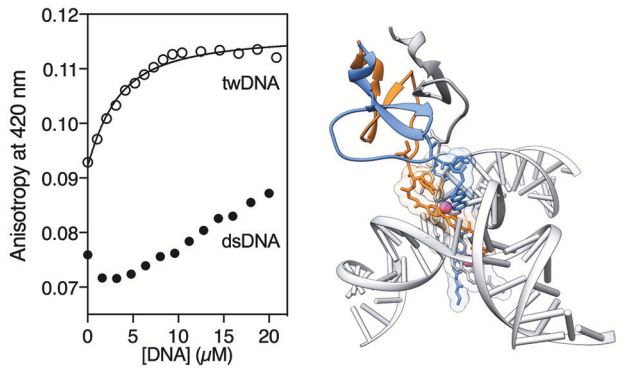

FIGURE 3 | First cluster representative frame of the MD trajectory for the ΛΛ-**[(βAlaBpy)$_2$-T4Ff]**$_3$Fe$_2^{+4}$ system showing the stable structure of the T4Ff domain. Note the flexible hinge region between the rigid helicate and the T4Ff domain.

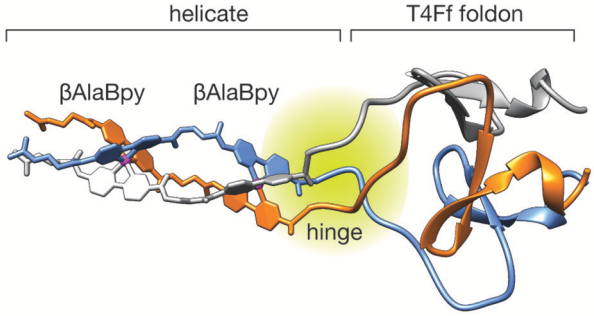

FIGURE 4 | (Left) Anisotropy titration of **[(βAlaBpy)$_2$-T4Ff]**$_3$Fe$_2$ in 1 mM phosphate buffer, 10 mM NaCl with increasing concentrations of **tw-DNA**. The best fit to a 1:1 binding mode is shown (curve fitting was performed using *DynaFit*).(Kuzmic, 1996, 2009) **tw-DNA** sequences: 5′–CAC CGC TCT GGT CCT C–3′; 5′–CAG GCT GTG AGC GGT G–3′; 5′–GAG GAC CAA CAG CCT G–3′. Right: Model of the interaction between the **[(βAlaBpy)$_2$-T4Ff]**$_3$Fe$_2$ and the three-way junction, based on the reported pdb structures of an helicate bound to a three-way junction (pdb code 4NCU), and the structure of the fibritin foldon (pdb code 2ET0; Oleksy et al., 2006).

MD analysis revealed a hinge region with increased flexibility connecting the more rigid helicate and foldon domains, which suggests the replacement of the N-terminal Gly reside for a more conformationally restricted residue in future designs.

Having made a preliminary characterization of the T4Ff helicate, we studied its DNA binding properties by titrating a 2 μM solution of **[(βAlaBpy)$_2$-T4Ff]**$_3$ (6 μM mononer) in the presence of saturating concentrations of Fe(II) according to the previous fluorescence titrations (20 μM) with increasing concentrations of a three-way DNA junction (**tw-DNA**), and measuring the fluorescence anisotropy of the bipyridine fluorophores at 420 nm after each addition of DNA. The titration profile could be fitted to a 1:1 binding mode, with a dissociation constant of 2.17 ± 0.45 μM of the **[(βAlaBpy)$_2$-T4Ff]**$_3$Fe$_2$ complex to **tw-DNA**. Titrations under the same conditions with a model double stranded DNA (**ds-DNA**) led to a small, monotonic increase in the anisotropy, which is in tune with the the formation of weak complexes or non-specific binding (**Figure 3**). The low affinity to dsDNA is consistent with previous studies with other helicates (**Figure 4**; Tuma et al., 1999; Oleksy et al., 2006; Gamba et al., 2016). Control titrations adding with **[(βAlaBpy)$_2$-T4Ff]**$_3$ foldon in absence of metal did not show any response to added DNA (See **Supplementary Material**), thus confirming that the formation of the helicate structure is required for DNA recognition, and the foldon only have a structural role in the formation of the helicate.

In addition to the spectroscopic studies, we also studied the DNA binding properties of the **[(βAlaBpy)$_2$-T4Ff]**$_3$Fe$_2$ helicate by electrophoretic mobility assays (EMSA) in polyacrylamide gel under non-denaturing conditions (Liebler and Diederichsen, 2004), visualizing the DNA in the gel using *SybrGold* staining (Vázquez et al., 2007). In agreement with the fluorescence titration studies discussed previously, incubation of the target **tw-DNA** with the **[(βAlaBpy)$_2$-T4Ff]**$_3$Fe$_2$ helicate resulted in the concentration-dependent appearance of a new retarded band, which is consistent with the formation of the expected **tw-DNA**/**[(βAlaBpy)$_2$-T4Ff]**$_3$Fe$_2$ complex (**Figure 5**, lanes 1–6). Additionally, the overall intensity of the lanes of the gel is progressively reduced in the presence of increasing concentrations of the **[(βAlaBpy)$_2$-T4Ff]**$_3$Fe$_2$ complex, which suggests the formation of higher-order aggregates with the three-way junction DNA in the gel conditions (Chanvorachote et al., 2009; Thordarson, 2010). On the other hand, incubation of a model double-stranded DNA with the peptide helicate did not show any new slow-migrating bands (**Figure 5**, lanes 7-10), which is in agreement with the expected low affinity for this form of DNA, and demonstrates that the small increase observed

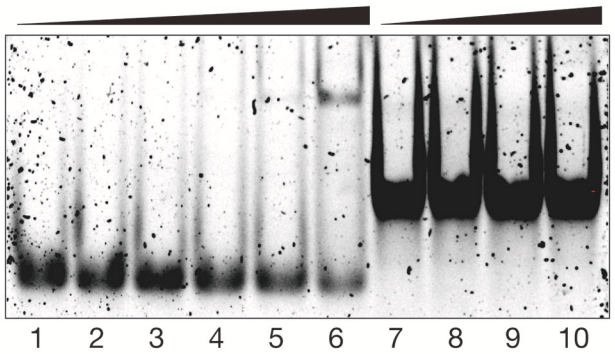

FIGURE 5 | EMSA DNA binding studies results for [**(βAlaBpy)$_2$-T4Ff**]$_3$Fe$_2$ helicate. Lanes 1–6, 200 nM **tw-Rho-DNA** with 0, 150, 250, 500, 1,000, and 2,000 nM of [**(βAlaBpy)$_2$-T4Ff**]$_3$ and 14 eq. of $(NH4)_2Fe(SO_4)_2 \bullet 6\ H_2O$ in each lane; lanes 7–10, 200 nM dsDNA with 0, 500, 1,000, and 2,000 nM of [**(βAlaBpy)$_2$-T4Ff**]$_3$ and 14 eq. of $(NH4)_2Fe(SO_4)_2 \bullet 6\ H_2O$ in each lane. Samples were resolved on a 10% nondenaturing polyacrylamide gel and 1× TBE buffer over 35 min at 25°C, and stained with SyBrGold (5 μL in 50 mL of 0.5× TBE) for 10 min, followed by fluorescence visualization. Oligonucleotide sequences: **tw-DNA,** 5′–CAC CGC TCT GGT CCT C–3′; 5′–CAG GCT GTG AGC GGT G–3′; 5′–GAG GAC CAA CAG CCT G–3′; **dsDNA** (only one strand shown) 5′–AAC ACA TGC AGG ACG GCG CTT–3′.

in the fluorescence anisotropy titration of dsDNA (**Figure 4**) arises from weak interactions that are not seen at the lower concentrations used in the EMSA experiment.

CONCLUSIONS

In summary, we have shown the potential of small protein domains for the precise structural organization of coordination complexes. Modification of the T4 Fibritin foldon with metal-chelating bipyridines results allows the assembly of unique three-strand helicates in which the parallel orientation of the three helicate ligands is directed by the self-assembled T4Ff domain, and the chirality of the dinuclear helicate (*M* helicity or ΛΛ-configuration in the metal complexes) is selected by the relative orientation of the natural polyproline helices at the N-terminus of the T4Ff trimer. The final supramolecular peptide helicate [**(βAlaBpy)$_2$-T4Ff**]$_3$Fe$_2$ displays good *in vitro* DNA binding and selectivity toward three-way DNA junctions. We are currently exploring alternative peptide sequences to improve the solubility of the peptide/DNA complexes, and modifications with positively charged residues that might increase the overall affinity.

AUTHOR CONTRIBUTIONS

JG-G and DGP performed the experimental work (synthesis of the bipyridine building block, peptide synthesis, metal and DNA binding studies), GB did preliminary studies with the (βAlaBpy)2-T4Ff peptide. GS and J-DM did the computational work and contributed to the preparation of the final manuscript. MVL and MEV conceived the project, supervised the experimental work. MEV wrote the manuscript with the collaboration of MVL, and prepared the graphic material.

ACKNOWLEDGMENTS

Financial support from the Spanish grants CTQ2015-70698-R, CTQ2017-87889-P, the Xunta de Galicia (Centro singular de investigación de Galicia accreditation 2016–2019, ED431G/09) and the European Union (European Regional Development Fund - ERDF), is gratefully acknowledged. JG-G, thanks the Spanish MINECO for his FPI fellowship, GB thanks the ERC for her EU METALIC-II 2013-2442/001-001-EMA2 mobility scheme fellowship, and GS. thanks the Universitat Autònoma de Barcelona for its support to his PhD. J-DM and GS are thankful for the support given by the Generalitat de Catalunya 2017SGR1323. Support of COST Action CM1306 is kindly acknowledged. MEV, also wish to acknowledge the generous support by the Fundación Asociación Española Contra el Cáncer AECC (IDEAS197VAZQ grant).

SUPPLEMENTARY MATERIAL

The Supplementary Material for this article can be found online at: https://www.frontiersin.org/articles/10.3389/fchem.2018.00520/full#supplementary-material

REFERENCES

Albrecht, M. (2001). "Let's Twist Again" double-stranded, triple-stranded, and circular helicates. *Chem. Rev.* 101, 3457–3497. doi: 10.1021/cr0103672

Albrecht, M. (2005). Artificial molecular double-stranded helices. *Angew. Chem. Int. Ed. Engl.* 44, 6448–6451. doi: 10.1002/anie.200501472

Apostolovic, B., Danial, M., and Klok, H.-A. (2010). Coiled coils: attractive protein folding motifs for the fabrication of self-assembled, responsive and bioactive materials. *Chem. Soc. Rev.* 39, 3541–3575. doi: 10.1039/b914339b

Ball, Z. T. (2013). Designing enzyme-like catalysts: a rhodium(II) metallopeptide case study. *Acc. Chem. Res.* 46, 560–570. doi: 10.1021/ar300261h

Bayly, C. I., Cieplak, P., Cornell, W., and Kollman, P. A. (1993). A well-behaved electrostatic potential based method using charge restraints for deriving atomic charges: the resp model. *J. Phys. Chem.* 97, 10269–10280. doi: 10.1021/j100142a004

Berthelmann, A., Lach, J., Gräwert, M. A., Groll, M., and Eichler, J. (2014). Versatile C(3)-symmetric scaffolds and their use for covalent stabilization of the foldon trimer. *Org. Biomol. Chem.* 12, 2606–2614. doi: 10.1039/C3OB42251H

Berwick, M. R., Lewis, D. J., Jones, A. W., Parslow, R. A., Dafforn, T. R., Cooper, H. J., et al. (2014). *De novo* design of Ln(III) coiled coils for imaging applications. *J. Am. Chem. Soc.* 136, 1166–1169. doi: 10.1021/ja408741h

Boyle, A. L., and Woolfson, D. N. (2011). *De novo* designed peptides for biological applications. *Chem. Soc. Rev.* 40, 4295–4306. doi: 10.1039/c0cs00152j

Cardo, L., Sadovnikova, V., Phongtongpasuk, S., Hodges, N. J., and Hannon, M. J. (2011). Arginine conjugates of metallo-supramolecular cylinders prescribe helicity and enhance DNA junction binding and cellular activity. *Chem. Commun.* 47, 6575–6577. doi: 10.1039/c1cc11356a

Case, D. A., Botello-Smith, R. M. B. W., Cerutti, D. S., Cheatham, T. E., Darden T. A. III, Duke, R. E. et al. (2016). *Kollman Amber 16,* San Francisco: University of California.

Chanvorachote, B., Nimmannit, U., Muangsiri, W., and Kirsch, L. (2009). An evaluation of a fluorometric method for determining binding parameters of drug-carrier complexes using mathematical models based on total drug concentration. *J. Fluoresc.* 19, 747–753. doi: 10.1007/s10895-009-0471-1

Chen, W., Tang, X., Dou, W., Wang, B., Guo, L., Ju, Z., et al. (2017). The Construction of Homochiral lanthanide quadruple-stranded helicates with multiresponsive sensing properties toward fluoride anions. *Chem. Eur. J.* 23, 9804–9811. doi: 10.1002/chem.201700827

Coin, I., Beyermann, M., and Bienert, M. (2007). Solid-phase peptide synthesis: from standard procedures to the synthesis of difficult sequences. *Nat. Protoc.* 2, 3247–3256. doi: 10.1038/nprot.2007.454

Dhanya, S., and Bhattacharyya, P. K. (1992). Fluorescence behaviour of 2,2′-bipyridine in aqueous solution. *J. Photochem. Photobiol. A Chem.* 63, 179–185. doi: 10.1016/1010-6030(92)85134-G

Dong, Y., Liu, T., Wan, X., Pei, H., Wu, L., and Yao, Y. (2017). Facile one-pot synthesis of bipyridine-based dual-channel chemosensor for the highly selective and sensitive detection of aluminum ion. *Sens. Actuators B Chem.* 241, 1139–1144. doi: 10.1016/j.snb.2016.10.022

Du, L., Leung, V. H., Zhang, X., Zhou, J., Chen, M., He, W., et al. (2011). A recombinant vaccine of H5N1 HA1 fused with foldon and human IgG Fc induced complete cross-clade protection against divergent H5N1 viruses. *PLoS ONE* 6:e16555. doi: 10.1371/journal.pone.0016555

Eastman, P., Swails, J., Chodera, J. D., McGibbon, R. T., Zhao, Y., Beauchamp, K. A., et al. (2017). Openmm 7: rapid development of high performance algorithms for molecular dynamics. *PLoS Comput. Biol.* 13:e1005659. doi: 10.1371/journal.pcbi.1005659

Ehlers, A., Böhme, M., Dapprich, S., Gobbi, A., Höllwarth, A., Jonas, V., et al. (1993). A set of f-polarization functions for pseudo-potential basis sets of the transition metals sc-cu, y-ag and la-au. *Chem. Phys. Lett.* 208, 111–114. doi: 10.1016/0009-2614(93)80086-5

Frisch, M. J., Trucks, G. W., Schlegel, H. B., Scuseria, G. E., Robb, M. A., Cheeseman, J. R., et al. (2010). *Gaussian 09, Revision c.01*. Wallingford, CT: Gaussian, Inc.

Gamba, I., Rama, G., Ortega-Carrasco, E., Berardozzi, R., Sánchez-Pedregal, V. M., Di Bari, L., et al. (2016). The folding of a metallopeptide. *Dalton Trans.* 45, 881–885. doi: 10.1039/C5DT02797G

Gamba, I., Rama, G., Ortega-Carrasco, E., Maréchal, J.-D., Martínez-Costas, J., Vázquez, M. E., et al. (2014). Programmed stereoselective assembly of DNA-binding helical metallopeptides. *Chem. Commun.* 50, 11097–11100. doi: 10.1039/C4CC03606A

Gamba, I., Salvadó, I., Rama, G., Bertazzon, M., Sánchez, M. I., Sánchez-Pedregal, V. M., et al. (2013). Custom-fit ruthenium(II) metallopeptides: a new twist to DNA binding with coordination compounds. *Chem. Eur. J.* 19, 13369–13375. doi: 10.1002/chem.201301629

Gazit, E. (2007). Self-assembled peptide nanostructures: the design of molecular building blocks and their technological utilization. *Chem. Soc. Rev.* 36, 1263–1269. doi: 10.1039/b605536m

Ghadiri, M. R., Soares, C., and Choi, C. (1992). Design of an artificial four-helix bundle metalloprotein via a novel ruthenium(II)-assisted self-assembly process. *J. Am. Chem. Soc.* 114, 4000–4002. doi: 10.1021/ja00036a072

Guan, Y., Du, Z., Gao, N., Cao, Y., Wang, X., Scott, P., et al. (2018). Stereochemistry and amyloid inhibition: asymmetric triplex metallohelices enantioselectively bind to Aβ peptide. *Sci. Adv.* 4:eaao6718. doi: 10.1126/sciadv.aao6718

Güthe, S., Kapinos, L., Möglich, A., Meier, S., Grzesiek, S., and Kiefhaber, T. (2004). Very fast folding and association of a trimerization domain from bacteriophage T4 fibritin. *J. Mol. Biol.* 337, 905–915. doi: 10.1016/j.jmb.2004.02.020

Habazettl, J., Reiner, A., and Kiefhaber, T. (2009). NMR structure of a monomeric intermediate on the evolutionarily optimized assembly pathway of a small trimerization domain. *J. Mol. Biol.* 389, 103–114. doi: 10.1016/j.jmb.2009.03.073

Haino, T., Shio, H., Takano, R., and Fukazawa, Y. (2009). Asymmetric induction of supramolecular helicity in calix[4]arene-based triple-stranded helicate. *Chem. Commun.* 2009, 2481–2483. doi: 10.1039/B900599D

Hellman, L. M., and Fried, M. G. (2007). Electrophoretic mobility shift assay (EMSA) for detecting protein-nucleic acid interactions. *Nat. Protoc.* 2, 1849–1861. doi: 10.1038/nprot.2007.249

Hornak, V., Abel, R., Okur, A., Strockbine, B., Roitberg, A., and Simmerling, C. (2006). Comparison of multiple amber force fields and development of improved protein backbone parameters. *Proteins Struct. Funct. Bioinf.* 65, 712–725. doi: 10.1002/prot.21123

Howson, S. E., Bolhuis, A., Brabec, V., Clarkson, G. J., Malina, J., Rodger, A., et al. (2012). Optically pure, water-stable metallo-helical "flexicate" assemblies with antibiotic activity. *Nat. Chem.* 4, 31–36. doi: 10.1038/nchem.1206

Ishida, H., Maruyama, Y., Kyakuno, M., Kodera, Y., Maeda, T., and Oishi, S. (2006). Artificial metalloproteins with a ruthenium tris(bipyridyl) complex as the core. *Chembiochem* 7, 1567–1570. doi: 10.1002/cbic.200600162

Kaes, C., Katz, A., and Hosseini, M. W. (2000). Bipyridine: the most widely used ligand. A review of molecules comprising at least two 2,2′-bipyridine units. *Chem. Rev.* 100, 3553–3590. doi: 10.1021/cr990376z

Kaner, R. A., Allison, S. J., Faulkner, A. D., Phillips, R. M., Roper, D. I., Shepherd, S. L., et al. (2015). Anticancer metallohelices: nanomolar potency and high selectivity. *Chem. Sci.* 7, 951–958. doi: 10.1039/C5SC03677A

Kobayashi, N., Yanase, K., Sato, T., Unzai, S., Hecht, M. H., and Arai, R. (2015). Self-assembling nano-architectures created from a protein nano-building block using an intermolecularly folded dimeric *de novo* protein. *J. Am. Chem. Soc.* 137, 11285–11293. doi: 10.1021/jacs.5b03593

Kuzmic, P. (1996). Program DYNAFIT for the analysis of enzyme kinetic data: application to HIV proteinase. *Anal. Biochem.* 237, 260–273. doi: 10.1006/abio.1996.0238

Kuzmic, P. (2009). DynaFit—a software package for enzymology. *Methods Enzymol.* 467, 247–280. doi: 10.1016/S0076-6879(09)67010-5

Lai, Y.-T., King, N. P., and Yeates, T. O. (2012). Principles for designing ordered protein assemblies. *Trends Cell Biol.* 22, 653–661. doi: 10.1016/j.tcb.2012.08.004

Lehn, J. M., Rigault, A., Siegel, J., Harrowfield, J., Chevrier, B., and Moras, D. (1987). Spontaneous assembly of double-stranded helicates from oligobipyridine ligands and copper(I) cations: structure of an inorganic double helix. *Proc. Natl. Acad. Sci. U.S.A.* 84:2565. doi: 10.1073/pnas.84.9.2565

Li, P., and Merz, K. M. Jr. (2016). MCPB.py: a python based metal center parameter builder. *J. Chem. Inf. Model.* 56, 599–604. doi: 10.1021/acs.jcim.5b00674

Li, X., Suzuki, K., Kashiwada, A., Hiroaki, H., Kohda, D., and Tanaka, T. (2000). Soft metal ions, Cd(II) and Hg (II), induce triple-stranded α-helical assembly and folding of a *de novo* designed peptide in their trigonal geometries. *Protein Sci.* 9, 1327–1333. doi: 10.1110/ps.9.7.1327

Lieberman, M., and Sasaki, T. (1991). Iron(II) organizes a synthetic peptide into three-helix bundles. *J. Am. Chem. Soc.* 113, 1470–1471. doi: 10.1021/ja00004a090

Liebler, E. K., and Diederichsen, U. (2004). From IHF protein to design and synthesis of a sequence-specific DNA bending peptide. *Org. Lett.* 6, 2893–2896. doi: 10.1021/ol049016a

Luo, X., Wang, T. A., Zhang, Y., Wang, F., and Schultz, P. G. (2016). Stabilizing protein motifs with a genetically encoded metal-ion chelator. *Cell Chem Biol.* 23, 1098–1102. doi: 10.1016/j.chembiol.2016.08.007

Matsuura, K., Hayashi, H., Murasato, K., and Kimizuka, N. (2010). Trigonal tryptophane zipper as a novel building block for pH-responsive peptide nano-assemblies. *Chem. Commun.* 47, 265–267. doi: 10.1039/C0CC01324B

Matsuura, K., Murasato, K., and Kimizuka, N. (2005). Artificial peptide-nanospheres self-assembled from three-way junctions of β-sheet-forming peptides. *J. Am. Chem. Soc.* 127, 10148–10149. doi: 10.1021/ja052644i

Mitchell, D. E., Clarkson, G., Fox, D. J., Vipond, R. A., Scott, P., and Gibson, M. I. (2017). Antifreeze protein mimetic metallohelices with potent ice recrystallization inhibition activity. *J. Am. Chem. Soc.* 139, 9835–9838. doi: 10.1021/jacs.7b05822

Newkome, G. R., Gross, J., and Patri, A. K. (1997). Synthesis of unsymmetrical 5,5'-disubstituted 2,2'-Bipyridines1. *J. Org. Chem.* 62, 3013–3014.

Oleksy, A., Blanco, A. G., Boer, R., Usón, I., Aymam,í, J., Rodger, A., et al. (2006). Molecular recognition of a three-way DNA junction by a metallosupramolecular helicate. *Angew. Chem. Int. Ed.* 45, 1227–1231. doi: 10.1002/anie.200503822

Papanikolopoulou, K., Teixeira, S., Belrhali, H., Forsyth, V. T., Mitraki, A., and van Raaij, M. J. (2004). Adenovirus fibre shaft sequences fold into the native triple β-spiral fold when N-terminally fused to the bacteriophage T4 fibritin foldon trimerisation motif. *J. Mol. Biol.* 342, 219–227. doi: 10.1016/j.jmb.2004.07.008

Pazos, E., Sleep, E., Rubert Pérez, C. M., Lee, S. S., Tantakitti, F., and Stupp, S. I. (2016). Nucleation and growth of ordered arrays of silver nanoparticles on peptide nanofibers: hybrid nanostructures with antimicrobial properties. *J. Am. Chem. Soc.* 138, 5507–5510. doi: 10.1021/jacs.6b01570

Peacock, A. F., Bullen, G. A., Gethings, L. A., Williams, J. P., Kriel, F. H., and Coates, J. (2012). Gold-phosphine binding to *de novo* designed coiled coil peptides. *J. Inorg. Biochem.* 117, 298–305. doi: 10.1016/j.jinorgbio.2012.05.010

Peberdy, J. C., Malina, J., Khalid, S., Hannon, M. J., and Rodger, A. (2007). Influence of surface shape on DNA binding of bimetallo helicates. *J. Inorg. Biochem.* 101, 1937–1945. doi: 10.1016/j.jinorgbio.2007.07.005

Pedregal, J. R.-G., Alonso-Cotchico, L., Velasco, L., and Maréchal, J.-D. (2018). *OMMProtocol: A Command Line Application to Launch Molecular Dynamics Simulations With OpenMM*. Available online at: http://bit.ly/2CN0khh

Pettersen, E. F., Goddard, T. D., Huang, C. C., Couch, G. S., Greenblatt, D. M., Meng, E. C., et al. (2004). Ucsf chimera—a visualization system for exploratory research and analysis. *J. Comput. Chem.* 25, 1605–1612. doi: 10.1002/jcc.20084

Piguet, C., Bernardinelli, G., and Hopfgartner, G. (1997). Helicates as versatile supramolecular complexes. *Chem. Rev.* 97, 2005–2062. doi: 10.1021/cr960053s

Rama, G., Ardá, A., Maréchal, J-D., Gamba, I., Ishida, H., Jiménez-Barbero, J., et al. (2012). Stereoselective formation of chiral metallopeptides. *Chem. Eur. J.* 18, 7030–7035. doi: 10.1002/chem.201201036

Robson Marsden, H., and Kros, A. (2010). Self-assembly of coiled coils in synthetic biology: inspiration and progress. *Angew. Chem. Int. Ed.* 49, 2988–3005. doi: 10.1002/anie.200904943

Salvadó, I., Gamba, I., Montenegro, J., Martínez-Costas, J., Brea, J. M., Loza, M. I., et al. (2016). Membrane-disrupting iridium(iii) oligocationic organometallopeptides. *Chem. Commun.* 52, 11008–11011. doi: 10.1039/C6CC05537K

Stetefeld, J., Frank, S., Jenny, M., Schulthess, T., Kammerer, R. A., Boudko, S., et al. (2003). Collagen stabilization at atomic level: crystal structure of designed (GlyProPro)10foldon. *Structure* 11, 339–346. doi: 10.1016/S0969-2126(03)00025-X

Tao, Y., Strelkov, S. V., Mesyanzhinov, V. V., and Rossmann, M. G. (1997). Structure of bacteriophage T4 fibritin: a segmented coiled coil and the role of the C-terminal domain. *Structure* 5, 789–798. doi: 10.1016/S0969-2126(97)00233-5

Thordarson, P. (2010). Determining association constants from titration experiments in supramolecular chemistry. *Chem. Soc. Rev.* 40, 1305–1323. doi: 10.1039/C0CS00062K

Torrado, A., Walkup, G. K., and Imperiali, B. (1998). Exploiting polypeptide motifs for the design of selective Cu(II) ion chemosensors. *J. Am. Chem. Soc.* 120, 609–610. doi: 10.1021/ja973357k

Tuma, R. S., Beaudet, M. P., Jin, X., Jones, L. J., Cheung, C. Y., Yue, S., et al. (1999). Characterization of SYBR Gold nucleic acid gel stain: a dye optimized for use with 300-nm ultraviolet transilluminators. *Anal. Biochem.* 268, 278–288. doi: 10.1006/abio.1998.3067

Ulijn, R. V., and Smith, A. M. (2008). Designing peptide based nanomaterials. *Chem. Soc. Rev.* 37, 664–675. doi: 10.1039/b609047h

Vázquez, O., Vázquez, M. E., Blanco, J. B., Castedo, L., and Mascareñas, J. L. (2007). Specific DNA recognition by a synthetic, monomeric Cys2His2 zinc-finger peptide conjugated to a minor-groove binder. *Angew. Chem. Int. Ed Engl.* 46, 6886–6890. doi: 10.1002/anie.200702345

Yagi, M., Kaneshima, T., Wada, Y., Takemura, K., and Yokoyama, Y. (1994). The effects of conformation and coordination to zinc(II) ions on the luminescence properties of 2,2′-bipyridine, methyl-substituted 2,2′-bipyridines and 2,2′-biquinoline. *J. Photochem. Photobiol. A Chem.* 84, 27–32. doi: 10.1016/1010-6030(94)03842-2

Yanai, T., Tew, D. P., and Handy, N. C. (2004). A new hybrid exchange–correlation functional using the coulomb-attenuating method (cam-b3lyp). *Chem. Phys. Lett.* 393, 51–57. doi: 10.1016/j.cplett.2004.06.011

Conflict of Interest Statement: The authors declare that the research was conducted in the absence of any commercial or financial relationships that could be construed as a potential conflict of interest.

frontiers in Chemistry

ORIGINAL RESEARCH
published: 18 February 2019
doi: 10.3389/fchem.2019.00068

Exo-Functionalized Metallacages as Host-Guest Systems for the Anticancer Drug Cisplatin

*Ben Woods, Margot N. Wenzel, Thomas Williams, Sophie R. Thomas, Robert L. Jenkins and Angela Casini**

School of Chemistry, Cardiff University, Cardiff, United Kingdom

Within the framework of designing new self-assembled metallosupramolecular architectures for drug delivery, seven $[Pd_2L_4]^{4+}$ metallacages (L = 2,6-bis(pyridine-3-yl ethynyl)pyridine) featuring different groups in *exo*-position, selected to enhance the cage solubility in aqueous environment, were synthesized. Thus, carboxylic acids, sugars, and PEG groups were tethered to the bispyridyl ligands directly or via disulfide bond formation, as well as via click chemistry. The ligands and respective cages were characterized by different methods, including NMR spectroscopy and high-resolution electrospray mass spectrometry (HR-ESI-MS). While the two ligands featuring carboxylic acid-functionalized groups showed improved solubility in water, the other ligands were soluble only in organic solvents. Unfortunately, all the respective self-assembled cages were also insoluble in water. Afterwards, the encapsulation properties of the anticancer drug cisplatin in selected $[Pd_2L_4]X_4$ cages ($X = NO_3^-$, BF_4^-) were studied by ^1H, ^1H DOSY, and ^{195}Pt NMR spectroscopy. The effect of the counter ions as well as of the polarity of the solvent in the drug encapsulation process were also investigated, and provided useful information on the host-guest properties of these experimental drug delivery systems. Our results provide further experimental support for previous studies that suggest the desolvation of guests from surrounding solvent molecules and the resulting solvent rearrangement may actually be the primary driving force for determining guest binding affinities in metallacages, in the absence of specific functional group interactions.

Keywords: metallacages, supramolecular coordination complexes, water solubility, host-guest chemistry, cisplatin

OPEN ACCESS

Edited by:
Leyong Wang,
Nanjing University, China

Reviewed by:
Xiao-Yu Hu,
Nanjing University of Aeronautics and Astronautics, China
Laia Vilà Nadal,
University of Glasgow, United Kingdom
Robert Elmes,
Maynooth University, Ireland

****Correspondence:***
Angela Casini
casinia@cardiff.ac.uk

Specialty section:
This article was submitted to Supramolecular Chemistry, a section of the journal Frontiers in Chemistry

Received: *05 November 2018*
Accepted: *24 January 2019*
Published: *18 February 2019*

Citation:
Woods B, Wenzel MN, Williams T, Thomas SR, Jenkins RL and Casini A (2019) Exo-Functionalized Metallacages as Host-Guest Systems for the Anticancer Drug Cisplatin. Front. Chem. 7:68. doi: 10.3389/fchem.2019.00068

INTRODUCTION

Supramolecular chemistry has its roots in biology, and in recent years the unique and often advantageous properties of supramolecular materials have led to their extensive exploration in the fields of biomolecular recognition, drug delivery, disease diagnosis, and imaging. In this context, supramolecular coordination complexes (SCCs) hold great promise (Cook et al., 2013; Casini et al., 2017). In fact, the number of reports on the bioactivity of three-dimensional (3D) SCCs with different shapes has substantially increased (Kaner et al., 2016; Preston et al., 2016; Casini et al., 2017) and includes helicates (Schmitt et al., 2012), metallacages (Vajpayee et al., 2011), cubes (Ahmedova et al., 2016), prisms(Ahmad et al., 2015), and capsules (Therrien, 2013). These systems are of general formula M_nL_m, where M is usually Fe(II), Pd(II), Pt(II), or half-sandwich organometallic clips based on Ru(II), Os(II), or Ir(III) and Rh(III), and L is the ligand of the coordination complex.

In 2012, Lewis et al. reported on the encapsulation properties of the anticancer drug cisplatin within cationic $[Pd_2L_4]^{4+}$ cages (L = 2,6-bis(pyridine-3-ylethynyl)pyridine as the bidentate ligand) studied by NMR and X-ray diffraction analysis (Lewis et al., 2012). Following these promising results, as part of our efforts to develop functional metallosupramolecular drug delivery vectors, we have recently expanded the family of *exo*-functionalized $[Pd_2L_4]^{4+}$ cages coupled to fluorescent groups for imaging by fluorescence microscopy (Kaiser et al., 2016; Schmidt et al., 2016a,b), as well as to peptides for targeted drug delivery of cisplatin to cancer cells (Han et al., 2017, 2018). It is worth mentioning that while cisplatin occupies a crucial role in the treatment of various malignant tumors, its efficacy, and applicability are heavily restricted by severe systemic toxicities and drug resistance. Thus, our recent studies have exploited the host-guest properties of targeted metallacages to enhance the activity of cisplatin in cancer cells, protecting it from metabolism (Han et al., 2017). Of note, the reduced toxicity of cisplatin encapsulated in integrin targeted metallacages has also been demonstrated by us in an *ex vivo* model (Han et al., 2017).

As the initially developed cage architectures displayed scarce water solubility, we were interested in improving their hydrophilicity via derivatization of the ligand scaffold. Thus, here, a small library of bis(pyridyl) ligands—of general scaffold 3,5-bis(3-ethynylpyridine)phenyl (**Scheme 1**) - *exo*-functionalized with chemical groups envisioned to improve the aqueous solubility, were synthesized and self-assembled into the corresponding $[Pd_2L_4]^{4+}$ cages. The products were characterized by NMR, HR-ESI-MS, and IR. The solubility of the resulting metallacages was then tested in water, as well as in a range of common organic solvents. Furthermore, in order to elucidate the host-guest chemistry of the metallacages and the factors that favor cisplatin's retention in the supramolecular complexes, essential aspects to exploit the cages as drug delivery systems, the drug encapsulation was studied by ^{1}H, ^{1}H DOSY, and ^{195}Pt NMR spectroscopy under different conditions.

RESULTS AND DISCUSSION

Adapting previously reported procedures (Schmidt et al., 2016b), the synthesis of the *exo*-functionalized ligand scaffold with carboxylic acid groups, **L1,** and **L2** was first achieved by Sonogashira cross-coupling of a benzyl-protected 1,3-dibromophenyl precursor with 3-ethynylpyridine, followed by basic deprotection of the benzyl ester to afford the free acid, forming the highly conjugated bispyridyl ligand scaffold in good yields (**Scheme S1**). A polyethylene glycol *exo*-functionalized ligand (**L3**) was also synthesized. In this case, a ligand bearing a central phenol aromatic ring was synthesized via Sonogashira cross-coupling, which was then was coupled to 1-chloro-2-(2-methoxyethoxy) ethane under basic conditions to achieve ligand **L3** (**Scheme S2**). In addition, ligands **L4** and **L5,** featuring water-soluble thio-β-D-glucose moieties, were synthesized for the first time. This was achieved by first synthesizing an alkyl bromide *exo*-functionalized ligand via classic Appel reaction using triphenylphosphine, carbon tetrabromide, and 3,5-bis(3-ethynylpyridine)-benzylalcohol; the latter having been synthesized via Sonogashira cross-coupling (**Scheme S3**). The 1-thio-β-D-glucose tetraacetate group was then conjugated under basic conditions following a S_N2 type reaction to afford the ligand **L4**. Ligand **L5** was achieved by deacetylation of **L4** using Amberlite-IRA 401 (OH^-) ion exchange beads, which were stirred together at room temperature overnight, following previously reported procedures (Lewis et al., 2014). Finally, the ligands **L6** and **L7** were synthesized using standard CuAAC "Click" reaction conditions (**Scheme S4**) following similar procedures reported for analogous tris-pyridyl ligand scaffolds (Lewis et al., 2013). Noteworthy, the latter were reported to be soluble in water, and therefore, offered a logical starting point for functionalization of the herein selected 3,5-bis(3-ethynylpyridine) phenyl ligands. All the ligands were characterized by NMR (^{1}H, ^{13}C) and HR-ESI-MS. A summary of the synthesized ligands and cages can be found in **Scheme S5**.

The solubility of the ligands in water was assessed by overnight sonication in D_2O (10 mg/mL, 20°C), before filtration (pore size 450 μm). The filtrate was analyzed by ^{1}H NMR to determine if detectable amounts of ligand were present. Unfortunately, the *exo*-functionalized bispyridyl ligand scaffolds were found to be scarcely soluble, and were all undetectable in D_2O solution, except for the carboxylic acid functionalized ligands (**L1** = 10 mg/mL, **L2** > 100 mg/mL). The latter could be analyzed by ^{1}H NMR in D_2O (data not shown).

Afterwards, $[Pd_2L_4]^{4+}$ cage formation was achieved via self-assembly by reacting two equivalents of Pd(II) nitrate pentahydrate with four equivalents of the functionalized ligand (**L1**-**L7**) in DMSO at room temperature, to form the corresponding homoleptic metallacages (**C1**-**C7**) (**Scheme 1**). The products were analyzed by NMR (^{1}H, ^{13}C, ^{11}B, and ^{19}F), HR-ESI-MS (**Figures S1–S3**, **S5–S9**) and IR. Following previously reported examples (Schmidt et al., 2016c), quantitative cage formation was monitored by ^{1}H NMR, whereby the peaks corresponding to the protons alpha to the coordinating nitrogen of the terminal pyridine rings of the ligand undergo a large downfield shift, attributable to the withdrawal of electron density from the aromatic system following coordination to palladium (added in stoichiometric amounts). A representative ^{1}H NMR spectra for cage **C2** formation is shown in **Figure S4**.

In order to assess whether the synthesized metallacages were soluble in water, the products were suspended in D_2O (8 mg per mL) and sonicated at 37°C for 24 h. The fine suspension was then filtered, and the filtrate was analyzed by ^{1}H NMR. Despite the tetra-cationic nature of the metallacages, and the incorporation of solubilizing entities to the ligand scaffold, none of the metallacages (**C1**-**C7**) were soluble in D_2O. In fact, the filtrate solution was colorless and no trace of a proton signal could be found in the ^{1}H NMR spectra.

As a second attempt to water solubilization, and taking inspiration from previous work by Altmann and Pöthig (2016) on the synthesis of water soluble Ag(I) and Au(I) pillarplexes,

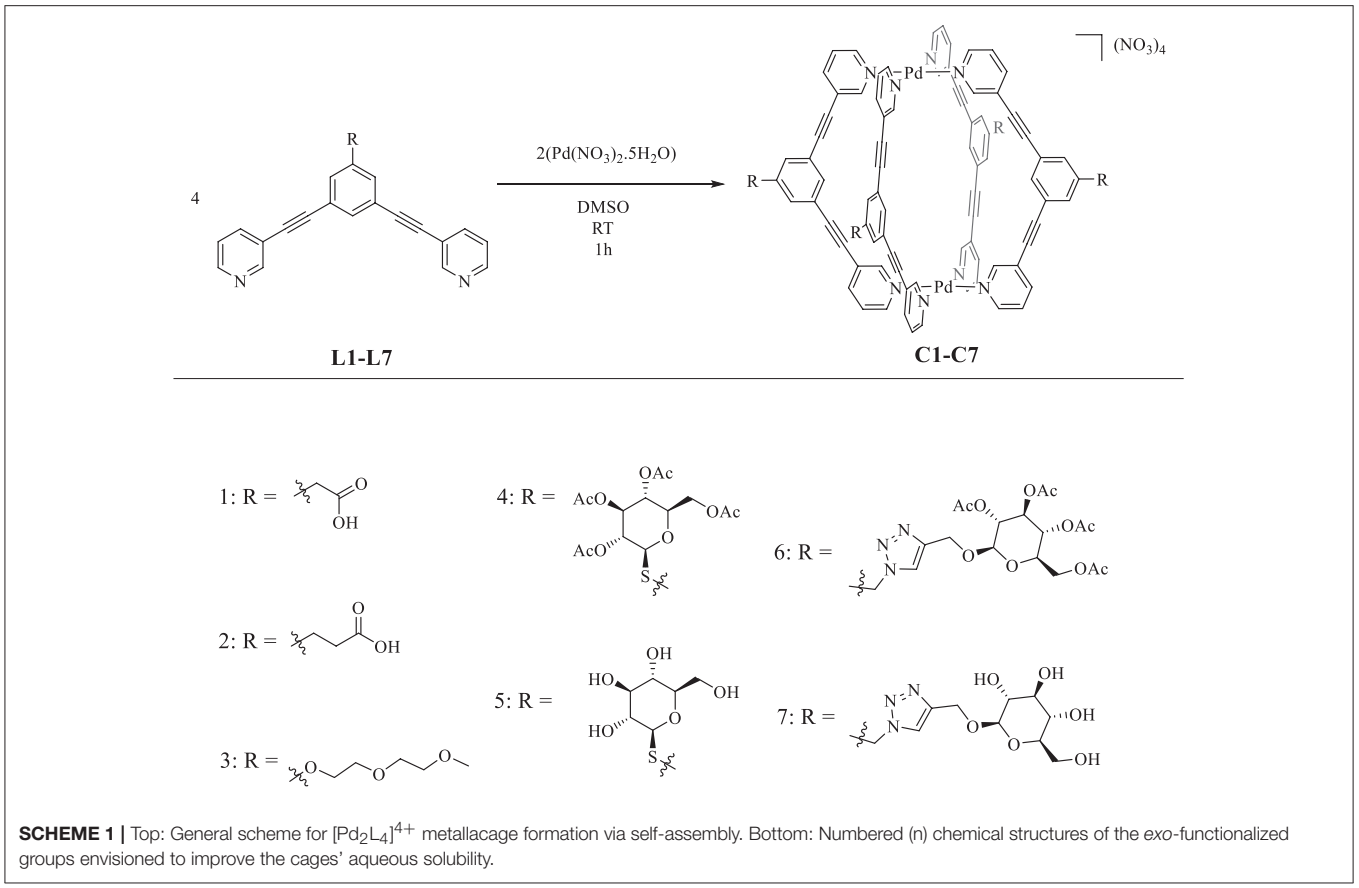

SCHEME 1 | Top: General scheme for $[Pd_2L_4]^{4+}$ metallacage formation via self-assembly. Bottom: Numbered (n) chemical structures of the *exo*-functionalized groups envisioned to improve the cages' aqueous solubility.

we synthesized new cages featuring acetate as the counterion by the use of palladium(II) acetate as the precursor in the self-assembly. However, this attempt produced an insoluble residue that could not be dissolved in either organic solvents or water.

Concerning cisplatin encapsulation, in the case of previously reported $[Pd_2L_4]BF_4$ cages (L = (2,6-bis(pyridin-3-ylethynyl)pyridine)) it was hypothesized that their central cavities are lined with four hydrogen bond accepting pyridine units which enable the encapsulation of two cisplatin molecules within the metallosupramolecular architecture through hydrogen bonding interactions between the cage and the amine ligands of the cisplatin guest (Lewis et al., 2012). This idea has been supported by NMR spectroscopy studies (Lewis et al., 2012), where chemical shifts of hydrogens in the trispyridyl ligands were observed upon cisplatin encapsulation. Control experiments confirm the importance of the hydrogen bonding interaction between the cage and the amine ligands of the cisplatin guest. It was also observed that upon addition of small amounts of D_2O to a solution of the cisplatin-cage host-guest adduct in acetonitrile, the H_a, and H_b proton signals of the cage sharpen and shift upfield again, indicating evacuation of cisplatin from the cavity (Lewis et al., 2012).

In this context, information on the encapsulation process of cisplatin within the more hydrophobic cavity of the bispydridyl ligand forming our $[Pd_2L_4]^{4+}$ cages, as opposed to the less hydrophobic cavity of trispyridyl-ligand Pd_2L_4 metallacages (Lewis et al., 2012, 2014), needs to be achieved still. Thus, we investigated if the encapsulation of the anticancer drug cisplatin could occur in the metallacages using ^{1}H NMR spectroscopy. In order to avoid DMSO as the solvent, since it is known to exchange cisplatin's chlorido ligands, the experiment was carried out in DMF-d_7. Cage **C1** $[Pd_2L_4](NO_3)_4$ was selected to study the encapsulation process due to its solubility in this solvent. **Figure 1** shows the variation of the chemical shifts of selected cage protons upon cisplatin encapsulation. Specifically, we could clearly observe the chemical shifts of peaks H_a and H_b: the peak of H_a, a cavity-facing proton, showed a small upfield shift of δ −1.0 Hz. The *exo*-facing proton, H_b, showed a downfield shift upon cisplatin encapsulation, in accordance with previously reported studies (Lewis et al., 2012). Unfortunately, the cavity facing peak H_e, likely to interact with the guest Pt(II) complex, was masked by the peak of H_f, and therefore, could not be analyzed.

It is worth mentioning that the observed smaller chemical shifts of the cavity facing proton H_a, with respect to those reported by Lewis et al. (2012) can be due to the lack of the H-bonding with the cisplatin guest (via N—H_3N). Moreover, it has been previously reported that NO_3^- counterions are encapsulated within the cage architecture of trispyridyl Pd_2L_4 metallacages featuring a nitrogen in *endo*-position, while BF_4^- ions are not (Lewis and Crowley, 2014). Thus, we hypothesized

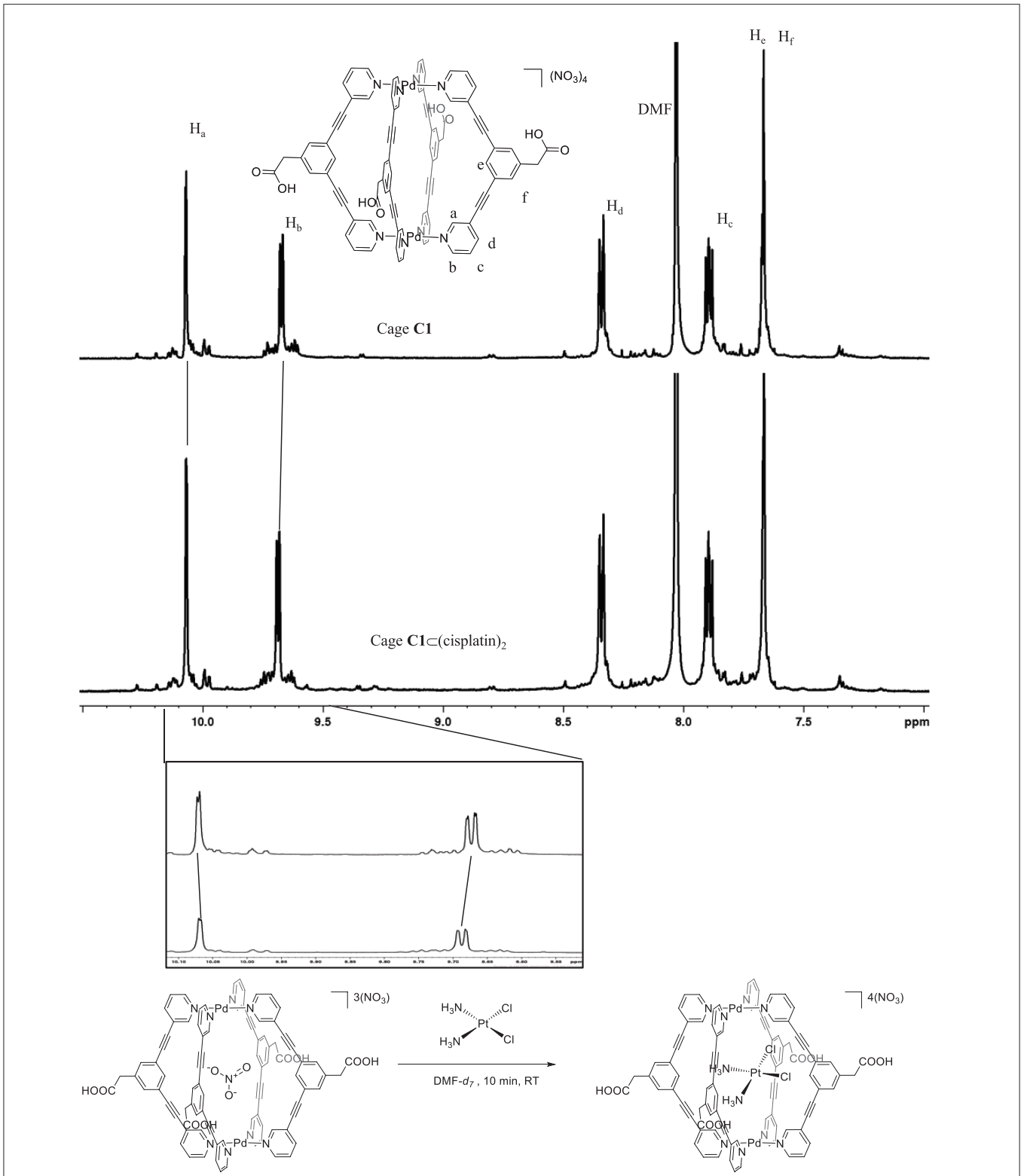

FIGURE 1 | Cisplatin encapsulation in a metallacage following displacement of nitrate ions from the cavity. Stacked spectra of cage **C1** in DMF-d_7 (top) and cage **C1** after the addition of 2 equation of cisplatin (bottom). **Box**: Zoom-in of signals for peaks H_a and H_b with chemical shifts of $\delta = -0.002$ ppm (upfield) and +0.01 ppm (downfield), respectively.

that the observed small chemical shift of H_a following cisplatin encapsulation was due to the presence of NO_3^- ions inside the cage, which already induced chemical shifts of H_a and H_b and thus, acted to "mask" the effect of the cisplatin encapsulation process. In fact, upon evacuation of the anionic NO_3^- counterion, the "de-shielding" effect of the cavity facing protons from NO_3^- would be reduced as the neutral guest, cisplatin, occupies the metallacage cavity.

Afterwards, we also investigated if cisplatin would preferentially be encapsulated within our bispyridyl type Pd_2L_4 metallacages featuring a different counter ion. Therefore, an analogous metallacage was synthesized with BF_4^- as the counterion, **C1.BF$_4$** and studied for its cisplatin encapsulation properties by ^{1}H NMR spectroscopy. **Supporting Figure S10** shows the stacked ^{1}H NMR spectrum of **C1.BF$_4$**, alone or encapsulating cisplatin [**C1.BF$_4$⊂(cisplatin)**] in DMF-d_7. Indeed, both H_a and H_b show marked downfield shifts upon cisplatin encapsulation of 0.044 and 0.033 ppm, respectively. In addition, H_e also shows a downfield shift of 0.03 ppm. Furthermore, the peaks of both H_a and H_b of **C1** (before addition of cisplatin) are already shifted further downfield (**Figure 1**, ca. 0.095 and 0.001 ppm, respectively) when compared to H_a and H_b of **C1.BF$_4$** (**Figure S10**) consistent with encapsulation of NO_3^-.

To continue our investigation, the effect of the solvent polarity was hypothesized to be the driving force of the cisplatin encapsulation process. Thus, the latter was also tested using **C1.BF$_4$** in MeCN-d_3, with reduced polarity with respect to DMF-d_7. However, upon addition of 2 eq. cisplatin to the MeCN-d_3 solution of **C1.BF$_4$** (1 equation) a precipitate was formed, even after several hours of sonication. The suspension was filtered, and the resulting solution was analyzed by ^{1}H NMR spectroscopy. However, the resulting spectra showed no indication of cisplatin encapsulation (data not shown). Instead, the large upfield shift of the peaks corresponding to the α-protons of the coordinating pyridyl is indicative of the ligands no longer coordinated to Pd(II) ions. Moreover, the NMR spectrum suggests that the structure of the ligand has also been altered.

Therefore, in order to study the effects of the solvent on cisplatin encapsulation, we synthesized a derivative of cage **C1.BF$_4$**, but where the carboxylic function was protected by a benzyl group, namely cage **C1Bn.BF$_4$**. Thus, cisplatin encapsulation was followed by ^{1}H NMR in MeCN-d_3 and the results are presented in **Figure S11**. As it can be observed, no chemical shifts could be seen for any of the cage's proton peaks even after 24 h incubation of cisplatin at room temperature. We could conclude that in acetonitrile, cisplatin encapsulation is not favored. In order to check that metallodrug encapsulation was not prevented by the presence of the benzyl group on the cage, we also monitored the process once more in DMF-d_7. The results are depicted in **Figure S12** and indicate that, in these conditions, cisplatin encapsulation occurs, as shown by the chemical shifts of H_a (downfield, $\delta = +0.009$ ppm), H_b (downfield, $\delta = +0.021$ ppm), and a small shift for the cavity-facing proton H_e (upfield, $\delta = -0.002$ ppm). The encapsulation of cisplatin in cage **C1Bn.BF$_4$** was further studied in DMF-d_7 using ^{195}Pt NMR to see if a complementary shift could be observed for the guest cisplatin molecules. Indeed, an upfield shift of −5 ppm was observed upon addition of either 1 eq. or 2 eq. of cisplatin in the presence of metallacage **C1Bn.BF$_4$** (**Figure S13**), supporting cisplatin encapsulation. The obtained results are in agreement with previously reported ones from our group on similar cage systems *exo*-functionalized with different type of ligands (Schmidt et al., 2016c), indicating that surface functionalization does not prevent the guest from entering the cavity.

The encapsulation of cisplatin in **C1Bn.BF$_4$** was also studied by ^{1}H DOSY NMR in DMF-d_7. Cisplatin alone shows a broad signal at 4.18 ppm, H_{NH3} with a diffusion coefficient $= -8.9 \times 10^{-10}$ m^2/s (**Figure S14**, red traces). Clear quenching of this signal was observed upon addition of 1 eq. of metallacage **C1Bn.BF$_4$** (**Figure S14**, blue traces). The cisplatin peak reappears slightly upon addition of a second equivalent of cisplatin to **C1Bn.BF$_4$⊂(cisplatin)** (**Figure S14**, black traces), which may suggest that the metallacage cavity has been saturated to form **C1Bn.BF$_4$⊂(cisplatin)$_2$** and residual cisplatin remains free in solution, or that upon addition of a second equivalent of cisplatin, a dynamic equilibrium occurs.

CONCLUSIONS

In conclusion, we report here on a series of *exo*-functionalized $[Pd_2L_4]^{4+}$ metallacages featuring bispydridyl ligands. Despite the addition of hydrophilic groups to the ligands' scaffold, or the use of different counter ions, the increase in water solubility of the resulting cages was not achieved. Thus, different strategies are necessary to address this problem, including the conjugation of the ligands to peptides. The latter approach has already proved to be successful (Han et al., 2017).

Furthermore, the encapsulation of the anticancer drug cisplatin in selected cages has been studied by NMR spectroscopy, and the obtained results show that if the solvent is of sufficient polarity, metallodrug encapsulation can easily occur in the hydrophobic cavity of the cage despite the absence of hydrogen-bond accepting central pyridine units (Lewis and Crowley, 2014). Conversely, polar solvent molecules capable of forming hydrogen-bond networks (including DMF and water) are likely to prefer not to be encapsulated by hydrophobic cage cavities, as in our case, and will not compete with the cisplatin molecules. This hypothesis is corroborated by previous studies on M_4L_6 metallacages for which guest encapsulation in polar protic solvents, such as water, appears to be driven by initial desolvation of the guest with concomitant rearrangement of the hydrogen bond networks in solution, more than by host-guest interactions alone (Leung et al., 2008). In general, energetically favorable solvent rearrangement during guest desolvation also explains the ability of the supramolecular host to encapsulate neutral guests such as cisplatin, in spite of the lack of possible electrostatic attraction or H-bond interactions with the charged host, as in our case. Further studies are ongoing in our lab to validate this hypothesis.

AUTHOR CONTRIBUTIONS

AC and BW contributed conception and design of the study. BW, MW, and ST contributed to the design, synthesis, and characterization of the ligands, and of the palladium cages. TW contributed to the HR-ESI-MS analysis of the cages. BW and RJ performed the encapsulation studies by NMR spectroscopy. AC and BW wrote the first draft of the manuscript, while MW wrote sections of the manuscript. All authors contributed to manuscript revision, read, and approved the submitted version.

ACKNOWLEDGMENTS

Authors thank Cardiff University for funding.

SUPPLEMENTARY MATERIAL

The Supplementary Material for this article can be found online at: https://www.frontiersin.org/articles/10.3389/fchem.2019.00068/full#supplementary-material

REFERENCES

Ahmad, N., Younus, H. A., Chughtai, A. H., and Verpoort, F. (2015). Metal–organic molecular cages: applications of biochemical implications. *Chem. Soc. Rev.* 44, 9–25. doi: 10.1039/C4CS00222A

Ahmedova, A., Momekova, D., Yamashina, M., Shestakova, P., Momekov, G., Akita, M., et al. (2016). Anticancer potencies of Pt(II)-and Pd(II)-linked M_2L_4 coordination capsules with improved selectivity. *Chem. Asian J.* 11, 474–477. doi: 10.1002/asia.201501238

Altmann, P. J., and Pöthig, A. (2016). Pillarplexes: a metal-organic class of supramolecular hosts. *J. Am. Chem. Soc.* 138, 13171–13174. doi: 10.1021/jacs.6b08571

Casini, A., Woods, B., and Wenzel, M. (2017). The promise of self-assembled 3D supramolecular coordination complexes for biomedical applications. *Inorg. Chem.* 56, 14715–14729. doi: 10.1021/acs.inorgchem.7b02599

Cook, T. R., Vajpayee, V., Lee, M. H., Stang, P. J., and Chi, K. W. (2013). Biomedical and biochemical applications of self-assembled metallacycles and metallacages. *Acc. Chem. Res.* 46, 2464–74. doi: 10.1021/ar400010v.

Han, J., Rader, A., Reichart, F., Aikman, B., Wenzel, M. N., Woods, B., et al. (2018). Bioconjugation of supramolecular metallacages to integrin ligands for targeted delivery of cisplatin. *Bioconjug. Chem.* 29, 3856–3865. doi: 10.1021/acs.bioconjchem.8b00682

Han, J., Schmidt, A., Zhang, T., Permentier, H., Groothuis, G. M. M., Bischoff, R., et al. (2017). Bioconjugation strategies to couple supramolecular: exo - functionalized palladium cages to peptides for biomedical applications. *Chem. Commun.* 53, 1405–1408. doi: 10.1039/c6cc08937b

Kaiser, F., Schmidt, A., Heydenreuter, W., Altmann, P. J., Casini, A., Sieber, S. A., et al.(2016). Self-assembled palladium and platinum coordination cages: photophysical studies and anticancer activity. *Eur. J. Inorg. Chem.* 2016:5189–5196. doi: 10.1002/ejic.201601282

Kaner, R. A., Allison, S. J., Faulkner, A. D., Phillips, R. M., Roper, D. I., Shepherd, S. L., et al. (2016). Anticancer metallohelices: nanomolar potency and high selectivity. *Chem. Sci.* 7, 951–958. doi: 10.1039/C5SC03677A

Leung, D. H., Bergman, R. G., and Raymond, K. N. (2008). Enthalpy-entropy compensation reveals solvent reorganization as a driving force for supramolecular encapsulation in water. *J. Am. Chem. Soc.* 130, 2798–2805. doi: 10.1021/ja075975z

Lewis, J. E., John McAdam, C., Gardiner, M. G., and Crowley, J. D. (2013). A facile "click" approach to functionalised metallosupramolecular architectures. *Chem. Commun.* 49, 3398–3400. doi: 10.1039/c3cc41209a

Lewis, J. E. M., and Crowley, J. D. (2014). *Exo* - and *endo* -hedral interactions of counteranions with tetracationic Pd_2L_4 metallosupramolecular architectures. *Supramol. Chem.* 26, 173–181. doi: 10.1080/10610278.2013.842644

Lewis, J. E. M., Elliott, A. B. S., McAdam, C. J., Gordon, K. C., and Crowley, J. D. (2014). 'Click' to functionalise: synthesis, characterisation and enhancement of the physical properties of a series of exo- and endo-functionalised Pd_2 L_4 nanocages. *Chem. Sci.* 5, 1833–1843. doi: 10.1039/C4SC00434E

Lewis, J. E. M., Gavey, E. L., Cameron, S. A., and Crowley, J. D. (2012). Stimuli-responsive Pd_2L_4 metallosupramolecular cages: towards targeted cisplatin drug delivery. *Chem. Sci.* 3, 778–784. doi: 10.1039/c2sc00899h

Preston, D., McNeill, S. M., Lewis, J. E. M., Giles, G. I., and Crowley, J. D. (2016). Enhanced kinetic stability of $[Pd_2$ $L_4]^{4+}$ cages through ligand substitution. *Dalton Trans.* 45, 8050–8060. doi: 10.1039/C6DT00133E

Schmidt, A., Hollering, M., Drees, M., Casini, A., and Kühn, F. E. (2016a). Supramolecular exo-functionalized palladium cages: fluorescent properties and biological activity. *Dalton Trans.* 45 8556–8565. doi: 10.1039/C6DT00654J

Schmidt, A., Hollering, M., Han, J., Casini, A., and Kühn, F. E. (2016b). Self-assembly of highly luminescent heteronuclear coordination cages. *Dalton Trans.* 45, 12297–12300. doi: 10.1039/c6dt02708c

Schmidt, A., Molano, V., Hollering, M., Pöthig, A., Casini, A., and Kühn, F. E. (2016c). Evaluation of new palladium cages as potential delivery systems for the anticancer drug cisplatin. *Chem. A Eur. J.* 22, 2253–2256. doi: 10.1002/chem.201504930

Schmitt, F., Barry, N. P. E., Juillerat-Jeanneret, L., and Therrien, B. (2012). Efficient photodynamic therapy of cancer using chemotherapeutic porphyrin-ruthenium metalla-cubes. *Bioorg. Med. Chem. Lett.* 22, 178–180. doi: 10.1016/j.bmcl.2011.11.058

Therrien, B. (2013). Drug delivery by water-soluble organometallic cages. *Top. Curr. Chem.* 11, 13–35. doi: 10.1007/128

Vajpayee, V., Yang, Y. J., Kang, S. C., Kim, H., Kim, I. S., Wang, M., et al. (2011). Hexanuclear self-assembled arene-ruthenium nano-prismatic cages: potential anticancer agents. *Chem. Commun.* 47, 5184–5186. doi: 10.1039/c1cc10167f

Conflict of Interest Statement: The authors declare that the research was conducted in the absence of any commercial or financial relationships that could be construed as a potential conflict of interest.

frontiers in Chemistry

ORIGINAL RESEARCH
published: 27 November 2018
doi: 10.3389/fchem.2018.00584

Antimicrobial Activity and Cytotoxicity of Ag(I) and Au(I) Pillarplexes

Alexander Pöthig[1], Sara Ahmed[2], Hanne Cecilie Winther-Larsen[2], Shengyang Guan[1], Philipp J. Altmann[1], Jürgen Kudermann[1], Adriana Magalhães Santos Andresen[2], Tor Gjøen[2] and Ove Alexander Høgmoen Åstrand[3]**

[1] Department of Chemistry and Catalysis Research Center, Technical University of Munich, Garching, Germany, [2] Department of Pharmaceutical Biosciences, School of Pharmacy, University of Oslo, Oslo, Norway, [3] Department of Pharmaceutical Chemistry, School of Pharmacy, University of Oslo, Oslo, Norway

The biological activity of four pillarplex compounds featuring different metals and anions was investigated. The toxicity of the compounds against four bacterial strains [*Bacillus subtilis* (ATCC6633), *Staphylococcus aureus* (ATCC6538), *Escherichia coli* (UVI isolate), *Pseudomonas aeruginosa*], one fungus (*Candida albicans*), and a human cell line (HepG2) was determined. Additionally, a UV-Vis titration study of the pillarplexes was carried out to check for stability depending on pH- and chloride concentration changes and evaluate the applicability in physiological media. All compounds are bioactive: the silver compounds showed higher activity against bacteria and fungi, and the corresponding gold pillarplexes were less toxic against human cells.

Keywords: NHC, silver, gold, antimicrobial, cytotoxicity, organometallic, supramolecular, stability

OPEN ACCESS

Edited by:
Angela Casini,
Cardiff University, United Kingdom

Reviewed by:
Zoe Pikramenou,
University of Birmingham, United Kingdom
Stephane Bellemin-Laponnaz,
Centre National de la Recherche Scientifique (CNRS), France

****Correspondence:***
Alexander Pöthig
alexander.poethig@tum.de
Ove Alexander Høgmoen Åstrand
o.a.h.astrand@farmasi.uio.no

Specialty section:
This article was submitted to Supramolecular Chemistry, a section of the journal Frontiers in Chemistry

Received: *30 September 2018*
Accepted: *08 November 2018*
Published: *27 November 2018*

Citation:
Pöthig A, Ahmed S, Winther-Larsen HC, Guan S, Altmann PJ, Kudermann J, Santos Andresen AM, Gjøen T and Høgmoen Åstrand OA (2018) Antimicrobial Activity and Cytotoxicity of Ag(I) and Au(I) Pillarplexes. Front. Chem. 6:584. doi: 10.3389/fchem.2018.00584

INTRODUCTION

Since the early 2000s, coinage metal complexes featuring N-heterocyclic carbenes (NHC)—a ligand class with a facile tunability toward sterics, electronics, and solubility—have been employed as bioactive compounds (Herrmann, 2002; Mercs and Albrecht, 2010; Hopkinson et al., 2014). As first examples, silver (I) NHC complexes have been used as antimicrobial compounds, pioneered by Youngs et al. (Kascatan-Nebioglu et al., 2004; Melaiye et al., 2004), and a respective applicability of such compounds has been shown for a variety of complexes ever since (**Figure 1**) (Kascatan-Nebioglu et al., 2007; Hindi et al., 2009; Oehninger et al., 2013; Liang et al., 2018). Hereby, a slow release of silver ions originating from the decomposition of the NHC complexes is expected to be the cause of their activity, which can be rationalized by the comparably labile metal-carbene bond (with respect to other late transition metal-NHC bonds) (Kascatan-Nebioglu et al., 2007). The more stable gold (I) NHC complexes were also employed in studies investigating their antibiotic potential (Lazreg and Cazin, 2014). One possible target are (seleno)-cysteine moieties in proteins, e.g., thioredoxin reductase, accompanied by the inhibition of the enzyme, which is similar to the mode of action proposed for the approved metallodrug Auranofin (Baker et al., 2005; Schuh et al., 2012). This is expected in particular for gold(I) mono-carbene complexes, which can dissociate one (labile non-NHC) ligand to coordinate the sulfur or selenium atom (Rubbiani et al., 2011, 2013; Cheng et al., 2014; Meyer et al., 2014; Arambula et al., 2016; Bertrand et al., 2017; Karaca et al., 2017a; Schmidt et al., 2017; Zhang et al., 2018). In case of the di-NHC complexes, which are more stable toward dissociation, a different mode of action can be observed. Casini and coworkers were able to show stacking of Au(I) di-caffeine NHC complexes in G4 quadruplex DNA

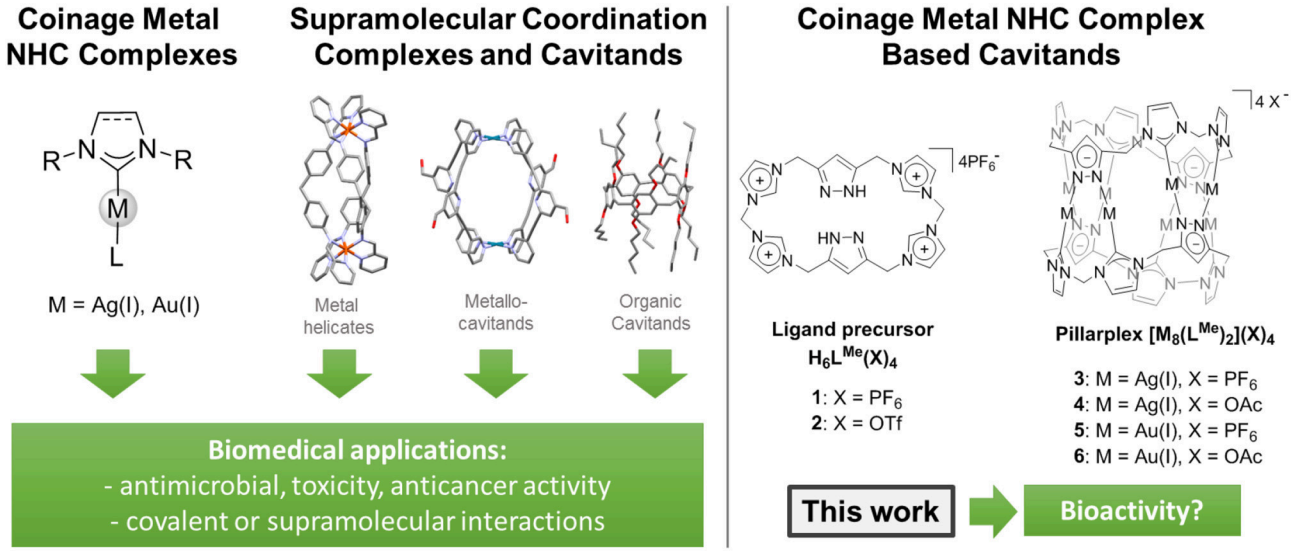

FIGURE 1 | (Left) Overview of related known biomedical relevant compound classes. **(Right)** NHC based organometallocavitands including precursor investigated in this study.

structures, inhibiting telomerase activity (Bertrand et al., 2014; Bazzicalupi et al., 2016; Karaca et al., 2017b). Hereby, the overall structure of the intact complex (being planar, cationic, and possessing a conjugated system for stacking) determines the ability to interact in a non-covalent binding, forming supramolecular aggregates. A related supramolecular recognition of biomolecules causing bioactivity was discovered by Michael Hannon and coworkers, who were using cylindrical metal helicates—a class of supramolecular coordination complexes (SCCs, **Figure 1**)—to interact with different DNA structures (Meistermann et al., 2002; Oleksi et al., 2006; Hannon, 2007; Ducani et al., 2010; Phongtongpasuk et al., 2013; Malina et al., 2016). They showed, that the overall charge of the compounds (4+) as well as the aromatic parts of the ligands were crucial for supramolecular recognition of the negatively charged DNA. In general, such supramolecular coordination compounds are discussed as a promising class for future applications as metallodrugs or drug delivery systems (Casini et al., 2017).

We recently introduced the pillarplexes (**Figure 1**), a new family of SCCs which are structurally similar to Hannon's cylindrical helicates yet additionally exhibit a pore which allows for encapsulation of guest molecules inside the complex (Altmann and Pöthig, 2016). These compounds are octanuclear coinage metal complexes with two coordinating macrocyclic NHC ligands. Due to their in-built functionality (e.g., luminescence, easy tunable solubility) caused by the metal-complex character, the pillarplexes are even more versatile than their highly successful organic relatives—the pillararenes (Ogoshi et al., 2008, 2016). The latter have also been applied in biomedical applications very recently, for reducing cytotoxicity, and improving the anticancer bioactivity of oxaliplatin (Hao et al., 2018). In case of the pillararenes and metallocage systems (Casini et al., 2017), the cavitand itself shows no bioactivity and therefore can be used to modulate the selectivity and activity of an actual metallodrug.

Our pillarplexes combine the possibilities to behave like NHC complexes, i.e., as a metallodrug themselves, with the possible applications of cavitands. Therefore, to explore the future potential of our pillarplexes in the biomedical context, we conducted a toxicity study. We tested the antimicrobial activity of the four metal complexes (**3–6**), the metal salts as well as the ligand precursor salts (**1**, **2**) toward four different bacterial strains [*Bacillus subtilis* (ATCC6633), *Staphylococcus aureus* (ATCC6538), *Escherichia coli* (UVI isolate), *Pseudomonas aeruginosa*] as well as one fungus (*Candida albicans*). We also evaluated the toxicity of the complexes toward a human cell line (HepG2) in order to clarify if related future research directions might be promising to follow. Finally, we conducted a stability study of the pillarplexes toward changes in pH and chloride ion concentration, which has implications on the use of the compounds under physiological conditions.

EXPERIMENTAL SECTION

General Details

Compounds **1**–**6** were prepared according to the reported procedures (Altmann et al., 2015; Altmann and Pöthig, 2016). Chemicals were purchased from commercial suppliers and used without further purification if not stated otherwise. Liquid NMR spectra were recorded on a Bruker Avance DPX 400 and a Bruker DRX 400 at room temperature if not stated otherwise. Chemical shifts are given in parts per million (ppm) and the spectra were referenced by using the residual solvent shift as internal standards. Emission spectra were recorded on a Agilent Cary 60 UV-Vis. Nutrient agar plates were prepared according to the instructions provided by Oxoid where 28 g of nutrient

agar (CM0003) was needed to make 1 L of nutrient agar broth. 11.2 g of the agar was added to three 400 ml glass bottles. Four hundred milliliters of distilled water was added into each bottle containing the nutrient agar and was dissolved by stirring. After sterilization, the nutrient agar bottles were cooled to 50°C and then placed into a 50°C water bath for the temperature to remain constant. The nutrient agar was then poured halfway into 9 cm sterile petri dishes in HEPA filtered laminar flow cabinets to minimize the risk of contamination. The nutrient agar plates were then left to solidify and were refrigerated at 4°C. Mueller-Hinton agar plates were prepared from Mueller-Hinton agar medium (Sigma-Aldrich) and agar (Oxoid LP0011). Twenty-two grams of the Mueller-Hinton medium was added into 1 L of distilled water in a volumetric flask and dissolved with a magnetic flea at speed 6–7 and temperature 300°C for ∼10 min (IKA Labortechnik). Fifteen grams of agar was added to the mixture and the stirring continued at speed 5–6 and at temperatures between 200 and 250°C until the mixture began to boil. After sterilization, the Mueller-Hinton broth was cooled to 50°C and stirred slightly with a magnetic flea for ∼1 min (IKA Labortechnik). Sixty milliliters of the Mueller-Hinton broth was poured into each 13 cm petri dish using the media dispensing machine (IBS Integra Biosciences Technomat) using aseptic techniques. The Mueller-Hinton plates were allowed to cool and then stored in a refrigerator at 4°C. Plates were sterilized and stored at 4°C in the refrigerator before use. One liter of a 0.9% solution of sodium chloride was prepared and sterilized at 121°C for 20 min at 1 atm. The bacteria were streaked onto a nutrient agar plate using a sterile loop and incubated at 37°C overnight. The fungus was streaked using a sterile loop onto a TSA plate and incubated at 25°C for 48 h. Fresh streaks were prepared for each disc diffusion assay.

Disc Diffusion Assays for Antimicrobial Activity

Antimicrobial activity was measured using the disc diffusion assay essentially as described in guidelines from Clinical and Laboratory Standards Institute CLSI (2012). The bacteria were maintained on Nutrient agar (Oxoid), while the fungus was maintained on Sabouraud dextrose agar (Oxoid). An inoculum of the test microorganisms were made by resuspending freshly overnight grown colonies into 2 mL of a sterile salt solution (0.9% NaCl). The test organism was diluted to McFarland standard density no. 2 and mixing thoroughly (McFarland, 1907). For the Gram-negative bacteria and fungus, 60 μL of the inoculum was added to 25 mL of sterile salt solution, while 120 μL was added for the Gram-positive bacteria.

To prepare the plates for the disc diffusion assay Mueller-Hinton agar 2 (Sigma-Aldrich) were covered with 5 mL of the freshly made inoculate. The surplus inoculate was removed and the plates were then left in a laminar flow hood until the surface of the plates were completely dry.

Six millimeter filter discs were impregnated with 10 μL volume of the ligand precursor compounds **1** $[L(PF_6)_4]$ and **2** $[L(OTf)_4]$, silver pillarplexes **3** $[Ag_8L_2(PF_6)_4]$ and **4** $[Ag_8L_2(OAc)_4]$, and gold pillarplexes **5** $[Au_8L_2(PF_6)_4]$ and **6** $[Au_8L_2(OAc)_4]$. The concentration of the compounds used were 10 mM. Further filter discs were also impregnated with 10 μl of: dimethyl sulfoxide (DMSO) acting as a negative control; 10 mM of silver nitrate, 10 mM of gold chloride acting as model compounds for free metal ions; and antibiotic discs including pre-impregnated 30 mg/ml gentamycin sulfate discs (BD BBL Sensi-Disk) (*E. coli*, *S. aureus, P. aeruginosa*), pre-impregnated 30 mg/ml tetracycline discs (BD Sensi-Disc) (*B. subtilis*), and 10 mM of Miconazole nitrate discs (Sigma-Aldrich) (*C. albicans*), acting as positive controls. The filter discs were placed evenly on 13 cm Mueller-Hinton agar plates separated to avoid overlapping inhibitions zones. The plates were incubated overnight at 32°C for the bacteria or 25°C for the fungus. The inhibition zones were measured with a caliper. All experiment was performed at least three times.

In vitro Toxicity in HepG2 Liver Cells

Human hepatocarcinoma cell line HepG2 (HB-8065, ATCC, Manassas, VA, USA) was cultured in MEM-Glutamax (5.5 mM glucose) supplemented with 10% fetal bovine serum (Gibco, Life Technologies AG, Basel, Switzerland), 100 μg/mL streptomycin, and 100 units/mL penicillin (both from Gibco, Life Technologies AG, Basle, Switzerland). Cells were incubated at 37°C under a 5% CO_2 atmosphere. For viability assays, cells were seeded in white 96-well Nunc plates at a density of 20,000 cells/well and left overnight to adhere before experiments were conducted.

The compounds were dissolved in DMSO at concentrations ranging from 10^{-3} to 10^{-6} M and were added to white 96-well plates (maximum DMSO concentration in wells was lower than 1%) containing 20,000 HepG2 cells/well. Plates were incubated for 24 h at 37°C in a 5% CO_2 atmosphere. After 24 h, AlamarBlue cell viability reagent (Thermo Fisher, Carlsbad, CA, USA) was added as a 10% solution, and plates were placed back in the incubator for 4 h. AlamarBlue is a redox indicator yielding a fluorescence signal proportional to the number of viable cells in each well (O'Brien et al., 2003). The fluorescence signal was measured in a microplate reader (Clariostar, BMG Labtech, Ortenberg, Germany) at 550 nm/603 nm (excitation/ emission). Data from four replicates were used to calculate the half-maximal inhibitory concentration (IC_{50}) using Sigmoidal, 4PL, where X is log(concentration) analysis, and a four-parameter logistic regression from GraphPad Prism 7 (GraphPad Software Inc., USA). The experiment was repeated twice with similar results.

UV-Vis Experiments

Stability Tests of Pillarplexes Against Chloride

The titrations of the silver pillarplex **4** and gold pillarplex **6** against chloride ions were carried out by stepwise addition of an increasing volume of a 3.072 M sodium chloride solution to 2 mL of a $1.38 \cdot 10^{-5}$ M aqueous pillarplex solution followed by thorough mixing in a quartz cuvette. The UV-Vis absorption spectra were recorded immediately after the addition. The measured

absorbance was corrected for the increase of the sample volume.

Stability Tests of Pillarplexes Against pH

The stability of silver pillarplex **4** and gold pillarplexes **6** in different concentrations of trifluoromethanesulfonic acid (HOTf) was monitored by UV-Vis spectroscopy. One milliliter of a $2.76 \cdot 10^{-5}$ M aqueous pillarplex solution were injected into an equal volume of 1 mL HOTf solution with pH-values 2, 4, 5, and 6 in the quartz cuvette. The absorption spectra were recorded after 1 min, 1, 7, 24, 48, and 72 h (see **Supplementary Material**).

RESULTS AND DISCUSSION

Antimicrobial Activity Studies

The results of the antimicrobial studies are summarized in **Table 1**.

Both silver compounds (entries 3 and 4) show antimicrobial activity against all bacterial strains as well as the fungus. Hereby, the activity is independent of the anion present, as the results are identical within the margin of errors. In comparison to the positive controls (entries 10–12) the overall activity is moderate, however, (by means of statistic uncertainty) it is identical to that of $AgNO_3$ (entry 7), which has been used as an antibiotic since ancient times (Danscher and Locht, 2010). Hence we suspect the release of silver ions via decomposition of the pillarplexes, which is in agreement with the general behavior of silver(I) NHC complexes, as stated above.

The gold pillarplexes show lower to no activity (entries 5 and 6). Compound **6**, the completely water soluble acetate, shows no activity against any of the microbes, whereas, the more lipophilic compound **5** shows a selective moderate activity against Gram-negative *E. coli* and Gram-positive *S. aureus*. In contrast, $AuCl_3$ shows activity against all bacterial strains (interestingly not against the fungus), which of course might be additionally influenced by the redox activity of the gold(III) ion. However, we suspect the gold pillarplexes being more stable in the physiological environment, therefore not releasing uncoordinated metal ions, which would explain the lower activity. Similarly, if the gold complexes would decompose, a similar toxicity as in case of the free ligand precursors would be expected. In general, such imidazolium salts are known to be potentially toxic, depending on different factors, e.g., lipophilicity or anions (Gravel and Schmitzer, 2017). In our case, the two macrocyclic polyimidazolium ligand precursors (entries 1 and 2) show only moderate and very selective toxicity only against the Gram-positive bacteria *S. aureus* and *B. subtilis*. Gram-positive bacteria lacks the outer membrane surrounding the cell wall. This outer membrane excludes, by various mechanisms, certain drugs from penetrating the bacterial cell (Hancock, 1997) and could be the reason for antimicrobial selectivity of compound **2**. For the latter, no activity at all was observed in case of the gold pillarplexes, why we rule out a possible decomposition.

Cell Toxicity Studies

The results for the toxicity study of the compounds against human HepG2 liver cells are summarized in **Table 2**. The IC_{50}-values were determined for all compounds, however, the silver pillarplexes (3 and 4) as well as $AgNO_3$ and $AuCl_3$ all showed precipitation to some degree. This can influence both uptake of the compounds by the cells and the absorbance read, resulting in ambiguous measurement results, which we have pointed out by an asterisk in **Table 2**.

In general, all tested compounds exhibit biological activity. Both ligand precursors (**1** and **2**) exhibited low toxicity levels which corresponds to the determined IC_{50}–values. In contrast, high cell toxicity was observed in concentration higher than 100 μM for all pillarplexes (see figures in the **Supplementary Material**). According to the determined IC_{50}-values, the gold congeners are more active within the pairs of pillarplexes with the same anions (**3** vs. **5** and **4** vs. **6**).

TABLE 1 | Results from the disc diffusion assay for compounds **1**–**8** (10 mM) as well as reference substrates (30 mg/ml for tetracycline and gentamycine sulfate, and 10 mM for miconazole nitrate).

Entry	Compound	mm no growth zone				
		E. coli	*P. aeruginosa*	*S. aureus*	*B. subtilis*	*C. albicans*
1	$H_6L^{Me}(PF_6)_4$ (**1**)	0 ± 0	0 ± 0	0 ± 0	6.4 ± 0.4	0 ± 0
2	$H_6L^{Me}(OTf)_4$ (**2**)	0 ± 0	0 ± 0	6.7 ± 0.4	6.8 ± 0.3	0 ± 0
3	$[Ag_8(L^{Me})_2]$ $(PF_6)_4$ (**3**)	8.6 ± 0.2	8.0 ± 0.7	9.1 ± 1.7	8.3 ± 0.3	10.1 ± 0.4
4	$[Ag_8(L^{Me})_2]$ $(OAc)_4$ (**4**)	8.0 ± 0	8.2 ± 0.6	9.2 ± 2.1	7.8 ± 0.4	9.2 ± 0.9
5	$[Au_8(L^{Me})_2]$ $(PF_6)_4$ (**5**)	7.4 ± 0.4	0 ± 0	7.4 ± 0.6	0 ± 0	0 ± 0
6	$[Au_8(L^{Me})_2]$ $(OAc)_4$ (**6**)	0 ± 0	0 ± 0	0 ± 0	0 ± 0	0 ± 0
7	$AgNO_3$	7.8 ± 0.3	7.4 ± 0.6	8.9 ± 1.8	6.3 ± 0.5	9.6 ± 0.4
8	$AuCl_3$	8.6 ± 0.4	8 ± 0	8.9 ± 1.7	7.3 ± 0.4	0 ± 0
9	DMSO*	0 ± 0	0 ± 0	0 ± 0	0 ± 0	0 ± 0
10	Miconazole nitrate**	–	–	–	–	17.1 ± 0.8
11	Tetracycline**	–	–	–	28.9 ± 0.5	–
12	Gentamycin sulfate**	23.7 ± 1.6	23.0 ± 0.7	23.7 ± 1.6	–	–

**negative control, **positive control.*

However, they also show a higher base RFU compared to the silver compounds, indicating the gold compounds to be less toxic. With regard to the effect of the anions, the more water-soluble compounds (**2**, **4**, **6**: triflates or acetates) show higher activity than the less water-soluble hexafluorophosphate salts (**1**, **3**, **5**). In general, the same trend as in the antimicrobial assay are observed with the HepG2 cells. The silver pillarplexes appear to be more toxic and more active than their gold counterparts. Precipitation was observed in case of the silver pillarplexes as well as for $AgNO_3$ and $AuCl_3$, whereas the gold pillarplexes did not exhibit any stability or solubility issues.

Stability Tests

To evaluate possible reasons for the observations made during the bacterial and cell tests, we conducted an UV-Vis titration study. In detail, we checked the influence of a varying chloride and proton concentration on the stability or solubility of the pillarplex compounds. Therefore, we first evaluated the absorption properties of the two water-soluble pillarplex acetates **4** and **6** in aqueous solution, as well as the ligand precursor (**Figure 2A**). All compounds absorb in the UV range: the silver complex **4** shows an absorption maximum at 226 nm whereas the gold complex **6** absorbs at 245 nm. The ligand precursor absorbs at 209 nm. The molar extinction coefficients for the pillarplex compounds at the wavelengths of the individual maximal absorption are $9.33 \cdot 10^4 \pm 6.41 \cdot 10^2$ $M^{-1}cm^{-1}$ (**4**) and $1.21 \cdot 10^5 \pm 4.64 \cdot 10^3$ $M^{-1}cm^{-1}$ (**6**).

The titration results of the pillarplexes against an increasing amount of chloride ions present in aqueous solution show a very different behavior of the silver compared to the gold compound (**Figure 2B**). The absorption signal of silver complex **4** immediately drops up to addition of 0.5 mmol NaCl (which is about 17,000-fold excess of chloride). After that, no significant change can be observed in the absorption spectra upon addition of more equivalents of chloride. Apparently, this is close to the physiological concentration of chloride (0.9%) which might be a possible explanation why precipitation was observed in the biological tests for the silver containing pillarplexes. The gold compound **6** also shows a decay if the absorption signal upon chloride addition. However, the drop is less pronounced and at 0.9% chloride concentration, there is still a significant absorption (85% of the initial value). At higher chloride contents we observed a higher variation of the measured values, which we cannot explain up to now. However, even after addition of 1 mmol NaCl (about 35,000-fold excess) the characteristic absorption band at 245 nm can be observed for compound **6** (see **Supplementary Material**), strongly indicating that the gold complex is significantly less effected by chloride addition and still present in solution under physiological conditions.

Figure 3 shows the pH-dependent decay of pillarplex compounds **4** and **6** over time. From our previous work on pillarplex rotaxanes we already knew, that in case of silver, the metal ions can be released quickly in the presence of an excess of the strong trifluoromethanesulfonic acid (Altmann and Pöthig, 2017). This was reproduced also in case of the empty pillarplex **4** (**Figure 3A**) for which an immediate drop of absorption signal at 226 nm was observed at pH 2, indicating very

TABLE 2 | IC_{50}-values for compounds **1**–**6** as well as reference salts against human liver cells (HepG2).

Compound	1	2	3	4	5	6	$AgNO_3$	$AuCl_3$ $3H_2O$
IC_{50} ± SE (μM)	467.5 ± 1.4	402.2 ± 1.1	88*	56*	72.4 ± 1.0	29.9 ± 1.0	127*	274*

Precipitation occurred, therefore IC_{50} results are ambiguous and no SE could be estimated for these compounds (see **Supplementary Material).*

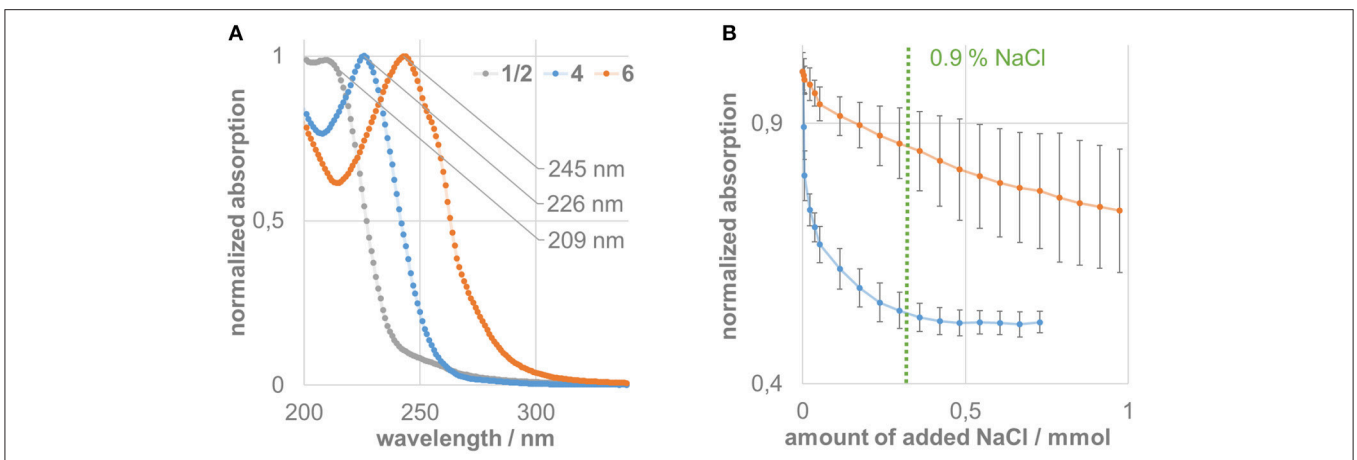

FIGURE 2 | (A) Normalized UV-Vis absorption spectra of the ligand precursor (gray) and pillarplexes **4** (blue), and **6** (orange). **(B)** Titration experiment of compounds **4** (blue) and **6** (orange) against sodium chloride, showing the decay of the normalized signal at the individual absorption maximum (226 nm for **4**, 245 nm for **6**) including statistical uncertainties.

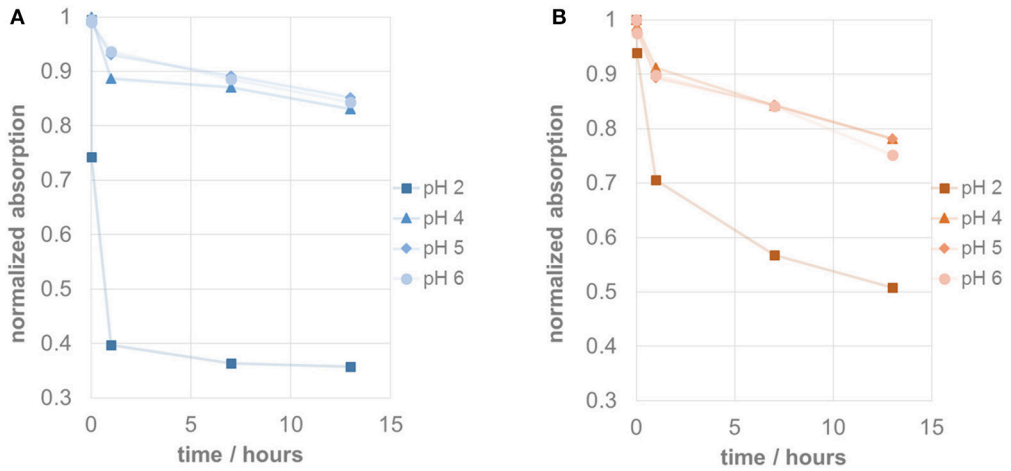

FIGURE 3 | (A) Stability test at different pH-values showing decay of normalized absorption of silver pillarplex **4** (blue) at 226 nm over time. **(B)** Stability test at different pH-values showing decay of normalized absorption of gold pillarplex **6** (orange) at 245 nm over time.

fast decomposition to the protonated imidazolium precursor. The resulting UV-Vis spectrum is also in agreement to that measured for the ligand precursor (**Figure 2A**). At higher pH-values, the decomposition of **4** is significantly slower and almost identical for pH 4–6. A similar behavior was observed for the gold complex **6** although the decay at pH 2 is significantly slower than that of its silver analog (**Figure 3B**). Interestingly, at the higher pH-values the relative drop of the absorption signal is more pronounced compared to the silver complex. However, in case of **6** the resulting absorption spectrum after the assumed decomposition is not resembling that of the ligand precursor, and rather corresponds to the spectrum of **6** just with lower absorption intensity. Therefore, we additionally conducted a NMR experiment to check for protonation of the NHC ligands at pH 2. As a result, no protonated species was detected strongly indicating that the gold pillarplexes are stable even at low pH (see **Supplementary Information Figure S15**).

CONCLUSION

In general, the silver pillarplexes behave like similar silver complexes and show antimicrobial and antifungal activity as well as moderate toxicity toward human HepG2 cells. The corresponding gold complexes were inactive against most bacterial strains and fungi, as well as had lower HepG2 toxicity. The observed effects originate most likely from the increased stability of the gold pillarplexes compared to the silver pillarplexes, as evident by the UV-Vis titration and the ^{1}H NMR experiment. The fact that the gold complexes seem comparably non-toxic and stable opens up the possibility of them being used as drug carriers for selective drug delivery or modified release of drugs that could fit inside the cavity in the pillarplexes.

AUTHOR CONTRIBUTIONS

AP: project conception and supervision, manuscript composition, and writing. PA: synthesis and characterization of pillarplexes. SG: synthesis and characterization of pillarplexes, UV-Vis studies. JK: UV-Vis studies. OH: biological testing supervision, data analysis, manuscript writing. SA biological testing, data analysis. HWL: biological testing, supervision, data analysis. AS: biological testing, data analysis. TG: biological testing supervision, data analysis.

FUNDING

This work was funded by FCI (AP), CSC (SG), TUM-GS (SG), and RCN (OH).

ACKNOWLEDGMENTS

AP thanks the Fonds der chemischen Industrie (FCI) for funding of the project (Sachkostenzuschuss) as well as the Leonhard-Lorenz-Stiftung for financial support. SG thanks the CSC for a personal scholarship and the TUM Graduate School for financial support. OH thanks the Research Council of Norway (RCN) for a mobility grant (grant number: 240215).

SUPPLEMENTARY MATERIAL

The Supplementary Material for this article can be found online at: https://www.frontiersin.org/articles/10.3389/fchem.2018.00584/full#supplementary-material

Additional information on the IC_{50} determinations as well as the UV-Vis experiments is available as supplementary material.

REFERENCES

Altmann P. J., and Pöthig, A. (2017). A pH-dependent, mechanically interlocked switch: organometallic [2]rotaxane vs. organic [3]rotaxane. *Angew. Chem. Int. Ed.* 56, 15733–15736. doi: 10.1002/anie.201709921

Altmann, P. J., Jandl, C., and Pöthig, A. (2015). Introducing a pyrazole/imidazole based hybrid cyclophane: a hydrogen bond sensor and binucleating ligand precursor. *Dalton Trans.* 44, 11278–11281. doi: 10.1039/C5DT01775K

Altmann, P. J., and Pöthig, A. (2016). Pillarplexes: a metal–organic class of supramolecular hosts. *J. Am. Chem. Soc.* 138, 13171–13174. doi: 10.1021/jacs.6b08571

Arambula, J. F., McCall, R., Sidoran, K. J., Magda, D., Mitchell, N. A., Bielawski, C. W., et al. (2016). Targeting antioxidant pathways with ferrocenylated N-heterocyclic carbene supported gold(i) complexes in A549 lung cancer cells. *Chem. Sci.* 7, 1245–1256. doi: 10.1039/C5SC03519H

Baker, M. V., Barnard, P. J., Berners-Price, S. J., Brayshaw, S. K., Hickey, J. L., Skelton, B. W., et al. (2005). Synthesis and structural characterization of linear Au(I) N-heterocyclic carbene complexes: new analogues of the Au(I) phosphine drug auranofin. *J. Organomet. Chem.* 690, 5625–5635. doi: 10.1016/j.jorganchem.2005.07.013

Bazzicalupi, C., Ferraroni, M., Papi, F., Massai, L., Bertrand, B., Messori, L., et al. (2016). Determinants for tight and selective binding of a medicinal dicarbene gold(I) complex to a telomeric DNA G-quadruplex: a joint ESI MS and XRD investigation. *Angew. Chem. Int. Ed.* 55, 4256–4259. doi: 10.1002/anie.201511999

Bertrand, B., Romanov, A. S., Brooks, M., Davis, J., Schmidt, C., Ott, I., et al. (2017). Synthesis, structure and cytotoxicity of cyclic (alkyl)(amino) carbene and acyclic carbene complexes of group 11 metals. *Dalton Trans.* 46, 15875–15887. doi: 10.1039/C7DT03189K

Bertrand, B., Stefan, L., Pirrotta, M., Monchaud, D., Bodio, E., Richard, P., et al. (2014). Caffeine-based gold(I) N-heterocyclic carbenes as possible anticancer agents: synthesis and biological properties. *Inorg. Chem.* 53, 2296–2303. doi: 10.1021/ic403011h

Casini, A., Woods, B., and Wenzel, M. (2017). The promise of self-assembled 3D supramolecular coordination complexes for biomedical applications. *Inorg. Chem.* 56, 14715–14729. doi: 10.1021/acs.inorgchem.7b02599

Cheng, X., Holenya, P., Can, S., Alborzinia, H., Rubbiani, R., Ott, I., et al. (2014). A TrxR inhibiting gold(I) NHC complex induces apoptosis through ASK1-p38-MAPK signaling in pancreatic cancer cells. *Mol. Cancer* 13:221. doi: 10.1186/1476-4598-13-221

CLSI (2012). *Methods for Dilution Antimicrobial Susceptibility Tests for Bacteria That Grow Aerobically*; *Approved Standard, 9th Edn*. Wayne, PA: CLSI.

Danscher, G., and Locht, L. J. (2010). *In vivo* liberation of silver ions from metallic silver surfaces. *Histochem. Cell Biol.* 133, 359–366. doi: 10.1007/s00418-009-0670-5

Ducani, C., Leczkowska, A., Hodges, N. J., and Hannon, M. J. (2010). Noncovalent DNA-binding metallo-supramolecular cylinders prevent DNA transactions *in vitro*. *Angew. Chem. Int. Ed.* 49, 8942–8945. doi: 10.1002/anie.201004471

Gravel, J., and Schmitzer, A. R. (2017). Imidazolium and benzimidazolium-containing compounds: from simple toxic salts to highly bioactive drugs. *Org. Biomol. Chem.* 15, 1051–1071. doi: 10.1039/C6OB02293F

Hancock, R. E. (1997). The bacterial outer membrane as a drug barrier. *Trends Microbiol.* 5, 37–42. doi: 10.1016/S0966-842X(97)81773-8

Hannon, M. J. (2007). Supramolecular DNA recognition. *Chem. Soc. Rev.* 36, 280–295. doi: 10.1039/B606046N

Hao, Q., Chen, Y., Huang, Z., Xu, J.-F., Sun, Z., and Zhang, X. (2018). Supramolecular chemotherapy: carboxylated pillar[6]arene for decreasing cytotoxicity of oxaliplatin to normal cells and improving its anticancer bioactivity against colorectal cancer. *ACS Appl. Mater. Interfaces* 10, 5365–5372. doi: 10.1021/acsami.7b19784

Herrmann, W. A. (2002). N-heterocyclic carbenes: a new concept in organometallic catalysis. *Angew. Chem. Int. Ed.* 41, 1290–1309. doi: 10.1002/1521-3773(20020415)41:8<1290::AID-ANIE1290>3.0.CO;2-Y

Hindi, K. M., Panzner, M. J., Tessier, C. A., Cannon, C. L., and Youngs, W. J. (2009). The medicinal applications of imidazolium carbene-metal complexes. *Chem. Rev.* 109, 3859–3884. doi: 10.1021/cr800500u

Hopkinson, M. N., Richter, C., Schedler, M., and Glorius, F. (2014). An overview of N-heterocyclic carbenes. *Nature* 510, 485–496. doi: 10.1038/nature13384

Karaca, Ö., Meier-Menches, S. M., Casini, A., and Kuehn, F. E. (2017b). On the binding modes of metal NHC complexes with DNA secondary structures: implications for therapy and imaging. *Chem. Commun.* 53, 8249–8260. doi: 10.1039/C7CC03074F

Karaca, Ö., Scalcon, V., Meier-Menches, S. M., Bonsignore, R., Brouwer, J. M. J. L., Tonolo, F., et al. (2017a). Characterization of hydrophilic gold(I) N-heterocyclic carbene (NHC) complexes as potent TrxR inhibitors using biochemical and mass spectrometric approaches. *Inorg. Chem.* 56, 14237–14250. doi: 10.1021/acs.inorgchem.7b02345

Kascatan-Nebioglu, A., Panzner, M. J., Garrison, J. C., Tessier, C. A., and Youngs, W. J. (2004). Synthesis and structural characterization of N-heterocyclic carbene complexes of silver(I) and rhodium(I) from caffeine. *Organometallics* 23, 1928–1931. doi: 10.1021/om030689r

Kascatan-Nebioglu, A., Panzner, M. J., Tessier, C. A., Cannon, C. L., and Youngs, W. J. (2007). N-Heterocyclic carbene–silver complexes: a new class of antibiotics. *Coord. Chem. Rev.* 251, 884–895. doi: 10.1016/j.ccr.2006.08.019

Lazreg, F., and Cazin, C. S. J. (2014). "Medical applications of NHC-gold and -copper complexes," in *N-Heterocyclic Carbenes : Effective Tools for Organometallic Synthesis,* ed S. Nolan (Weinheim: Wiley-VCH Verlag GmbH & Co. KGaA), 173–198.

Liang, X., Luan, S., Yin, Z., He, M., He, C., Yin, L., et al. (2018). Recent advances in the medical use of silver complex. *Eur. J. Med. Chem.* 157, 62–80. doi: 10.1016/j.ejmech.2018.07.057

Malina, J., Hannon, M. J., and Brabec, V. (2016). Iron(II) supramolecular helicates interfere with the HIV-1 Tat-TAR RNA interaction critical for viral replication. *Sci. Rep.* 6, 29674. doi: 10.1038/srep29674

McFarland, J. (1907). The nephelometer:an instrument for estimating the number of bacteria in suspensions used for calculating the opsonic index and for vaccines. *J. Am. Med. Assoc.* 49, 1176–1178. doi: 10.1001/jama.1907.25320140022001f

Meistermann, I., Moreno, V., Prieto, M. J., Moldrheim, E., Sletten, E., Khalid, S., et al. (2002). Intramolecular DNA coiling mediated by metallo-supramolecular cylinders: differential binding of P and M helical enantiomers. *Proc. Natl. Acad. Sci. U.S.A.* 99, 5069–5074. doi: 10.1073/pnas.062634499

Melaiye, A., Simons, R. S., Milsted, A., Pingitore, F., Wesdemiotis, C., Tessier, C. A., et al. (2004). Formation of water-soluble pincer silver(I)–carbene complexes: a novel antimicrobial agent. *J. Med. Chem.* 47, 973–977. doi: 10.1021/jm030262m

Mercs, L., and Albrecht, M. (2010). Beyond catalysis: N-heterocyclic carbene complexes as components for medicinal, luminescent, and functional materials applications. *Chem. Soc. Rev.* 39, 1903–1912. doi: 10.1039/b902238b

Meyer, A., Oehninger, L., Geldmacher, Y., Alborzinia, H., Woelfl, S., Sheldrick, W. S., et al. (2014). Gold(I) N-heterocyclic carbene complexes with naphthalimide ligands as combined thioredoxin reductase inhibitors and DNA intercalators. *ChemMedChem* 9, 1794–1800. doi: 10.1002/cmdc.201402049

O'Brien, J., Wilson, I., Orton, T., and Pognan, F. (2003). Investigation of the alamar blue (resazurin) fluorescent dye for the assessment of mammalian cell cytotoxicity. *Eur. J. Biochem.* 267, 5421–5426. doi: 10.1046/j.1432-1327.2000.01606.x

Oehninger, L., Rubbiani, R., and Ott, I. (2013). N-Heterocyclic carbene metal complexes in medicinal chemistry. *Dalton Trans.* 42, 3269–3284. doi: 10.1039/C2DT32617E

Ogoshi, T., Kanai, S., Fujinami, S., Yamagishi, T.-A., and Nakamoto, Y. (2008). para-Bridged symmetrical pillar[5]arenes: their lewis acid catalyzed synthesis and host–guest property. *J. Am. Chem. Soc.* 130, 5022–5023. doi: 10.1021/ja711260m

Ogoshi, T., Yamagishi, T. A., and Nakamoto, Y. (2016). Pillar-shaped macrocyclic hosts pillar[n]arenes: new key players for supramolecular chemistry. *Chem. Rev.* 116, 7937–8002. doi: 10.1021/acs.chemrev.5b00765

Oleksi, A., Blanco, A. G., Boer, R., Uson, I., Aymami, J., Rodger, A., et al. (2006). Molecular recognition of a three-way DNA junction by a metallosupramolecular helicate. *Angew. Chem. Int. Ed.* 45, 1227–1231. doi: 10.1002/anie.200503822

Phongtongpasuk, S., Paulus, S., Schnabl, J., Sigel, R. K. O., Spingler, B., Hannon, M. J., et al. (2013). Binding of a designed anti-cancer drug to the central cavity of an RNA three-way junction. *Angew. Chem. Int. Ed.* 52, 11513–11516. doi: 10.1002/anie.201305079

Rubbiani, R., Can, S., Kitanovic, I., Alborzinia, H., Stefanopoulou, M., Kokoschka, M., et al. (2011). Comparative *in vitro* evaluation of n-heterocyclic carbene gold(I) complexes of the benzimidazolylidene type. *J. Med. Chem.* 54, 8646–8657. doi: 10.1021/jm201220n

Rubbiani, R., Schuh, E., Meyer, A., Lemke, J., Wimberg, J., Metzler-Nolte, N., et al. (2013). TrxR inhibition and antiproliferative activities of structurally diverse gold N-heterocyclic carbene complexes. *MedChemComm* 4, 942–948. doi: 10.1039/c3md00076a

Schmidt, C., Karge, B., Misgeld, R., Prokop, A., Franke, R., Broenstrup, M., et al. (2017). Gold(I) NHC complexes: antiproliferative activity, cellular uptake, inhibition of mammalian and bacterial thioredoxin reductases, and gram-positive directed antibacterial effects. *Chem. Eur. J.* 23, 1869–1880. doi: 10.1002/chem.201604512

Schuh, E., Pfluger, C., Citta, A., Folda, A., Rigobello, M. P., Bindoli, A., et al. (2012). Gold(I) carbene complexes causing thioredoxin 1 and thioredoxin 2 oxidation as potential anticancer agents. *J. Med. Chem.* 55, 5518–5528. doi: 10.1021/jm300428v

Zhang, C., Maddelein, M.-L., Wai-Yin Sun, R., Gornitzka, H., Cuvillier, O., and Hemmert, C. (2018). Pharmacomodulation on Gold-NHC complexes for anticancer applications - is lipophilicity the key point? *Eur. J. Med. Chem.* 157, 320–332. doi: 10.1016/j.ejmech.2018.07.070

Conflict of Interest Statement: The authors declare that the research was conducted in the absence of any commercial or financial relationships that could be construed as a potential conflict of interest.

frontiers in Chemistry

ORIGINAL RESEARCH
published: 24 April 2019
doi: 10.3389/fchem.2019.00270

Stepwise Synthesis of *Tetra*-imidazolium Macrocycles and Their *N*-Heterocyclic Carbene Metal Complexes

*Zili Li, Nuchareenat Wiratpruk and Peter J. Barnard**

Department of Chemistry and Physics, La Trobe Institute for Molecular Science, La Trobe University, Melbourne, VIC, Australia

A modular stepwise synthetic method has been developed for the preperation of *tetra*-imidazolium macrocycles. Initially a series of three *bis*(imidazolylmethyl)benzene precursors were alkylated with 1,2-dibromoethane to produce the corresponding *bis*-bromoethylimidazolium bromide salts. In the second step the *bis*-bromoethylimidazolium bromide salts were reacted with selected *bis*(imidazolylmethyl)benzene molecules to produce a series of two symmetrical and three asymmetrical *tetra*-imidazolium macrocycles. These *tetra*-imidazolium salts act receptors for anions and ^{1}H-NMR titration studies were used to determine the association constants between two of the macrocycles and the halide anions chloride, bromide and iodide. The *tetra*-imidazolium salts are precursors for *N*-heterocyclic carbene (NHC) ligands and the corresponding silver(I), gold(I), and palladium(II) NHC complexes have been prepared. Varied structures were obtained, which depend on the chosen macrocyclic ligand and metal ion and in the case of the coinage metals Ag(I) and Au(I), mono, di, and hexanuclear complexes were formed.

Keywords: N-heterocycle carbene, macrocycle, anion receptor, N-heterocarbene-gold(I) complexes, tetra-imidazolium

OPEN ACCESS

Edited by:
Angela Casini,
Cardiff University, United Kingdom

Reviewed by:
Alexander Pöthig,
Technische Universität München, Germany
Greta Bergamaschi,
Istituto di Chimica del Riconoscimento Molecolare (ICRM), Italy

****Correspondence:***
Peter J. Barnard
p.barnard@latrobe.edu.au

Specialty section:
This article was submitted to Supramolecular Chemistry, a section of the journal Frontiers in Chemistry

Received: *17 December 2018*
Accepted: *02 April 2019*
Published: *24 April 2019*

Citation:
Li Z, Wiratpruk N and Barnard PJ (2019) Stepwise Synthesis of Tetra-imidazolium Macrocycles and Their N-Heterocyclic Carbene Metal Complexes. Front. Chem. 7:270. doi: 10.3389/fchem.2019.00270

INTRODUCTION

Imidazolium linked macrocycles have attracted significant recent attention because of their capacity to act as anion receptors and to function as pro-ligands for the synthesis of *N*-heterocyclic carbene metal complexes. Due to the great importance of negatively charged anionic species in biology, the preparation of receptor molecules designed to recognize and sense anions is an area of great research interest (Beer and Gale, 2001; Gale, 2003; Martínez-Máñez and Sancenón, 2003). Imidazolium groups are now well-recognized for their favorable features for the generation of anion receptors, which result both from electrostatic and hydrogen bonding interactions (Alcalde et al., 1999, 2007; Chellappan et al., 2005; Wong et al., 2005; Yoon et al., 2006; Xu et al., 2010). For example, a series of *tetra*-imidazolium linked macrocyclic compounds e.g., **I** (**Figure 1**) were shown to bind to biologically relevant anions such as chloride and hydrogen sulfate (Wong et al., 2005; Serpell et al., 2011). Additionally, compounds of this type have been used as selective luminescent sensors for nucleic acids and nucleotide derivatives such as DNA, RNA, ATP, and GTP and to sense and image RNA in the living cells, as a result of strong C-H$^+ \cdots$A$^-$ hydrogen bonding interations (Neelakandan and Ramaiah, 2008; Ahmed et al., 2011, 2012; Shirinfar et al., 2013).

A range of imidazolium linked macrocyclic compounds have been previously reported and both direct macrocyclization (Bass et al., 2010; Altmann et al., 2015; Toure et al., 2016) and stepwise macrocyclization (Mesquida et al., 2013) processes have been previously described for the synthesis of compounds of this type. In the direct macrocyclization approach, equal quantities of a *bis*-imidazole precursor, and a dihaloalkane are combined under high dilution conditions to produce the desired macrocyclic compound. For example, the imidazolium linked macrocycles **II** and **III** were prepared using the direct macrocyclization approach (Hahn et al., 2008; Schulte to Brinke et al., 2013). This approach can be limited due to unintended reactivity between the precursor compounds, which can produce complex reaction mixtures and poor yields of the desired product. Alternatively, stepwise macrocyclization can be used for the synthesis of polyimidazolium linked macrocyclic compounds (Schulte to Brinke and Hahn, 2015) and the synthesis of the *tetra*-imidazolium macrocycle **I** was achieved via sequential alkylation of *bis*-imidazolium precursors (Wong et al., 2005).

Polyimidazolium linked macrocycles have also been utilized as precursors for *N*-heterocyclic carbene metal complexes and previously the Au(III) complex **IV** (**Figure 2**) was prepared the reaction of $KAuCl_4$ with a macrocyclic *tetra*-imidazolium salt **II** (Mageed et al., 2017). Additionally, dinuclear Au(II) and mixed valence Au(I)/Au(III) complexes of have been prepared by the oxidation of dinuclear Au(I) complexes of macrocyclic NHC ligands (Mageed et al., 2018). In the past decade, a number of Ag(I) complexes of macrocyclic NHC ligands that display wide range of structures have been reported (Mckie et al., 2007; Hahn et al., 2008; Schulte to Brinke et al., 2013; Altmann et al., 2016; Fei et al., 2017; Lu et al., 2017, 2018). For example, a sandwich like tetranuclear Ag(I) complex featuring two *tetra*-NHC ligands was prepared **V** (**Figure 2**) and this complex was utilized as a precursor for the preparation of Au(I), Ni(II), Pd(II), and Pt(II) complexes (Altmann et al., 2016). In addition, macrocyclic *tetra*-NHC ligands have been shown to act as tetradentate ligand for square-planer metals such as Pd(II), Ni(II), Cu(I), and Pt(II) (Fei et al., 2017) and the interesting square-planar Pt(II) complex **VI** (**Figure 2**) was prepared by metal-template reaction from the *tetrakis*(trimethylphosphane)platinum(II) triflate and 2-azidophenylisocyanide (Hahn et al., 2005). The biological properties of metal complexes of NHC-based cyclophane and macrocyclic ligands have also been of significant recent interest and Ag(I) and Au(I) complexes have been shown to possess potent antimicrobial and anticancer activities, respectively (Aweda et al., 2013; Shah et al., 2013; Nomiya et al., 2018; Pöthig et al., 2018). Youngs et al. have been particularly active in this field (Hindi et al., 2009; Johnson et al., 2017) and have described the potent antimicrobrial properties of a Ag(I)-NHC complexes of cyclophane ligands (Melaiye et al., 2005). Additionally, a series of Au(I) complexes of related cyclophane-based NHC ligand systems were shown to be selectively toxic to cancer cells as a result of an antimitochondrial mechanism (Barnard et al., 2004, 2006). Meyer and more recently Kühn have also extended the application of macrocyclic tetra-NHC ligands to the synthesis of iron complexes, that provide fascinating models of reactive intermediates that are generated in the catalytic cycles of a range of heme and non-heme iron enzymes (Meyer et al., 2013; Anneser et al., 2015).

As imidazolium linked macrocycles offer the potential for the generations of novel sensors for biologically significant anions and as precursors for NHC metal complexes of metals that are well-known for their biological properties, we became interested in developing new strategies for the synthesis of compounds of this type. In the present paper, we report a novel modular stepwise synthetic approach for the synthesis of *tetra*-imidazolium macrocycles. This approach involves the initial synthesis of *bis*-bromoethylimidazolium bromide precursors, which can then be utilized for the formation of either symmetrical or asymmetrical *tetra*-imidazolium macrocycles. These *tetra*-imidazolium salts bind anions in solution and association constants between two of the macrocycles and the halide anions chloride, bromide, and iodide were determined for two macrocycles. A range of silver(I), gold(I), and palladium(II) NHC complexes have been prepared from these pro-ligands.

RESULTS AND DISCUSSION

Synthesis of *Tetra*-imidazolium Macrocycles

The *ortho*-phenylene linked *tetra*-imidazolium macrocycle **9·Br$_4$** was prepared via a stepwise macrocyclization procedure. Initially, 1,2-*bis*(imidazolylmethyl)benzene **1**(Baker et al., 2001) was alkylated with an excess of 1,2-dibromoethane (30 equivalents) to obtain the *bis*-bromoethylimidazolium bromide salt **5·Br$_2$** in a moderate yield (**Scheme 1**). The ^{1}H-NMR spectrum of **5·Br$_2$** shows the imidazolium C2-H proton resonates as a singlet signal at 9.50 ppm, while the ethylene group protons resonate as two upfield shifted triplet signals at 4.00 and 4.68 ppm. The macrocycle **9·Br$_4$**, was prepared by heating an equimolar mixture of **5·Br$_2$** and **1** in a solvent system consisting of a 1:4 mixture of DMF and acetonitrile under high dilution conditions (**Scheme 1**) and was isolated in a moderate yield of 29.7%. Compound **9·Br$_4$** gave a simple ^{1}H-NMR spectrum consistent with its high symmetry (point group D_{2h}) with downfield shifted signals for the imidazolium protons which resonated at 9.45 (C2-H) and 7.98 and 7.88 ppm (C4-H/C5-H). The protons of the ethylene linker groups resonated as a singlet signal at 4.81 ppm. A similar method was adopted for the synthesis of the *meta*-phenylene linked macrocycle **10·Br$_4$** from a mixture of **2** and **6·Br$_2$** (**Scheme 1**).

With the successful synthesis of the symmetrical macrocycles **9·Br$_4$** and **10·Br$_4$**, we were interested in further exploring the versatility of our stepwise synthetic methodology with the synthesis of asymmetric *tetra*-imidazolium salts. In initial studies, reaction of either **3** with **5·Br$_2$** or **1** with **7·Br$_2$** (**Scheme 1**) under high dilution condition did not successfully produce the desired asymmetrical *tetra*-imidazolium salts. Additionally, attempts to use *tetra*-n-butylammonium bromide (Bu_4N·Br) as a templation reagent in the reaction of **3** with **5·Br$_4$** also did not give the desired product. By contrast, the reaction of compound **1** with

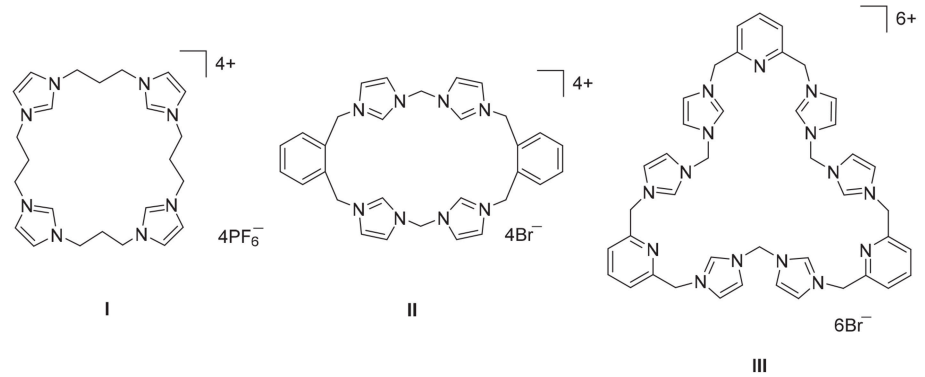

FIGURE 1 | Polyimidazolium linked macrocyclic compound prepared by stepwise macrocyclization (I) and direct macrocyclization (II) and (III) methodologies.

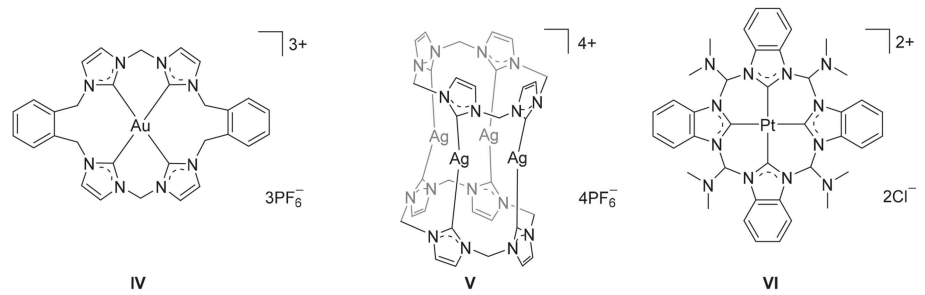

FIGURE 2 | Selected metal complexes derived from macrocyclic imidazolium pro-ligands.

7·Br$_2$ under high dilution condition in presence of $Bu_4N{\cdot}Br$ gave the desired product **11·Br$_4$** in a low yield. The ^{1}H-NMR spectrum of **11·Br$_4$** showed the imidazolium C2-H proton as singlet signal at 9.76 ppm and the methyl group on the imidazolium C2 carbon resonated as a singlet signal at 2.64 ppm. In addition, consistent with the lower symmetry structure (point group C_{2h}) the benzylic proton resonates as two singlet signals at 5.47 and 5.52 ppm. The asymmetrical pro-ligands **12·Br$_4$** and **13·Br$_4$** were prepared in a similar manner from the reaction of either **2** and **8·Br$_2$** or **2** and **5·Br$_2$,** respectively, in presence of $Bu_4N{\cdot}Br$. Again, the ^{1}H-NMR spectrum for **13·Br$_4$** is consistent with the lower symmetry structure, with the C2-H protons resonating as two singlet signals at 8.99 and 9.13 ppm.

Synthesis of Ag(I), Au(I), and Pd(II) Complexes

The Ag(I) complex **14·(PF$_6$)$_6$** was prepared by the reaction of pro-ligand **9·Br$_4$** with Ag_2O in DMF with the exclusion of light (**Scheme 2**) and product was isolated as a white crystalline solid in a yield of 21%. The ^{1}H-NMR spectrum of **14·(PF$_6$)$_6$** showed no imidazolium C2-H proton signal, indicating that the C2 carbon is deprotonated and coordinated to the metal center as a carbene. The ortho-substituted phenyl-linker group protons resonate as two set of doublets (5.68 and 6.94 ppm) and triplet (7.17 and 7.52 ppm) signals, consistent with a more complex magnetic environment for the Ag(I) complex when compared to the pro-ligand. The ^{13}C-NMR spectrum for **14·(PF$_6$)$_6$** revealed a downfield shifted signal at 182 ppm, for which ^{107}Ag-^{13}C (d, ^1J = 182.32 Hz) and ^{109}Ag-^{13}C (d, ^1J = 209.99 Hz) couplings were observed, which is also consistent with coordination of the C2 carbon to Ag(I). The high-resolution mass spectrum for **14·(PF$_6$)$_6$** produced a series of peaks consistent with a hexanuclear structure with the general formula $[Ag_6L_3]^{6+}$ (where L is the macrocyclic *tetra*-carbene ligand). For example, a peak was observed at m/z = 372.0334, which corresponds to the formula $[C_{96}H_{96}N_{24}Ag_6]^{6+}$ (calculated = 372.0419).

Using a similar approach, the Ag(I) complex **17·(PF$_6$)$_3$** was prepared from the pro-ligand **10·Br$_4$**, however for this compound the ^{1}H-NMR spectrum showed a signal at 8.37 ppm, consistent with the C2-H proton being present in the complex. However, the ^{13}C-NMR spectrum of **17·(PF$_6$)$_3$** showed a downfield shifted signal at 180.4 ppm that displays ^{107}Ag-^{13}C (d, ^1J = 183.58 Hz) and ^{109}Ag-^{13}C (d, ^1J = 211.24 Hz) couplings, indicating coordination of the imidazole C2 carbon to Ag(I). These NMR results are consistent with a mononuclear complex, where two of the imidazole units are coordinated to the metal, while the other two remain uncoordinated imidazolium units (**Scheme 3**). To further investigate this result, a different synthetic method was undertaken where the pro-ligand **10·(PF$_6$)$_4$** was reacted with $AgNO_3$ in present of NH_4OH, however the same mononuclear Ag(I) complex was obtained (**Scheme 3**).

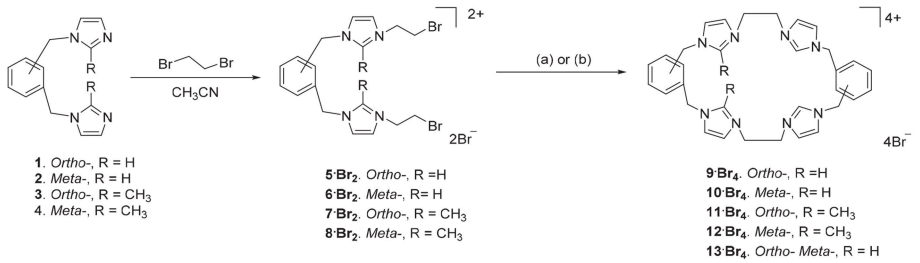

SCHEME 1 | Synthesis of *tetra*-imidazolium macrocyclic compounds **9·Br$_4$-13·Br$_4$.** (a) DMF/CH_3CN 1:4, 110°C. (b) Bu_4N·Br (6.0 eq.), DMF/CH_3CN 1:4, 110°C.

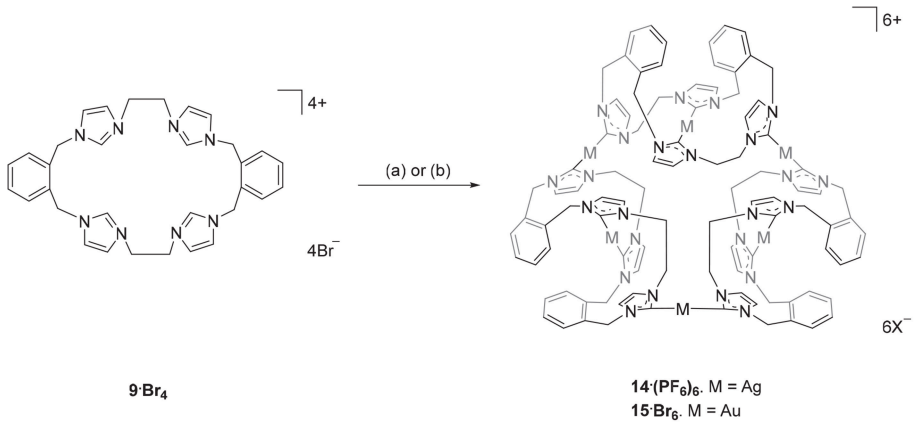

9·Br$_4$

14·(PF$_6$)$_6$. M = Ag
15·Br$_6$. M = Au

SCHEME 2 | Synthesis of the Ag(I) and Au(I) complexes derived from pro-ligand **9·Br$_4$.** (a) Ag_2O (4.0 eq.), DMF, 50°C, 3 d. (b) (THT)AuCl (2.2 eq.), NaOAc, DMF, 110°C, 1 h.

The hexanuclear Au(I) complex **15·Br$_6$** was prepared by the reaction of **9·Br$_4$** with (THT)AuCl in present of the mild base sodium acetate (**Scheme 2**) and the complex was obtained as an off-white solid in 54.2% yield. The same approach was used in an attempt to prepare the Au(I) complex of pro-ligand **10·Br$_4$**, however no complex could be isolated from the reaction mixture. In the next set of reactions, the pro-ligand **11·Br$_4$** (with both normal and C2-blocked imidazolium groups) was reacted with (THT)AuCl in presence of sodium acetate. It was anticipated that this ligand might produce a complex displaying both "normal" and "abnormal" NHC coordination modes, however the dinuclear Au(I) complex **18·(PF$_6$)$_2$** was obtained, which displayed only the "normal" NHC coordination mode (**Scheme 4**). Using the same method, a dinuclear Au(I) complex derived from **19·(PF$_6$)$_4$** was also prepared.

Due to their potential to act as tetradentate ligands with metals that adopt square-planar coordination geometries, the Pd(II) complex of pro-ligand **9·Br$_4$** was prepared. A range of approached have been previously employed for the preparation of Pd(II)-NHC complexes, including *in situ* deprotonation and metallation (Baker et al., 2001; Fei et al., 2017) and transmetallation via an intermediate Ag(I) complex (Schulte to Brinke et al., 2013; Andrew et al., 2016). In this work the former *in situ* deprotonation and metallation approach was initially investigated by reacting **9·(PF$_6$)$_4$** with $Pd(OAc)_2$ in DMSO, however the desired Pd(II) complex could not be isolated. As described previously, a hexanuclear Ag(I) complex could be prepared from the pro-ligand **9·(PF$_6$)$_4$** and in a second attempt to synthesize the Pd(II) complex, pro-ligand **9·Br$_4$** was first reacted with Ag_2O to form the Ag(I) complex *in situ* followed by addition of K_2PdCl_4 (**Scheme 5**). ^{1}H-NMR analysis of Pd(II) complex **16·(PF$_6$)$_2$** showed a relatively simple spectrum with the C4/5 protons of the NHC groups resonating as two sets of doublets at 7.48 and 7.83 ppm. The benzylic protons resonate as two sets of doublet signals at 5.20 and 6.44 ppm (AX pattern), which is consistent with a rigid molecular structure in solution. Furthermore, the ^{13}C-NMR spectrum showed a downfield shifted signal at 167.41 ppm, which corresponds to the NHC carbene carbon coordinated to the Pd(II) metal center.

The Ag(I) transmetallation approach did not successfully produced a Pd(II) complex of pro-ligand **11·Br$_4$**. In this attempt, Ag_2CO_3 was used instead of Ag_2O to avoid the undesirable oxidative cleavage of the C2-blocking methyl group which has been observed previously (Chianese et al., 2004). In a second synthetic attempt, the pro-ligand **11·Br$_4$** was reacted with K_2PdCl_4 in presence of NaOAc. The ^{1}H-NMR of the crude product showed no peak for the C2-H proton for the "unblocked" imidazole units indicating that these groups are coordinated to the metal center. The C4/5 protons of the C2 "blocked" imidazolium group at 7.34 and 7.66 ppm suggesting

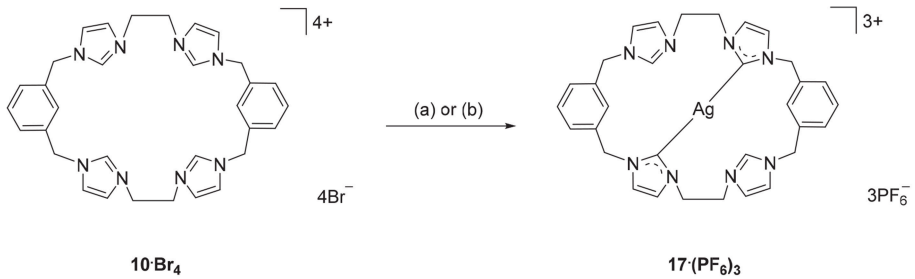

10·Br4 **17·(PF6)3**

SCHEME 3 | Synthesis of Ag(I) complex **17·(PF6)3** from the pro-ligand **10·Br4**. (a) Ag_2O (4.0 eq.), DMF, 70°C, 3 d. (b) $AgNO_3$ (4.0 eq.), NH_4OH (eq.), CH_3CN, RT, overnight.

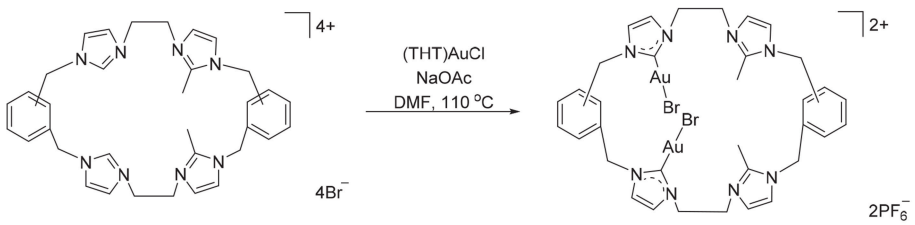

11·Br4. *Ortho-*
12·Br4. *Meta-*

18·(PF6)2. *Ortho-*
19·(PF6)2. *Meta-*

SCHEME 4 | Synthesis of dinuclear Au(I) complex derived from **11·Br4** to **12·Br4**.

that C2 blocked imidazolium unit did not react with the metal. Furthermore, the benzylic proton signals at 5.24 and 5.26 ppm and the ethylene linker signal at 4.61–4.70 ppm also indicated an asymmetrical structure of the title complex. The crystal structure in **Figure 5** also suggested the Pd(II) complex **20·(PF6)2** was successfully synthesized. Unfortunately, it was unable to separate this complex as pure product.

Structural Studies

Compounds **5·Br2**, **9·Br4**, **10·Br3PF6**, **11·Br4**, **15·Br2(PF6)4,** and **20·(PF6)2** were characterized by X-ray crystallography. A representation of the precursor compound **5·Br2** is shown in **Figure S1** while representations of the *tetra*-imidazolium macrocycles **9·Br4**, **10·Br3PF6,** and **11·Br4** are shown in **Figure 3**. In all cases these imidazolium salts display hydrogen bonding interactions between various hydrogens on the cationic imidazolium units and the bromide counter anions. For example, the shortest C2· · · Br distances for **5·Br2**, **9·Br4**, **10·Br3PF6,** and **11·Br4,** respectively, are: 3.4496(3); 3.42219(5) Å; 3.4822(4) Å; and 3.6552 (5) Å, respectively, which fall within a typical range of C-H· · · Br distance caused by hydrogen bonding (Yuan et al., 2002).

Two representations of the X-ray crystal structure for the Au(I) complex **15·Br2(PF6)4** are shown in **Figure 4**. This remarkable structure reveals that the Au(I) complex adopts a cyclic hexanuclear supramolecular assembly with the overall formula $[Au_6L_3]^{6+}$. In the cation, each of the Au(I) centers adopt linear two-coordinate geometries, and they can be divided into two distinct groups of three atoms each. For the first group, each Au(I) atoms (Au1, Au4, and Au5) is bound to two NHC units on opposite sides of each of the three ligand molecules. While each of the Au(I) atoms in the second group (Au2, Au3, and Au6) are coordinated to NHC donors from adjacent ligand molecules, resulting in the formation of a metallo-macrocycle. In each case, the ligand molecules are bowl shaped to accommodate the two Au(I) coordination modes. Interestingly, the metallo-macrocycle is arrayed around an encapsulated central bromide counterion. This bromide ion displays interactions with Au(I) atoms Au1, Au4, and Au5 with the distances being 3.19488(5), 3.24731(5), and 3.23064(4) Å, respectively. Previously, a hexanuclear Ag(I) complex was reported for a *tetra*-carbene ligand linked by aliphatic butyl chains (Fei et al., 2017).

A representation of the X-ray crystal structure for the Pd(II) **20·(PF6)2** is shown in **Figure 5**. The molecular structure shows that the ligand is coordinated to the metal center through the "normal" NHC groups, with the C2 "blocked" groups present as cationic imidazolium units. The Pd(II) center is four-coordinate, with the two-remaining sited being occupied by bromide ions.

Anion Binding Studies

Due to the tetracationic charge of the imidazolium linked macrocycles prepared in this work, the propensity of **9·(PF6)4** and **10·(PF6)4** to bind to the halide anions F^- Cl^-, Br^-, and I^- (as their *tetra*-n-butylammonium halide salts) was evaluated using ^{1}H-NMR titration experiments. In initial studies, it was

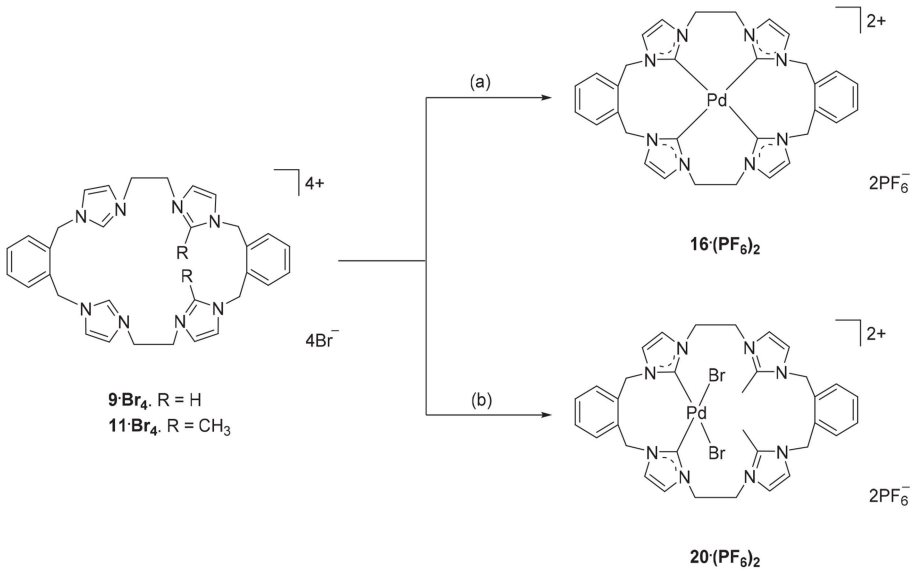

SCHEME 5 | Synthesis of Pd(II) complex **16·(PF$_6$)$_2$** and **20·(PF6)$_2$**. (a) **9·Br$_4$,** Ag_2O (4.0 eq.), K_2PdCl_4, DMF, 85°C. (b) **11·Br$_4$**, K_2PdCl_4, DMSO, 85°C, overnight.

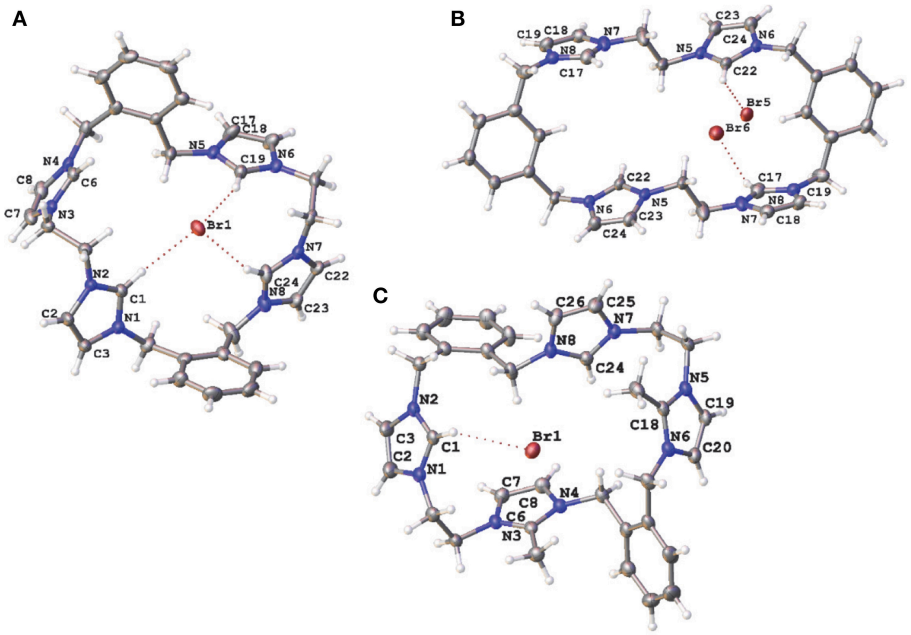

FIGURE 3 | Representations of the X-ray crystal structures of **(A) 9·Br$_4$, (B) 10·Br$_3$PF$_6$**, and **(C) 11·Br$_4$**. Only counter ions involved in hydrogen bonding are included for clarity. Atomic displacement ellipsoids are shown at the 50% probability level.

found that the addition of $Bu_4N{\cdot}F$ to **10·(PF$_6$)$_4$** in d_6-DMSO caused an immediate color change to pale yellow. The ^{1}H-NMR analysis showed that the color change occurred concurrently with a significant broadening and downfield shift of the imidazolium C2-H signal. In addition, the appearance of new unidentified ^{1}H-NMR signals were observed which were consistent with decomposition of the macrocyclic receptor. As such this anion was not studied further.

Addition of increasing equivalents of $Bu_4N{\cdot}Cl$ (0.25–14.0 eq.) to a solution of **9·(PF$_6$)$_4$** in d_6-DMSO caused a significant downfield shift of the resonance corresponding to the imidazolium C2-H signal from 8.96 to 9.64 ppm. In addition, the benzylic proton signal was also shifted downfield from 5.34 to 5.76 ppm. Unfortunately, this study was hampered by the gradual precipitation of the imidazolium salt at higher Cl^- concentrations. In a similar manner, addition of increasing

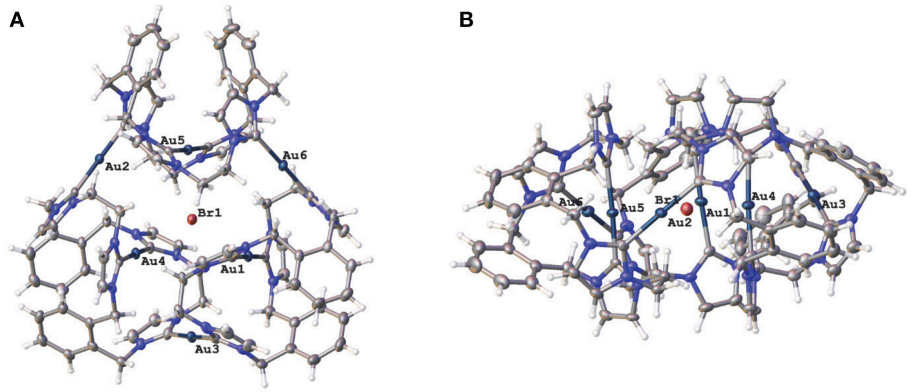

FIGURE 4 | (A) Two representations of the X-ray crystal structures of **15·Br$_2$(PF$_6$)$_4$ (A)** top view and **(B)** edge view. Hydrogen atoms are excluded and only the encapsulated bromide counterion included for clarity. Atomic displacement ellipsoids are shown at the 50% probability level.

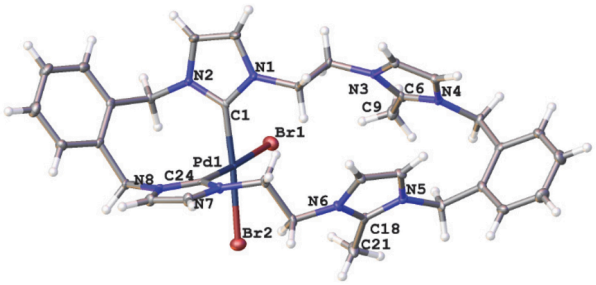

FIGURE 5 | Representations of the X-ray crystal structures of the Pd(II) complex **20·(PF$_6$)$_2$**. Atomic displacement ellipsoids are shown at the 50% probability level.

equivalents of $Bu_4N{\cdot}Br$ and $Bu_4N{\cdot}I$ to **9·(PF$_6$)$_4$** caused downfield shifts in the imidazolium C2-H signal, although to a lesser extent than that seen for $Bu_4N{\cdot}Cl$, however for these anions no precipitation of the macrocycle was seen. **Figure 6** shows the ^{1}H-NMR titration between **9·(PF$_6$)$_4$** and $Bu_4N{\cdot}Br$, while **Figure 7** shows the change in the imidazolium C2-H chemical shift for **9·(PF$_6$)$_4$** in response to increasing equivalents of the added halide anion (solid black lines). Similar results were seen for the macrocyclic receptor **10·(PF$_6$)$_4$** and the plot of experimental titration data is shown in **Figure S2**. Job plot analysis was then used to evaluate the stoichiometry of the interactions between the macrocyclic receptors and the anions Cl^-, Br^-, and I^-. The results of these studies **Figures S3**, **S4** showed that maxima occurred at close to $\chi = 0.5$ indicating 1:1 stoichiometry for both receptor **9**$^{4+}$ and **10**$^{4+}$ with these anions.

Binding (association) constants K_a (M^{-1}) for the *tetra*-imidazolium macrocycles **9·(PF$_6$)$_4$** and **10·(PF$_6$)$_4$** were determined by analysis of the ^{1}H-NMR titration data using the computer program HypNMR 2018 (Frassineti et al., 1995, 2003). The fitted binding isotherms are shown in **Figure 6** and **Figure S2** (red dashed lines) and the calculated binding constants are given in **Table 1**. The values obtained for the compounds studied in this work are similar in magnitude to those reported previously for related compounds. For example, Beer et al. reported association constants of 420(23), 241(3), and 120(1) M^{-1} for a *tetra*-imidazolium macrocycle in d_6-DMSO solution with the anions Cl^-, Br^- and I^-, respectively (Serpell et al., 2011).

CONCLUSION

In conclusion, a novel stepwise synthetic strategy is reported that allows for the synthesis of both symmetrical and asymmetrical *tetra*-imidazolium linked macrocyclic compounds. The synthetic strategy is modular as initially a range of *bis*-bromoethylimidazolium bromide precursors were synthesized, which when combined with chosen *bis*(imidazolylmethyl)benzene molecules produced a range of *tetra*-imidazolium linked macrocycles. These *tetra*-imidazolium salts are of significant interest as they bind anions in solution and offer the potential for the development of sensors for biologically relevant anions. Using ^{1}H-NMR titration studies, the association constants between **9·(PF$_6$)$_4$** and **10·(PF$_6$)$_4$** and the halide anions Cl^-, Br^-, and I^- were determined and these ranged between 501 and 20 M^{-1}. Imidazolium salts are precursors for *N*-heterocyclic carbene (NHC) ligands and given that Ag(I) and Au(I) complexes of NHC ligands have been shown to display antimicrobial (Aweda et al., 2013; Shah et al., 2013) and anticancer(Barnard et al., 2004) properties, respectively, the Ag(I), Au(I), and Pd(II) NHC complexes derived from these *tetra*-imidazolium linked macrocycles were prepared. The Ag(I) complexes **14**$^{6+}$ and the analogous Au(I) complex **15**$^{6+}$ adopted intriguing hexanuclear structures with the general formula $[M_6L_3]^{6+}$. Currently we are exploring the development of silver complexes of NHC ligands as potential antimicrobial agents and supramolecular assemblies such as complex **14**$^{6+}$ are a particular focus for the slow release of silver ions and the results of these studies will be reported in due course.

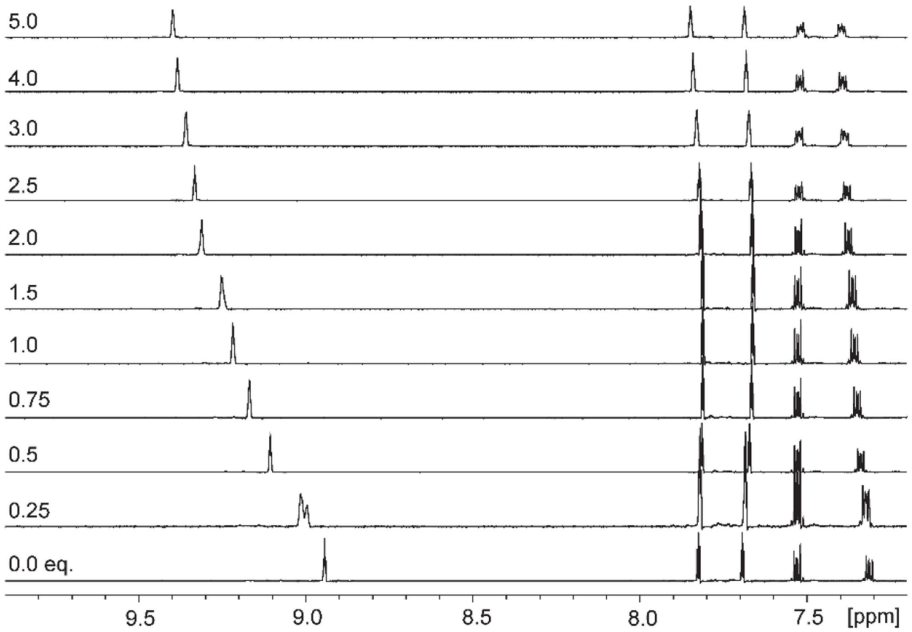

FIGURE 6 | ^{1}H-NMR titration of **9·(PF$_6$)$_4$** in d$_6$-DMSO in the presence of increasing concentrations of Bu$_4$N·Br.

EXPERIMENTAL

General Details

All solvents and chemicals were purchased from Sigma-Aldrich, Chem Supply, Alfa Aesar, and were used as received unless otherwise stated. Where necessary, solvents were further purified using an Innovative Technology Pure Solv solvent purification system. All experiments were performed under an atmosphere of N_2 unless otherwise stated. ^{1}H-NMR and ^{13}C-NMR spectra were recorded on Bruker Advance 500 (500.023 MHz for ^{1}H and 125.74 MHz for ^{13}C) and spectra were referenced to solvent resonances. Where required, COZY, HSQC, HMBC, and NOESY 2-dimensional experiments were used to assist assignments. Mass spectra were obtained using an Agilent 6530 Q-TOF LC/MS mass spectrometer fitted with an Agilent electrospray ion (ESI) source.

X-ray Crystallography

Single crystals suitable for X-ray diffraction studies were grown as follows: **5·Br$_2$** and **9·Br$_4$** diffusion of diethyl ether into an methanol solution of the title compound; **10·Br$_3$PF$_6$** diffusion of diethyl ether into an acetonitrile solution of the title compound containing two drops of a solution of *tetra*-n-butylammonium bromide in acetonitrile; **11·Br$_4$** slow evaporation of a methanol solution of the title compound; **15·Br$_2$(PF$_6$)$_4$** diffusion of ethyl acetate into an acetonitrile solution of the title compound; **20·(PF$_6$)$_2$** was grown by slow diffusion of diethyl ether into an acetonitrile solution of the titled compound. Crystallographic data for all structures determined are given in **Table S1**. For all samples, crystals were removed from the crystallization vial and immediately coated with paratone oil on a glass slide. A suitable crystal was mounted in Paratone oil on a glass fiber and cooled rapidly to 173 K in a stream of cold N_2 using an Oxford low temperature device. Diffraction data were measured using an Rigaku Oxford Diffraction SuperNova X-ray Diffraction System mounted with Mo-Kα λ = 0.71073 Å and Cu-Kα λ = 1.54184. Data were reduced and corrected for absorption using the CrysAlis Pro program. The SHELXL2013-2 program was used to solve the structures with Direct Methods, with refinement by the Full-Matrix Least-Squares refinement techniques on F2. The non-hydrogen atoms were refined anisotropically and

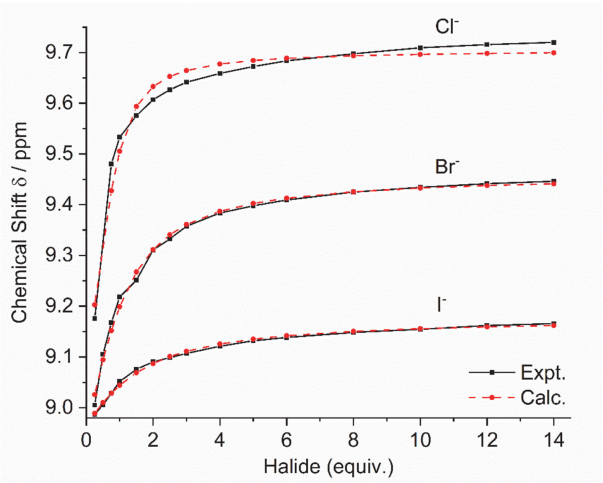

FIGURE 7 | Experimental titration data (black line, squares) and fitted binding isotherms (red dashed line, circles) for the addition of the Bu$_4$N$^+$ halide anion to a solution of **9·(PF$_6$)$_4$** in d$_6$-DMSO.

TABLE 1 | Association constants of the *tetra*-imidazolium macrocycles **9·(PF$_6$)$_4$** and **10·(PF$_6$)$_4$** with F^-, Cl^-, Br^-, and I^-.

	9·(PF$_6$)$_4$	**10·(PF$_6$)$_4$**
Cl^-	501 (12)[a]	ppt[b]
Br^-	126 (15)	63 (6)
I^-	63 (6)	20 (2)

[a] *Precipitate forms after four equivalents of $Bu_4N{\cdot}Cl$ added;* [b] *precipitate forms rapidly and measurement of association constant not possible.*

hydrogen atoms were placed geometrically and refined using the riding model. Coordinates and anisotropic thermal parameters of all non-hydrogen atoms were refined. All calculations were carried out using the program Olex2. Further XRD details are provided in the **Supporting Information**. CCDC 1885400-1885405 contains the supplementary crystallographic data for this paper. These data can be obtained free of charge from The Cambridge Crystallographic Data Centre via www.ccdc.cam.ac.uk/data_request/cif.

^{1}H-NMR Titration Studies

A solution of the title compound (10 mg) in d_6-DMSO (600 μL) and a 1.5 M solution of $Bu_4N{\cdot}X$ (X = Cl, Br and I) in d_6-DMSO were prepared, respectively. To the solution of title compound, increasing equivalents (0.25–14.0 eq.) of 1.5 M $Bu_4N{\cdot}X$ solution was added and the resultant solution was thoroughly mixed. The ^{1}H-NMR spectrum was recorded ∼2 min after each addition at 302 K.

Jobs Plot Analysis

A solution of the title compound (10 mg/mL) in d_6-DMSO and a 0.050 M solution of $Bu_4N{\cdot}X$ (X=Cl, Br and I) in d_6-DMSO were prepared, respectively. A varied fraction of title compound solution and $Bu_4N{\cdot}X$ solution was added and diluted with d_6-DMSO to 600 μL to maintain the total concentration of substance at 10 mM. The resultant solution was thoroughly mixed and ^{1}H-NMR spectrum was recorded at 302 K.

Synthesis

4. Sodium hydride (1.14 g, 47.35 mmol) was added to a solution of 2-methylimidazole (3.11 g, 37.88 mmol) in DMF (50 mL) cooled to 0°C and the resultant mixture was stirred at RT for 1 h and α,α′-dibromo-*m*-xylene (5.00 g, 18.94 mmol) was then added. Stirring was continued at RT for 12 h and the mixture was then diluted with water (100 mL). The mixture was then extracted with CH_2Cl_2 (5 × 10 mL) and the combined organic extracts were washed with water (5 × 50 mL) and then brine (20 mL). The organic layer was dried with $MgSO_4$ and the solvent was evaporated *in vacuo* yielding a yellow oil. Yield: 2.18 g, 43.2%. ^{1}H-NMR (500.02 MHz, d_6-DMSO): δ = 7.33 (t, $^3J_{H-H}$ = 7.5 Hz, 1H, Ar*H*), 7.08 (d, $^3J_{H-H}$ = 1.0 Hz, 2H, H_{imi}), 7.02 (d, $^3J_{H-H}$ = 8.0 Hz, 2H, Ar*H*), 6.96 (s, 1H, Ar*H*), 6.76 (d, $^3J_{H-H}$ = 1.5 Hz, 2H, H_{imi}), 5.12 (s, 4H, CH_2), 2.19 (s, 6H, CH_3). ^{13}C-NMR (125.74 MHz, d_6-DMSO): δ = 144.36 (C_q), 138.55 (C_q), 129.64 (C_{Ar}), 126.96 (C_{imi}), 126.59 (C_{Ar}), 126.07 (C_{Ar}), 120.70 (C_{imi}), 48.94 (CH_2), 13.18 (CH_3). HRESI-MS$^+$ (CH_3CN): $C_{14}H_{15}N_4^+$ m/z = 267.1543, calcd = 267.1604.

5·Br$_2$. To a solution of 1,2-dibromoethane (21.69 mL, 251.7 mmol) in CH_3CN (50 mL) stirred at 110°C, was added dropwise a solution of **1** (2.0 g, 8.39 mmol) in CH_3CN (100 mL) over a period of 3 h. The resultant mixture was stirred at the same temperature for 12 h and then filtered whilst still hot. The filtrate was then evaporated *in vacuo* and the resulting solid was recrystallized from hot ethanol (20 mL) yielding a white crystalline solid. Yield: 2.19 g, 41.2%. ^{1}H-NMR (500.02 MHz, d_6-DMSO): δ = 9.50 (s, 2H, H_{imi}), 7.98 (t, $^3J_{H-H}$ = 1.8 Hz, 2H, H_{imi}), 7.88 (t, $^3J_{H-H}$ = 1.8 Hz, 2H, H_{imi}), 7.49 (dd, $^3J_{H-H}$ = 5.8 Hz, $^4J_{H-H}$ = 3.5 Hz, 2H, Ar*H*), 7.30 (dd, $^3J_{H-H}$ = 5.5 Hz, $^4J_{H-H}$ = 3.5 Hz, 2H, Ar*H*), 5.75 (s, 4H, CH_2), 4.69 (t, $^3J_{H-H}$ = 6.0 Hz, 4H, CH_2), 4.01 (t, $^3J_{H-H}$ = 6.0 Hz, 4H, CH_2). ^{13}C-NMR (125.74 MHz, d_6-DMSO): δ = 137.56 (C_{imi}), 133.38 (C_q), 130.10 (C_{Ar}), 129.83 (C_{Ar}), 123.42 (C_{imi}), 123.38 (C_{imi}), 50.76 (CH_2), 49.61 (CH_2), 32.90 (CH_2). HRESI-MS$^+$ (CH_3OH): $C_{18}H_{22}N_4Br_2^{2+}$ m/z = 227.0094, calcd = 227.0090, $C_{18}H_{22}N_4Br_3^+$ m/z = 532.9367, calcd = 532.9369.

6·Br$_2$. This compound was prepared using the same method as described for **5·Br$_2$** from 1,2-dibromoethane (10.80 mL, 125.90 mmol) and **2** (1.00 g, 4.20 mmol). The crude product was purified by a trituration with diethyl ether (3 × 10 mL) yielding a light brown oil. Yield: 0.62 g, 24.0%. ^{1}H-NMR (500.02 MHz, d_6-DMSO): δ = 9.63 (s, 2H, H_{imi}), 7.95 – 7.97 (m, 4H, H_{imi}), 7.65 (s, 1H, Ar*H*), 7.44 – 7.50 (m, 3H, Ar*H*), 5.56 (s, 4H, CH_2), 4.69 (t, $^3J_{H-H}$ = 5.9 Hz, 4H, CH_2), 4.01 (t, $^3J_{H-H}$ = 5.9 Hz, 4H, CH_2). ^{13}C-NMR (125.74 MHz, d_6-DMSO): δ = 137.31 (C_{imi}), 136.02 (C_q), 130.19 (C_{Ar}), 129.08 (C_{Ar}), 128.90 (C_{Ar}), 123.36 (C_{imi}), 123.16 (C_{imi}), 52.05 (CH_2), 50.76 (CH_2), 32.90 (CH_2). HRESI-MS$^+$ (CH_3OH): $C_{18}H_{22}N_4Br_2^{2+}$ m/z = 227.0102, calcd = 227.0090.

7·Br$_2$. This compound was using the same method as described for **5·Br$_2$** from 1,2-dibromoethane (4.85 mL, 56.31 mmol) and **3** (0.50 g, 1.88 mmol). The crude product was recrystallized from ethanol yielding a white solid. Yield: 0.62 g, 51.6%. ^{1}H-NMR (500.02 MHz, d_6-DMSO): δ =7.90 (d, $^3J_{H-H}$ = 2.1 Hz, 2H, H_{imi}), 7.68 (d, $^3J_{H-H}$ = 2.1 Hz, 2H, H_{imi}), 7.40 (dd, $^3J_{H-H}$ = 5.5 Hz, $^4J_{H-H}$ = 3.4 Hz, 2H, Ar*H*), 6.82 (dd, $^3J_{H-H}$ = 5.7 Hz, $^4J_{H-H}$ = 3.5 Hz, 2H, Ar*H*), 5.67 (s, 4H, CH_2), 4.68 (t, $^3J_{H-H}$ = 5.9 Hz, 4H, CH_2), 4.00 (t, $^3J_{H-H}$ = 5.9 Hz, 4H, CH_2), 2.69 (s, 6H, CH_3). ^{13}C-NMR (125.74 MHz, d_6-DMSO): δ = 146.15 (C_q), 132.62 (C_q), 129.28 (C_{Ar}), 126.95 (C_{Ar}), 122.65 (C_{imi}), 122.43 (C_{imi}), 49.29 (CH_2), 48.85 (CH_2), 31.96 (CH_2), 10.70 (CH_3). HRESI-MS$^+$ (CH_3OH): $C_{20}H_{26}N_4Br_2^{2+}$ m/z = 241.0306, calcd = 241.0246.

8·Br$_2$. This compound was prepared using the same method as described for **5·Br$_2$** from 1,2-dibromoethane (8.15 mL, 94.61 mmol) and **4** (0.84 g, 3.15 mmol). The crude product was recrystallized from ethanol yielding a white solid. Yield: 0.76 g, 37.5%. ^{1}H-NMR (500.02 MHz, d_6-DMSO): δ = 7.81 (s, 2H, H_{imi}), 7.79 (s, 2H, H_{imi}), 7.46 (t, $^3J_{H-H}$ = 7.8 Hz, 1H, Ar*H*), 7.33 (s, 1H, Ar*H*), 7.27 (d, $^3J_{H-H}$ = 7.7 Hz, 2H, Ar*H*), 5.47 (s, 4H, CH_2), 4.62 (t, $^3J_{H-H}$ = 6.0 Hz, 4H, CH_2), 3.93 (t, $^3J_{H-H}$

= 5.9 Hz, 4H, CH_2), 2.67 (s, 6H, CH_3). ^{13}C-NMR (125.74 MHz, d_6-DMSO): δ = 145.47 (C_q), 135.76 (C_q), 130.32 (C_{Ar}), 128.15 (C_{Ar}), 127.59 (C_{Ar}), 122.40 (C_{imi}), 122.35 (C_{imi}), 50.88 (CH_2), 49.17 (CH_2), 31.78 (CH_2), 10.37 (CH_3). HRESI-MS$^+$ (CH_3OH): $C_{20}H_{26}N_4Br_2^{2+}$ m/z = 241.0294, calcd = 241.0246, HRESI-MS$^+$ (CH_3OH): $C_{20}H_{26}N_4Br_3^+$ m/z = 560.9702, calcd = 560.9682.

9·Br$_4$. Solutions of **1** (0.31 g, 1.30 mmol) in CH_3CN (100 mL) and **5·Br$_2$** (0.80 g, 1.30 mmol) in DMF (100 mL) were added simultaneously dropwise to 150 mL of CH_3CN heated at 110°C over a period of 3 h. The mixture was then stirred at the same temperature for a further 5 d during which time a precipitate formed. The precipitate was collected and washed with CH_3CN (3 × 5 mL) and recrystallized from a mixture of methanol and isopropanol yielding a white crystalline solid. Yield: 0.33 g, 29.7%. ^{1}H-NMR (500.02 MHz, d_6-DMSO): δ = 9.45 (s, 4H, H_{imi}), 7.90 (t, $^3J_{H-H}$ = 1.5 Hz, 4H, H_{imi}), 7.77 (t, $^3J_{H-H}$ = 1.5 Hz, 4H, H_{imi}), 7.52 (dd, $^3J_{H-H}$ = 5.8 Hz, $^4J_{H-H}$ = 3.0 Hz, 4H, ArH), 7.40 (dd, $^3J_{H-H}$ = 5.5 Hz, $^4J_{H-H}$ = 3.5 Hz, 4H, ArH), 5.68 (s, 8H, CH_2), 4.81 (s, 8H, CH_2). ^{13}C-NMR (125.74 MHz, d_6-DMSO): δ = 136.75 (C_{imi}), 133.13 (C_q), 131.04 (C_{Ar}), 130.38 (C_{Ar}), 123.66 (C_{imi}), 123.51(C_{imi}), 49.95 (CH_2). HRESI-MS$^+$ (CH_3CN): $C_{32}H_{36}N_8^{4+}$ m/z = 133.0655, calcd = 133.0760, $C_{32}H_{36}N_8P_3F_{18}^+$ m/z = 967.2020, calcd = 967.1967.

10·Br$_4$. This compound was prepared using the same method as described for **9·Br$_4$**. from **2** (0.24 g, 1.01 mmol) and **6·Br$_2$** (0.62 g, 1.01 mmol). Yield: 0.16 g, 18.0%. ^{1}H-NMR (500.02 MHz, d_6-DMSO): δ = 9.53 (s, 4H, H_{imi}) 7.83 (t, $^3J_{H-H}$ = 1.7 Hz, 4H, H_{imi}), 7.80 (t, $^3J_{H-H}$ = 1.7 Hz, 4H, H_{imi}), 7.51 (s, 2H, ArH), 7.36 (t, $^3J_{H-H}$ = 7.7 Hz, 4H, ArH), 7.26–7.28 (m, 4H, ArH), 5.45 (s, 8H, CH_2), 4.84 (s, 8H, CH_2). ^{13}C-NMR (125.74 MHz, d_6-DMSO): δ = 137.50 (C_{imi}), 135.80 (C_q), 130.70 (C_{Ar}), 128.92 (C_{Ar}), 128.87 (C_{Ar}), 128.39 (C_{imi}), 52.21 (CH_2), 48.83 (CH_2). HRESI-MS$^+$ (CH_3CN): $C_{32}H_{36}N_8^{4+}$ m/z = 133.0686, $C_{32}H_{36}N_8^{4+}$ calcd = 133.0760, $C_{32}H_{36}N_8P_2F_{12}^{2+}$ m/z = 411.1099, $C_{32}H_{36}N_8P_2F_{12}^{2+}$ calcd = 411.1163, $C_{32}H_{36}N_8P_3F_{18}^+$ m/z = 967.1990, $C_{32}H_{36}N_8P_3F_{18}^+$ calcd = 967.1967.

11·Br$_4$. Solutions of **1** (0.19 g, 0.80 mmol) in CH_3CN (50 mL) and **7·Br$_2$** (0.50 g, 0.80 mmol) in DMF (50 mL) were added simultaneously dropwise to a solution of Bu_4N·Br (1.55 g, 4.80 mmol) in CH_3CN (150 mL) heated at 110°C over a period of 3 h. The mixture was stirred at the same temperature for a further 5 d during which time a precipitate formed. The precipitate was collected and washed with CH_3CN (3 × 5 mL) and then recrystallized from a mixture of methanol and diethyl ether yielding a white crystalline solid. Yield: 0.10g, 7.5%. ^{1}H-NMR (500.02 MHz, d_6-DMSO): δ = 9.76 (s, 2H, H_{imi}), 8.00 (s, 2H, H_{imi}), 7.65 (s, 2H, H_{imi}), 7.49–7.53 (m, 10H, ArH, H_{imi}), 7.23 (dd, $^3J_{H-H}$ = 5.4 Hz, $^4J_{H-H}$ = 3.6 Hz, 4H, ArH), 5.52 (s, 4H, CH_2), 5.47 (s, 4H, CH_2), 4.81 – 4.83 (m, 4H, CH_2), 4.70 – 4.72 (m, 4H, CH_2), 2.64 (s, 6H, CH_3). ^{13}C-NMR (125.74 MHz, d_6-DMSO): δ = 145.98 (C_q), 137.44 (C_{imi}), 132.92 (C_q), 132.34 (C_q), 131.15 (C_{Ar}), 130.47 (C_{Ar}), 129.97 (C_{Ar}), 129.56 (C_{Ar}), 123.98 (C_{imi}), 123.42 (C_{imi}), 122.83 (C_{imi}), 122.67 (C_{imi}), 49.48 (CH_2), 49.38 (CH_2), 49.19 (CH_2), 47.90 (CH_2), 10.02 (CH_3). HRESI-MS$^+$ (CH_3CN): $C_{32}H_{36}N_8P_2F_{12}^{2+}$ m/z = 425.1335, calcd = 425.1324, $C_{34}H_{40}N_8P_3F_{18}^+$ m/z = 995.2323, calcd 995.2296.

12·Br$_4$. This compound was prepared using the same method described for **11·Br$_4$** from **2** (0.11g, 0.47 mmol) and **8·Br$_2$** (0.30 g, 0.47 mmol). The crude product was recrystallized from methanol yielding a white crystalline solid. Yield: 0.068 g, 16.5%. ^{1}H-NMR (500.023 MHz, d_6-DMSO): δ = 9.53 (s, 2H, H_{imi}), 7.80-7.84 (m, 4H, H_{imi}), 7.62 (d, $^3J_{H-H}$ = 2.2 Hz, 2H, H_{imi}), 7.48 (d, $^3J_{H-H}$ = 2.2 Hz, 2H, H_{imi}), 7.46 (s, 1H, ArH), 7.40 (t, $^3J_{H-H}$ = 7.7 Hz, 1H, ArH), 7.34 (s, 1H, ArH), 7.24 – 7.30 (m, 3H, ArH), 7.12 (dd, $^3J_{H-H}$ = 7.7 Hz, $^4J_{H-H}$ = 1.3 Hz, 2H, ArH), 5.42 (s, 4H, CH_2), 5.38 (s, 4H, CH_2), 4.74 (s, 8H, CH_2), 2.63 (s, 6H, CH_3). ^{13}C-NMR (125.74 MHz, d_6-DMSO): δ = 145.85 (C_q), 137.61 (C_{imi}), 135.54 (C_q), 135.39 (C_q), 128.47 (C_{Ar}), 128.04 (C_{Ar}), 123.50 (C_{imi}), 123.41 (C_{imi}), 122.30 (C_{imi}), 122.23 (C_{imi}), 52.19 (CH_2), 50.92 (CH_2), 48.33 (CH_2), 47.73 (CH_2), 10.49 (CH_3). HRESI-MS$^+$ (CH_3CN): $C_{32}H_{36}N_8Br_2^{2+}$ m/z = 360.0861, calcd = 360.0865.

13·(PF$_6$)$_4$ This compound was prepared using the same method described for **11·Br$_4$** from **2** and **5·Br$_2$** (0.52 g, 0.85 mmol) and Bu_4N·Br (1.37 g, 4.25 mmol). The crude product was then dried *in vacuo* and re-dissolved in water (5 mL) and then filtered through a plug of celite. To this solution, a solution of KPF_6 saturated in aqueous (3 mL) was added to obtain a white precipitate. The precipitate was washed with isopropanol (5 mL) and recrystallized by vapor diffusion of CH_3CN/diethyl ether to obtain a white crystalline. Yield: 0.15 g, 16.0%. ^{1}H-NMR (500.023 MHz, d_6-DMSO): δ = 9.13 (s, 2H, H_{imi}), 8.99 (s, 2H, H_{imi}), 7.84 (t, $^3J_{H-H}$ = 1.8 Hz, 2H, H_{imi}), 7.72 (t, $^3J_{H-H}$ = 1.8 Hz, 2H, H_{imi}), 7.71 (t, $^3J_{H-H}$ = 1.8 Hz, 2H, H_{imi}), 7.65 (t, $^3J_{H-H}$ = 1.8 Hz, 2H, H_{imi}), 7.39 – 7.43 (m, 3H, ArH), 7.11 (s, 1H, ArH), 7.02 (dd, $^3J_{H-H}$ = 7.7 Hz, $^4J_{H-H}$ = 1.1 Hz, 2H, ArH), 6.92 – 6.96 (m, 2H, ArH), 5.37 (s, 4H, CH_2), 5.36 (s, 4H, CH_2), 4.72–4.80 (m, 8H, CH_2). ^{13}C-NMR (125.74 MHz, d_6-DMSO): δ = 137.40 (C_{imi}), 137.28 (C_{imi}), 135.56 (C_q), 132.55 (C_q), 130.16 (C_{Ar}), 130.04 (C_{Ar}), 129.30 (C_{Ar}), 127.75 (C_{Ar}), 127.35(C_{Ar}), 123.99 (C_{imi}), 123.74 (C_{imi}), 123.72 (C_{imi}), 123.57 (C_{imi}), 52.14 (CH_2), 49.50 (CH_2), 49.20 (CH_2). HRESI-MS$^+$ (CH_3CN): $C_{32}H_{36}N_8^{4+}$ m/z = 133.0750, calcd = 133.0760, $C_{32}H_{36}N_8P_2F_{12}^{2+}$ m/z = 411.1158, calcd = 411.1168, $C_{32}H_{36}N_8P_3F_{18}^+$ m/z = 967.1985, calcd = 967.1983.

14·(PF$_6$)$_6$. A slurry of **9·Br$_4$** (0.10 g, 0.12 mmol) and Ag_2O (0.11 g, 0.47 mmol) in DMF (10 mL) was stirred at 50°C for 3 d with the exclusion of light. Diethyl ether (∼50 mL) was then added to the mixture and a gray precipitate formed which was collected and dissolved in hot water (5 mL). The solution was clarified by filtration through syringe filter and a saturated solution of KPF_6 (2 mL) was added to obtain an off-white precipitate. The solid collected and washed with hot isopropanol (2 mL) and then recrystallized from a mixture of CH_3CN and diethyl ether to obtain a white crystalline solid. Yield: 0.026 g, 21.4%. ^{1}H-NMR (500.02 MHz, d_6-DMSO): δ = 7.70 (s, 6H, H_{imi}), 7.68 (s, 6H, H_{imi}), 7.52 (d, $^3J_{H-H}$ = 7.5 Hz, 6H, ArH), 7.17 (t_{app}, J = 7.5 Hz, 6H, ArH,), 7.09 (s, 6H, H_{imi}), 6.94 (t_{app}, J = 7.5 Hz, 6H, ArH), 6.76 (s, 6H, H_{imi}), 5.75 (d, $^2J_{H-H}$ = 15.0 Hz, 12H, CH_2),

5.68 (d, $^3J_{H-H}$ = 7.5 Hz, 6H, Ar*H*), 5.60 (d, $^2J_{H-H}$ = 17.0 Hz, 6H, CH_2), 4.98 (d, $^2J_{H-H}$ = 14.5 Hz, 6H, CH_2), 4.65 (t, $^3J_{H-H}$ = 12.5 Hz, 6H, CH_2), 4.52 (t, $^3J_{H-H}$ = 12.5 Hz, 6H, CH_2), 4.21 (d, $^3J_{H-H}$ = 12.0 Hz, 6H, CH_2), 2.48 (s, 6H, CH_2). ^{13}C-NMR (125.74 MHz, d_6-DMSO): δ = 186.31 (d, ^1J = 182.32 Hz, ^{107}Ag-$C_{carbene}$), 186.31 (d, ^1J = 209.99 Hz, ^{109}Ag-$C_{carbene}$), 178.75 (d, ^1J = 182.32 Hz, ^{107}Ag-$C_{carbene}$), 178.75 (d, ^1J = 209.99 Hz, ^{109}Ag-$C_{carbene}$), 135.80 (C_q), 131.60 (C_q), 130.88 (C_{Ar}), 129.41 (C_{Ar}), 128.14 (C_{Ar}), 124.63 (C_{Ar}), 123.90 (C_{imi}), 123.78(C_{imi}), 121.75 (C_{imi}), 55.37 (CH_2), 52.58 (CH_2), 51.66 (CH_2), 51.24 (CH_2), 50.50 (CH_2). HRESI-MS$^+$ (CH_3CN): $C_{96}H_{96}N_{24}Ag_6^{6+}$ m/z = 372.0334, calcd = 372.0419, $C_{96}H_{96}N_{24}Ag_6P_3F_{18}^{3+}$ m/z = 889.0490, calcd = 889.0485.

15·Br$_6$. A slurry of **9·Br$_4$** (0.10 g, 0.12 mmol) and (THT)AuCl (0.083 g, 0.26 mmol) in DMF (10 mL) was stirred at 110°C for 0.5 h. To this mixture NaOAc (0.050 g, 0.59 mmol) was added and the solution was stirred at the same temperature for 1 h. The resultant mixture was cooled to RT and then diethyl ether (50 mL) was added to obtain a white precipitate. The precipitate was collected and recrystallized from hot methanol (∼5 mL). Yield: 0.048 g, 54.2%. ^{1}H-NMR (500.02 MHz, d_6-DMSO): δ = 7.83 (s, 6H, H_{imi}), 7.72 (s, 6H, H_{imi}), 7.57 (d, $^3J_{H-H}$ = 7.5 Hz, 6H, Ar*H*), 7.21 (t_{app}, J = 7.5 Hz, 6H, Ar*H*) 7.11 (s, 6H, H_{imi}), 6.93 (t_{app}, J = 7.5 Hz, 6H, Ar*H*) 6.84 (s, 6H, H_{imi}), 6.07 (d, $^2J_{H-H}$ = 16.5 Hz, 6H, CH_2), 5.74 – 5.78 (m, 12H, Ar*H*, CH_2), 5.66 (d, $^3J_{H-H}$ = 16.5 Hz, 6H, CH_2), 5.06 (d, $^3J_{H-H}$ = 14.0 Hz, 12H, CH_2), 4.49 (t, $^3J_{H-H}$ = 12.8 Hz, 6H, CH_2), 4.37 (d, $^3J_{H-H}$ = 12.5 Hz, 6H, CH_2), 2.33 (d, $^3J_{H-H}$ = 12.5 Hz, 6H, CH_2). ^{13}C-NMR (125.74 MHz, d_6-DMSO): δ = 186.31 ($C_{carbene}$), 181.48 ($C_{carbene}$), 135.84 (C_q), 131.37 (C_q), 131.02 (C_{Ar}), 129.62 (C_{Ar}), 127.99 (C_{Ar}), 124.59 (C_{Ar}), 123.95 (C_{imi}), 123.64 (C_{imi}), 121.86 (C_{imi}), 51.89 (CH_2), 51.27 (CH_2), 50.22 (CH_2). HRESI-MS$^+$ (CH_3CN): $C_{96}H_{96}N_{24}Au_6^{6+}$ m/z = 461.1022, calcd = 461.1035.

16·(PF$_6$)$_2$. A slurry of **9·Br$_4$** (0.050 g, 0.059 mmol) and Ag_2O (0.030 g, 0.13 mmol) in DMF (5 mL) was stirred at 50°C for 12 h with the exclusion of light. To this mixture K_2PdCl_4 (0.019 g, 0.059 mmol) was added and stirring was continued for a further stirred for 12 h at 80°C. The reaction mixture was clarified by centrifugation and diethyl ether (30 mL) was added to the supernatant yielding a gray precipitate. The precipitate was collected and re-dissolved in hot water (5 mL) and the solution filtered through a syringe filter. To the filtrate, a saturated solution of KPF_6 (2 mL) was added to obtain an off-white precipitate. The precipitate was dried *in vacuo* and then recrystallized from a mixture of CH_3CN and diethyl ether to obtain a white crystalline solid. Yield: 0.0052 g, 9.6%. ^{1}H-NMR (500.02 MHz, d_6-DMSO): δ = 7.87 – 7.92 (m, 4H, Ar*H*), 7.83 (d, $^3J_{H-H}$ = 2.0 Hz, 4H, H_{imi}), 7.48 (d, $^3J_{H-H}$ = 2.0 Hz, 4H, H_{imi}), 7.42 – 7.47 (m, 4H, Ar*H*), 6.44 (d, $^3J_{H-H}$ = 15.0 Hz, 4H, CH_2), 5.20 (d, $^3J_{H-H}$ = 14.7 Hz, 4H, CH_2), 4.98 – 5.06 (m, 4H, CH_2), 4.54 – 4.61 (m, 4H, CH_2). ^{13}C-NMR (125.74 MHz, d_6-DMSO): δ =167.41 ($C_{carbene}$), 135.56 (C_q), 131.73 (C_{Ar}), 129.83 (C_{Ar}), 124.96 (C_{imi}), 122.68 (C_{imi}), 50.79 (CH_2), 47.39 (CH_2). HRESI-MS$^+$ (CH_3CN): $C_{32}H_{32}N_8Pd^{2+}$ m/z = 317.0889, calcd = 317.0887.

17·(PF$_6$)$_3$. This compound was prepared using the same method as described for **14·(PF$_6$)$_6$** from **10·Br$_4$** (0.050 g, 0.059 mmol) and Ag_2O (0.057 g, 0.24 mmol). Yield: 0.0050 g, 6.2%. ^{1}H-NMR (500.02 MHz, CD_3CN): δ = 8.37 (t, J = 1.5 Hz, 2H, H_{imi}), 7.45 – 7.53 (m, 12H, Ar*H*, H_{imi}), 7.21 (t, $^3J_{H-H}$ = 1.8 Hz, 2H, H_{imi}), 6.98 (s, 2H, Ar*H*), 6.95 (t, $^3J_{H-H}$ = 1.9 Hz, 2H, H_{imi}) 5.31 (s, 4H, CH_2), 5.08 (s, 4H, CH_2), 4.60 (d, $^3J_{H-H}$ = 4.3 Hz, 4H, CH_2), 4.55 (d, $^3J_{H-H}$ = 4.7 Hz, 4H, CH_2). ^{13}C-NMR (125.74 MHz, CD_3CN): δ = 180.39 (d, ^1J = 183.58 Hz, ^{107}Ag-$C_{carbene}$), 180.39 (d, ^1J = 211.24 Hz, ^{109}Ag-$C_{carbene}$), 138.62 (C_q), 136.79 (C_q), 136.18 (C_{imi}), 130.86 (C_{Ar}), 129.82 (C_{imi}), 129.48 (C_{imi}), 126.74 (C_{Ar}), 125.47 (C_{Ar}), 125.42 (C_{Ar}), 124.47 (C_{imi}), 124.12 (C_{imi}), 122.39 (C_{Ar}), 122.35 (C_{Ar}), 55.33 (CH_2), 53.45 (CH_2), 52.73 (CH_2), 50.96 (CH_2). HRESI-MS$^+$ (CH_3CN): $C_{32}H_{34}N_8Ag^{3+}$ m/z = 213.0643, calcd = 213.0646, $C_{32}H_{34}N_8AgPF_6^{2+}$ m/z = 391.2845, calcd = 391.0794, $C_{32}H_{34}N_8AgP_2F_{12}^{+}$ m/z = 927.1228, calcd = 927.1235.

18·(PF$_6$)$_2$. This compound was prepared using the same method as described for **15·Br$_6$** from **11·Br$_4$** (0.050 g, 0.057 mmol), (THT)AuCl (0.040 g, 0.13 mmol), and NaOAc (0.019 g, 0.23 mmol). For exchange of the bromide anion to hexafluorophosphate the crude product was dissolved in water (3 mL) and the solution filtered through celite. To this solution, a saturated solution of KPF_6 (2 mL) was added to obtain a white precipitate which was then recrystallized from a mixture of CH_3CN and diethyl ether yielding a white crystalline solid. Yield: 0.020 g, 29.9%. ^{1}H-NMR (500.02 MHz, CD_3CN): δ = 7.55 – 7.57 (m, 1H, Ar*H*), 7.46 – 7.48 (m, 1H, Ar*H*), 7.44 (d, $^3J_{H-H}$ = 2.0 Hz, 1H, H_{imi}), 7.41−7.42 (m, 1H, Ar*H*), 7.38 (s, 1H, H_{imi}), 7.23 (d, $^3J_{H-H}$ = 2.1 Hz, 1H, H_{imi}), 7.21-7.22 (m, 1H, Ar*H*), 7.15 (d, $^3J_{H-H}$ = 1.9 Hz, 1H, H_{imi}), 5.53 (s, 2H, CH_2), 5.49 (s, 2H, CH_2), 4.66 – 4.67 (m, 2H, CH_2), 4.57 – 4.59 (m, 2H, CH_2), 2.54 (s, 3H, CH_3). ^{13}C-NMR (125.74 MHz, CD_3CN): δ = 145.20 ($C_{carbene}$), 133.61 (C_q), 130.51 (C_{Ar}), 130.43 (C_{Ar}), 130.22 (C_{Ar}), 129.75 (C_{Ar}), 122.74 (C_{imi}), 122.50 (C_{imi}), 122.24 (C_{imi}), 122.05 (C_{imi}), 51.84 (CH_2), 50.05 (CH_2), 49.69 (CH_2), 48.48 (CH_2), 10.36 (CH_3). HRESI-MS$^+$ (CH_3CN): $C_{34}H_{38}N_8Au_2Br_2^{2+}$ m/z = 556.0369, calcd = 556.0443.

19·(PF$_6$)$_2$. This compound was prepared using the same method as that described for **15·Br$_6$** from **11·Br$_4$** (0.030 g, 0.034 mmol), (THT)AuCl (0.024 g, 0.075 mmol), and NaOAc (0.11 g, 0.14 mmol). For exchange of the bromide anion to hexafluorophosphate the crude product was dissolved in water (3 mL) and the solution filtered through celite. To this solution, a saturated solution of KPF_6 (2 mL) was added to obtain a white precipitate which was then recrystallized from a mixture of CH_3CN and diethyl ether yielding a white crystalline solid. Yield: 0.0070 g, 1.5%. ^{1}H-NMR (500.02 MHz, d_6-DMSO): δ = 7.71 (d, $^3J_{H-H}$ = 1.9 Hz, 2H, H_{imi}), 7.62 (d, $^3J_{H-H}$ = 1.9 Hz, 2H, H_{imi}), 7.56 (d, $^3J_{H-H}$ = 1.9 Hz, 2H, H_{imi}), 7.39−7.43 (m, 3H, Ar*H*, H_{imi}), 7.28 – 7.38 (m, 3H, Ar*H*), 7.14 – 7.19 (m, 1 H, Ar*H*), 7.07 – 7.14 (m, 1H, Ar*H*), 6.56 – 6.69 (m, 2H, Ar*H*), 5.31 (s, 4H, CH_2), 5.06 (s, 4H, CH_2), 4.67 (s, 4H, CH_2), 4.66 (s, 4H, CH_2), 2.40 (s, 6H, CH_3). ^{13}C-NMR (125.74 MHz, d_6-DMSO): δ = 172.52 ($C_{carbene}$), 144.61 (C_q), 136.79 (C_q), 134.11 (C_q), 130.12 (C_{Ar}), 127.96 (C_{Ar}), 125.29 (C_{Ar}), 123.45 (C_{imi}), 122.28 (C_{imi}), 121.98 (C_{imi}), 121.91 (C_{imi}), 52.82 (CH_2), 50.44 (CH_2),

49.84 (CH_2), 48.11 (CH_2), 9.19 (CH_3). HRESI-MS$^+$ (CH_3CN): $C_{34}H_{38}N_8Au_2Br_2^{2+}$ m/z = 556.0422, calcd = 556.0443.

20·$(PF_6)_2$. To a solution of **11·Br_4** (0.050 g, 0.057 mmol) and K_2PdCl_4 (0.019 g, 0.057 mmol) in DMSO (5 mL) at 85°C, NaOAc (0.019 g, 0.23 mmol) was added and the reaction mixture was stirred same temperature for 12 h. The resultant mixture was then diluted with acetone (5 mL) followed by adding diethyl ether (20 mL) to form a precipitate. The crude precipitate was collected and then re-dissolved in water and filtered through a plug of Celite followed by addition of a saturated solution of KPF_6 (3 mL). The resultant precipitate was collected and washed with isopropanol (5 mL) and diethyl ether (2 × 5 mL) and then recrystallized from a mixture of CH_3CN and diethyl ether yielding the product as a pale yellow solid. NMR analysis showed this material to be impure and the ^{1}H-NMR spectrum is reported for the impure material. ^{1}H-NMR (500.02 MHz, CD_3CN): δ = 7.66 (s, 2H, H_{imi}), 7.55 – 7.57 (m, 4H, Ar*H*), 7.35−7.40 (m, 2H, Ar*H*), 7.34 (s, 2H, H_{imi}), 7.22 – 7.24 (m, 2H, H_{imi}), 7.03 (s, 2H, H_{imi}), 7.02 (s, 2H, H_{imi}), 5.26 (s, 4H, CH_2), 5.24 (s, 4H, CH_2), 4.61 – 4.70 (m, 8H, CH_2), 2.57 (s, 6H, CH_3). A crystal suitable for single crystal X-ray diffraction analysis of **20·$(PF_6)_2$** was grown from diffusion of diethyl ether into an acetonitrile solution of **20·$(PF_6)_2$**.

AUTHOR CONTRIBUTIONS

PB conceived of the presented idea. ZL synthesized compounds and recorded NMR spectra. NW recorded and analyzed high resolution mass spectra. PB and ZL collected X-ray diffraction data. All authors discussed the results and contributed to the final manuscript.

FUNDING

This research was financially supported by The Australia Research Council, DP150102741 and ZL acknowledges receipt of a La Trobe University postgraduate award.

SUPPLEMENTARY MATERIAL

The Supplementary Material for this article can be found online at: https://www.frontiersin.org/articles/10.3389/fchem.2019.00270/full#supplementary-material

Supporting Information | Synthetic details for compounds **1**-**3**, Crystallographic data for compounds **5·Br_2**, **9·Br_4**, **10·Br_3PF_6**, **11·Br_4**, **15·$Br_2(PF_6)_4$,** and **20·$(PF_6)_2$** and further X-ray crystallographic details and anion binding Job plots for compounds **9·$(PF_6)_4$** and **10·$(PF_6)_4$** and 1H and 13C NMR spectra for tetra-imidazolium salts and metal complexes.

REFERENCES

Ahmed, N., Shirinfar, B., Geronimo, I., and Kim, K. S. (2011). Fluorescent imidazolium-based cyclophane for detection of guanosine-5′-triphosphate and I– in aqueous solution of physiological pH. *Org. Lett.* 13, 5476–5479. doi: 10.1021/ol202183t

Ahmed, N., Shirinfar, B., Youn, I. S., Bist, A., Suresh, V., and Kim, K. S. (2012). A highly selective fluorescent chemosensor for guanosine-5′-triphosphatevia excimer formation in aqueous solution of physiological pH. *Chem. Commun.* 48, 2662–2664. doi: 10.1039/c2cc17145g

Alcalde, E., Mesquida, N., Perez-Garcia, L., Alvarez-Rua, C., Garcia-Granda, S., and Garcia-Rodriguez, E. (1999). Hydrogen bonded driven anion binding by dicationic [14]imidazoliophanes. *Chem. Commun.* 0, 295–296. doi: 10.1039/a808503j

Alcalde, E., Mesquida, N., Vilaseca, M., Alvarez-Rúa, C., and García-Granda, S. (2007). Imidazolium-based dicationic cyclophanes. solid-state aggregates with unconventional (C–H)+···Cl– hydrogen bonding revealed by X-ray diffraction. *Supramol. Chem.* 19, 501–509. doi: 10.1080/10610270601132624

Altmann, P. J., Jandl, C., and Pöthig, A. (2015). Introducing a pyrazole/imidazole based hybrid cyclophane: a hydrogen bond sensor and binucleating ligand precursor. *Dalton Trans.* 44, 11278–11281. doi: 10.1039/C5DT01775K

Altmann, P. J., Weiss, D. T., Jandl, C., and Kühn, F. E. (2016). Exploring coordination modes: late transition metal complexes with a methylene-bridged macrocyclic tetra-NHC ligand. *Chem. Asian J.* 11, 1597–1605. doi: 10.1002/asia.201600198

Andrew, R. E., Storey, C. M., and Chaplin, A. B. (2016). Well-defined coinage metal transfer agents for the synthesis of NHC-based nickel, rhodium and palladium macrocycles. *Dalton Trans.* 45, 8937–8944. doi: 10.1039/C6DT01263A

Anneser, M. R., Haslinger, S., Pöthig, A., Cokoja, M., Basset, J.-M., and Kühn, F. E. (2015). Synthesis and characterization of an iron complex bearing a cyclic tetra-N-heterocyclic carbene ligand: an artifical heme analogue? *Inorg. Chem.* 54, 3797–3804. doi: 10.1021/ic503043h

Aweda, T. A., Ikotun, O., Mastren, T., Cannon, C. L., Wright, B., Youngs, W. J., et al. (2013). The use of 111Ag as a tool for studying biological distribution of silver-based antimicrobials. *Med. Chem. Commun.* 4, 1015–1017. doi: 10.1039/c3md00082f

Baker, M. V., Skelton, B. W., White, A. H., and Williams, C. C. (2001). Palladium carbene complexes derived from imidazolium-linked ortho-cyclophanes. *J. Chem. Soc. Dalton Trans.* 111–120. doi: 10.1039/b007293l

Barnard, P. J., Baker, M. V., Berners-Price, S. J., and Day, D. A. (2004). Mitochondrial permeability transition induced by dinuclear gold(I)–carbene complexes: potential new antimitochondrial antitumour agents. *J. Inorg. Biochem.* 98, 1642–1647. doi: 10.1016/j.jinorgbio.2004.05.011

Barnard, P. J., Wedlock, L. E., Baker, M. V., Berners-Price, S. J., Joyce, D. A., Skelton, B. W., et al. (2006). Luminescence studies of the intracellular distribution of a dinuclear Gold(I) N-heterocyclic carbene complex. *Angew. Chem. Int. Ed.* 45, 5966–5970. doi: 10.1002/anie.200601526

Bass, H. M., Cramer, S. A., Price, J. L., and Jenkins, D. M. (2010). 18-atom-ringed macrocyclic tetra-imidazoliums for preparation of monomeric tetra-carbene complexes. *Organometallics* 29, 3235–3238. doi: 10.1021/om100625g

Beer, P. D., and Gale, P. A. (2001). Anion recognition and sensing: the state of the art and future perspectives. *Angew. Chem. int. Ed.* 40, 486–516. doi: 10.1002/1521-3773(20010202)40:3<486::AID-ANIE486>3.0.CO;2-P

Chellappan, K., Singh, N. J., Hwang, I. C., Lee, J. W., and Kim, K. S. (2005). A Calix[4]imidazolium[2]pyridine as an anion receptor. *Angew. Chem. Int. Ed.* 44, 2899–2903. doi: 10.1002/anie.200500119

Chianese, A. R., Zeglis, B. M., and Crabtree, R. H. (2004). Unexpected oxidative C–C cleavage in the metallation of 2-substituted imidazolium salts to give N-heterocyclic carbene complexes. *Chem. Commun.* 2176–2177. doi: 10.1039/B409672J

Fei, F., Lu, T., Chen, X., and Xue, Z. (2017). Synthesis and structural characterization of metal complexes with macrocyclic tetracarbene ligands. *N. J. Chem.* 41, 13442–13453. doi: 10.1039/C7NJ02485A

Frassineti, C., Alderighi, L., Gans, P., Sabatini, A., Vacca, A., and Ghelli, S. (2003). Determination of protonation constants of some fluorinated polyamines by means of 13C NMR data processed by the new computer program HypNMR2000. Protonation sequence in polyamines. *Anal. Boianal. Chem.* 376, 1041–1052. doi: 10.1007/s00216-003-2020-0

Frassineti, C., Ghelli, S., Gans, P., Sabatini, A., Moruzzi, M. S., and Vacca, A. (1995). Nuclear magnetic resonance as a tool for determining protonation constants of natural polyprotic bases in solution. *Anal. Biochem.* 231, 374–382. doi: 10.1006/abio.1995.9984

Gale, P. A. (2003). Anion and ion-pair receptor chemistry: highlights from 2000 and 2001. *Coord. Chem. Rev.* 240, 191–221. doi: 10.1016/S0010-8545(02)00258-8

Hahn, F. E., Langenhahn, V., Lügger, T., Pape, T., and Le Van, D. (2005). Template synthesis of a coordinated tetracarbene ligand with crown ether topology. *Angew. Chem. Int. Ed.* 44, 3759–3763. doi: 10.1002/anie.200462690

Hahn, F. E., Radloff, C., Pape, T., and Hepp, A. (2008). Synthesis of silver(I) and gold(I) complexes with cyclic tetra- and hexacarbene ligands. *Chem. Eur. J.* 14, 10900–10904. doi: 10.1002/chem.200801877

Hindi, K. M., Panzner, M. J., Tessier, C. A., Cannon, C. L., and Youngs, W. J. (2009). The medicinal applications of imidazolium carbene–metal complexes. *Chem. Rev.* 109, 3859–3884. doi: 10.1021/cr800500u

Johnson, N. A., Southerland, M. R., and Youngs, W. J. (2017). Recent developments in the medicinal applications of silver-NHC complexes and imidazolium salts. *Molecules* 22:1263. doi: 10.3390/molecules22081263

Lu, T., Yang, C., Steren, C. A., Fei, F., Chen, X., and Xue, Z. (2018). Synthesis and characterization of Ag(I) and Au(I) complexes with macrocyclic hybrid amine N-heterocyclic carbene ligands. *N. J. Chem.* 42, 4700–4713. doi: 10.1039/C7NJ04020B

Lu, T., Yang, C. F., Zhang, L. Y., Fei, F., Chen, X. T., and Xue, Z. L. (2017). Metal complexes with a hexadentate macrocyclic diamine-tetracarbene ligand. *Inorg. Chem.* 56, 11917–11928. doi: 10.1021/acs.inorgchem.7b01896

Mageed, A. H., Skelton, B. W., and Baker, M. V. (2017). Stable AuIII complexes with four N-heterocyclic carbene groups can be prepared in high yield directly from $KAuCl_4$. *Dalton Trans.* 46, 7844–7856. doi: 10.1039/C7DT01272A

Mageed, A. H., Skelton, B. W., Sobolev, A. N., and Baker, M. V. (2018). Formation of dinuclear AuII and AuI/AuIII mixed-valence complexes is directed by structural constraints imposed by cyclophane-NHC ligands. *Eur. J. Inorg. Chem.* 2018, 109–120. doi: 10.1002/ejic.201701272

Martínez-Máñez, R., and Sancenón, F. (2003). Fluorogenic and chromogenic chemosensors and reagents for anions. *Chem. Rev.* 103, 4419–4476. doi: 10.1021/cr010421e

Mckie, R., Murphy, J. A., Park, S. R., Spicer, M. D., and Zhou, S. Z. (2007). Homoleptic crown N-heterocyclic carbene complexes. *Angew. Chem. Int. Ed.* 46, 6525–6528. doi: 10.1002/anie.200702138

Melaiye, A., Sun, Z., Hindi, K., Milsted, A., Ely, D., Reneker, D. H., et al. (2005). Silver(I)–imidazole cyclophane gem-diol complexes encapsulated by electrospun tecophilic nanofibers: formation of nanosilver particles and antimicrobial activity. *J. Am. Chem. Soc.* 127, 2285–2291. doi: 10.1021/ja040226s

Mesquida, N., Dinarès, I., Ibáñez, A., and Alcalde, E. (2013). [14]Heterophane prototypes containing azolium and/or azole anion-binding motifs. *Org. Biomol. Chem.* 11, 6385–6396. doi: 10.1039/c3ob41214h

Meyer, S., Klawitter, I., Demeshko, S., Bill, E., and Meyer, F. (2013). A tetracarbene–oxoiron(IV) complex. *Angew. Chem. Int. Ed.* 52, 901–905. doi: 10.1002/anie.201208044

Neelakandan, P. P., and Ramaiah, D. (2008). DNA-assisted long-lived excimer formation in a cyclophane. *Angew. Chem. Int. Ed.* 47, 8407–8411. doi: 10.1002/anie.200803162

Nomiya, K., Morozumi, S., Yanagawa, Y., Hasegawa, M., Kurose, K., Taguchi, K., et al. (2018). Syntheses, structures, and antimicrobial activities of gold(I)– and copper(I)–N-heterocyclic carbene (NHC) complexes derived from basket-shaped dinuclear Ag(I)–NHC complex. *Inorg. Chem.* 57, 11322–11332. doi: 10.1021/acs.inorgchem.8b00011

Pöthig, A., Ahmed, S., Winther-Larsen, H. C., Guan, S., Altmann, P. J., Kudermann, J., et al. (2018). Antimicrobial activity and cytotoxicity of Ag(I) and Au(I) pillarplexes. *Front. Chem.* 6:584. doi: 10.3389/fchem.2018.00584

Schulte to Brinke, C., and Hahn, F. (2015). Synthesis of a flexible macrocyclic tetraimidazolium salt–precursor for a tetracarbene ligand with metal dependent coordination modes. *Dalton Trans.* 44, 14315–14322. doi: 10.1039/C5DT02115D

Schulte to Brinke, C., Pape, T., and Hahn, F. E. (2013). Synthesis of polynuclear Ag(I) and Au(I) complexes from macrocyclic tetraimidazolium salts. *Dalton Trans.* 42, 7330–7337. doi: 10.1039/c2dt32905k

Serpell, C. J., Cookson, J., Thompson, A. L., and Beer, P. D. (2011). A dual-functional tetrakis-imidazolium macrocycle for supramolecular assembly. *Chem. Sci.* 2, 494–500. doi: 10.1039/C0SC00511H

Shah, P. N., Lin, L. Y., Smolen, J. A., Tagaev, J. A., Gunsten, S. P., Han, D. S., et al. (2013). Synthesis, characterization, and *in vivo* efficacy of shell cross-linked nanoparticle formulations carrying silver antimicrobials as aerosolized therapeutics. *ACS Nano.* 7, 4977–4987. doi: 10.1021/nn400322f

Shirinfar, B., Ahmed, N., Park, Y. S., Cho, G. S., Youn, I. S., Han, J. K., et al. (2013). Selective fluorescent detection of RNA in living cells by using imidazolium-based cyclophane. *J. Am. Chem. Soc.* 135, 90–93. doi: 10.1021/ja3112274

Toure, M., Charles, L., Chendo, C., Viel, S., Chuzel, O., and Parrain, J.-L. (2016). Straightforward and controlled shape access to efficient macrocyclic imidazolylboronium anion receptors. *Chem. Eur. J.* 22, 8937–8942. doi: 10.1002/chem.201601174

Wong, W. W., Vickers, M. S., Cowley, A. R., Paul, R. L., and Beer, P. D. (2005). Tetrakis(imidazolium) macrocyclic receptors for anion binding. *Org. Biomol. Chem.* 3, 4201–4208. doi: 10.1039/b510068b

Xu, Z., Kim, S. K., and Yoon, J. (2010). Revisit to imidazolium receptors for the recognition of anions: highlighted research during 2006–2009. *Chem. Soc. Rev.* 39, 1457–1466. doi: 10.1039/b918937h

Yoon, J., Kim, S. K., Singh, N. J., and Kim, K. S. (2006). Imidazolium receptors for the recognition of anions. *Chem. Soc. Rev.* 35, 355–360. doi: 10.1039/b513733k

Yuan, Y., Gao, G., Jiang, Z., You, J., Zhou, Z., Yuan, D., et al. (2002). Synthesis and selective anion recognition of imidazolium cyclophanes. *Tetrahedron* 58, 8993–8999. doi: 10.1016/S0040-4020(02)01153-5

Conflict of Interest Statement: The authors declare that the research was conducted in the absence of any commercial or financial relationships that could be construed as a potential conflict of interest.

Advantages of publishing in Frontiers

OPEN ACCESS
Articles are free to read for greatest visibility and readership

FAST PUBLICATION
Around 90 days from submission to decision

HIGH QUALITY PEER-REVIEW
Rigorous, collaborative, and constructive peer-review

TRANSPARENT PEER-REVIEW
Editors and reviewers acknowledged by name on published articles

Frontiers
Avenue du Tribunal-Fédéral 34
1005 Lausanne | Switzerland

Visit us: www.frontiersin.org
Contact us: info@frontiersin.org | +41 21 510 17 00

REPRODUCIBILITY OF RESEARCH
Support open data and methods to enhance research reproducibility

DIGITAL PUBLISHING
Articles designed for optimal readership across devices

FOLLOW US
@frontiersin

IMPACT METRICS
Advanced article metrics track visibility across digital media

EXTENSIVE PROMOTION
Marketing and promotion of impactful research

LOOP RESEARCH NETWORK
Our network increases your article's readership